10/1-26-96 JS ①

LBL-36948
UC-413
CONF-9402145 (February)
CONF-9407188 (July)

Hard Processes in Hadronic Interactions

by H. Satz and X.-N. Wang
(Editors)

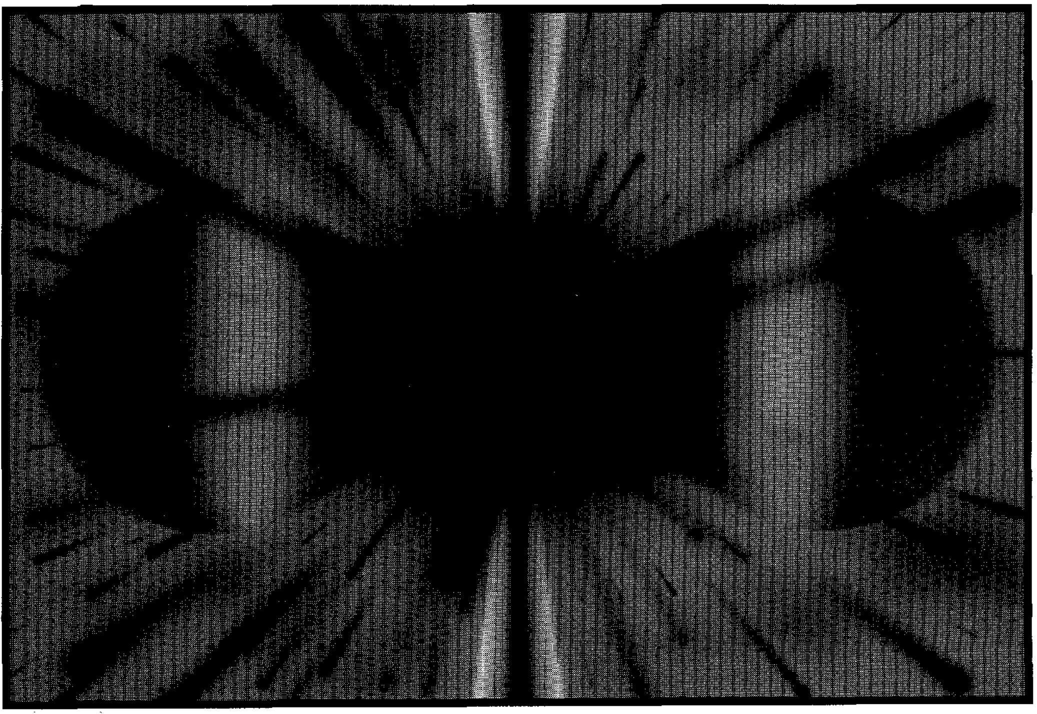

July 1995

DISTRIBUTION OF THIS DOCUMENT IS UNLIMITED

Lawrence Berkeley National Laboratory
University of California

Prepared for the U.S. Department of Energy under Contract DE-AC03-76SF00098

This document was prepared as an account of work sponsored by the United States Government. While this document is believed to contain correct information, neither the United States Government nor any agency thereof, nor The Regents of the University of California, nor any of their employees, makes any warranty, express or implied, or assumes any legal liability or responsibility for the accuracy, completeness, or usefulness of any information, apparatus, product, or process disclosed, or represents that its use would not infringe privately owned rights. Reference therein to any specific commercial product, process, or service by its trade name, trademark, manufacturer, or otherwise, does not necessarily constitute or imply its endorsement, recommendation, or favoring by the United States Government or any agency thereof, or The Regents of the University of California. The views and opinions of authors expressed herein do not necessarily state or reflect those of the United States Government or any agency thereof or The Regents of the University of California and shall not be used for advertising or product endorsement purposes.

Lawrence Berkeley Laboratory is an Equal Opportunity Employer

LBL-36948
UC-413
CONF-9402145 (February)
CONF-9407188 (July)
CERN-95-05

Hard Processes in Hadronic Interactions

H. Satz[a,b] and X.-N. Wang[c]
(Editors)

[a]Theory Division, CERN, CH-1211 Geneva 23, Switzerland
and
bFakultat für Physik, Universität Bielefeld, D-33501 Bielefeld, Germany

[c]Nuclear Science Division
Lawrence Berkeley Laboratory
University of California
Berkeley, California 94720

July 1995

This work was supported by the Director, Office of Energy Research, Office of High Energy and Nuclear Physics, Division of High Energy Physics, of the U.S. Department of Energy under Contract No. DE-AC03-76SF00098.

LBL-36948, CERN-95-05

HARD PROCESSES IN HADRONIC INTERACTIONS

(Published in Int. J. Mod. Phys. A **10**, 2881-3090)

H. Satz and X.-N. Wang
(Editors)

CONTENTS

HARD PROCESSES IN HADRONIC INTERACTIONS

H. SATZ[a,b] and X.-N. WANG[c]

[a]*Theory Division, CERN, CH-1211 Geneva 23, Switzerland*
and
[b]*Fakultät für Physik, Universität Bielefeld, D-33501 Bielefeld, Germany*

[c]*Nuclear Science Division, MS 70A-3307*
Lawrence Berkeley Laboratory,
University of California, Berkeley, California 94720, USA

Quantum chromodynamics is today accepted as the fundamental theory of strong interactions, even though most hadronic collisions lead to final states for which quantitative QCD predictions are still lacking. For viable collisions studies, at least part of the interaction must be accessible to a perturbative treatment, and this assigns a very special role to hard processes in hadronic interactions. They provide the test of QCD in hadronic collisions, and they show what uncertainties are at present scales still inherent in the predictions obtained. These uncertainties have different origins. On one hand, the perturbative part is calculated up to some fixed order, and higher orders can still lead to corrections, such as the familiar "K-factor". On the other hand, the non-perturbative parts – structure functions of hadrons, hadronisation features – introduce elements which at this time can only be determined from experiment. In recent years, higher order calculations were carried out for a number of processes, and new data from HERA have led to considerable changes in structure functions. It therefore seems worthwhile to take stock of where we stand today and to what extent the presently available data on hard processes in hadronic collisions can be accounted for in terms of QCD. This is one reason for our work.

The second reason – and in fact its original trigger – is the search for the quark-gluon plasma in high energy nuclear collisions. This new state of matter, predicted by statistical QCD, consists of deconfined quarks and gluons of high density, and to check if the early phases of nuclear collisions have indeed produced such a plasma, sufficiently hard probes are needed to resolve the short distance nature of the medium. Hard processes in hadronic collisions probe the partonic nature of hadrons and are therefore ideally suited for this endeavor. In hadronic matter, partons are confined to their "parent" hadrons; in the quark-gluon plasma, they become deconfined, and hard hadronic processes should indicate this transition in the partonic infrastructure. In order to use them for this purpose, we should first understand the basic process, in the absence of any medium, and then check what modifications each basic process experiences in confined hadronic matter. After these two "normalisation" steps, we would be prepared to look for parton deconfinement. The present work addresses the first of the two steps; for the second, a similar analysis should be carried out for hadron-nucleus collisions, and we hope to take this up in a subsequent work.

The hard processes to be considered here are the production of

- prompt photons,
- Drell-Yan dileptons,
- open charm,
- quarkonium states,
- hard jets.

For each of these, we shall discuss the present theoretical understanding, compare the resulting predictions to available data, and then show what behaviour it leads to at RHIC and LHC energies. All of these processes have the structure mentioned above: they contain a hard partonic interaction, calculable perturbatively, but also the non-perturbative parton distribution within a hadron. These parton distributions, however, can be studied theoretically in terms of counting rule arguments, and they can be checked independently by measurements of the parton structure functions in deep inelastic lepton-hadron scattering.

Since the parton distributions thus play a fundamental role in all hard hadronic interactions, we begin our survey with a status report on the present status of structure function studies. It is followed by a report on how to access the latest distribution function parametrisations kept in the Parton Distribution Function Library (PDFLib) at CERN. Next, the main concepts (renormalisation and factorisation scales, higher order contributions) are introduced in a section on Drell-Yan dilepton production, where perturbative studies have been carried out in particular detail. With this basis given, we then turn to the theoretical description of the specific hard processes, the comparison with present data and the corresponding predictions for RHIC and LHC energies. In most cases, these predictions can now be compared to recent very high energy data from the CERN $p\bar{p}$ collider and from the Tevatron at Fermilab, and this comparison is carried out wherever possible. This clearly makes the RHIC and LHC predictions for proton-proton collisions quite reliable.

Although hard processes are here considered only for hadron-hadron interactions and high energy predictions are given only for $p-p$ (or $p-\bar{p}$) collisions, our results also provide a reference frame for $p - A$ and $A - B$ studies. Let us assume that the rates for hard hadron-nucleus or nucleus-nucleus interactions are given by all two-body interactions between incident nucleons along a common path through the nucleus. The nuclear collision rates can then be obtained from our tabulated $p - p$ values by multiplying the $p - p$ cross section with nuclear overlap functions. These are tabulated in the Appendix, together with some examples. The predictions obtained in this way describe nuclear collisions in the absence of any specific nuclear or other collective effects.

The present volume is the work of *Hard Probe Collaboration*, a group of theorists who are interested in the problem and were willing to dedicate a considerable amount of their time to work on it. In addition, we had the valuable help of a number of outside experts on hard processes. It is a great pleasure for us to thank them for their essential assistance. All contributors to this first phase of our project are listed below.

The necessary preparation, planning and coordination of the project were carried out in two workshops of two weeks' duration each, in February 1994 at CERN in Geneva and in July 1994 at LBL in Berkeley. We express our sincere gratitude to CERN and LBL for the moral and financial support that made these meetings possible. The next phase, the study of hard processes in hadron-nucleus collisions, will begin in the summer of 1995 at the European Nuclear Theory Institute ECT* in Trento/Italy.

Contributors to Hard Processes in Hadronic Interactions

The Hard Probe Collaboration

J. Cleymans, K. Eskola, R. V. Gavai, S. Gavin, S. Gupta, D. Kharzeev, E. Quack,
K. Redlich, P. V. Ruuskanen, H. Satz, G. Schuler, K. Sridhar, D. K. Srivastava,
R. L. Thews, R. Vogt, X.-N. Wang

with

P. Aurenche, R. Kauffman, A. D. Martin, P. L. McGaughey, H. Plothow-Besch,
G. Ridolfi, R. G. Roberts, W. J. Stirling, W. L. van Neerven

STRUCTURE FUNCTIONS AND PARTON DISTRIBUTIONS

A. D. MARTIN[a], R. G. ROBERTS[b] and W. J. STIRLING[a]

[a]*Department of Physics, University of Durham,*
Durham DH1 3LE, England
[b]*Rutherford Appleton Laboratory,*
Chilton, Didcot OX11 0QX, England

The MRS parton distribution analysis is described. The latest sets are shown to give an excellent description of a wide range of deep-inelastic and other hard scattering data. Two important theoretical issues—the behavior of the distributions at small x and the flavor structure of the quark sea—are discussed in detail. A comparison with the new structure function data from HERA is made, and the outlook for the future is discussed.

INTRODUCTION

The parton distribution functions $f_{i/p}(x, Q^2)$ $(i = u, d, s, \ldots, g)$ describe how the proton's momentum is shared between its quark and gluon constituents, when probed at length scale Q^{-1}. They are directly related to the structure functions $F_i(x, Q^2)$ measured in lepton-nucleon deep-inelastic scattering (DIS) experiments. There are two main reasons—one experimental and one theoretical—why these distributions are important. First, a detailed knowledge of parton distributions is necessary in order to make precise calculations of 'hard scattering' cross sections at current and future hadron-hadron colliders. Second, the parton structure is interesting in its own right, providing tests of perturbative QCD and insight into the non-perturbative long-distance structure of hadrons. For example, novel perturbative QCD effects are expected to become apparent at small x ($\lesssim 10^{-3}$), where soft gluon emission off the incoming parton leads to a power series in $\alpha_s \log(1/x)$. Resummation of this series, via the Lipatov (or BFKL) equation [1], gives a gluon distribution which behaves as

$$x f_g \sim x^{-\lambda} \tag{1}$$

as $x \rightarrow 0$, with λ predicted, typically, to be about 0.5. Parton distributions also reveal how SU(3) flavor symmetry is broken in the quark-antiquark sea, which has important implications for non-perturbative models of the structure of hadrons.

There is a long history of determining parton distributions from data on deep-inelastic and other hard-scattering processes. In this review we will describe the

'MRS' series of distributions, which have provided some of the most accurate, up-to-date information on parton structure, making full use of the ever-increasing precision of the experimental measurements. Although broadly similar to other 'modern' sets of distributions, the MRS distributions do differ in some important respects. In what follows we shall, where appropriate, draw attention to these differences.

Table 1 lists the MRS sets of recent years, together with the data fitted.[*] The original sets MRS(1,2,3) were constrained mainly by DIS data from EMC. When these data were found to be in disagreement with new BCDMS data[8], two new sets HMRS(E,B) were provided. With the advent of data from NMC, this discrepancy was resolved in favor of the BCDMS-type fits. The KMRS sets explored the small-x behavior of the distributions with the B$_-$ set incorporating, for the first time, the Lipatov behavior $xg, xq \sim x^{-0.5}$ as $x \to 0$. The most significant recent (pre-HERA) experimental developments were the new NMC measurements [9] of $F_2^{\mu p}$ and $F_2^{\mu n}$ (from $F_2^{\mu D}$) and the CCFR measurements [10] of $F_2^{\nu N}$ and $xF_3^{\nu N}$. These provided the first detailed information on quark distributions in the $0.01 \lesssim x \lesssim 0.1$ range . The KMRS sets (and almost all others) considerably underestimated the structure functions in this region, see Fig. 1. The 1992 MRS(S$_0$,D$_0$,D$_-$) sets incorporated these new data. A new feature was the provision for the first time of light quark flavor asymmetry in the sea, *i.e.* $\bar{u} \neq \bar{d}$, motivated by the NMC measurements [11] of the Gottfried Sum Rule (see below). When the NMC and CCFR data were finally published, the fits were fine-tuned, resulting in the most recent MRS(S$'_0$,D$'_0$,D$'_-$) sets.

set	μ-DIS	ν-DIS	Prompt γ	D-Yan	W, Z
MRS '88 [3] (sets 1,2,3)	EMC + ...	CDHSW	AFS ($+J/\psi$)	—	—
HMRS '90 [4] (sets E,B)	EMC BCDMS NMC(n/p)	CDHSW	WA70	E605	—
KMRS '90 [5] (sets B$_0$,B$_-$)	BCDMS NMC(n/p)	CDHSW	WA70	E605	—
MRS (Apr '92) [6] (sets D$_0$,D$_-$)	BCDMS NMC(p, n)†	CDHSW CCFR†	WA70	E605	(UA2, CDF
MRS (Nov '92) [7] (sets D$'_0$,D$'_-$)	BCDMS NMC(p, n)	CCFR	WA70	E605	(UA2, CDF)

Table 1: MRS parton distributions together with the data used in the various analyses. Data marked † were used in preliminary form.

---

[*] The FORTRAN code for all of these can be found, for example, in the PDFLIB compilation [2]

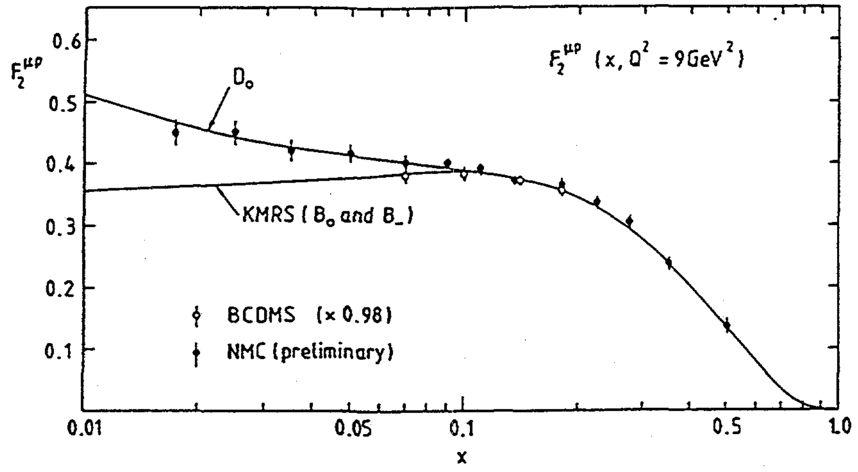

Figure 1: The structure function $F_2^{\mu p}(x,Q^2)$ as a function of x at $Q^2 = 9$ GeV^2 obtained by interpolating the measurements of the BCDMS collaboration [8] and preliminary measurements from NMC [9]. The upper curve corresponds to the D$_0$ set of partons [6], and the lower curve to the earlier KMRS sets of partons [5] obtained before the NMC data were available.

Deep-inelastic muon and neutrino data tightly constrain the valence and sea quark distributions. In contrast, the gluon distribution only enters indirectly at NLO, and is therefore much less well determined. Essentially the only constraint is the momentum sum rule, which shows that the gluon carries just less than 50% of the proton's momentum at $Q^2 \sim 4$ GeV^2. On the other hand, the gluon enters at *leading* order in large-p_T prompt photon production in hadron-hadron collisions: for $pp \to \gamma X$, the dominant QCD subprocess is $gq \to \gamma q$, in contrast to $p\bar{p} \to \gamma X$ where the annihilation process $q\bar{q} \to \gamma g$ is much more important. Particularly useful are data from the WA70 collaboration [12], which determine the gluon in the region $x \sim 0.35$. Combined with the momentum sum rule constraint, this leads to an input gluon behavior proportional to $(1-x)^{5.3}$ at large x. The Drell-Yan $pN \to \mu^+\mu^- X$ process, which is mediated at leading order by $q_{\text{val}}\bar{q}_{\text{sea}} \to \gamma^*$, constrains the large-$x$ $(1-x)^{\eta_S}$ behavior of the sea quark distributions. The most precise data here are from the E605 collaboration [13]. Finally, data on W and Z production at $\bar{p}p$ colliders [14, 15] provide additional constraints on the u and d distributions, particularly when the accurate NMC measurements of $F_2^{\mu n}/F_2^{\mu p}$ are fitted simultaneously. Other hadron collider data, in particular on inclusive jet, prompt photon and $b\bar{b}$ production, provide important cross-checks on the gluon distribution, while not yet being of sufficient precision to influence the fits [16].

In the following section we describe in detail the theoretical framework used in the MRS parton distribution analysis. In subsequent sections we address two topical issues which impinge directly on the fits: the flavor structure of the quark sea and the form of the distributions at very small x. In Section 4 we compare our predictions at small x with the new data on F_2^{ep} from HERA.

THE MRS(1992) ANALYSIS

Table 1 shows that the parton distributions f_i are determined from global fits to a wide range of deep-inelastic and related data. The basic procedure is to parametrize the f_i at a sufficiently large Q_0^2, (4 GeV^2 in the MRS analyses), so that $f_i(x, Q^2)$ can be calculated at higher Q^2 in perturbative QCD via the next-to-leading order (NLO) DGLAP evolution equations. In view of the quantity and variety of data to be fitted, it is remarkable that the starting distributions at Q_0^2 can be described by very simple parametrizations; in total only about 15 parameters are required. For the recent (S_0',D_0',D_-') sets we use

$$\begin{aligned} x\,[u_V + d_V] &= A_{ud}\, x^{\eta_1}\, (1-x)^{\eta_2}\, (1 + \epsilon_{ud}\sqrt{x} + \gamma_{ud} x) \\ x\, d_V &= A_d\, x^{\eta_3}\, (1-x)^{\eta_4}\, (1 + \epsilon_d\sqrt{x} + \gamma_d x) \\ x\, S &= A_S\, x^{\delta_g}\, (1-x)^{\eta_S}\, (1 + \epsilon_S\sqrt{x} + \gamma_S x) \\ x\, g &= A_g\, x^{\delta_g}\, (1-x)^{\eta_g}\, (1 + \gamma_g x)\ . \end{aligned} \tag{2}$$

The flavor structure of the quark sea is

$$\begin{aligned} 2\,\bar{u} &= 0.4\,S\, -\, \Delta \\ 2\,\bar{d} &= 0.4\,S\, +\, \Delta \\ 2\,\bar{s} &= 0.2\,S \\ x\,\Delta &= A_\Delta\, x^{\eta_1}\, (1-x)^{\eta_S} \\ h &= 0, \quad Q^2 \leq 4m_h^2 \quad \text{for } h = c, b, \ldots\ . \end{aligned} \tag{3}$$

The numerical values of the parameters are listed in Table 2. Note that the distributions are defined in the $\overline{\mathrm{MS}}$ renormalization and factorization scheme. The fitted value of the QCD scale parameter is $\Lambda_{\overline{\mathrm{MS}}}^{(4)} = 230$ MeV ($\alpha_s(M_Z^2) = 0.112_5$), consistent with what is found by the experimental collaborations in fits to their own DIS data sets.

Figures showing fits to all the input data and tables of the corresponding values of χ^2 can be found in Refs. [6, 7] and will not be presented again here. An example of the quality of the fit to the high precision muon deep-inelastic data has already been shown in Fig. 1. Figure 2 [7] shows the corresponding fit to the neutrino scattering data from CCFR [10]. Note that the data have been rescaled by a constant factor 0.95 (the normalization of the NMC data is taken as standard and other DIS sets are rescaled to give the best overall fit) and corrected for the effect of the heavy nuclear target [6]. To parametrize the uncertainty in this, a theory error of ±2% is included in the errors on the data shown in Fig. 2.

		S_0'	D_0'	D_-'	H
Glue	(A_g)	2.78	2.78	0.338	0.787
	δ_g	0	0	−0.5	−0.3
	η_g	5.3	5.3	5.3	5.3
	γ_g	0	0	10.6	5.20
Valence	η_1	0.31	0.42	0.42	0.33
	η_2	3.85	3.92	3.92	3.89
	ϵ_{ud}	6.12	2.31	2.59	5.06
	γ_{ud}	9.86	4.43	4.21	8.80
	η_3	0.82	0.24	0.24	0.22
	η_4	4.60	4.67	4.67	4.64
	ϵ_d	−1.38	43.3	28.7	101.
	γ_d	1.10	7.62	8.58	5.31
Sea	A_S	1.98	2.03	0.083	0.386
	η_S	10	10	7.4	9.0
	ϵ_S	−2.68	−2.98	8.57	0.013
	γ_S	7.98	8.47	15.8	12.0
	A_Δ	0	0.152	0.164	0.05

Table 2: Numerical values of the starting distribution parameters in the latest MRS(1992) fits. Note that A_g is fixed by the momentum sum rule, and is therefore not a free parameter.

A key feature of the MRS analysis is that the parametrization of the starting distributions is designed not only to be 'minimal', in that extra parameters are included only when required by the data, but also to allow a clear picture of the underlying *physics* as revealed in the distributions. For example, the large-x behavior of the various distributions (controlled by the parameters η_2, η_4, η_S and η_g) can be compared directly with predictions from dimensional counting, while the small-x behavior (η_1, η_3 and δ_g) can be compared with the predictions of resummed perturbation theory and Regge theory.

FLAVOR STRUCTURE OF THE QUARK SEA

Up-down Flavor Asymmetry

It is difficult to determine $\bar{u}$ and $\bar{d}$ separately from the deep-inelastic data. In fact, prior to 1992 most analyses assumed that the non-strange sea was flavor symmetric, *i.e.* $\bar{u} = \bar{d}$. The motivation for allowing $\bar{u} \neq \bar{d}$ came from comparing the NMC measurement [11] of the Gottfried Sum

$$\int_{0.004}^{0.8} \frac{dx}{x} \left(F_2^{\mu p} - F_2^{\mu n}\right) = 0.227 \pm 0.007\ (\mathrm{stat.}) \pm 0.014\ (\mathrm{sys.}) \tag{4}$$

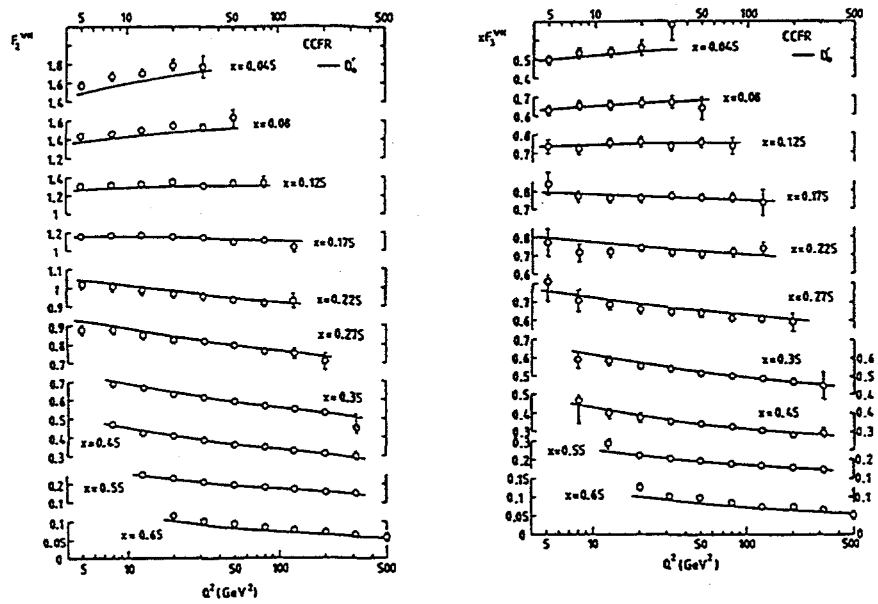

Figure 2: The $F_2^{\nu N}(x, Q^2)$ structure function measured by the CCFR collaboration [10]. The data are shown after correction for the heavy target effects and after an overall renormalization of 0.95 required by the global fit. The statistical, systematic and heavy target correction errors have been combined in quadrature. The curves correspond to the D_0' fit [7].

at $Q^2 = 4$ GeV^2 with the theoretical expectation

$$\begin{aligned} I_{\rm GSR} = \int_0^1 \frac{dx}{x}\,(F_2^{\mu p} - F_2^{\mu n}) &= \tfrac{1}{3}\int_0^1 \frac{dx}{x}\,(u_V - d_V) + \tfrac{2}{3}\int_0^1 \frac{dx}{x}\,(\bar{u} - \bar{d}) \\ &= \tfrac{1}{3}\,, \quad \text{if } \bar{u} = \bar{d}\,. \end{aligned} \qquad (5)$$

A straightforward comparison of (4) and (5) implies $\bar{u} \neq \bar{d}$. In the MRS 'D' fits [6, 7] $\bar{d} - \bar{u}$ is parametrized according to (3), with the parameter A_Δ chosen such that the measured value of $I_{\rm GSR}$ is reproduced. It is interesting to note, however, that even including the NMC data it is still possible to maintain $\bar{u} = \bar{d}$ and obtain an equally good global description of the data, at the expense of a contrived small-x behavior of the valence distributions, as in set S_0 [6] or S_0' [7]. On the other hand, the lack of Regge $\rho - a_2$ exchange degeneracy suggests that it is more reasonable to allow $\bar{u} \neq \bar{d}$, as in sets D_0' and D_-'. The fits to the NMC data on $F_2^{\mu p} - F_2^{\mu n}$ are shown in Fig. 3.[†]

[†] Note that the latest MRS(D_0',D_-',H) sets have $I_{\rm GSR} = 0.256, 0.240, 0.290$. An updated analysis of the Gottfried Sum by NMC gives $I_{\rm GSR} = 0.258 \pm 0.010$(stat.) $\pm$ 0.015(sys.) at $Q^2 = 4$ GeV^2 [17].

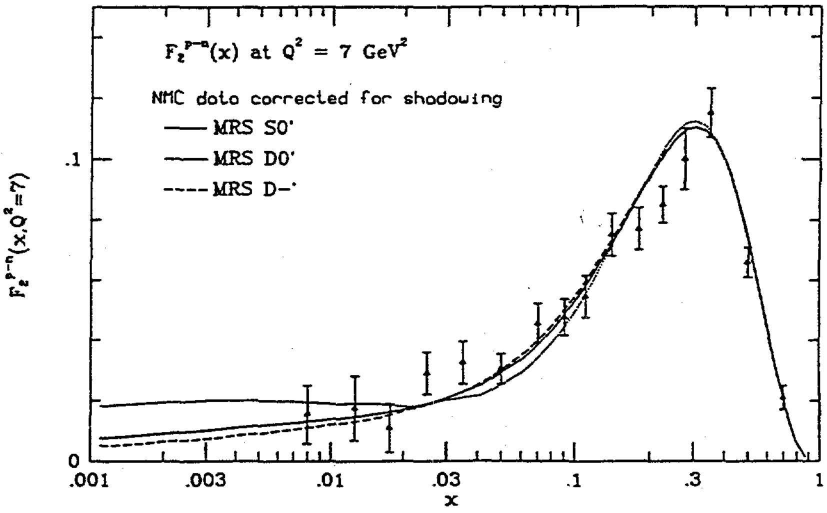

Figure 3: The structure function difference $F_2^{\mu p} - F_2^{\mu n}$ from NMC [11], with the $((\mathrm{S}_0', \mathrm{D}_0', \mathrm{D}_-')$ fits [18].

The detailed structure of $\bar{d} - \bar{u}$ is not determined by the available DIS data. All we really know is that on average $\bar{d} > \bar{u}$ at small x. An independent method for obtaining further information on $\bar{d} - \bar{u}$ [19] is to compare (Drell-Yan) lepton-pair production in pp and pn collisions, via the asymmetry

$$A_{\mathrm{DY}} = \frac{\sigma_{pp} - \sigma_{pn}}{\sigma_{pp} + \sigma_{pn}} \, . \tag{6}$$

Because $u > d$ in the proton, the asymmetry is positive for sets with $\bar{d} - \bar{u}$ zero or small at large x. A measurement [20] of the asymmetry to an accuracy of a few per cent will provide a powerful discriminator of the possible behaviors of $\bar{d} - \bar{u}$. Predictions of various sets of parton distributions and a more complete discussion can be found in Ref. [18].

Strange Quarks

The strange quark distribution can be extracted directly from accurate measurements of the *difference* between the F_2 structure functions measured in neutrino scattering off a heavy isoscalar target and muon scattering off a deuterium target:

$$xs(x) = \tfrac{5}{6} F_2^{\nu N}(x) - 3 F_2^{\mu D}(x) \, . \tag{7}$$

This method for obtaining $s(x)$ is, however, subject to considerable uncertainties. It relies on an accurate knowledge of the structure function normalization in the two types of experiment and, in the case of neutrino scattering, is sensitive to the heavy target corrections used. A more reliable method is to use the presence of an extra muon in deep-inelastic neutrino scattering to tag events originating in $sW^+ \rightarrow c(\rightarrow \mu^+ + \ldots)$, *i.e.*

$$\sigma(\nu N \rightarrow \mu^- \mu^+ + \ldots) \; \propto \; \{(u+d)|V_{cd}|^2 + 2s|V_{cs}|^2\} \, D^{c\rightarrow\mu^+} \; \simeq \; 2s|V_{cs}|^2 \, D^{c\rightarrow\mu^+} \; . \quad (8)$$

Early measurements of the dimuon rate were, in fact, the motivation for the 50% suppression of the strange quarks in the MRS analyses, see Eq. (3). By utilizing both neutrino and antineutrino scattering it is possible to measure this suppression directly, through the ratio $\kappa = 2\int s/(\int \bar{u} + \int \bar{d})$ where $\int s \equiv \int_0^1 s(x)dx$ *etc.* A recent next-to-leading order QCD analysis by the CCFR collaboration [21] gives

$$\kappa \; = \; 0.435 \; \pm 0.058\,(\text{stat.}) \; \pm 0.012\,(\text{sys.}) \; . \quad (9)$$

This result is in almost perfect agreement with the MRS predictions. Figure 4 shows the strange quark distribution extracted by CCFR at $Q^2 = 4$ GeV^2 (in the form of a '1σ' band of distributions) together with the MRS(D$'_0$,D$'_-$) predictions [7].

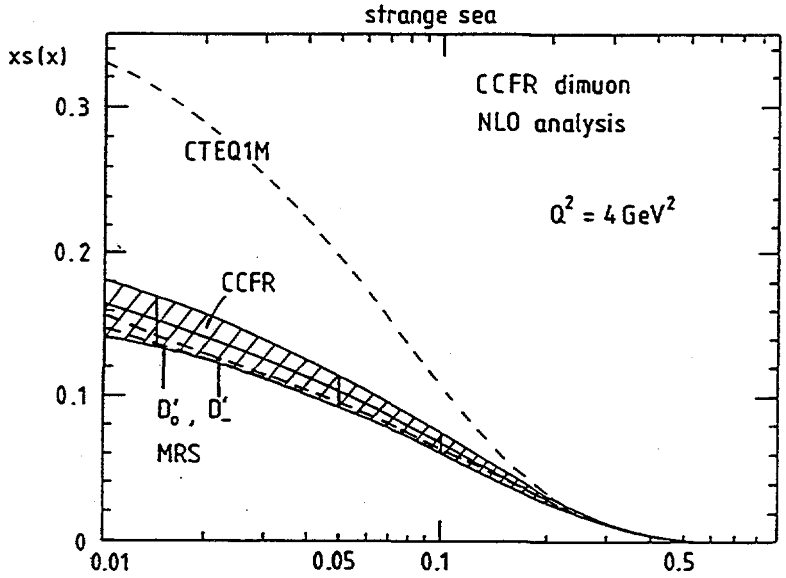

Figure 4: The strange quark distribution (shaded band) at $Q^2 = 4$ GeV^2 as extracted from the dimuon cross section using a next-to-leading order QCD analysis, from the CCFR collaboration [21]. Also shown are the MRS(D$'_0$,D$'_-$) [7] and the CTEQ [23] predictions.

Figure 4 also shows the predictions of set 1M from the recent CTEQ analysis [23]. This has a much larger strange sea and is clearly disfavored by the dimuon data. The reason lies in the different treatment of the sea quark distributions in the two analyses. In contrast to MRS, the CTEQ sea distributions are freely and independently parametrized, with no *ab initio* strange suppression. The large strange sea originates from their simultaneous fit to the F_2 structure functions, which essentially corresponds to using Eq. (7). There *is* a slight disagreement between the MRS fits and the $F_2^{\nu N}$ data at small x, see Fig. 2, although not as large as the size of the CTEQ strange sea would suggest. The reason is that in the MRS analysis, the CCFR data are renormalized by 0.95 relative to the NMC data, and allowance is made in the neutrino data errors for the uncertainty in the heavy target correction [22]. It is interesting to speculate whether the slight disagreement evident at small x in Fig. 2 is due to some experimental problem or whether, as argued for example in Ref. [25], there *should* be some difference in the strange sea as measured in neutrino and muon scattering. Such a difference could result, for example, from the different mass thresholds involved in the two types of scattering, $W^+g \to c\bar{s}$ *vs.* $\gamma^* g \to s\bar{s}$, if the heavy flavors are assumed to originate in gluon splitting.

PARTON DISTRIBUTIONS AT SMALL x

In the MRS fits, the small-x form of the gluon and sea-quark distributions at Q_0^2 is fixed at either $xf \sim x^0$ or $xf \sim x^{-1/2}$. These represent two 'extreme' forms of theoretical behavior: x^0 is the standard non-perturbative Regge prediction, based on the high energy behavior of the photon-quark forward scattering amplitude:

$$\lim_{\nu \to \infty} \mathrm{Im}\, A(\gamma q \to \gamma q) \sim \nu^{\alpha_P} \Rightarrow \lim_{x \to 0} F_2 \sim x^{1-\alpha_P} \, . \tag{10}$$

Assuming Pomeron exchange dominance gives $\alpha_P \simeq 1$ and therefore $xf \sim x^0$. It is likely, however, that in practice the more dominant effect at small x comes from perturbatively calculable multiple soft-gluon emission, as embodied in the 'Lipatov' (or BFKL) equation [1]. The k_T differential distribution, defined by

$$xg(x, Q^2) = \int^{Q^2} \frac{dk_T^2}{k_T^2} f(x, k_T^2) \tag{11}$$

satisfies an evolution equation in $\log(1/x)$,

$$-x \frac{\partial f}{\partial x} = \int dk'^2 K(k, k') f(x, k'^2) \, , \tag{12}$$

and the small-x behavior is controlled by the largest eigenvalue λ of the eigenfunction equation $K \otimes f_n = \lambda_n f_n$, for then $f \sim \exp(\lambda \log(1/x)) \sim x^{-\lambda}$ as $x \to 0$. For fixed strong coupling $\lambda = 4C_A(\log 2)\, \alpha_s/\pi \approx 0.5$, which gives the small-$x$ behavior assumed for the set D'_-.

It should be stressed, however, that this is a leading-logarithm, fixed-coupling prediction—it is not yet known if the $x^{-1/2}$ behavior survives a proper treatment of subleading effects, for example, from next-to-leading logarithms, infra-red cut-offs, parton saturation, kinematic constraints *etc.* It is likely that the net effect of these is to slow down the growth of the distributions at small x, see for example Ref. [24].

The predictions of the MRS(D'_0,D'_-) sets for F_2^{ep} in the small-x HERA regime are shown in Fig. 5. Note that the predictions are essentially identical for $x \gtrsim 0.02$ (the fixed target DIS data are equally well fitted by both sets) but, by construction, are dramatically different at small x. Also shown are (i) the CTEQ1M and

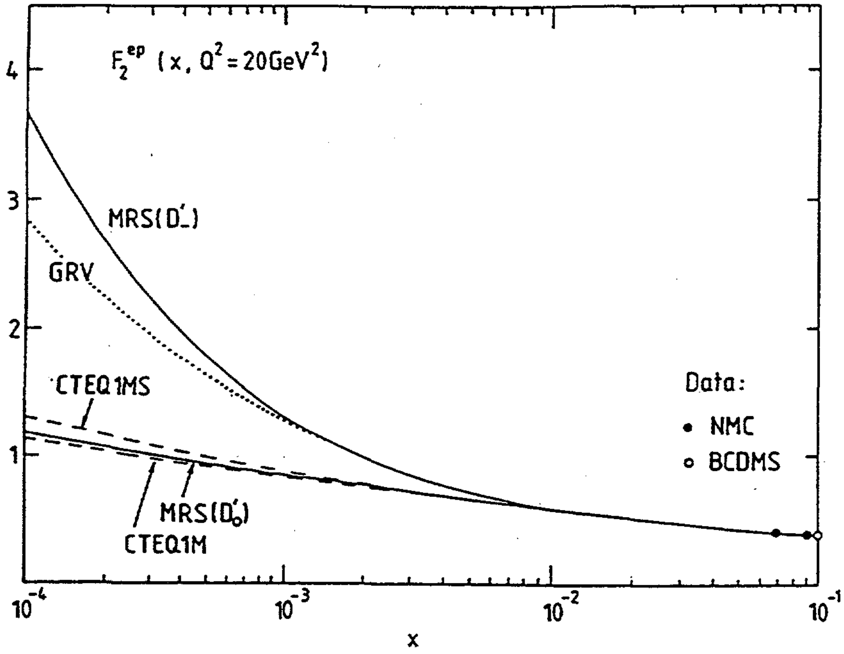

Figure 5: Predictions for F_2^{ep} at $Q^2 = 20$ GeV^2 obtained from the parton sets from Refs. [7, 23, 26].

CTEQ1MS predictions [23] and (ii) the predictions from the 'dynamical quark' model of Glück, Reya and Vogt (GRV) [26]. For the former analysis, the small x behavior is essentially determined by the lowest x points of the fixed-target DIS data, with no particular theoretical constraints imposed. In the latter approach, 'valence-like' distributions at very low Q ($Q_0^2 = 0.3$ GeV^2) are evolved and fitted to MRS valence quark distributions at a higher Q. The growth seen for GRV at small x is thus a result of perturbative DGLAP Q^2 evolution. By coincidence, it is not unlike that seen for D'_-, at least in the HERA regime.

FIRST RESULTS FROM HERA

The new results on F_2 from the H1 [27] and ZEUS [28] collaborations confirm the dramatic behavior first evident in the preliminary data analysis—the structure function rises at small x, in line with the expected Lipatov behavior. This

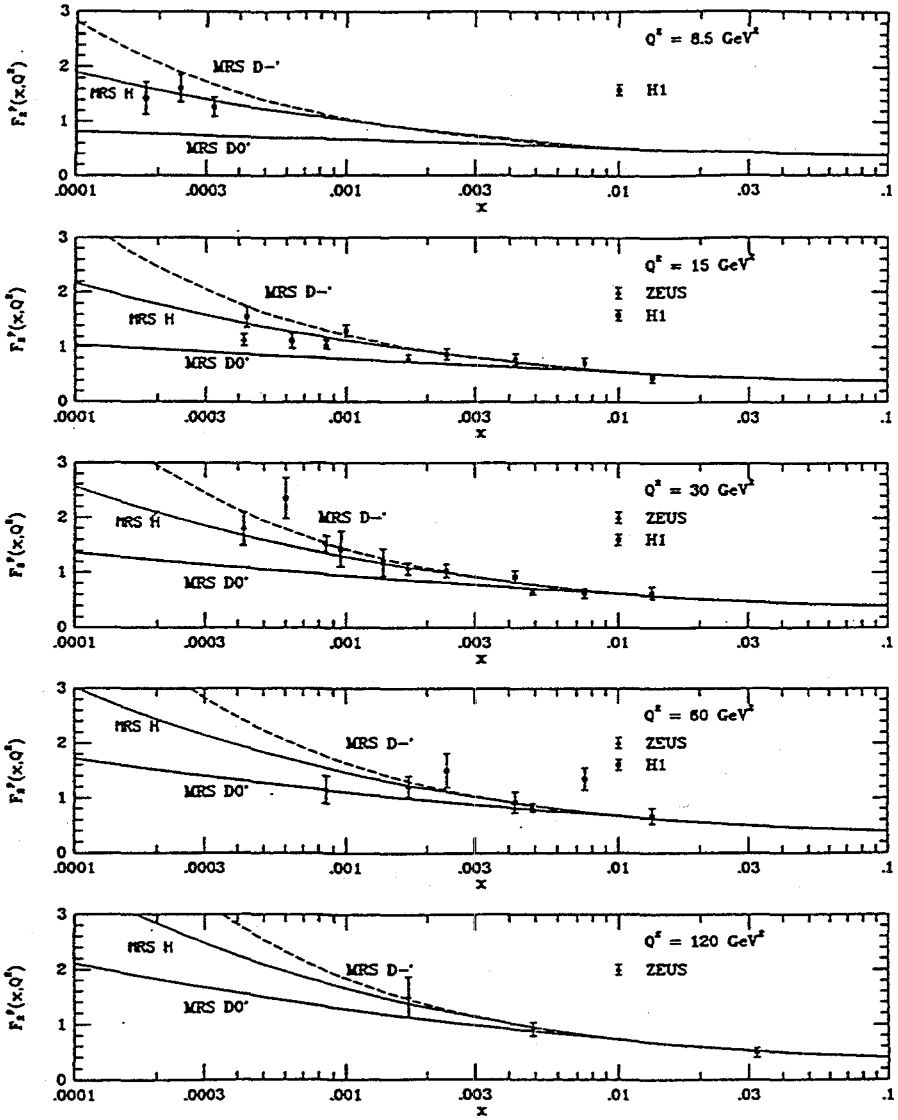

Figure 6: The structure function F_2^{ep} from H1 [27] and ZEUS [28] at HERA, with the predictions from the MRS parton sets D_0' and D_-' [7]. Also shown is a new fit MRS(H) with $\delta_g = -0.3$, which minimizes the overall χ^2.

is illustrated in Fig. 6, which shows the new data together with the MRS(D_0',D_-') predictions. The data clearly prefer the D_-' prediction.‡ The errorbars are still too large to make a truly quantitative comparison: one would like, for example, to see whether the data favored a pure $x^{-\lambda}$ form over the more complicated form of the dynamical quark model [26]. In the meantime, it is straightforward to 'tune' the exponent δ_g of the input sea and gluon distributions (Eq. (2)) to obtain a best fit to the new data. The result of doing this - set MRS(H) with $\delta_g = -0.3$ - is shown as the dotted curve in Fig. 6. The other parameters for this new fit are listed in Table 2.

The measurements of F_2^{ep} at HERA probe primarily the sea quark distribution at small x. If the 'perturbative pomeron' is indeed responsible for the steep rise, then the same behavior should also be seen in the gluon distribution. Methods for directly extracting the gluon distribution from HERA measurements of the longitudinal structure function F_L [29] and $dF_2/d\log Q^2$ have been suggested. These are based on the observation that in the leading-order expressions

$$
\begin{aligned}
F_L(x,Q^2) &= \frac{\alpha_s(Q^2)}{\pi}\left\{\frac{4}{3}\int_x^1 \frac{dy}{y}\left(\frac{x}{y}\right)^2 F_2(y,Q^2)\right. \\
&\quad \left. +2\sum_q e_q^2 \int_x^1 \frac{dy}{y}\left(\frac{x}{y}\right)^2\left(1-\frac{x}{y}\right) yg(y,Q^2)\right\} \qquad (13)
\end{aligned}
$$

$$
\begin{aligned}
\frac{dF_2(x,Q^2)}{d\log Q^2} &= \frac{\alpha_s(Q^2)}{2\pi}\left\{\int_x^1 \frac{dy}{y}\left(\frac{x}{y}\right) P_{qq}\left(\frac{x}{y}\right) F_2(y,Q^2)\right. \\
&\quad \left. +2\sum_q e_q^2 \int_x^1 \frac{dy}{y}\left(\frac{x}{y}\right) P_{qg}\left(\frac{x}{y}\right) yg(y,Q^2)\right\} \qquad (14)
\end{aligned}
$$

it is the gluon term on the right-hand-side that dominates at small x in each case. The predictions of the MRS(D_0',D_-') sets for these two quantities are shown, with the gluon distributions, in Fig. 7. The clear correlations lend support to the case for making precise measurements of these two quantities, leading to qualitative estimates of the underlying gluon behavior.

Finally, we can ask whether any further information on the small x partons can be obtained from hadron colliders, in particular that Fermilab $p\bar{p}$ collider. It is straightforward to show that at $\sqrt{s} = 1.8$ TeV, x values comparable to those currently measured at HERA can be probed either by very small mass systems produced centrally, or by more massive final states at large rapidity. The Drell-Yan process offers some possibilities for the former (see for example Ref. [30]) while 'medium-p_T' forward jet production is ideal for the latter. As an illustration, Fig. 8 shows the ratio of same-side to opposite-side jet cross sections from CDF [31], as a function of the equal and opposite jet rapidities y. The curves are the MRS(D_0',D_-') predictions evaluated at leading order with a renormalization/factorization scale chosen to mimic the NLO corrections. Further details of this analysis can be found in Ref. [32]. At large rapidity, the ratio is sensitive to the small-x *gluon* distribution, and it is interesting to note that, despite the uncertainties from both theory and experiment, once again the D_-' prediction is preferred.

---

‡Note that the Q^2 dependence is also consistent, within large errors, with DGLAP evolution.

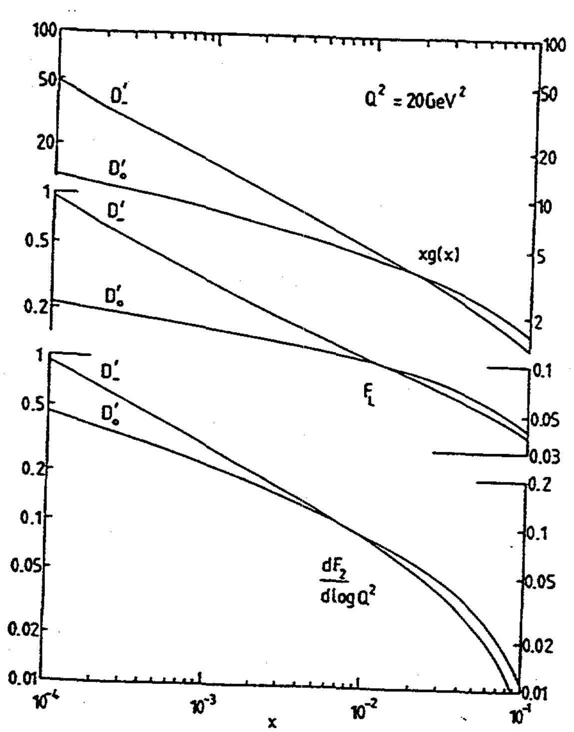

Figure 7: The sensitivity of two structure function methods of determining the small x gluon at HERA, illustrated in terms of the gluon distributions of [7]. F_L is the longitudinal structure function for deep-inelastic ep scattering. The curves are calculated using the full next-to-leading order QCD expressions.

OUTLOOK

The structure function data from HERA shown in the previous section is based on only about 25 nb^{-1} at each detector, accumulated during 1992. Since the corresponding integrated luminosity is already close to 500 nb^{-1}, it is clear that our knowledge of the small-x region will be significantly improved over the next year. The increased precision of the gluon and sea distributions will not only shed light on the topical question of the dynamics of perturbative QCD at low x, but will also allow the predictions for many processes at LHC and SSC to be sharpened. Continuing to improve our knowledge of the partonic structure of the proton will clearly be a high priority for some time to come.

Since this talk was given, there have been refinements and updates to the global analyses presented. New measurements of proton structure functions from HERA, both from H1 and Zeus, based on data taken during 1993 [33] together with precise measurements of asymmetries in W production by CDF [34] and in the Drell-Yan process [35] have allowed more precise estimates for the parton densities. Details

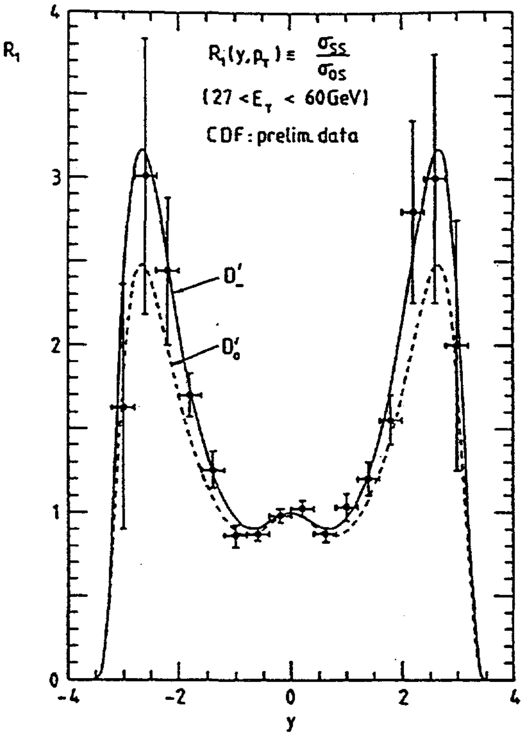

Figure 8: The curves show the same-side/opposite-side dijet ratio predictions from the D'_- and D'_0 partons [7], for $27 < p_T < 60$ GeV. The data points are the preliminary CDF measurements [31], but note that the measured jet p_T values have not been corrected for CDF detector effects and therefore do not correspond directly to the true jet transverse energies.

of the new MRS(A) parametrisation and the new CTEQ3 parametrisation can be found in refs [36, 37].

References

[1] E.A. Kuraev, L.N. Lipatov and V.S. Fadin, Sov. Phys. JETP **45** (1977) 199. Ya.Ya. Balitsky and L.N. Lipatov, Sov. J. Nucl. Phys. **28** (1978) 822.

[2] H. Plothow-Besch, Comp. Phys. Commun. **75** (1993) 396; and contribution in these proceedings.

[3] A. D. Martin, R. G. Roberts and W. J. Stirling, Phys. Rev. D **37** (1988) 1161; see also Phys. Lett. **206B** (1988) 327; Mod. Phys. Lett. **A4** (1989) 1135.

[4] P. N. Harriman, A. D. Martin, R. G. Roberts and W. J. Stirling, Phys. Rev. D **42** (1990) 798.

[5] J. Kwiecinski, A. D. Martin, R. G Roberts and W. J. Stirling, Phys. Rev. D **42** (1990) 3645.

[6] A. D. Martin, W. J. Stirling and R. G. Roberts, Phys. Rev. D **47** (1993) 867.

[7] A. D. Martin, W. J. Stirling and R. G. Roberts, Phys. Lett. **306B** (1993) 145.

[8] BCDMS collaboration: A. C. Benvenuti *et al.*, Phys. Lett. **223B** (1989) 485.

[9] NMC: P. Amaudruz *et al.*, Phys. Lett. **295B** (1992) 159.

[10] CCFR collaboration: Phys. Rev. Lett., to be published.

[11] NMC: P. Amaudruz *et al.*, Phys. Rev. Lett. **66** (1991) 2712; E.M. Kabuß, Nucl. Phys. B (Proc. Supp.) **29A** (1992) 1.

[12] WA70 collaboration: M. Bonesini *et al.*, Z. Phys. C **38** (1988) 371.

[13] E605 collaboration: C. N. Brown *et al.*, Phys. Rev. Lett. **63** (1989) 2637.

[14] UA2 collaboration: J. Alitti *et al.*, Phys. Lett. **276B** (1992) 365.

[15] CDF collaboration: F. Abe *et al.*, Phys. Rev. D **44** (1991) 29.

[16] See for example: W. J. Stirling, Proc. Conf. on 'QCD – 20 Years Later', Aachen, eds. P. M. Zerwas and H. A. Kastrup, World Scientific, Vol.1, p.387 (1993).

[17] NMC: M. Arneodo *et al.*, preprint CERN-PPE/93-117 (1993).

[18] A. D. Martin, R. G. Roberts and W. J. Stirling, Phys. Lett. **B308** (1993) 377.

[19] S. D. Ellis and W. J. Stirling, Phys. Lett. **B256** (1991) 258.

[20] M. C. Abreu *et al.*, CERN proposal SPSLC 92-15 (1992).
G. T. Garvey *et al.*, Fermilab proposal P866 (1992).

[21] CCFR collaboration: A. Bazarko *et al.*, Columbia University preprint NEVIS–1492 (1993).

[22] A. D. Martin, R. G. Roberts and W. J. Stirling, 'Present status of parton distributions', Proc. of the Durham Workshop on 'HERA – the new frontier for QCD', to be published in J. Phys. **G**, RAL preprint RAL-93-027 (1993).

[23] CTEQ collaboration: J. Botts, J. Morfin, J. Owens, J. Qiu, W.-K. Tung and H. Weerts, Phys. Lett. **304B** (1993) 159.

[24] A. J. Askew, J. Kwiecinski, A. D. Martin and P. J. Sutton, Phys. Rev. D **47** (1993) 3775.

[25] V. Barone *et al.*, Phys. Lett. **B268** (1991) 279; University of Turin preprints DFTT-28/93, DFTT-39/93 (1993).

[26] M. Glück, E. Reya and A. Vogt, Z. Phys. C **48** (1990) 471, C **53** (1992) 127; Phys. Lett. **B306** (1993) 391.

[27] H1 collaboration: I. Abt *et al.*, preprint DESY-93-117 (August 1993).

[28] ZEUS collaboration: M. Derrick *et al.*, preprint DESY-93-110 (August 1993).

[29] A. M. Cooper-Sarkar *et al.*, Z. Phys. C **39** (1988) 281.

[30] CDF collaboration: F. Abe *et al.*, preprint FERMILAB-PUB-93-133-E (1993).

[31] CDF collaboration: contribution to the EPS Conference on High Energy Physics, Marseilles, July 1993, preprint FERMILAB-Conf-93/203-E (1993).

[32] A. D. Martin, R. G. Roberts and W.J. Stirling, University of Durham preprint DTP/93/48 (1993).

[33] H1 collaboration: K. Müller, Proc. of 29th Rencontre de Moriond, March 1994. ZEUS collaboration: G. Wolf, Proc. of International Workshop on Deep Inelastic Scattering, Eilat, Feb. 1994; M. Roco, Proc. of 29th Rencontre de Moriond, March 1994.

[34] CDF collaboration: A. Bodek, Proc. of International Workshop on Deep Inelastic Scattering, Eilat, Feb. 1994.

[35] NA51 collaboration: A. Baldit *et al.*, Phys. Lett. **B332** (1994) 244.

[36] A. D. Martin, W. J. Stirling and R. G. Roberts, preprint RAL-94-055, DTP/94/34 to be published in Phys. Rev. D.

[37] H.L. Lai *et al.*, preprint MSU-HEP-41024, CTEQ-404

THE PARTON DISTRIBUTION FUNCTION LIBRARY

H. PLOTHOW-BESCH

Physik IV, Universität Dortmund
D - 44221 Dortmund, Germany

This article describes an integrated package of Parton Density Functions called PDFLIB which has been added to the CERN Program Library Pool W999 and is labelled as W5051. In this package all the different sets of parton density functions of the **Nucleon**, the **Pion** and the **Photon** which are available today have been put together. All these sets have been combined in a consistent way such that they all have similar calling sequences and no external data files have to be read in anymore. A default set has been prepared, although those preferring their own set or wanting to test a new one may do so within the package. The package also offers a program to calculate the strong coupling constant α_s to first or second order. The correct Λ_{QCD} associated to the selected set of structure functions and the number of allowed flavours with respect to the given Q^2 is automatically used in the calculation. The selection of sets, the program parameters as well as the possibilities to modify the defaults and to control errors occurred during execution are described.

THE LIBRARY OF PARTON DENSITIES: PDFLIB

Perturbative QCD describes the Q^2 dependence of the parton densities through the solution of the Altarelli-Parisi equations. Its predictive power is given by the universality of these densities. Usually these densities are extracted from precision measurements in fixed-target experiments of a given process at some scale - recently they have also been extracted from the HERA ep-collision experiments -, and then used to perform calculations for different reactions in an extrapolated range of Q^2 provided that the elementary cross sections at the parton level are known. To be able to predict cross sections for a wide range of hard scattering processes, it is of fundamental importance to have a reliable and precise set of parton density distributions, together with a precise value of the strong coupling constant α_s. Therefore the momentum distributions of quarks and gluons are key ingredients for the lepton-lepton, lepton-hadron and hadron-hadron collider phenomenology, whenever the hadronic structure of nucleons, pions or photons is involved. Apart from the obvious applications mentioned above, the study of parton distributions provides also information about flavour dependence, isospin symmetry, partons in nuclei, sum rules, polarized parton distibutions, etc.. For any application the parton densities should therefore be sufficiently well known, and the different sets should be easily accessible.

Structure Functions of the Nucleon

The number of sets of parton density functions of the **Nucleon** available today is about 70 and is still growing. The older sets are leading order (LO) evolutions of the Altarelli-Parisi equations only, like

- Buras and Gaemers (BEBC)[1],
- Owens and Reya (O-R)[2],
- Baier, Engels and Petersson (BEP)[3],
- Glück, Hoffmann and Reya (GHR)[4],
- Duke and Owens (DO)[5] sets 1 and 2,
- Eichten, Hinchliffe, Lane and Quigg (EHLQ)[6] sets 1 and 2,
- Diemoz, Ferroni, Longo and Martinelli (DFLM)[7] with $\Lambda^{[4]}_{QCD} = 200$ MeV for soft and hard valence quark and soft and hard gluon distributions,

and

- the set 1.1 of Owens (DO 1.1)[8], replacing DO[5] sets 1 and 2.

Most of the sets, essentially the more recent ones, are next-to-leading order (NLL) evolutions of the Altarelli-Parisi equations, like

- the different sets of Diemoz, Ferroni, Longo and Martinelli (DFLM)[7]
- Martin, Roberts and Stirling (MRS)[9] sets 1 to 3, sets E and B and sets E' and B',
- Harriman, Martin, Roberts and Stirling (HMRS)[10] sets E, E+, E- and B,
- Kwiecinski, Martin, Roberts and Stirling (KMRS)[11] sets B0 and B-, and for the B- set with different radii for shadowing,
- Martin, Roberts and Stirling (MRS-BΛ)[11] for the B0 set also with different values of $\Lambda^{[4]}_{QCD} = 135, 160, 200$ and 235 MeV,
- Martin, Roberts and Stirling (MRS)[12] sets S0, D0 and D- as well as the upgraded KMRS set B0, all having $\overline{up} \neq \overline{down}$.
- Morfin and Tung (M-T)[13] sets 1 to 6,
- Glück, Reya and Vogt (GRV)[14],
- the set of Aurenche et al. (ABFOW)[15],
- the upgraded Martin, Roberts and Stirling (MRS)[16] sets S0', D0' and D-' as well as the more recent MRS(H) set,
- the Berger and Meng (BM)[17] sets 1 and 2,
- the two versions of the CTEQ collaboration (CTEQ)[18],

and finally

- the recent set of Martin, Roberts and Stirling (MRS-A)[19] in form of a grid and in form of a parametrisation.

The different NLL sets use either the DIS[31] or the $\overline{MS}$ renormalisation scheme. Some of the sets are available in both renormalisation schemes. All sets are made using four flavours in the initial state (NF = 4). The value of the QCD scale factor, $\Lambda^{[4]}_{QCD}$, ranges from 45 to 500 MeV.

A summary of all parton density functions of the **Nucleon** available in the package can be found in Tables 1 and 2.

Structure Functions of the Pion

There is also a limited number of parton density functions of the **Pion** available. These are the set to leading order evolutions of

- Owens (OW)[20], sets 1 and 2,

and the next-to-leading order evolutions of

- Aurenche et al. (ABFKW-P)[21], sets 1, 2 and 3,
- Sutton, Martin, Roberts and Stirling (SMRS-P)[22] sets 1, 2 and 3, and
- Glück, Reya and Vogt (GRV-P)[23], the LO and NLL sets.

A summary of all parton density functions of the **Pion** available in the package can be found in Table 3.

Structure Functions of the Photon

In addition there are also a few parton density functions of the **Photon** available. These are the leading order evolutions of

- Duke and Owens (DO-G) (and the NLL)[24] using an asymptotic solution of the Altarelli-Parisi equation,
- Drees and Grassie (DG-G)[25] sets 1 to 4 using a full solution of the Altarelli-Parisi equation,
- Abramowicz, Charchula and Levy (LAC-G)[26] sets 1 to 3 using a full solution of the Altarelli-Parisi equation,

and the next-to-leading order evolutions of

- Gordon and Storrow (GS-G)[27], the LO sets 1 and 2 and the NLL set,
- Glück, Reya and Vogt (GRV-G)[28], the LO, NLL and the leading term of the NLL sets,
- Aurenche et al. (ACFGP-G)[29], sets 1 and 2, without and with massive charm, and finally
- the LO and NLL sets of Aurenche, Fontannaz and Guillet, (AFG-G)[30].

A summary of all parton density functions of the **Photon** available in the package can be found in Table 4.

Nptype	Ngroup	Nset	$\Lambda^{[4]}_{QCD}$	Q^2_{min}	Name of set			Reference
		0	**200**	**0.3**	**GRV HO**	$\overline{\mathbf{MS}}$	**NLL**	**Default**
1	1	1			PRIVATE to user			
1	1	2	45	0.5	BEBC		LO	[Nucl.Phys. B132 (1978) 249]
1	1	3	500	1.8	OR		LO	[Phys.Rev. D17 (1978) 3003]
1	1	4	470	5	BEP		LO	[Z. Phys. C2 (1979) 265]
1	1	5	400	4	GHR		LO	[Z. Phys. C13 (1982) 119]
1	1	6	200	4	DO Set 1		LO	[Phys.Rev. D30 (1984) 49]
1	1	7	400	4	DO Set 2		LO	
1	1	8	200	5	EHLQ Set 1		LO	[Rev.Mod. Phys. 56 (1984) 579;
1	1	9	290	5	EHLQ Set 2		LO	Rev.Mod. Phys. 58 (1985) 1065]
1	1	10	177	4	DO Set 1.1		LO	[Phys.Lett. 266B (1991) 126]
1	2	1	200	10	DFLM soft valence		LO	[Z. Phys. C39 (1988) 21]
1	2	2	200	10	DFLM hard valence		LO	
1	2	3	200	10	DFLM soft gluon		LO	
1	2	4	200	10	DFLM hard gluon		LO	
1	2	5	200	10	DFLM centr. average (LO)		LO	
1	2	6	300	10	DFLM centr. average (NLL)	DIS	NLL	
1	2	7	160	10	DFLM 160	DIS	NLL	[unpublished]
1	**2**	**8**	**260**	**10**	**DFLM 260**	**DIS**	**NLL**	
1	2	9	360	10	DFLM 360	DIS	NLL	
1	3	1	107	5	MRS 1	$\overline{MS}$	NLL	[Phys.Rev. D37 (1988) 1161]
1	3	2	250	5	MRS 2	$\overline{MS}$	NLL	
1	3	3	178	5	MRS 3	$\overline{MS}$	NLL	
1	3	4	91	5	MRS E	$\overline{MS}$	NLL	[Phys.Lett. 206B (1988) 327]
1	3	5	228	5	MRS B	$\overline{MS}$	NLL	
1	3	6	91	5	MRS E'	$\overline{MS}$	NLL	[Mod.Phys.Lett. A4 (1989) 1135]
1	3	7	228	5	MRS B'	$\overline{MS}$	NLL	
1	3	8	100	5	HMRS E (1.1990)	$\overline{MS}$	NLL	[retracted]
1	3	9	190	5	HMRS B (1.1990)	$\overline{MS}$	NLL	
1	3	10	100	5	HMRS E (3.1990)	$\overline{MS}$	NLL	
1	3	11	190	5	HMRS B (3.1990)	$\overline{MS}$	NLL	
1	3	12	100	5	HMRS E+ (4.1990)	$\overline{MS}$	NLL	[Phys.Lett. 243B (1990) 421]
1	3	13	100	5	HMRS E- (4.1990)	$\overline{MS}$	NLL	
1	3	14	100	5	HMRS E (4.1990)	$\overline{MS}$	NLL	[Phys.Rev. D42 (1990) 798]
1	3	15	190	5	HMRS B (4.1990)	$\overline{MS}$	NLL	
1	3	16	100	5	HMRS B (8.1990)	$\overline{MS}$	NLL	[unpublished]
1	3	17	300	5	HMRS B (8.1990)	$\overline{MS}$	NLL	
1	3	18	190	5	KMRS B- (7.1990)	$\overline{MS}$	NLL	[Phys.Rev. D42 (1990) 3645]
1	3	19	190	5	KMRS B-R2 Shad. (7.1990)	$\overline{MS}$	NLL	
1	3	20	190	5	KMRS B-R5 Shad. (7.1990)	$\overline{MS}$	NLL	
1	3	21	190	5	KMRS B0-190 (7.1990)	$\overline{MS}$	NLL	
1	3	22	135	5	MRS B0-135 (10.1990)	$\overline{MS}$	NLL	[Phys.Rev. D43 (1991) 3648]
1	3	23	160	5	MRS B0-160 (10.1990)	$\overline{MS}$	NLL	
1	3	24	200	5	MRS B0-200 (10.1990)	$\overline{MS}$	NLL	
1	3	25	235	5	MRS B0-235 (10.1990)	$\overline{MS}$	NLL	
1	3	26	215	5	MRS S0 (4.1992)	$\overline{MS}$	NLL	[retract.-Phys.Rev.D47 (1993) 867]
1	3	27	215	5	MRS D0 (4.1992)	$\overline{MS}$	NLL	
1	3	28	215	5	MRS D- (4.1992)	$\overline{MS}$	NLL	
1	3	29	230	5	MRS S0' (11.1992)	$\overline{MS}$	NLL	[Phys.Lett. 306B (1993) 145]
1	3	30	230	5	MRS D0' (11.1992)	$\overline{MS}$	NLL	
1	**3**	**31**	**230**	**5**	**MRS D-' (11.1992)**	$\overline{\mathbf{MS}}$	**NLL**	
1	3	32	230	5	MRS S0' (11.1992)	DIS	NLL	
1	3	33	230	5	MRS D0' (11.1992)	DIS	NLL	
1	**3**	**34**	**230**	**5**	**MRS D-' (11.1992)**	**DIS**	**NLL**	
1	3	35	230	5	MRS (H) (11.1993)	$\overline{MS}$	NLL	[RAL-93-077 (1993)]
1	3	36	230	5	MRS (H) (11.1993)	DIS	NLL	
1	3	37	230	5	MRS (A) (05.1994)	$\overline{MS}$	NLL	[RAL-94-055 (1994)]
1	3	38	230	5	MRS (A) (05.1994)	$\overline{MS}$	NLL	(Parametrisation of MRS (A))

Table 1: List of available sets of NUCLEON structure functions in PDFLIB version 5.02

Nptype	Ngroup	Nset	$\Lambda^{[4]}_{QCD}$	Q^2_{min}	Name of set			Reference
1	4	1	212	4	MT S1	DIS	NLL	[retract. - Z. Phys. C52 (1991) 13]
1	4	2	194	4	MT B1	DIS	NLL	
1	4	3	191	4	MT B2	DIS	NLL	
1	4	4	155	4	MT E1	DIS	NLL	
1	4	5	237	4	MT 6 (1/2s)	DIS	NLL	
1	4	6	212	4	MT S1	$\overline{MS}$	NLL	
1	4	7	194	4	MT B1	$\overline{MS}$	NLL	
1	4	8	191	4	MT B2	$\overline{MS}$	NLL	
1	4	9	155	4	MT E1	$\overline{MS}$	NLL	
1	4	10	237	4	MT 6 (1/2s)	$\overline{MS}$	NLL	
1	4	11	144	4	MT LO		LO	
1	4	12	168	4	CTEQ 1L		LO	[retracted]
1	4	13	231	4	CTEQ 1M	$\overline{MS}$	NLL	
1	4	14	231	4	CTEQ 1MS	$\overline{MS}$	NLL	
1	4	15	322	4	CTEQ 1ML	$\overline{MS}$	NLL	
1	4	16	247	4	CTEQ 1D	DIS	NLL	
1	4	17	190	4	CTEQ 2L		LO	[retracted]
1	4	18	213	4	CTEQ 2M	$\overline{MS}$	NLL	
1	4	19	208	4	CTEQ 2MS	$\overline{MS}$	NLL	
1	4	20	208	4	CTEQ 2MF	$\overline{MS}$	NLL	
1	4	21	322	4	CTEQ 2ML	$\overline{MS}$	NLL	
1	4	22	235	4	CTEQ 2D	DIS	NLL	
1	4	23	190	4	CTEQ 2pL		LO	[to be published]
1	**4**	**24**	**213**	**4**	**CTEQ 2pM**	$\overline{\mathbf{MS}}$	**NLL**	
1	4	25	208	4	CTEQ 2pMS	$\overline{MS}$	NLL	
1	4	26	208	4	CTEQ 2pMF	$\overline{MS}$	NLL	
1	4	27	322	4	CTEQ 2pML	$\overline{MS}$	NLL	
1	4	28	235	4	CTEQ 2pD	DIS	NLL	
1	5	1	160	0.2	old GRV HO	$\overline{MS}$	NLL	[retracted]
1	5	2	220	0.2	old GRV LO		LO	
1	**5**	**3**	**200**	**0.3**	**GRV HO**	$\overline{\mathbf{MS}}$	**NLL**	[Z. Phys. C53 (1992) 127]
1	5	4	200	0.25	GRV LO		LO	
1	6	1	230	2	ABFOW	$\overline{MS}$	NLL	[Phys.Rev. D39 (1989) 3275]
1	7	1	254	5	BM set A	$\overline{MS}$	NLL	[Phys.Lett. 304B (1993) 318;
1	7	2	254	5	BM set B	$\overline{MS}$	NLL	CERN-TH 6739/92 (1992)]

Table 2: List of available sets of NUCLEON structure functions, cont'd

Nptype	Ngroup	Nset	$\Lambda^{[4]}_{QCD}$	Q^2_{min}	Name of set			Reference
2	1	1	200	4	OW-P Set 1		LO	[Phys.Rev. D30 (1984) 943]
2	1	2	400	4	OW-P Set 2		LO	
2	3	1	190	5	SMRS-P 1	$\overline{MS}$	NLL	[Phys.Rev. D45 (1992) 2349]
2	**3**	**2**	**190**	**5**	**SMRS-P 2**	$\overline{\mathbf{MS}}$	**NLL**	
2	3	3	190	5	SMRS-P 3	$\overline{MS}$	NLL	
2	**5**	**1**	**200**	**0.3**	**GRV-P HO**	**MS**	**NLL**	[Z. Phys. C53 (1992) 651]
2	5	2	200	0.25	GRV-P LO		LO	
2	**6**	**1**	**231**	**2**	**ABFKW-P Set 1**	**MS**	**NLL**	[Phys.Lett. 233B (1989) 517]
2	6	2	181	2	ABFKW-P Set 2	$\overline{MS}$	NLL	
2	6	3	281	2	ABFKW-P Set 3	$\overline{MS}$	NLL	

Table 3: List of available sets of PION structure functions in PDFLIB version 5.02

Nptype	Ngroup	Nset	$\Lambda^{[4]}_{QCD}$	Q^2_{min}	Name of set			Reference
3	1	1	380	4	DO-G Set 1		LO	[Phys.Rev. D26 (1982) 1600]
3	**1**	**2**	**440**	**4**	**DO-G Set 2**	$\overline{\text{MS}}$	**NLL**	
3	**2**	**1**	**400**	**4**	**DG-G Set 1**		**LO**	[Z.Phys. C28 (1985) 451]
3	2	2	400	4	DG-G Set 2		LO	
3	2	3	400	4	DG-G Set 3		LO	
3	2	4	400	4	DG-G Set 4		LO	
3	**3**	**1**	**200**	**5**	**LAC-G Set 1**		**LO**	[Phys.Lett. 269B (1991) 458]
3	2	3	200	5	LAC-G Set 2		LO	
3	3	3	200	5	LAC-G Set 3		LO	
3	**4**	**1**	**200**	**5.3**	**GS-G HO**	$\overline{\text{MS}}$	**NLL**	[Z.Phys. C56 (1992) 307]
3	4	2	200	5.3	GS-G LO set 1		LO	
3	4	3	200	5.3	GS-G LO set 2		LO	
3	5	1	200	0.3	GRV-G LHO	DIS*)	LO	[Phys.Rev. D46 (1992) 1973;
3	**5**	**2**	**200**	**0.3**	**GRV-G HO**	**DIS*)**	**NLL**	Phys.Rev. D45 (1992) 3986]
3	5	3	200	0.25	GRV-G LO		LO	
3	6	1	200	2	ACFGP Set HO	$\overline{MS}$	NLL	[Z.Phys. C56 (1992) 589]
3	6	2	200	2	ACFGP Set HO-mc	$\overline{MS}$	NLL	
3	**6**	**3**	**200**	**2**	**AFG-G Set HO**	$\overline{\text{MS}}$	**NLL**	[LPTHE Orsay 93/37 (1993)]

*) not standard, please consult references.

Table 4: List of available sets of PHOTON structure functions in PDFLIB version 5.02

The Library PDFLIB

We have put together all these different sets of parton density functions in **one single package**[32]. We have modified the sets such that **no** external data files for the grids have to be read in anymore. All these structure function sets have been combined in a consistent way such that they all appear in an **identical structure** to the user. The selection is made via **three** parameters, NPTYPE, NGROUP and NSET, which identify a PDF set by its **particle type** (Nucleon: NPTYPE = 1, Pion: NPTYPE = 2, Photon: NPTYPE = 3), its **author group** (f.ex. MRS: NGROUP = 3) and its **PDF set within the group** (NSET = 1, 2, 3, etc.). These parameters should be set with a call to subroutine PDFSET at the initialization phase. A simple SUBROUTINE call, which is **identical** for all applications (nucleons, pions and photons), returns the parton densities for all partons (u, d, s, c, b, t, gluon and their antiquarks) at a given X value (where X is the fraction of the longitudinal momentum carried by the parton) and the Q-scale SCALE (in GeV). A **default** set has been prepared, although those preferring their **own private** set or wanting to test a **new** one may do so within the package. Error control can be obtained by setting a print flag to obtain output either during execution and/or as a summary at job termination via a call to the subroutine PDFSTA.

The source code of the different parton density sets has been modified in such a way that the library can be used on all the different computer systems known today. Full backward compatibility will always be assured. PDFLIB has been run under different operating systems like *VM/CMS, VAX/VMS and ULTRIX* without problems. The library has been tested on the different system areas to ensure identical results within the given machine precision. The program has been run and tested on the following computers: *IBM 3090, VAX, IBM-RISC, DECS, SUN, APOLLO, HP-UX, Silicon Graphics, CDC, CRAY, IBM-PC.* The programming language is FORTRAN 77; the program is also available in the PATCHY and the CMZ format. The required memory storage including testprograms and some documentation is about 5 700 000 bytes. The latest edition (September 1994) is version 5.02 and can be requested from the CERN Computer Program Library. To run PDFLIB a link to the CERN library (MATHLIB and KERNLIB) is required.

Calculations of the Strong Coupling Constant α_s

Within the **same package** a program is also provided to calculate the **strong coupling constant** α_s to second order (default) or to first order (by user's choice). The **correct Λ_{QCD}** associated to the selected set of structure functions and the number of allowed flavours with respect to the give Q^2 is automatically used in the calculation. For those structure functions where the evolution has been performed to leading order only, the α_s value to first order is returned.

APPLICATION OF THE PARTON DENSITIES PACKAGE PDFLIB

Parameter Setting and Selection of Sets

To access his/her preferred set of structure functions the user must define the **three** parameters, NPTYPE, NGROUP and NSET, which identify each set of parton density functions, via a call to the subroutine

```
CALL PDFSET(PARM,VALUE)
```

at the initialisation phase of his/her MAIN program, or may use the package as a 'black box' with the default values (see below). An example of the application of PDFLIB is given in the appendix. The arguments PARM and VALUE are **vectors** of dimension 20 and have the following meaning

PARM(I)=	character*20 variable, which defines in any order the variables 'NPTYPE', 'NGROUP', 'NSET', 'MODE', 'INIT0', 'NFL', 'LO', 'TMAS', 'QCDL4', 'QCDL5' and 'XMIN', 'XMAX', 'Q2MIN', 'Q2MAX'
VALUE(I)=	the corresponding numerical value of the variable PARM(I) (TMAS, QCDL4, QCDL5, XMIN, XMAX, Q2MIN and Q2MAX are DOUBLE PRECISION variables),

where

NPTYPE= number of particle type ranging from 1 to 3
(Nucleons: NPTYPE = 1, Pions: NPTYPE = 2, Photons: NPTYPE = 3)
(Default: NPTYPE = 1)

NGROUP= number of author group ranging from 1 to 7
(Default: NGROUP = 5)

NSET= number of a selected structure function set within the author group ranging from 1 to 34
(Default: NSET = 3)

(MODE= number of a selected structure function set ranging from 0 to 281
- **old** format !! -)
(Default: MODE = 45)

INIT0= in case of PARM(1) = 'INIT0' PDFSET fills as the only action the COMMON blocks /W505110/, /W505120/, /W505121/ and /W505122/

NFL= desired number of flavours in the α_s calculation ranging from 3 to 6
(Default: NFL = 5)

LO= order of α_s calculation; if LO = 1, α_s is calculated to first order only
(Default: LO = 2)

TMAS = the user defined value of the top-quark mass in GeV/c^2 (optional)
(Default: TMAS = 100.0D0)

QCDL4= QCD scale, $\Lambda^{[4]}_{QCD}$, in GeV for four flavours

QCDL5= QCD scale, $\Lambda^{[5]}_{QCD}$, in GeV for five flavours corresponding to QCDL4

and

XMIN= minimal allowed x value
XMAX= maximal allowed x value
Q2MIN= minimal allowed Q^2 value (in $(GeV/c)^2$)
Q2MAX= maximal allowed Q^2 value (in $(GeV/c)^2$)

for each set of structure functions.

Please note that PDFSET can be called as often as the user likes. In order to redefine the parameters to select other sets of structure functions which the user wants to investigate it might be necessary to call PDFSET in an alternating way, but it is always mandatory to transfer either the **three** parameters, NPTYPE, NGROUP, NSET, or the 'NAME' of the author group with their corresponding VALUE values. The subroutine PDFSET fills the **internal** COMMON blocks

```
COMMON/W50511/ NPTYPE,NGROUP,NSET,MODE,NFL,LO,TMAS
COMMON/W50512/ QCDL4,QCDL5
COMMON/W50513/ XMIN,XMAX,Q2MIN,Q2MAX
```

at the time the routine is called. Please note that in case of a multiple call to PDFSET with fewer parameters redefined than in a preceeding call, always the last parameters are kept in memory. All variables of the three COMMON blocks can be automatically printed at job initialisation by setting the print flag IFLPRT in the

COMMON block COMMON/W50510/ IFLPRT to IFLPRT = 2.

The program is protected against calculations of Q^2 values below Q2MIN (in this case Q^2 = Q2MIN) and of X values in unphysical regions ($X < 0$ or $X > 1$). The execution of the program is stopped in the later case. To control how often the X or Q^2 ranges have been exceeded during execution of the user's program a call to the subroutine

CALL PDFSTA

at the termination phase of his/her MAIN program allows to print a summary of these errors. The print flag in the COMMON/W50510/IFLPRT may be set to IFLPRT = 3 to print an error message **each time** a limit has been exceeded during job execution. Please note that this may produce an **enormous amount of output!**

The Calling Sequence: PDFLIB Format

The main steering routine for a set of structure functions is accessed as follows:

CALL STRUCTM(X,SCALE,UPV,DNV,USEA,DSEA,STR,CHM,BOT,TOP,GL)

Please note that all variables are defined as **DOUBLE PRECISION**. The user has to provide the following INPUTs:

X = x value of parton
SCALE = QCD scale in GeV

The subroutine STRUCTM returns the following OUTPUT:

UPV = up valence quark
DNV = down valence quark
USEA = sea ($\overline{up}$)
DSEA = sea ($\overline{down}$)
STR = strange quark
CHM = charm quark
BOT = bottom quark
TOP = top quark
GL = gluon

In case $\overline{up}$ is not given separately from $\overline{down}$ it is set USEA = DSEA.

The recommended set of structure functions from the different authors is put in bold characters. If NSET is set to zero (or if any of the parameters, NPTYPE, NGROUP or NSET, is undefined) **one default set** is selected which is always the Nucleon parton densities, the set of GRV HO (NPTYPE = 1, NGROUP = 5, NSET

= 3, former MODE = 72), also in case of NPTYPE = Pion or Photon.

Please note that in any of the calling sequences for the nucleon, the pion and the photon it is always returned **X × parton distribution function !**

The Calling Sequence: PDG Format

To allow the use of the package with the flavour code convention of the Particle Data Group (PDG) an interface has been written which translates the PDFLIB format (see Section 2.2) into the PDG format. Instead of calling the subroutine STRUCTM the user preferring the flavour code convention of the PDG accesses the package via a call to the subroutine

CALL PFTOPDG(X,SCALE,DXPDF).

All variables are defined as **DOUBLE PRECISION** as before, and X and SCALE are INPUTs provided by the user with the same meaning as before.

The subroutine PFTOPDG outputs a vector DXPDF(-6:6) of which its variables have the following meaning:

DXPDF(0) = gluon
DXPDF(1) = down valence quark + $\overline{down}$ sea
DXPDF(2) = up valence quark + $\overline{up}$ sea
DXPDF(3) = strange quark
DXPDF(4) = charm quark
DXPDF(5) = bottom quark
DXPDF(6) = top quark
and DXPDF(-1) to DXPDF(-6) are the corresponding antiquarks.

DXPDF(-1) = DXPDF(-2) stands for $\overline{down} = \overline{up}$ or $(\overline{down} + \overline{up})/2$ in allmost all parametrisations. In case where $\overline{down} \neq \overline{up}$ DXPDF(-1) = $\overline{down}$ and DXPDF(-2) = $\overline{up}$. In all sets is DXPDF(3) = DXPDF(-3), DXPDF(4) = DXPDF(-4), DXPDF(5) = DXPDF(-5) and DXPDF(6) = DXPDF(-6) so far.

PION AND PHOTON PARTON DENSITIES

The calling sequences to the *pion* and the *photon* sets of parton densities is kept identical to those described in Sections 2.2 and 2.3 for the nucleon structure functions.

In case of the pion structure functions it is set and returned UPV = DNV, SEA = STR (USEA = DSEA = STR) and TOP = 0 (DXPDF(1) = DXPDF(2), DXPDF(3) = DXPDF(-1) = DXPDF(-2) and DXPDF(6) = 0).

In case of the photon structure functions it is set and returned UPV = USEA, DNV = DSEA and TOP = 0 (DXPDF(1) = 2 * DXPDF(-1), DXPDF(2) = 2 * DXPDF(-2), as a result of the definitions - see Section 2.3 -, and DXPDF(6) = 0), while all the other quarks are set identical to their antiquark densities. Note that the α_{QED} has to be taken care of by the user !

α_s CALCULATION

Within the same package a program is provided to calculate the strong coupling constant α_s to second order as a function of Λ_{QCD} of five flavours and the desired number of flavours (NFL) for the selected set of structure functions, which fixes Λ_{QCD}. The formula on which the calculations are based upon can be found in Ref. 33. The same three parameters, NTYPE, NGROUP and NSET, which select a structure function set, is used to steer the calculation of the α_s value at a given scale from the Λ_{QCD} defined in the selected structure function.

The value of α_s is matched at the thresholds q = m_q. When invoked with NFL < 0, it chooses NFL as the number of flavours for which the masses are less then q. For the quark masses where thresholds are changed the following values have been used:

$$m_{charm} = 1.5\ GeV/c^2,\ m_{bottom} = 4.75\ GeV/c^2,\ m_{top} = 100\ GeV/c^2.$$

A call to the function:

FUNCTION ALPHAS2(SCALE),

where the user has to provide as INPUT only the QCD scale in GeV, provides as OUTPUT the value of alpha strong to second order, if LO not equal to one. For those structure functions, for which the evolution is done to leading order only, α_s to first order is returned.

The *internal* COMMON block COMMON/W50512/ QCDL4,QCDL5 with

QCDL4 = QCD scale, $\Lambda^{[4]}_{QCD}$, in GeV for four flavours
QCDL5 = QCD scale, $\Lambda^{[5]}_{QCD}$, in GeV for five flavours corresponding to QCDL4

provides the actual value of $\Lambda^{[4]}_{QCD}$ and $\Lambda^{[5]}_{QCD}$ used in the α_s calculation for four and five flavours, respectively, for each set of structure functions.

CONCLUSIONS

As an example, the **Nucleon** structure function distributions at the scale $Q^2 = m_W^2$ for the **up** valence quark is shown in Fig. 1 as a function of the parton X.

The average X values for CERN and FNAL as well as for LHC and SSC energies are indicated. It can be seen from that figure that there is a large spread in shape for the different sets leading to different results in a cross section calculation. It should be pointed out that the spread of different parametrisations in the **same** renormalisation scheme is **much larger** than the spread of parametrisations in **different** renormalisation schemes. This is valid for **all** parton densities, and in particular at small X values !

A comparison to recent data is shown in Fig. 2, where the ratio F_2^n/F_2^p at the Q^2 of the experimental points is displayed. Note that the older sets of structure functions, namely the set of Owens and Reya[2] and the set of Baier et al.[3] have only been implemented for completeness. These sets should not be used for cross section calculations of any hard process at high energies anymore. From Fig. 2 we conclude that also the other older sets of structure functions, namely the two sets of Duke and Owens[5] and the two sets of Eichten et al.[6], should be used with care, because they do not fit the recent low energy deep-inelastic lepton-nucleon data from NMC and BCDMS[34]. This is not surprising because these data were not available when the sets have been made. The new set of DO 1.1[8] superseeds the old DO sets 1 and 2, but still gives very limited results in the low X region, even though data are available there. We conclude that the recent sets of parton densities could be preferred for all theoretical predictions involving structure functions, because they fit the present nucleon data best.

In Fig. 3 the F_2^p distribution of Ref. 35 ($Q^2 = 5\ GeV^2$) together with recent data ($Q^2 = 15\ GeV^2$) from the H1 and the ZEUS experiments[36] at the ep-collider HERA is shown as a function of X. Overlayed on the same Figure are theoretical predictions of more recent parton parametrisations[12,13,14,15,16] at $Q^2 = 15\ GeV^2$. Please note that most of these parametrisations are **not true** predictions because the data are fully or partially used in the fits. ¿From Figs. 2 and 3 we conclude that the recent sets of parton densities, namely the GRV set HO[14], but also the old MT set B2[13] - both sets are true predictions - , and the updated MRS set H[16], could be preferred for all theoretical predictions involving nucleon structure functions, because they fit the present data best which, at the moment, are still suffering from large uncertainties.

Figure 4 shows a comparison of F_2^γ/α_{QED} at $Q^2 = 100\ GeV^2$ of the different **photon** structure function sets as a function of X. The charm quark density has been taken into account. The theoretical predictions are compared with experimental data from the JADE experiment[37] at the same Q^2 value. Because of large experimental uncertainties no distinction between the different parton density sets can be made yet.

The response from the Physics community has been very satisfactory, which is encouraging us to keep up-to-date with the latest developments in this area. Therefore, please **continue sending your feedback on the usage and possible improvements to us.** Coming new sets of structure functions should be easily implemented in the package. Authors of **new sets** are kindly asked to **provide** us with the relevant information. **Please return any problems, questions, suggestions for improvements to the author of the package** (e-mail address: PLOTHOW@CERNVM.CERN.CH).

Appendix

As an example how to use the package, the FORTRAN code to obtain Fig. 1 is given below:

Example for Fig. 1 :

```
      PROGRAM PDFUPV
C     define maximum number of PDF sets, the NAME and the cross reference
      PARAMETER (NPTYMX = 3, NGRMAX = 7, NSETMX = 36)
      COMMON /W505120/ NPGSMX(NPTYMX,NGRMAX),NSETFL(NPTYMX,NGRMAX,NSETMX)
      CHARACTER*8 SFNAME(NPTYMX,NGRMAX,NSETMX)
      COMMON /W505110/ SFNAME
      COMMON /W505122/ MODECR(NPTYMX,NGRMAX,NSETMX)
C     define HBOOK settings
      PARAMETER (NHBMEM = 500000)
      COMMON /PAWC/ HMEM(NHBMEM)
      PARAMETER (NB=900, ID=100)
C     define DOUBLE PRECISION variables for calling sequence to STRUCTM
      DOUBLE PRECISION DX,DSCALE,DUPV,DDNV,DUSEA,DDSEA,DSTR,DCHM,DBOT,DTOP,DGL
      DOUBLE PRECISION ALF,ALPHAS2
      REAL X, SCALE, UPV, DNV, USEA, DSEA, STR, CHM, BOT, TOP, GL
      COMMON/W50516/ FIRST
      LOGICAL FIRST
      CHARACTER*20 PARM(20)
      DOUBLE PRECISION VAL(20)
      DATA SCALE/80.140/
      DATA X00/0.002/,DX0/0.001/,XLOW/0.0015/,XUP/0.9015/
C
      CALL HLIMIT(NHBMEM)
      DSCALE = SCALE
C     first call to PDFSET to initialize COMMON /W505110/, /W505120/ and /W505122/
      PARM(1) = 'Init0'
      VAL(1) = 0.D0
      CALL PDFSET(PARM,VAL)
C     loop over all existing sets of Nucleon structure functions (SF)
      NPTYPE = 1
      NHB = 0
      DO 20 IGR = 1,NGRMAX
       IF(NPGSMX(NPTYPE,IGR).EQ.0) GOTO 20
       DO ISET = 1,NPGSMX(NPTYPE,IGR)
C     book histograms for each set of SF separately
       NHB = NHB + 1
       CALL HBOOK1(ID+NHB,' U Valence quark ',NB,XLOW,XUP,0.)
C     force label printing for each set of SF (not only the 1st)
       FIRST = .TRUE.
C     define and set parameters
       PARM(1) = 'Nptype'
       VAL(1) = NPTYPE
       PARM(2) = 'Ngroup'
       VAL(2) = IGR
       PARM(3) = 'Nset'
       VAL(3) = ISET
       CALL PDFSET(PARM,VAL)
C     loop over all x bins
       DO 10 I = 1,NB
       X = X00 + (I-1)*DX0
       IF(X.LT.XLOW .OR. X.GT.XUP) GOTO 10
       DX = X
       CALL STRUCTM(DX,DSCALE,DUPV,DDNV,DUSEA,DDSEA,DSTR,DCHM,DBOT,DTOP,DGL)
       UPV = DUPV
```

```
         IF(X.GT.0.499 .AND. X.LE.0.500) WRITE(6,1000) X,SCALE,UPV
1000     FORMAT(/,' X= ',F6.4,' Q= ',F6.3,' UPV= ',8.4)
         CALL HF1(ID+NHB,X,UPV)
10       CONTINUE
C       get alpha(s) for selected set of SF at Q = SCALE
         ALF = ALPHAS2(DSCALE)
         WRITE(6,4000) NPTYPE,IGR,ISET,SFNAME(NPTYPE,IGR,ISET),
 &           MODECR(NPTYPE,IGR,ISET),NHB
         WRITE(6,4001) DSCALE,ALF
4000     FORMAT(/,' Nptype = ',I1,' Ngroup = ',I1, ' Nset = ',I2,' Name = "',A8,'" CrMode = ',
 &           I3,' HBId = ',I3)
4001     FORMAT(1H ,' Scale = ',F8.4,' alpha(s) = ',F6.4)
C       get error summary for each set of SF
         CALL PDFSTA
        ENDDO
20      CONTINUE
C
        STOP
        END
```

This code will produce the following output:

1. HBOOK Output :

one histogram for each set of structure functions. The histogram output has then been accessed, and each histogram has been superimposed on one single frame using the PAW package [38] to obtain Fig. 1.

2. Print Output (Example is given for NPTYPE = 1, NGROUP = 5, NSET = 3 only) :

```
1***** PDFLIB Version: 5.02 Released on 940915 at 12.35 in the CERN Program Library W5051 *****
 ***** Library compiled on 940915 at 2135 *****

Nucleon PDFs : Ngroup = 5, Nset = 3, for GRV Set HO Structure Functions
----------------------------------------------------------------------

X= 0.5000 Q= 80.140 UPV= 0.1202

Nptype = 1 Ngroup = 5 Nset = 3 Name = "GRV-HO " CrMode = 72 HBId = 86
Scale = 80.1400 alpha(s) = 0.1109

PDFLIB : Summary from PDFSTA
Nptype = 1 Ngroup = 5 Nset = 3 Name = "GRV-HO " CrMode = 72
Nfl = -5, LO = 2, Tmas = 100.00 GeV/c**2
QCDL4 = 0.2000 GeV, QCDL5 = 0.1303 GeV
Xmin = 0.10E-05, Xmax = 0.99999E+00, Q2min = 0.300 (GeV/c)**2, Q2max = 0.10E+09 (GeV/c)**2

PDFSTA: NO errors occured
```

References

[1] A. J. Buras and K. J. F. Gaemers, Nucl. Phys. **B132** (1978) 249;
BEBC WA 59 Collaboration, K. Varnell *et al.*, Z. Phys. **C36** (1987) 1.

[2] J.F.Owens and E. Reya, Phys. Rev. D **17** (1978) 3003.

[3] R. Baier, J. Engels and B. Petersson, Z. Phys. C **2** (1979) 265.

[4] M. Glück, E. Hoffman and E. Reya, Z. Phys. C **13** (1982) 119.

[5] D. W. Duke and J. F. Owens, Phys. Rev. D **30** (1984) 49.

[6] E. Eichten, I. Hinchliffe, K. Lane and C. Quigg, Rev. Mod. Phys. **56** (1984) 579; Rev. Mod. Phys. **58** (1985) 1065.

[7] M. Diemoz, F. Ferroni, E. Longo and G. Martinelli, Z. Phys. C **39** (1988) 21.

[8] J. F. Owens : Phys. Lett. **266B** (1991) 126.

[9] A. D. Martin, R. G. Roberts and W. J. Stirling, Phys. Rev. D **37** (1988) 1161;
Phys. Lett. **206B** (1988) 327; Mod. Phys. Lett. **A4** (1989) 1135.

[10] P. N. Harriman, A. D. Martin, R. G. Roberts and W. J. Stirling, Phys. Rev. D **42** (1990) 798; Phys. Lett. **243B** (1990) 421.

[11] J. Kwiecinski, A. D. Martin, R. G. Roberts and W. J. Stirling, Phys. Rev. D **42** (1990) 3645;
A. D. Martin, R. G. Roberts and W. J. Stirling, Phys. Rev. D **43** (1991) 3648.

[12] A. D. Martin, R. G. Roberts and W. J. Stirling, Phys. Rev. D **47** (1993) 867.

[13] J. Morfin and W. K. Tung, Z. Phys. C **52** (1991) 13.

[14] M. Glück, E. Reya and A. Vogt, Z. Phys. C **48** (1990) 471; Z. Phys. C **53** (1992) 127; Phys. Lett. **306B** (1993) 391.

[15] P. Aurenche *et al.*, Phys. Rev. D **39** (1989) 3275.

[16] A. D. Martin, R. G. Roberts and W. J. Stirling, Phys. Lett. **306B** (1993) 147, Erratum-ibid. **309B** (1993) 492; Durham Preprint, DTP/93-86 (1993).

[17] E. L. Berger and R. Meng, Phys. Lett. **B304** (1993) 318; CERN-TH 6739/92; ANL-HEP-CP-92-108;
E. L. Berger, R. Meng and J. Qui : ANL-HEP-CP-92-79.

[18] CTEQ Collaboration, Phys. Lett. **B304** (1993) 159.

[19] A. D. Martin, R. G. Roberts and W. J. Stirling, Durham Preprint, DTP/94-55 (1994).

[20] J. F. Owens, Phys. Rev. D **30** (1984) 943.

[21] P. Aurenche *et al.*, Phys. Lett. **233B** (1989) 517.

[22] P. J. Sutton, A. D. Martin, R. G. Roberts and W. J. Stirling, Phys. Rev. D **45** (1992) 2349.

[23] M. Glück, E. Reya and A. Vogt, Z. Phys. C **53** (1992) 651.

[24] D. W. Duke and J. F. Owens, Phys. Rev. D **26** (1982) 1600.

[25] M. Drees and K. Grassie, Z. Phys. C **28** (1985) 451.

[26] H. Abramowicz, K. Charchula and A. Levy, Phys. Lett. **269B** (1991) 458.

[27] L. E. Gordon and J. K. Storrow, Z. Phys. C **56** (1992) 307.

[28] M. Glück, E. Reya and A. Vogt, Phys. Rev. D **46** (1992) 1973; *ibid.* D **45** (1992) 3986.

[29] P. Aurenche *et al.*, Z. Phys. C **56** (1992) 589.

[30] P. Aurenche, M. Fontannaz, J. Ph. Guillet, Preprint LPTHE Orsay 93-37 (1993).

[31] G. Altarelli, R. K. Ellis, G. Martinelli, Nucl. Phys. **B143** (1978) 521; *ibid.* **B157** (1979) 461.

[32] H. Plothow-Besch, Users's Manual - Version 1.00, W5051 PDFLIB, 1991.03.21; Comp. Phys. Comm. **75** (1993) 396.

[33] *Review of Particle Properties*, Phys. Rev. D **45** (1992), Part II, p. III. 54.

[34] BCDMS Collaboration, A.C. Benvenuti *et al.*, Phys. Lett. **237B** (1990) 592; *ibid.* **237B** (1990) 599; EMC Collaboration, M. Arneodo *et al.*, Nucl. Phys. **B333** (1990) 1;
NMC Collaboration, D. Allasia *et al.*, Phys. Lett. **249B** (1990) 366;
P. Amaudruz *et al.*, Nucl. Phys. **B371** (1992) 3.

[35] NMC Collaboration, P. Amaudruz *et al.*, Phys. Lett. **295B** (1992) 159.

[36] H1 Collaboration, I. Abt *et al.*, Nucl. Phys. **B407** (1993) 515;
ZEUS Collaboration, M. Derrick *et al.*, Phys. Lett. **316B** (1993) 412.

[37] W. Bartel *et al.*, Z. Phys. C **24** (1984) 231.

[38] PAW, CERN Program Library Entry Q121, Long Write-up, R. Brun, O. Couet, C. Vandoni, P. Zanarini; see also to References therein.

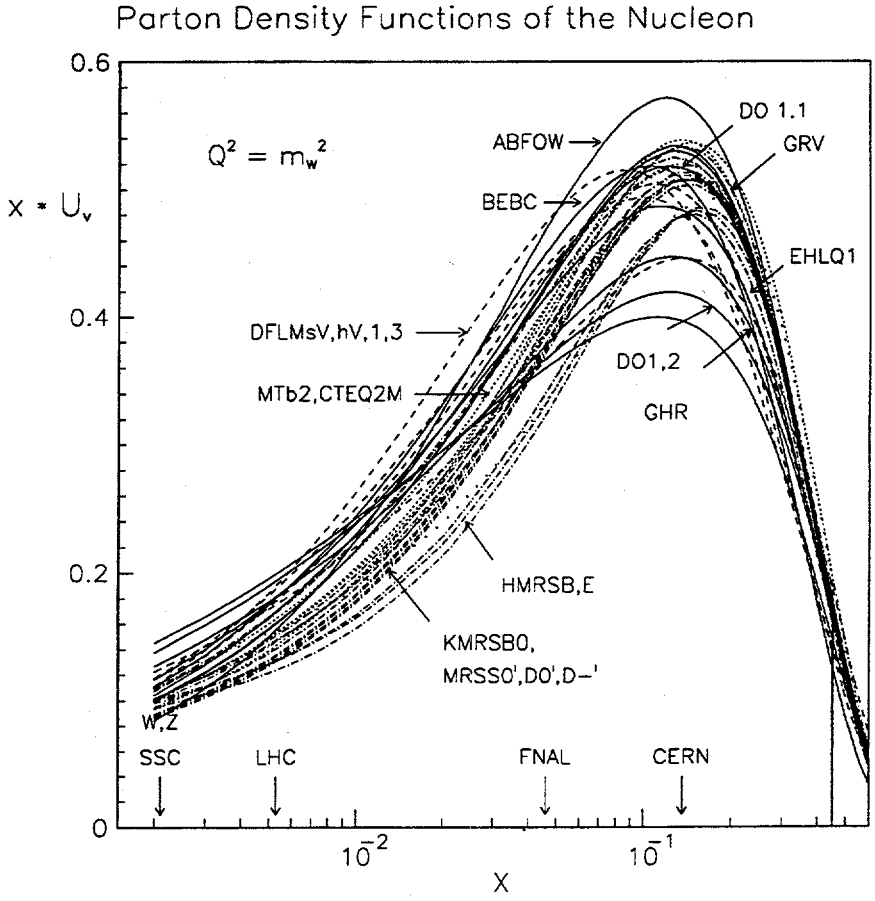

Figure 1: u valence quark distribution as a function of X

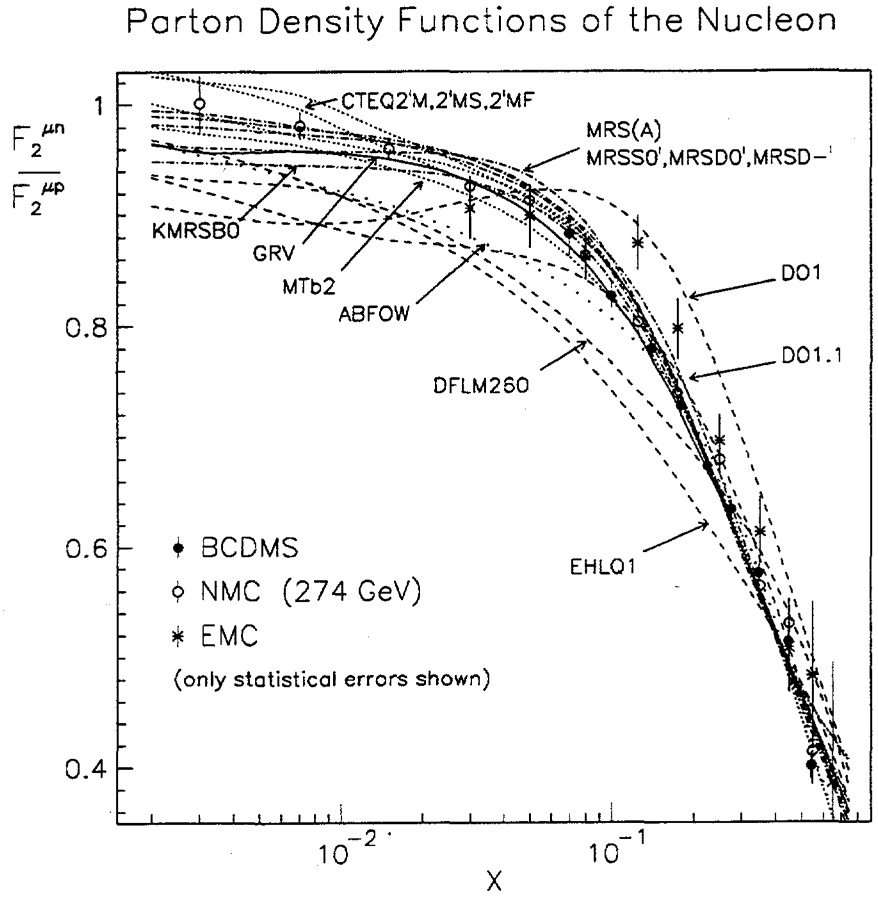

Figure 2: F_2^n/F_2^p ratio as a function of X

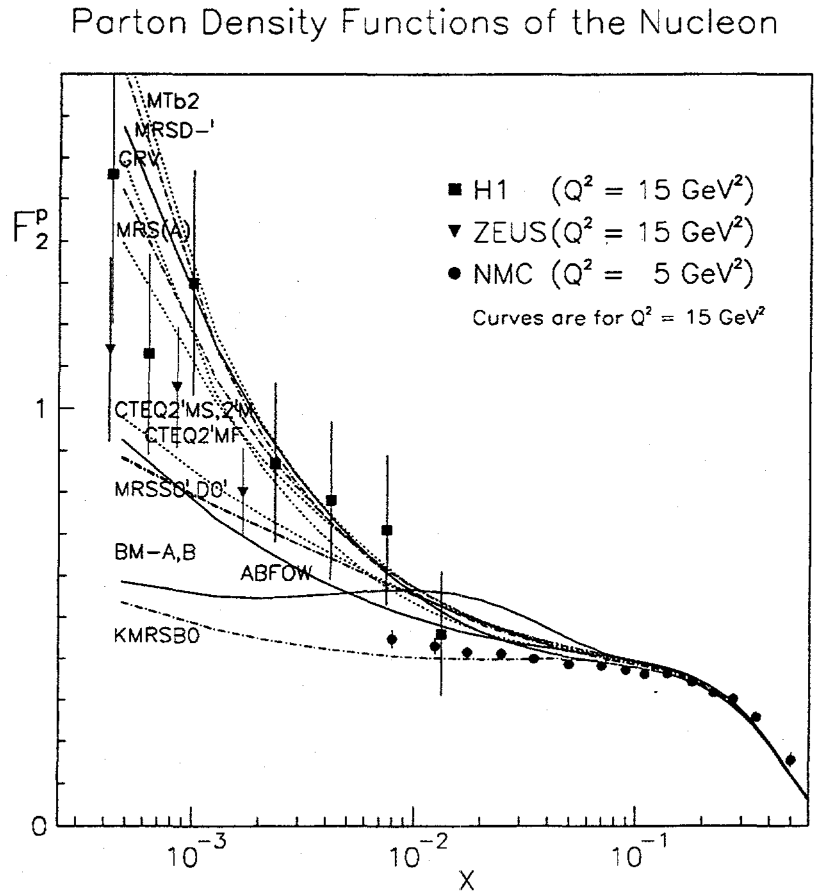

Figure 3: F_2^p as a function of X

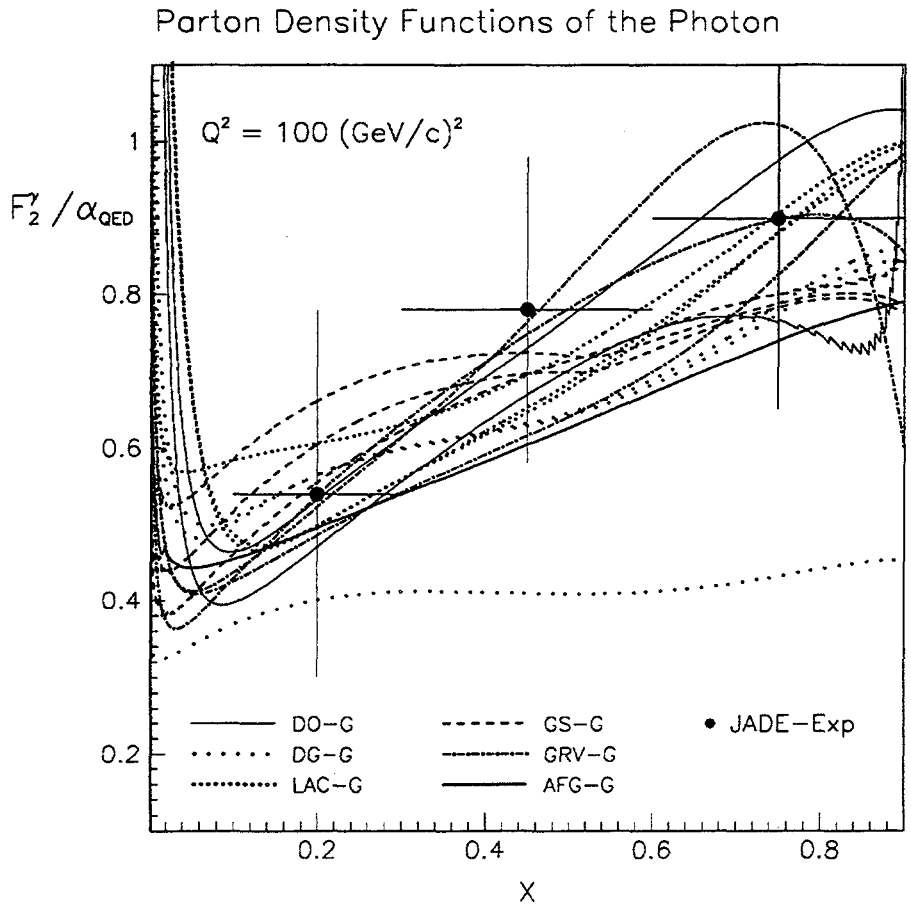

Figure 4: F_2^γ/α_{QED} distribution as a function of X

DRELL-YAN PRODUCTION AT COLLIDER ENERGIES

W. L. VAN NEERVEN

Instituut Lorentz, University of Leiden, P.O. Box 9506
2300 RA Leiden, The Netherlands

We present some results of the Drell-Yan cross sections $d\sigma/dm$ and $\sigma_{\rm tot}$ which includes the $\mathcal{O}(\alpha_s^2)$ contribution to the coefficient function. In particular we study the total cross section $\sigma_{\rm tot}$ for vector boson production and $d\sigma/dm$ for low invariant masses m of the lepton pairs at large hadron collider energies. This study includes a detailed discussion of the dependence of the cross sections on the chosen scheme ($\overline{\rm MS}$ versus DIS) and the factorization scale.

INTRODUCTION

Massive lepton pair production in hadron-hadron collisions proceeds through the following reaction:

$$\begin{array}{lcl} H_1 + H_2 & \rightarrow & V + "X" \\ & & \hookrightarrow l_1 + l_2 \end{array} \qquad (1)$$

where H_1 and H_2 denote the incoming hadrons and V is one of the vector bosons of the standard model (γ, Z or W) which subsequently decays into a lepton pair (l_1, l_2). The symbol "X" denotes any inlcusive final hadronic state allowed by quantum number conservation laws.
The above process is of interest because of the following reasons

♠ Like deep inelastic lepton-hadron scattering it is a semi leptonic process and therefore can provide us with a good test of perturbative quantum chromo dynamics (QCD). In particular we want to mention the scale evolution of the parton densities, although not yet observed in process (1), and the determination of the running coupling constant $\alpha_s(\mu^2)$.

◇ Besides deep inelastic lepton-hadron scattering one has an alternative way to measure the parton densities of the hadrons. Moreover one also can determine the parton densities of unstable hadrons like pions and kaons which is impossible in deep inelastic lepton-hadron scattering.

- ♣ It is an important background process for other production mechanisms of lepton pairs like J/ψ and Υ decays and thermal emission of lepton pairs in heavy-ion collisions [1].

- ♡ The Drell-Yan process is also of theoretical interest. It enables us to study issues like large QCD corrections which are due to soft gluon bremsstrahlung and virtual gluon contributions. In order to control the large terms in the perturbation series one has invented all kinds of resummation techniques mostly leading to the exponentiation of the leading terms. Because the perturbation series is truncated the theoretical cross section will depend on the renormalization and mass factorization scale μ. This dependence can be minimized by including higher order terms. An alternative way is to determine μ itself (optimal scale) by using so called improved perturbation theory like the principle of minimal sensitivity (PMS), fastest apparent convergence (FAC) or the Brodsky-Lepage-MacKenzie (BLM) method.

REVIEW OF THE CALCULATION OF THE DRELL-YAN CROSS SECTION

Since there exists such a vast amount of literature on the Drell-Yan process we will only mention some of the cross sections which have been calculated in the past. The most successful description of massive lepton pair production was given by S.D. Drell and T.M. Yan in the context of the parton model [2]. Later on, this production mechanism, called Drell-Yan (DY) after their inventors, was supplemented by perturbative QCD. Using renormalization group methods and the mass factorization theorem, for which an all order proof exists [3], one can compute QCD corrections to this process in all orders of perturbation theory. In general the DY cross section can be schematically written in the following way

$$d\sigma^{H_1H_2} = \sum_{a,b} f_a^{H_1}(\mu^2) \otimes f_b^{H_2}(\mu^2) \otimes d\hat{\sigma}_{ab}(\mu^2) \tag{2}$$

where $d\sigma^{H_1H_2}$ denotes the hadronic cross section and $f_a^{H_i}$ stands for the density of parton a in hadron H_i. In QCD the partons are identified by the quarks and gluons. The quantity $d\hat{\sigma}_{ab}(\mu^2)$ is called the partonic cross section or DY coefficient function which is obtained after coupling constant renormalization and mass factorization. The parton densities and the partonic cross section depend on the renormalization scale μ_R and mass factorization scale μ which for simplicity are put to be equal. In addition to these scales the parton density $f_a^{H_1}(\mu^2)$ also depends on the fraction x_a of the momentum of the incoming hadron H_1 carried away by parton a. The partonic cross section depends besides on μ on all kinematical variables over which one has not integrated.

Up to second order in the strong coupling constant $\alpha_s(\mu^2)$ the partonic subprocesses contributing to $d\hat{\sigma}_{ab}(\mu^2)$ are given by

$$\alpha_s^0 \quad : \quad q + \bar{q} \quad \rightarrow \quad V \tag{3}$$

$$\alpha_s^1 \quad : \quad q + \bar{q} \quad \rightarrow \quad V \ (\text{one} - \text{loop correction}) \tag{4}$$

$$
\begin{aligned}
q+\bar{q} &\rightarrow V+g && (5)\\
q(\bar{q})+g &\rightarrow V+q(\bar{q}) && (6)\\
\alpha_s^2 \;:\quad q+\bar{q} &\rightarrow V\ \text{(two} - \text{loop correction)} && (7)\\
q+\bar{q} &\rightarrow V+g\ \text{(one} - \text{loop correction)} && (8)\\
q+\bar{q} &\rightarrow V+g+g && (9)\\
q(\bar{q})+g &\rightarrow V+q(\bar{q})\ \text{(one} - \text{loop correction)} && (10)\\
q(\bar{q})+g &\rightarrow V+q(\bar{q})+g && (11)\\
q+\bar{q} &\rightarrow V+q+\bar{q} && (12)\\
q(\bar{q})+q(\bar{q}) &\rightarrow V+q(\bar{q})+q(\bar{q}) && (13)\\
g+g &\rightarrow V+q+\bar{q} && (14)
\end{aligned}
$$

¿From the above we infer that in lowest order the vector boson V can only be produced by quark anti-quark annihilation (3). In first order a second production mechanism appears i.e. (anti) quark-gluon collisions (6). The (anti) quark - (anti) quark scattering process (13) and the gluon-gluon fusion reaction (14) show up for the first time in order α_s^2. With the reactions mentioned above all possible parton-parton subprocesses are exhausted.

Let us now summarize the most important cross sections which have been calculated in the past. The first one is the angular distribution of the (positively charged) lepton l_1 (1) in the pair rest frame. It can be written as

$$\frac{d^2\sigma}{d\cos\theta\, d\phi} \sim 1 + \lambda\cos^2\theta + \mu\sin 2\theta\,\cos\phi + \frac{\nu}{2}\sin^2\theta\cos 2\theta \qquad (15)$$

where θ and ϕ denote the polar and azimuthal angle respectively. The parameters λ, μ and ν are functions of the other kinematical variables. The quantity (15) is calculated up to order α_s in [4]. The second quantity is the transverse momentum distribution of the lepton $d\sigma/dp_{l,T}$ which is calculated for W-production up to order α_s in [5]. The third quantity is given by the double differential cross section $d^2\sigma/dp_{V,T}/dX_F$ or $d^2\sigma/dp_{V,T}/dy$ where $p_{V,T}$ denotes the transverse momentum of the vector boson V. The longitudinal momentum fraction of V is given by $X_F = 2p_L/\sqrt{s}$ where $\sqrt{s}$ denotes the center of mass energy of the hadron-hadron system and p_L is the longitudinal momentum of the vector boson. The rapidity y is defined by $X_F = 2\sqrt{\tau}\sinh(y)$ where $\tau = Q^2/s$ denotes the Bjorken scaling variable and Q^2 is the invariant mass squared of the lepton pair. If one neglects the intrinsic transverse momentum of the incoming partons the Born process (3) does not contribute to this cross section. The lowest order contribution, starting in order α_s, can be found in [6]. The next to leading order corrections have been calculated in [7] for the $q\bar{q}$ subprocesses (8), (9) and (12). The complete order α_s^2 contribution is given in [8]. The fourth quantity is given by the distribution $d^2\sigma/dQ^2/dX_F$ and $d^2\sigma/dQ^2/dy$ where Q^2, X_F and y are defined above. These cross sections are calculated up to order α_s in [9] and [10]. The order α_s^2 corrections have not been completed yet. Only the contributions due to virtual gluons (process (7)), soft plus virtual gluons (process (8)), soft gluons (process (9)) and collinear quark anti-quark pairs (process (12)) have been calculated in [11]. These contributions are supposed to constitute the dominant part of the QCD corrections in particular when $\tau > 0.1$

which is the case at fixed target energies. The last quantity we are interested in is $d\sigma_V/dQ^2$ from which one can derive the total cross sections σ_V where V is represented by Z and W. The order α_s contributions are calculated in [9, 10] and [12].

The order α_s^2 contributions which include all processes mentioned in (7)-(14) are presented in [13] ($\overline{\text{MS}}$-scheme) and [14] (DIS-scheme). Notice that only the cross sections $d^2\sigma/dQ^2/dX_F$ ($d^2\sigma/dQ^2/dy$) and $d\sigma_V/dQ^2$ (σ_V) involve the computation of the two-loop virtual corrections due to process (7).

RESULTS

In this report we will only limit ourselves to the discussion of the cross sections $d\sigma_V/dQ^2$ and σ_V which we compute for large hadron collider energies. The colour-averaged inclusive cross section is given by

$$\frac{d\sigma_V}{dQ^2} = \tau\,\hat{\sigma}_V(Q^2, M_V^2)W_V(\tau, Q^2), \qquad \tau = \frac{Q^2}{s} \tag{16}$$

where the quantity $\hat{\sigma}_V$ denotes the pointlike total cross section of the process $q+\bar{q} \rightarrow V \rightarrow l_1 + l_2$ and $W_V(\tau, Q^2)$ is defined as the hadronic DY structure function which can be written as

$$\begin{aligned} W_V(\tau, Q^2) \;=\; & \sum_{a,b}\int_0^1 dx_a \int_0^1 dx_b \int_0^1 dx\;\delta(\tau - x x_a x_b) \\ & \qquad\qquad \mathrm{PD}_{ab}^V(x_a, x_b, \mu^2)\Delta_{ab}(x, Q^2, \mu^2) \end{aligned} \tag{17}$$

The functions $\mathrm{PD}_{ab}^V(x_a, x_b, \mu^2)$ stand for the usual combination of parton densities, which depend on the mass factorization scale μ (see (1)). The indices a and b refer to the incoming partons. Furthermore the PD_{ab}^V contain all the information on the couplings of the quarks to the vector bosons, such as the quark charges, the Weinberg angle θ_W and the Cabibbo angle θ_c (the other angles and phases of the Kobayashi-Maskawa matrix are neglected). The explicit way how to combine the functions PD_{ab}^V with the DY coefficient function Δ_{ab} is given in Appendix A of [13]. Notice that the parton densities do not only depend on the mass factorization scale μ but also on the renormalization scale μ_R. However in the existing parametrizations of the parton densities the two scales μ and μ_R are always set to be equal. Also the DY coefficient function Δ_{ab} depends on both scales which are set to be equal too.

The total cross section can be derived from (16) by integrating over the lepton pair mass squared (virtual vector boson mass) Q^2

$$\sigma_V(s) = \int dQ^2\,\tau\,\hat{\sigma}_V(Q^2, M_V^2)W_V(\tau, Q^2) \tag{18}$$

Notice that at large energies characteristic for $p\bar{p}$ and pp colliders the DY cross section is dominated by W- and Z-production provided $Q^2 \sim M_V^2$. Since the widths of these vector bosons are small compared to their masses the integral in (18) can be performed using the narrow-width approximation.

We will now present the DY cross section and its K-factor for both $p\bar{p}$ and pp collisions at past, current and future large energy colliders. The C.M. energies under consideration are $\sqrt{s} = 0.63$ TeV Sp$\bar{\text{p}}$S, $\sqrt{s} = 1.8$ TeV (Tevatron) and $\sqrt{s} = 16$ TeV (LHC). For the electroweak parameters we take the following values $M_Z = 91$ GeV, $M_W = 80$ GeV, $G_F = 1.166 \times 10^{-5}$ GeV^{-2} (Fermi constant), $\sin^2\theta_W = 0.227$ and $\sin^2\theta_C = 0.05$. The running coupling constant, determined in the $\overline{\text{MS}}$-scheme, is corrected up to two loops and the number of light flavours is chosen to be four. The DY coefficient function, calculated in the $\overline{\text{MS}}$ [13] and the DIS [14] scheme up to $\mathcal{O}(\alpha_s^2)$, have to be combined with the parton densities computed in the same scheme. Here we choose the next to leading log parametrization MRS(D-) with $\Lambda_4 = 0.215$ GeV ($\overline{\text{MS}}$) and $\Lambda_4 = 0.230$ GeV (DIS). Using this parametrization the sea-quark and gluon densities behave like $xs(x, Q_0^2) \sim x^{-1/2}$ and $xg(x, Q_0^2) \sim x^{-1/2}$ (BFKL pomeron). Q_0 denotes the input scale (here $Q_0 = 2$ GeV). The above densities lead to a deep inelastic structure function $F_2(x, Q^2)$ which steeply rises in the small x-region ($10^{-4} < x < 10^{-3}$). This behaviour is confirmed by the recent data obtained form the experiments carried out at HERA [15]. Finally we choose for the mass factorization scale μ (which is put equal to the renormalization scale μ_R) the value $\mu = M_V$ unless stated otherwise. Notice that in principle the $\mathcal{O}(\alpha_s^2)$ corrected DY coefficient function should be combined with the next-to-next-to leading log parametrization of the parton densities. However the latter do not exist because the three-loop contributions to the Altarelli-Parisi splitting functions, which are needed to compute them, have not been calculated yet.

In the table below we have listed the total cross sections for Z-boson production which are computed by adopting the $\overline{\text{MS}}$-scheme.

table 1

Total cross sections in nb for Z-production at Sp$\bar{\text{p}}$S, Tevatron and LHC

$\sqrt{s}$ [TeV]	Born	$\mathcal{O}(\alpha_s)$	$\mathcal{O}(\alpha_s^2)$
0.63	1.59	2.01 (1.26)	2.12 (1.33)
1.8	5.27	6.29 (1.19)	6.45 (1.22)
16.0	55.9	63.3 (1.13)	63.2 (1.13)

Between the brackets in column 3 and 4 we have put the $\mathcal{O}(\alpha_s^i)$ corrected K-factor which is defined by

$$K_i = \frac{\sigma_i}{\sigma_0} \tag{19}$$

where σ_0 denotes the Born contribution and σ_i is the $\mathcal{O}(\alpha_s^i)$ corrected cross section. One observes that the K-factor decreases at increasing energies. In particular it is much smaller than the one computed for fixed target energies where it can become $K_1 = 1.6$ and $K_2 = 2.2$ respectively. The same holds for the order α_s and $\mathcal{O}(\alpha_s^2)$ corrections which are smaller than the ones observed at fixed target energies.

Multiplying σ_Z by the branching ratio $B(Z \to l^+l^-) = 3.35 \cdot 10^{-2}$ one can compare our results with the data obtained from the UA1 [17], UA2 [18] and CDF [19] experiments.

table 2

$\sigma_Z \cdot B(Z \to l^+l^-)$ in pb for Sp$\bar{\text{p}}$S and Tevatron

$\sqrt{s}$ [TeV]	Born	order α_s	$\mathcal{O}(\alpha_s^2)$	Experiment
0.63	53.3	67.3	71.0	58.6 ± 7.8 ± 8.4 (UA1)
0.63	53.3	67.3	71.0	70.4 ± 5.5 ± 4.0 (UA2)
1.8	177	211	216	197 ± 12 ± 32 (CDF)

In the above we see a good agreement between the theoretical prediction and the experimental result. In particular we neeed the order α_s corrections to explain the UA2 result. In tables 3 and 4, presented below, we show the results for W^+ and W^- production by computing $\sigma_W = \sigma_{W^+} + \sigma_{W^-}$ and $\sigma_W \cdot B(W \to l\nu_l)$. The numbers in the tables are calculated in the $\overline{\text{MS}}$-scheme with $B(W \to l\nu_l) = 0.109$ and choosing the $\overline{\text{MS}}$-scheme.

table 3

Total cross sections in nb for W-production at Sp$\bar{\text{p}}$S, Tevatron and LHC

$\sqrt{s}$ [TeV]	Born	order α_s	$\mathcal{O}(\alpha_s^2)$
0.63	5.13	6.47 (1.26)	6.79 (1.32)
1.8	17.6	20.1 (1.14)	21.3 (1.21)
16.0	191	215 (1.12)	215 (1.12)

table 4

$\sigma_W \cdot B(W \to l\nu_l)$ in nb for Sp$\bar{\text{p}}$S and Tevatron

$\sqrt{s}$ [TeV]	Born	order α_s	$\mathcal{O}(\alpha_s^2)$	Experiment
0.63	0.559	0.705	0.740	0.609 ± 0.041 ± 0.094 (UA1)
0.63	0.559	0.705	0.740	0.660 ± 0.015 ± 0.037 (UA2)
1.8	1.92	2.19	2.32	2.06 ± 0.04 ± 0.34 (CDF)

The features of W-production are the same as those observed for Z-production except that in the case of the Sp$\bar{\text{p}}$S collider ($\sqrt{s} = 0.63$ TeV) the experimental results are below the theoretical predictions. This in particular holds for the UA1 data. ¿From the results of our calculations which are published in [13, 14] one can also draw other conclusions about the vector boson cross sections computed at large energies.

First the $q\bar{q}$ reaction, which always leads to a positive correction, dominates the cross sections. Furthermore at $\sqrt{s} = 0.63, 1.8$ TeV the qg, $\bar{q}g$ subprocesses give a negative contribution which is smaller than the correction due to the $q\bar{q}$ reaction at $\sqrt{s} = 0.63$. However at higher energies, like $\sqrt{s} = 16$ TeV for LHC, the correction due to qg, $\bar{q}g$ almost cancels the one coming from $q\bar{q}$. The other subprocesses given by qq, $\bar{q}\bar{q}$ and gg turn out to be negligable over the whole energy range. This explains why the higher order QCD corrections for vector-boson production are smaller than those computed for Drell-Yan production of lepton pairs at fixed target energies. In the latter case $\alpha_s(Q^2)$ is large because the values of Q^2 are small. Furthermore the variable $\tau = Q^2/s$ is much closer to one so that, except for soft gluon radiation, all the other production mechanisms are suppressed. As is known from the early papers on Drell-Yan production at fixed target energies the soft plus virtual gluon contribution constitute the bulk of the correction provided the DY coefficient function is computed in the DIS-scheme. However the $\mathcal{O}(\alpha_s^2)$ corrected soft plus virtual contribution overestimates the cross section at large hadron collider energies. The overestimate amounts to 27% ($\sqrt{s} = 0.63$ TeV), 75% ($\sqrt{s} = 1.8$ TeV) and even 170% ($\sqrt{s} = 16$) TeV) respectively.

The reliability of the higher order QCD corrections can be inferred from varying the cross section with respect to the mass factorization scale μ and the renormalization scale μ_R which here are put to be equal. In fig.1 we have plotted the total cross section for W-production at $\sqrt{s} = 0.63$ TeV (Sp$\bar{\text{p}}$S) and study its dependence on the chosen scale μ. We observe a considerable improvement of the scale independence when higher order corrections are included. Also the result obtained from the DIS-scheme is very close to the one computed by using the $\overline{\text{MS}}$-scheme showing the scheme independence of the cross section. The same we can conclude from fig.2 where the cross section is computed for $\sqrt{s} = 1.8$ TeV (Tevatron) although here the improvement in the scale independence is not that spectacular any more if one includes the $\mathcal{O}(\alpha_s^2)$ correction.

After having discussed the total cross sections for vector boson production we call the attention of the reader to the quantity $d\sigma/dm$ which is studied for small invariant lepton pair masses $m \equiv \sqrt{Q^2}$ at large hadron collider energies. Notice that at small m the virtual photon dominates the cross section whereas the contribution of the Z-boson can be neglected. In our subsequent plots we choose as factorization scale $\mu = m$ unless stated otherwise. In fig.3 we show how $d\sigma/dm$ changes when higher order corrections are included. Furthermore we have chosen the $\overline{\text{MS}}$-scheme and compare the theoretical predictions with the UA2-data [20]. The statistical and systematical errors are so large that the uncorrected as well as the corrected cross sections agree with the data. Finally we make some predictions for the LHC ($\sqrt{s} = 16$ TeV). Choosing again the $\overline{\text{MS}}$-scheme we have plotted $d\sigma/dm$ in fig.4. The higher order corrections are very small in particular the $\mathcal{O}(\alpha_s^2)$ correction is almost unobservable. This feature is also observed in fig.3. Although the running coupling constant $\alpha_s(m^2)$ is quite large, because m is small, the cancellation of the various parton subprocesses is so large that the net result for the QCD corrections is small except when $m < 5$ GeV. This becomes clear after a glance on fig.5 where we plotted the ratio $R^{(i)}$ which is defined by

$$R^{(i)} = \frac{d\sigma^{(i)}}{d\sigma^{(0)} + d\sigma^{(1)} + d\sigma^{(2)}} \tag{20}$$

where $d\sigma^{(i)}$ denotes the $\mathcal{O}(\alpha_s^i)$ contribution to the cross section. From fig.5 we also infer that the $\mathcal{O}(\alpha_s^2)$ contribution is negative for $m > 7.5$ GeV. This picture changes if we make the plot in the DIS scheme where now the $\mathcal{O}(\alpha_s^2)$ contribution is positive over the whole m-range (see fig.6). In fig.7 ($\overline{\text{MS}}$-scheme) and fig.8 (DIS-scheme) we also show the $\mathcal{O}(\alpha_s^i)$ corrected K-factor defined by

$$K_i = \frac{d\sigma_i}{d\sigma_0} \qquad\qquad d\sigma_i = \sum_{l=1}^{i} d\sigma^{(l)} \tag{21}$$

where $d\sigma_i$ is the $\mathcal{O}(\alpha_s^i)$ corrected cross section. At very small m ($m < 5$ GeV) the K-factor can become large in particular if it is computed in the DIS-scheme.

Finally we study the factorization scale dependence of $d\sigma/dm$. For that purpose we define the quantity

$$F(\mu) = \frac{d\sigma(\mu)}{d\sigma(m)} \tag{22}$$

If this quantity stays very close to one then the sensitivity of the cross section $d\sigma/dm$ to a variation of the factorization scale is small. The plots made for the $\overline{\text{MS}}$-scheme (fig.9) and the DIS-scheme (fig.10) show that this is the case. However the scheme dependence of the cross section expressed by $(d\sigma(m))_{\text{DIS}}/(d\sigma(m))_{\overline{\text{MS}}}$ in fig.9 and by $(d\sigma(m))_{\overline{\text{MS}}}/(d\sigma(m))_{\text{DIS}}$ in fig.10 (dashed lines) is much larger than one would have expected on the grounds of the factorization scale dependence. This is contrary to our observation in fig.1 and 2 for vector boson production where the result obtained in the DIS scheme is slightly below ($\sqrt{s} = 0.63$ TeV) or slightly above ($\sqrt{s} = 1.8$ TeV) the one computed in the $\overline{\text{MS}}$-scheme. Here it turns out that at small $m = \sqrt{Q^2}$ the cross section in the DIS-scheme is about 30% larger than the cross section in the $\overline{\text{MS}}$-scheme computed at the same scale $\mu = m$.

References

[1] See section C of "Heavy-ion Collisions" in the Proceedings of the "Large Hadron Collider Workshop", Aachen, 4-9 October 1990. Eds. G. Jarlskog and D. Rein, vol II, p. 1057-1234.

[2] S. D. Drell and T. M. Yan, Phys. Rev. Lett. **25** (1970) 316.

[3] J. C. Collins, D. E. Soper and G. Sterman, Phys. Lett. **134B** (1984) 263; Nucl. Phys. **B250** (1985) 199; **B308** (1988) 833;
G. T. Bodwin, Phys. Rev. D **31** (1985) 2616, E. D **34** (1986) 3932.

[4] K. Kajantie, J. Lindfors and R. Raito, Phys. Lett. **74B** (1978) 384;
J. C. Collins, Phys. Rev. Lett. **42** (1978) 291;
J. Cleymans and M. Kuroda, Phys. Lett **80B** (1979) 385;
R. L. Thews, Phys. Rev. Lett. **43** (1979) 987; Phys. Lett. **100B** (1981) 339.
R. Chiapetta and M. le Bellac, Z. Phys. C **32** (1986) 521.

[5] P. Aurenche and J. Lindfors, Nucl. Phys. **B185** (1981) 274; 301.

[6] H. Fritzsch and P. Minkowski, Phys. Lett. **73B** (1978) 80;
G. Altarelli, G. Parisi and R. Petronzio, Phys. Lett **76B** (1978) 351, 356;
K. Kajantie and R. Raito, Nucl. Phys. **B139** (1978) 72.

[7] R. K. Ellis, G. Martinelli and R. Petronzio, Phys. Lett. **B139** (1981) 45; Nucl. Phys. **B211** (1983) 106.

[8] P. B. Arnold and M. H. Reno, Nucl. Phys. **B319** (1989) 37, E. B330 (1990) 284;
R. J. Gonsalves, J. Pawlowski and C. F. Wai, Phys. Rev. D **40** (1989) 2245.

[9] G. Altareli. R. K. Ellis and G. Martinelli, Nucl. Phys. **B157** (1979) 461.

[10] J. Kubar, M. le Bellac, J. L. Meunier and G. Plaut, Nucl. Phys. **B175** (1980) 251;
P. Aurenche and P. Chiapetta, Z. Phys. C **34** (1987) 201.

[11] T. Matsuura and W. L. van Neerven, Z. Phys. C **38** (1988) 623;
T. Matsuura, S. C. van der Marck and W .L. van Neerven, Phys. Lett. **211B** (1988);
Nucl. Phys. **B319** (1989) 570.

[12] J. Kubar-Andre and F. E. Paige, Phys. Rev. D **19** (1979) 221;
B. Humpert and W. L. van Neerven, Phys. Lett. **84B** (1979) 327, E. 85B (1979) 471;
89B (1979) 69; Nucl. Phys. **B184** (1981) 225.

[13] R. Hamberg, W. L. van Neerven and T. Matsuura, Nucl. Phys. **B359** (1991) 343.

[14] W. L. van Neerven and E. B. Zijlstra, Nucl. Phys. **B382** (1992) 11.

[15] A, D, Martin, W. J. Stirling and R. G. Roberts, Phys. Rev. D **47** (1993) 867.

[16] I. Abt *et al.* (H1 collaboration), DESY 93-117.
M. Derrick *et al.* (ZEUS collaboration), DESY 93-110.

[17] C. Albajar *et al.* (UA1 collaboration), Phys. Lett. **253B** (1991) 503.

[18] J. Alitti *et al.* (UA2 collaboration), Z. Phys. C **47** (1990) 11.

[19] F. Abe *et al.* (CDF collaboration), Phys. Rev. Lett. **64** (1990) 152.

[20] A. Moulin, Talk given at the "International Symposium on Multiparticle Dynamics". Wuhan, China, Sept 1991, PITHA-91/22.

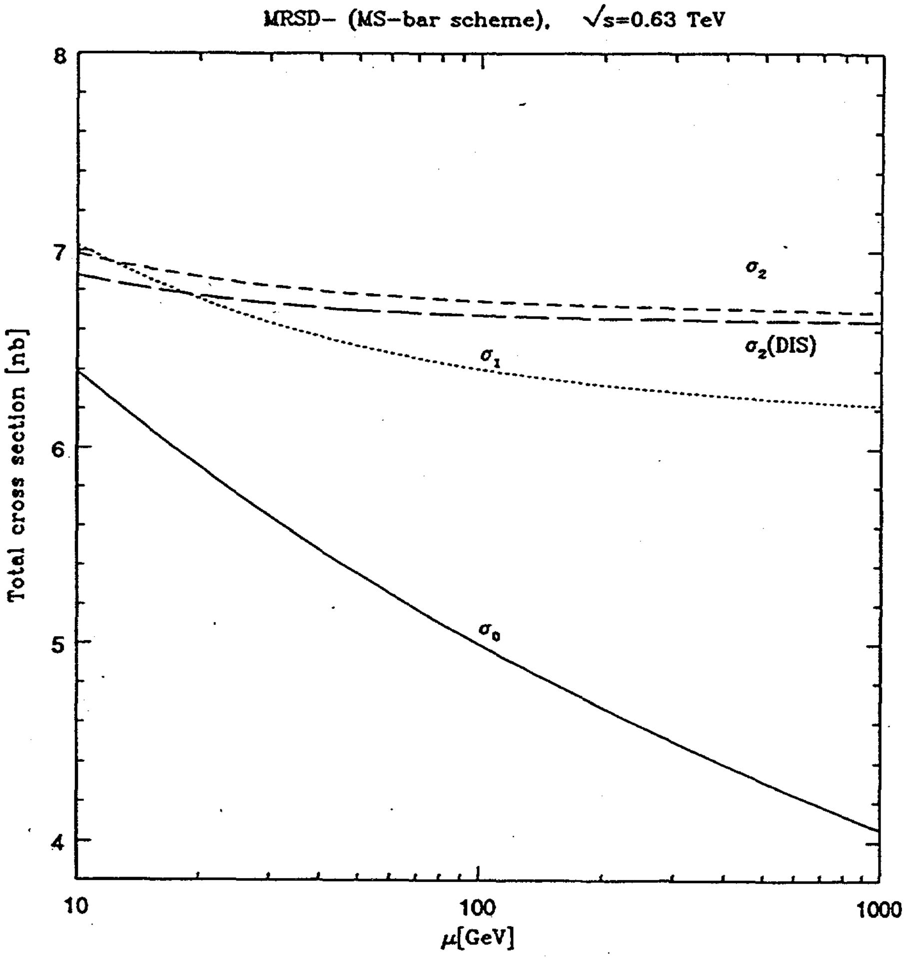

Figure 1: Mass factorization scale (μ) dependence of σ_W for Sp$\bar{\rm p}$S ($\sqrt{s}$ = 0.63 TeV) in the $\overline{\rm MS}$-scheme. Solid line: Born; long dashed line: order α_s corrected; dash-dotted line: $\mathcal{O}(\alpha_s^2)$ corrected. Also shown is the $\mathcal{O}(\alpha_s^2)$ corrected cross section (dotted line) in the DIS-scheme.

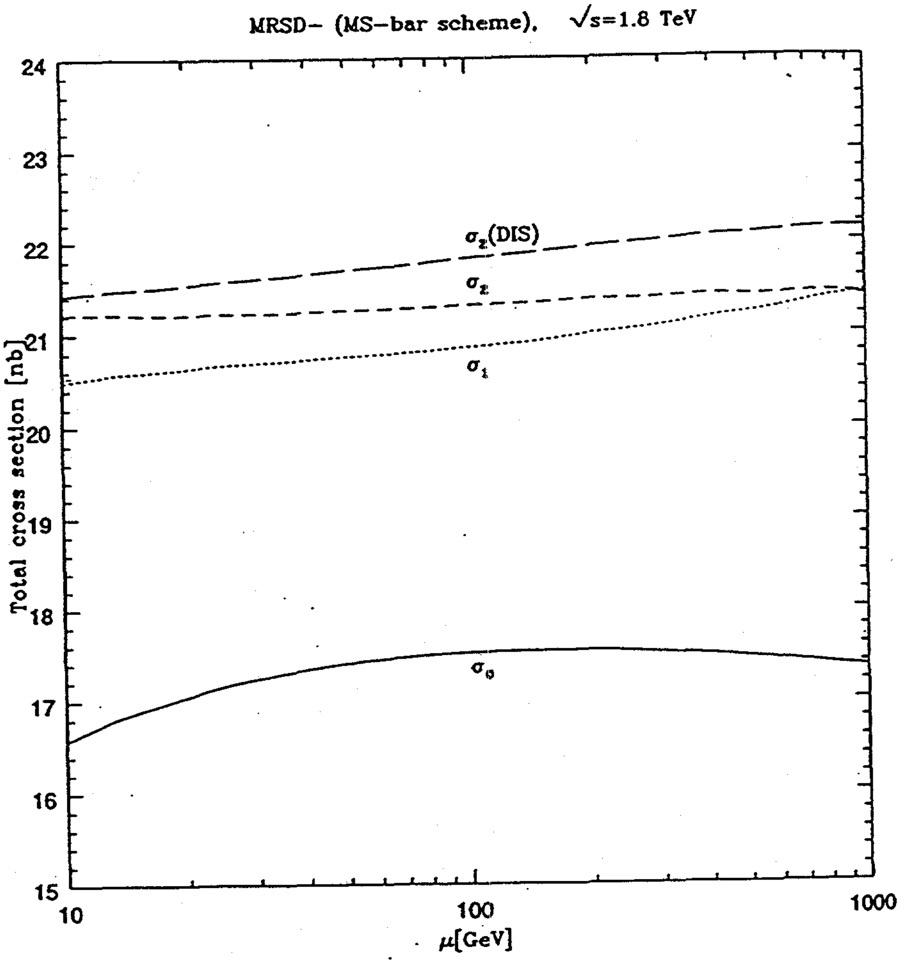

Figure 2: The same as in fig.1 but now for the Tevatron ($\sqrt{s} = 1.8$ TeV).

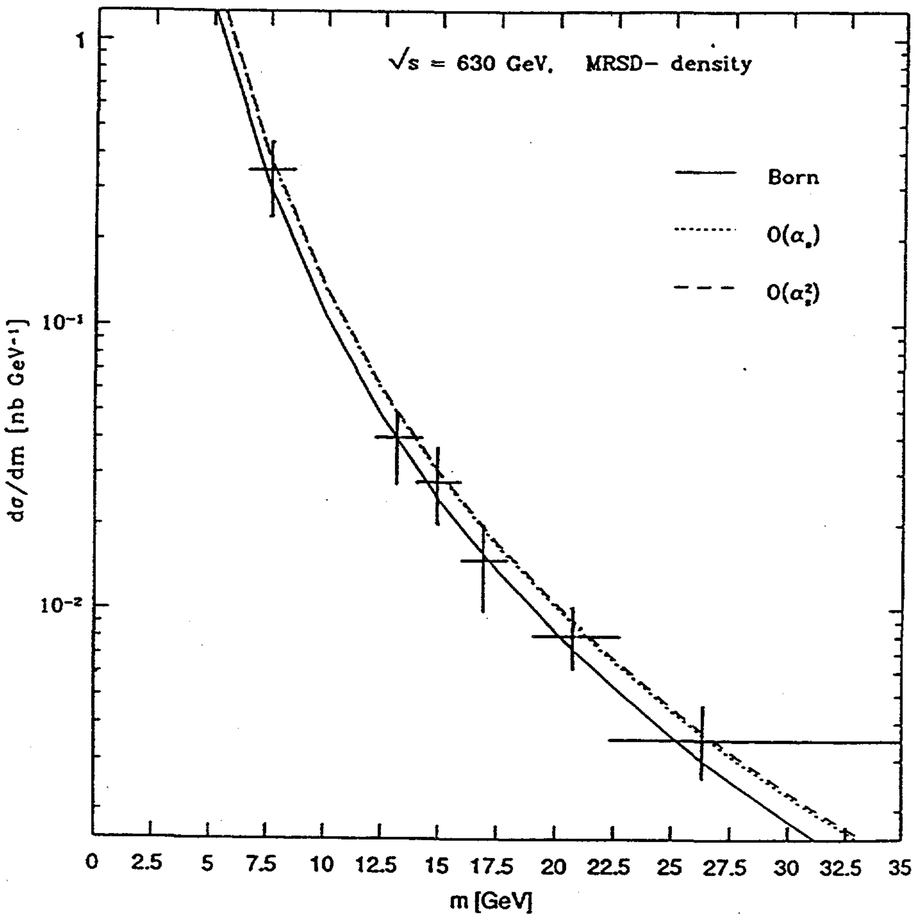

Figure 3: $d\sigma/dm$ computed in the $\overline{\text{MS}}$-scheme $2.5 < m < 35$ GeV at the $\sqrt{s} = 0.63$ TeV (Sp$\bar{\text{p}}$S). The data are obtained from the UA1 collaboration [20]. Solid line: Born; dotted line: order α_s corrected; dashed line: $\mathcal{O}(\alpha_s^2)$ corrected.

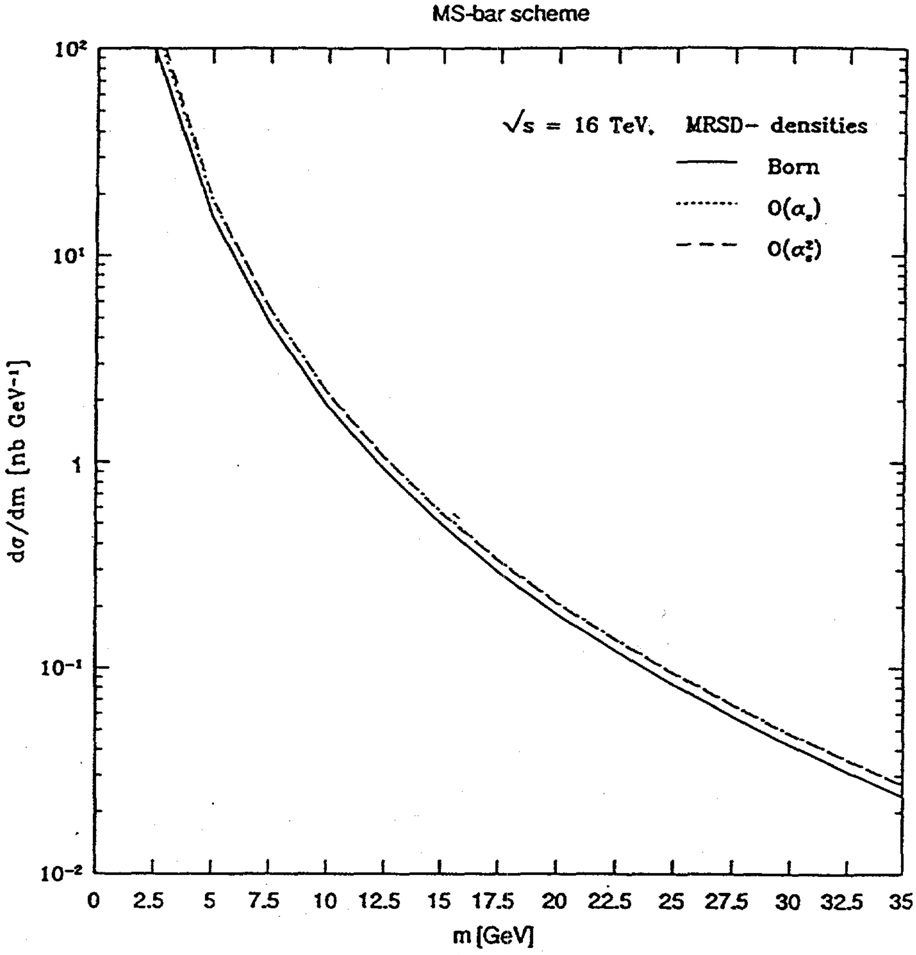

Figure 4: The same as in fig.3 but now for the LHC ($\sqrt{s} = 16$ TeV).

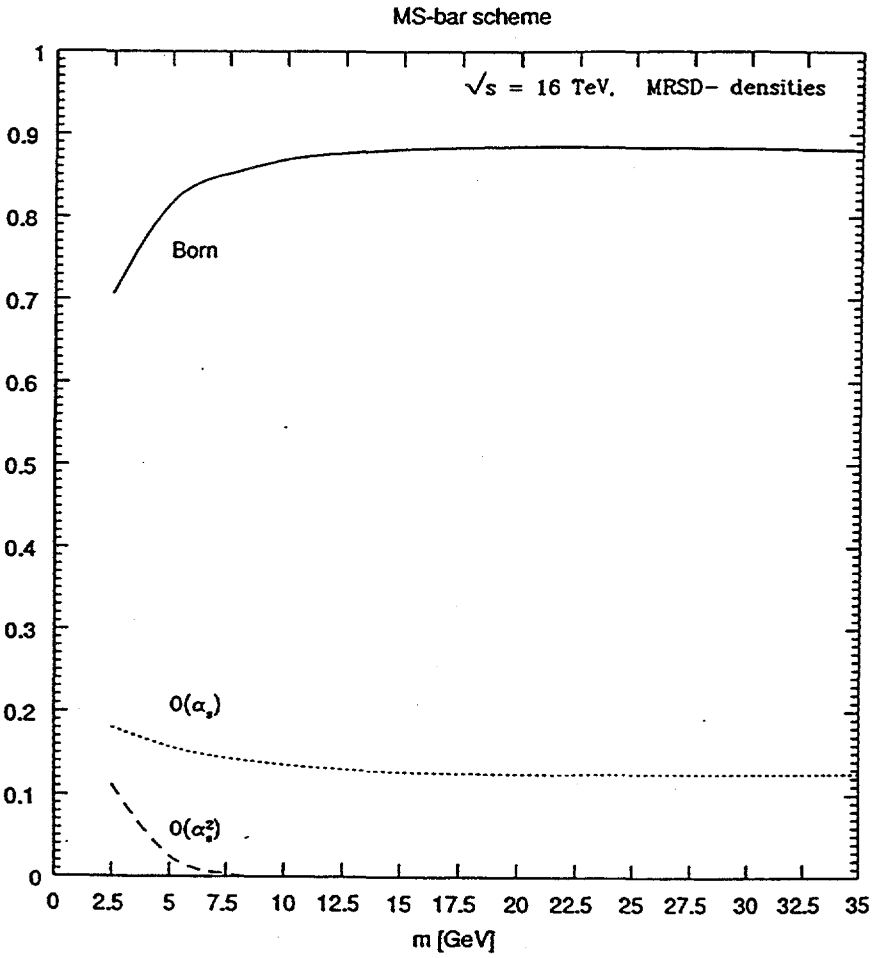

Figure 5: The ratio $R^{(i)}$ (20) in the $\overline{\text{MS}}$-scheme versus $2.5 < m < 35$ GeV at $\sqrt{s} = 16$ TeV. Solid line: Born; dotted line: order α_s contribution; dashed line: $\mathcal{O}(\alpha_s^2)$ contribution.

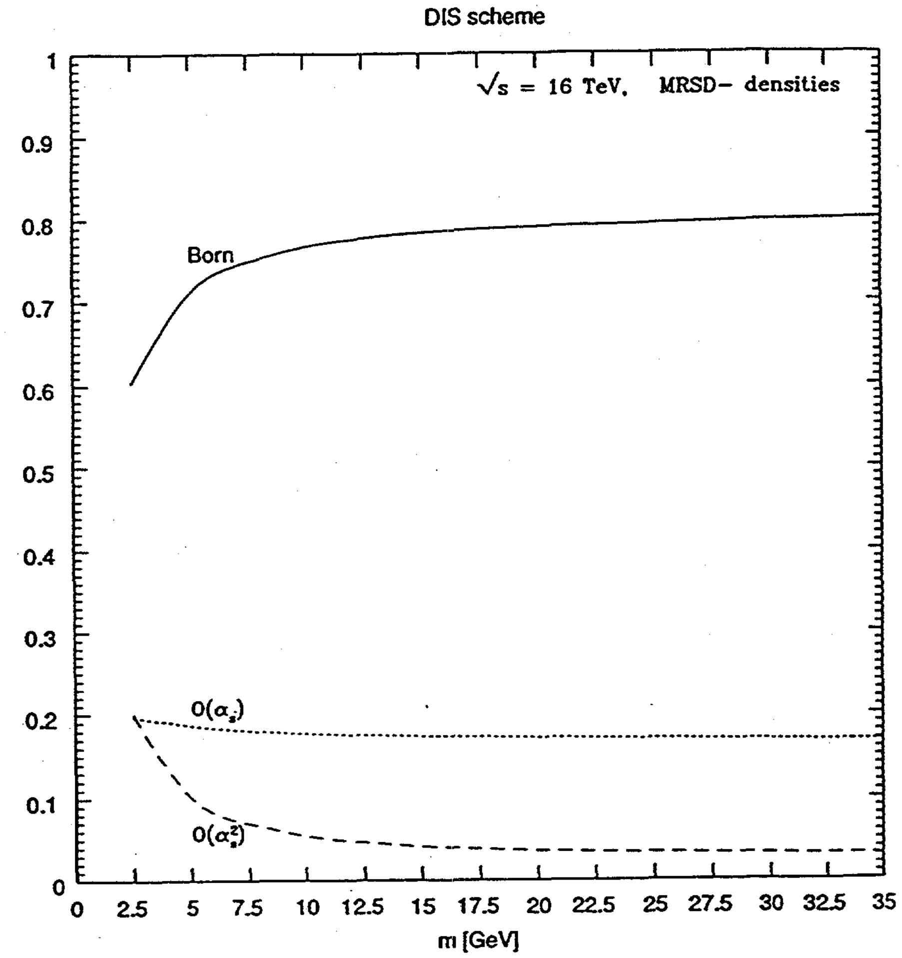

Figure 6: The same as in fig.5 but now for $R^{(i)}$ in the DIS-scheme.

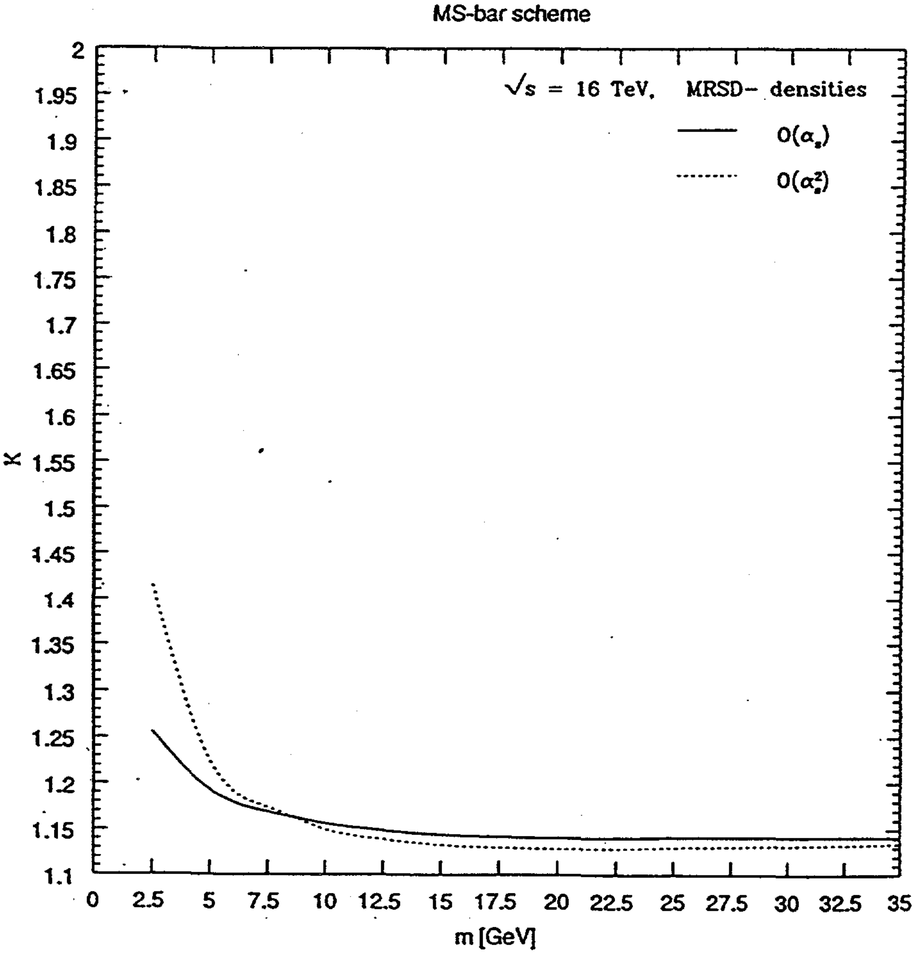

Figure 7: The K-factor computed in the $\overline{\text{MS}}$-scheme for $\sqrt{s} = 16$ TeV. Solid line: order α_s corrected; dotted line: $\mathcal{O}(\alpha_s^2)$ corrected.

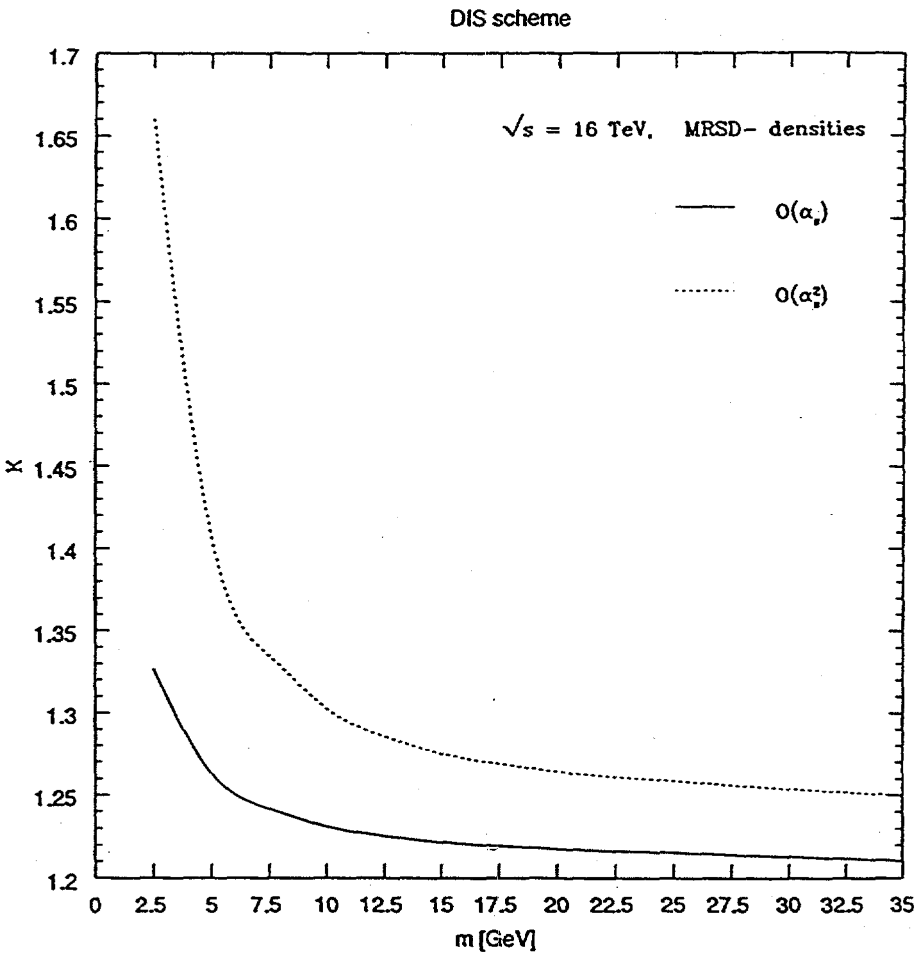

Figure 8: The same as in fig.6 but now for the K-factor computed in the DIS-scheme.

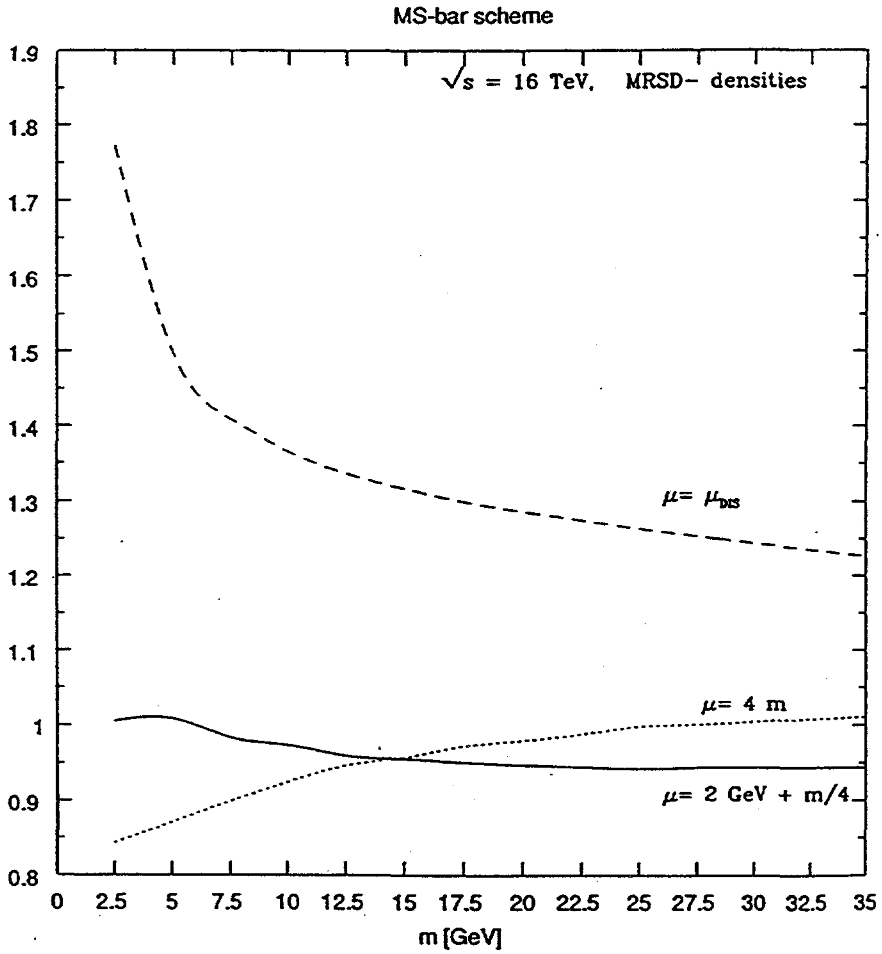

Figure 9: The factorization scale dependence of $\frac{d\sigma(\mu)}{dm}/\frac{d\sigma(m)}{dm}$ ($\overline{\text{MS}}$-scheme) versus $2.5 < m < 35$ GeV at $\sqrt{s} = 16$ TeV. Solid line: $\mu = 2 + \frac{m}{4}$ [GeV]; dotted line: $\mu = 4\,m$ [GeV]. Also shown is the factorization scheme dependence defined by $(\frac{d\sigma(m)}{dm})_{DIS}/(\frac{d\sigma(m)}{dm})_{\overline{\text{MS}}}$ (dashed line).

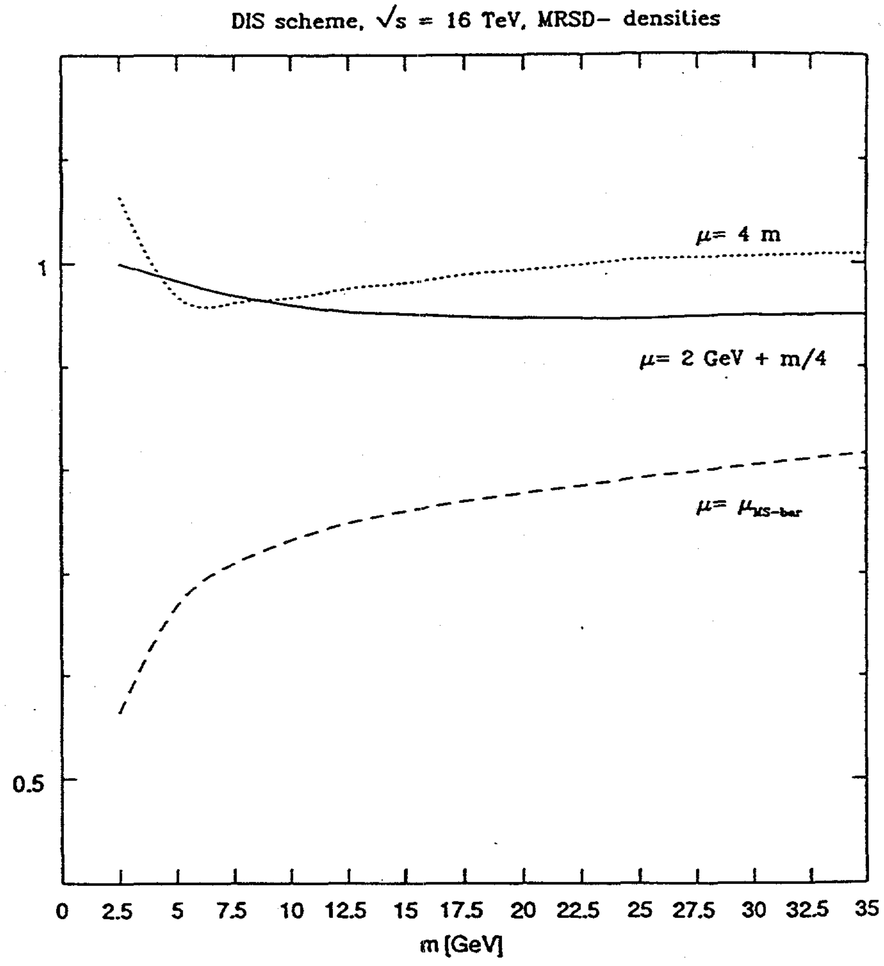

Figure 10: The factorization scale dependence of $\frac{d\sigma(\mu)}{dm}/\frac{d\sigma(m)}{dm}$ (DIS-scheme) versus $2.5 < m < 35$ GeV at $\sqrt{s} = 16$ TeV. Solid line: $\mu = 2 + \frac{m}{4}$ [GeV]; dotted line: $\mu = 4\,m$ [GeV]. Also shown is the factorization scheme dependence defined by $(\frac{d\sigma(m)}{dm})_{\overline{\mathrm{MS}}}/(\frac{d\sigma(m)}{dm})_{DIS}$ (dashed line).

PROMPT PHOTON PRODUCTION IN p-p COLLISIONS

J. CLEYMANS[a], E. QUACK[b], K. REDLICH[c*], D. K. SRIVASTAVA[d]

[a]*Department of Physics, University of Cape Town,*
Rondebosch 7700, South Africa
[b]*Gesellschaft für Schwerionenforschung (GSI),*
D-64220 Darmstadt, Germany
[c]*Fakultät für Physik, Universität Bielefeld,*
D-33501 Bielefeld, Germany
[d]*Variable Energy Cyclotron Centre,*
1/AF Bidhannagar, Calcutta, 700 064 India

A systematic study of the inclusive photon cross-section in $p-p$ collisions is presented. The dependence of the γ rates on the renormalization and factorization scales is discussed. A comparison is made with experimental data for centre-of-mass energies ranging from 23 GeV to 1.8 TeV. Predictions of the cross-sections are given for two different sets of structure functions for RHIC and LHC energies.

INTRODUCTION

We present estimates of the rates for prompt photon production in proton-proton collisions at SPS, RHIC and LHC energies, according to our present theoretical knowledge. They have been calculated using two sets of structure functions [1] giving good fits to recent data from HERA [2, 3]. Our results are summarized in the tables and figures at the end of this paper. The tables list separately the contributions from the lowest order QCD diagrams (denoted by BORN in the tables) and the sum of lowest and higher order terms as calculated by Aurenche et al. (denoted by INCLUSIVE in the tables) [4] – [8].

A comparison with experimental data from the NA24, WA70, UA6, E706, UA2, D0 and CDF collaborations [9] – [15] has been made and in general good agreement has been found. We can thus be fairly confident about the predictions for higher energies.

At higher energies the sensitivity to the choice of structure functions becomes more apparent and can be as large as a factor of three at $\sqrt{s}$ = 14 TeV. Other uncertainties are related to the the photon fragmentation function and the choice

---

[*] On leave of absence from : Department of Physics, University of Wroclaw, Poland

of scale parameters. These are discussed more fully in the text and in the cited literature.

THEORETICAL DESCRIPTION

At large values of the transverse momentum p_t of the photon, the inclusive cross section is dominated by hard collisions proceeding via subprocesses involving only a very few partons. To lowest order these are

$$\text{Compton}: \qquad q(\bar{q}) + g \rightarrow \gamma + q(\bar{q}) \tag{1}$$

$$\text{Annihilation}: \qquad q + \bar{q} \rightarrow \gamma + g \tag{2}$$

Contributions of higher order in the strong coupling have been calculated by Aurenche et al. [4] – [8], and our calculations are based on their programs. The general structure of the differential cross section is calculated from the following expression

$$E_\gamma \frac{d\sigma}{d^3p_\gamma}(A + B \rightarrow \gamma + \ldots) = \sum_{a,b} \int dx_a\, dx_b F(a, A; x_a) F(b, B; x_b) E_\gamma \frac{d\hat{\sigma}}{d^3p_\gamma} \tag{3}$$

The structure functions F give the probability of finding partons with momentum fractions x_i. They can be determined in deep inelastic scattering of electrons on protons. At high energies the main contribution to the cross section comes from the small x region and thus a precise knowledge of the structure functions in this region is essential.

To lowest order the invariant cross-section for the subprocess

$$a + b \rightarrow c + \gamma \tag{4}$$

can be written as

$$E_\gamma \frac{d\hat{\sigma}}{d^3p_\gamma} = \frac{\hat{s}}{\pi} \frac{d\sigma}{d\hat{t}} \delta(\hat{s} + \hat{t} + \hat{u}) \tag{5}$$

where $\hat{s}, \hat{t}$ and $\hat{u}$ are the Mandelstam variables for the subprocess.

The elementary cross-sections for the leading $(O(\alpha_s))$ subprocesses (2) and (3) are

$$\frac{d\sigma}{d\hat{t}}(qg \rightarrow q\gamma) = -\frac{\pi\alpha\alpha_s}{3\hat{s}^2} e_q^2 \frac{\hat{u}^2 + \hat{s}^2}{\hat{u}\hat{s}} \tag{6}$$

and

$$\frac{d\sigma}{d\hat{t}}(\bar{q}q \rightarrow g\gamma) = \frac{8\pi\alpha\alpha_s}{9\hat{s}^2} e_q^2 \frac{\hat{u}^2 + \hat{t}^2}{\hat{u}\hat{t}} \tag{7}$$

where e_q is the charge of the interacting quark.

The running coupling constant is given to lowest order by,

$$\alpha_s(Q^2) = \frac{12\pi}{(33 - 2N_f)\ln(Q^2/\Lambda^2)} \tag{8}$$

where N_f is the number of flavours and Λ is the QCD scale parameter. Following Aurenche et al [4, 8] we have taken the number of flavours as four and $\Lambda = 0.231$ GeV. The relation between Q^2 and p_T^2 for the evaluation of direct photons introduces a new parameter in the description.

Corrections to the Compton and annihilation graphs have been calculated by Aurenche et al. [4, 8], and we have used their programs to calculate the tables and figures presented at the end of this paper. The single-photon inclusive cross section can be written as

$$E\frac{d\sigma^{Inclusive}}{d^3p} = E\frac{d\sigma^B}{d^3p} + E\frac{d\sigma^{HO}}{d^3p} + E\frac{d\sigma^A}{d^3p} \tag{9}$$

where the separate terms are the leading order Born term, higher order and anomalous contribution.

The photon couples to the charge of the quark and the resulting fragmentation function to lowest order is ,

$$zD_{q\to\gamma}(z, Q_f^2) = e_q^2\frac{\alpha}{2\pi}[1 + (1 - z)^2]\ln(Q_f^2/\Lambda^2) \tag{10}$$

and

$$zD_{g\to\gamma}(z, Q_f^2) = 0 \tag{11}$$

where z represents the fraction of the jet momentum carried by the (collinear) photon.

In general there are three places where scales have to be discussed :

1. The renormalization scale in the running coupling constant. We will denote this by C_1, so that in Eq. (8) one has $Q^2 = C_1p_t^2$, typically C_1 varies between 1/16 and 16.

2. The factorization scale in the structure functions. This is chosen to be the same as the previous one.

3. The factorization scale in the fragmentation functions. This will be denoted by C_f. Thus the Q_f^2 appearing in Eq. (10) is given by $Q_f^2 = C_fp_t^2$.

In many cases it is possible to use a general prescription like the principle of minimal sensitivity (PMS)[19] to treat this arbitrariness in a more satisfactory way. In PMS one looks at the differential cross section as a function of C_1 and C_f, and tries to find a minimum. This procedure has been followed when comparing with the experimental data of the NA24 collaboration. It is however not always possible to find such a minimum and in many cases one has to accept that the cross section is not very sensitive to a change in scales.

COMPARISON WITH EXPERIMENTAL DATA

In the comparison to existing data, we consider $p-p$ and $p-\bar{p}$ collisions at various energies ranging from 23 GeV to 1.8 TeV. The cross-sections always refer to the invariant form

$$E\frac{d\sigma}{d^3p} = \frac{1}{2\pi p_t}\frac{d\sigma}{dp_t dy} \tag{12}$$

and are shown for fixed y or a y interval as a function of p_t.

The parametrization chosen for the structure functions used in all calculations is the one denoted by $D-'$ [1]. The change in the results when other structure functions such as $D0'$ [1] or ABFOW[18] are used is of the order of 10%. This relative insensitivity is due to the energy range at which present data are taken, higher energies probe the small x-region of the parton distribution functions and thus lead to a higher sensitivity on the precise form of the structure functions in the low x region.

In Fig. (1) we compare the data of the NA24 collaboration[9] with the results of our calculations. The data taken in a finite y interval were extrapolated to $y = 0$ using the procedure of Aurenche and Whalley[20]. The calculation is carried out using the PMS scheme (full line) and at a fixed scale of $Q^2 = p_t^2/4$ (dashed line). In both cases good agreement is obtained with the data.

For the other experiments we used the fixed scale of $Q^2 = p_t^2/4$.

Fig. (3) shows the comparison with UA6 pp data [11] taken at $\sqrt{s} = 24.3$ GeV. These data were averaged in the interval $-0.2 \leq y \leq 1.$, the same averaging was applied to the theoretical calculation.

In Fig. (2) this calculation is compared to the data of WA70 taken at $\sqrt{s} = 22.96$ GeV. The plotted data were measured in a small bin symmetric around $y = 0$.

The most recent data of the E706 collaboration [12] for $p - Be$ at $\sqrt{s} = 30.6$ GeV are shown in Fig. (4) together with the results of our calculations.

In Fig. (5) we compare results obtained from $p-\bar{p}$ collisions [16] at $\sqrt{s} = 630$ GeV. To test for the sensitivity on the choice of scale parameter the results are shown for $Q^2 = p_t^2/4$ and a somewhat higher value $Q^2 = 16p_t^2$. As seen in Fig. (5) the agreement with experimental dat is very good and only weakly dependent on the choice of the scale parameter.

In Figs. (6a) and (6b) we compare results obtained from $p-\bar{p}$ collisions at $\sqrt{s}$ = 1.8 TeV at the Tevatron by the D0 [14] and the CDF collaborations [15]. The agreement between data and theoretical prediction is illustrated in Fig. (7) where we show the relative difference. As can be seen the deviations in the whole p_t range are very small.

As two further typical cases we also show a comparison with low energy $\pi^- p$ and $\pi^+ - p$ data in Figs. (8a) and (8b) where the full lines correspond to the parametrization of structure functions given by SMRS-P1, the short-dashed line to SMR-P2 and the long-dashed line to SMRS-P3 [17].

In all cases good agreement with the data is obtained, sometimes even very good, which provides us with confidence for the extrapolation towards higher energies.

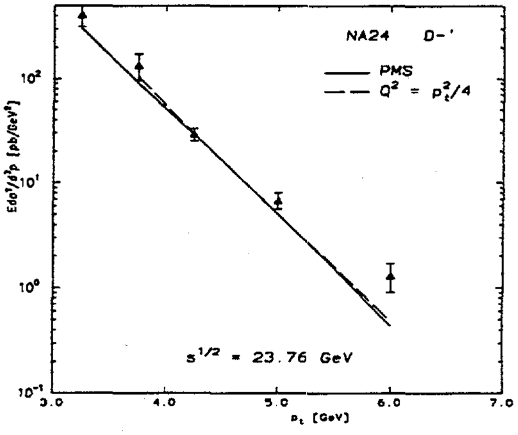

Figure 1

Figure 1: Comparison between data from the NA24 collaboration and theoretical calculations. Only statistical errors are shown.

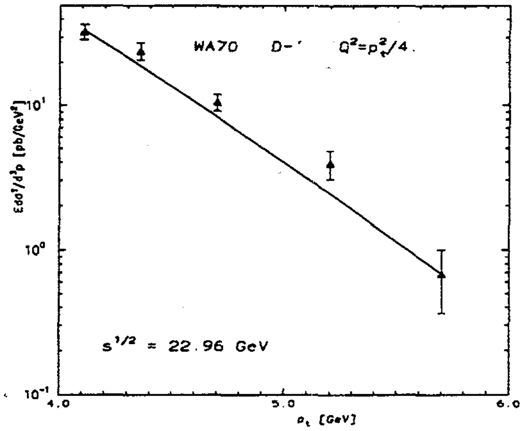

Figure 2

Figure 2: Comparison between data from the WA70 collaboration and theoretical calculations. Only statistical errors are shown.

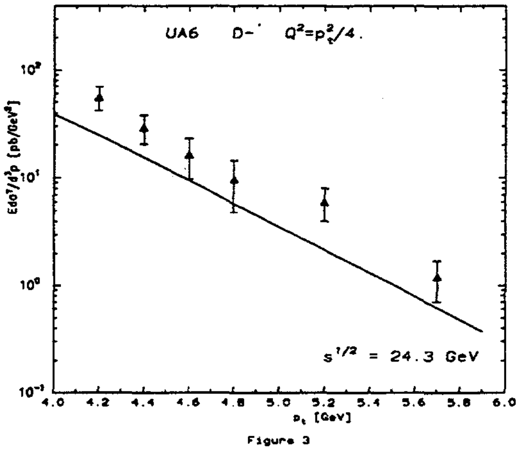

Figure 3: Comparison between data from the UA6 collaboration and theoretical calculations. Only statistical errors are shown.

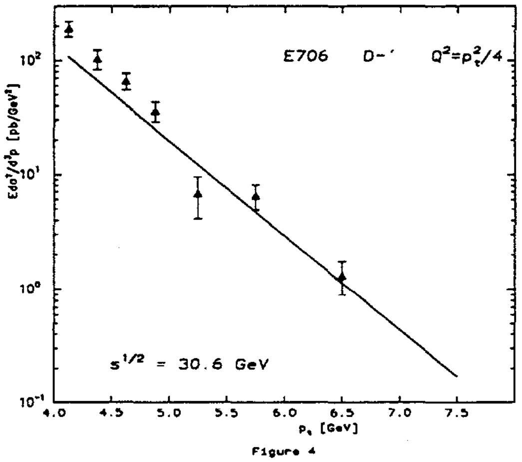

Figure 4: Comparison between data from the E706 collaboration and theoretical calculations. Only statistical errors are shown.

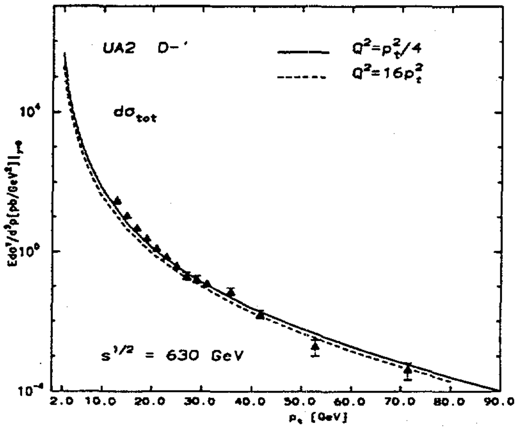

Figure 5

Figure 5: Comparison between data from the UA2 collaboration and theoretical calculations. Only statistical errors are shown.

PREDICTIONS

The calculations presented above were done for energies corresponding to RHIC energies, $s^{1/2} = 0.2$ and 0.5 TeV and for the LHC energy range, 5.5 and 14 TeV. These are presented in the form of tables and in the form of figures. In Fig. (9a) the dependence of γ-rates on C_1 defined above in section 2, for fixed $C_f = 16$ and $p_t = 2.0$ GeV is studied at the energy $\sqrt{s} = 14$ TeV. As seen in this figure the cross section is very flat for $C_1 > 2$. In Fig. (9b) we show the dependence on the factorization scale in the fragmentation function C_f for fixed C_1=16 at the same values of p_t and $\sqrt{s}$. It is seen that the cross section is only weakly dependent on C_f for $C_f > 5$. In conclusion from Figs. (9a-b), we use in the following the scale $C_1 = C_f = 16$ to get a result which is only weakly scale dependent for the rates. In the following figures (10) - (13) and tables (1) to (4) we present the predictions for the inclusive cross sections $d\sigma/dp_t dy$ (pb/GeV) for the energies relevant for RHIC and LHC using the structure functions $D-'$ (figures (10a)-(13a))and $D0'$ (figures (10b)-(13b)). Note that these cross sections differ by a factor $2\pi p_t$ as compared to those shown in section 3.

Finally in Fig. (14) we show the rapidity dependence of the cross section for a number of values of the transverse momentum. We see that the cross-section remains essentially constant up to large values of the rapidity y and then falls off rapidly near the kinematic limit.

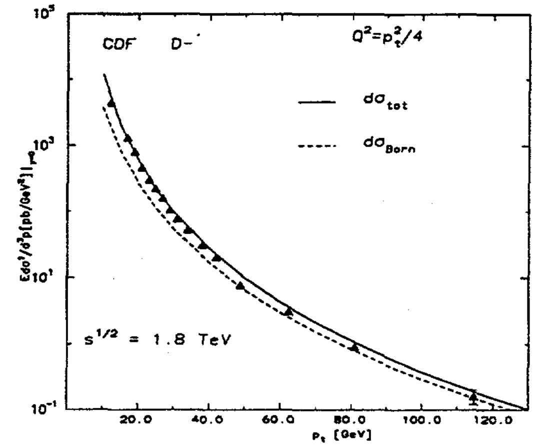

Figure 6a

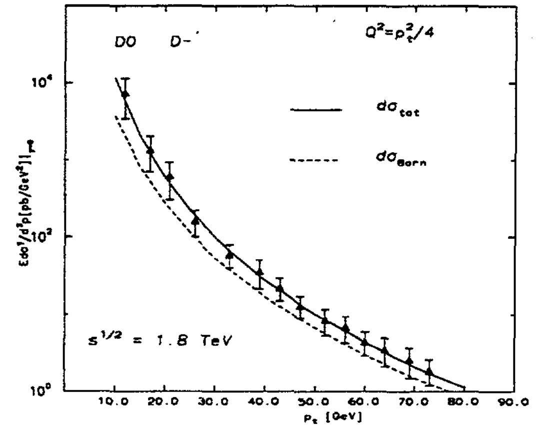

Figure 6b

Figure 6: Comparison between data from the (a) D0 and (b) CDF collaboration and theoretical calculations. Only statistical errors are shown.

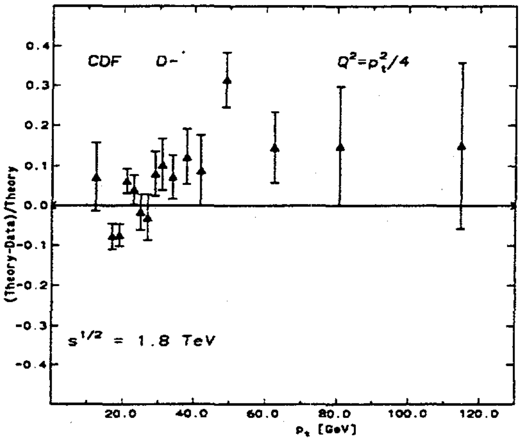

Figure 7

Figure 7: Deviation of the theoretical prediction from the experimental values measured by the CDF collaboration.

SUMMARY

It is felt that the predictions for photon production at RHIC and LHC energies are quite reliable as they reproduce most of the existing data. We also feel that they will be useful for planning experiments at these facilities.

Acknowledgment

We gratefully acknowledge the help of Patrick Aurenche in making his computer programs available to us. We would like to thank Helmut Satz and Xin-Nian Wang for encouragement and for the initiative in organizing these meetings. One of us (K. R.) would like to thank the Komitet Badan Naukowich KBN for financial support. E. Q. would like to thank the Physics Department at the University of Cape Town for the warm hospitality during the period when part of this work was done. We would like to thank the hospitality at CERN and LBL which made it possible for all of us to attend these meetings.

References

[1] A. D. Martin, W. J. Stirling and R. G. Roberts, Phys. Lett. **306B**, 145 (1993); H. Plothow-Besch, Comp. Phys. Comm. **75**, 396 (1993).

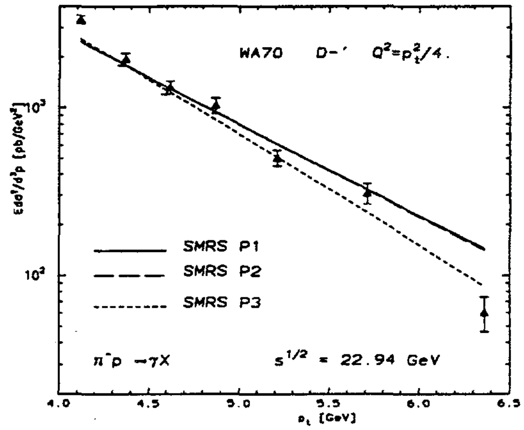

Figure 8a

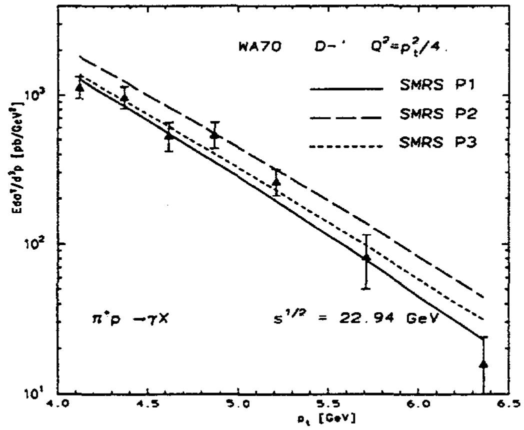

Figure 8b

Figure 8: Comparison between data from the WA70 collaboration on (a) $\pi^+ - p$, (b) $\pi^- - p$ collisions and theoretical calculations. Only statistical errors are shown.

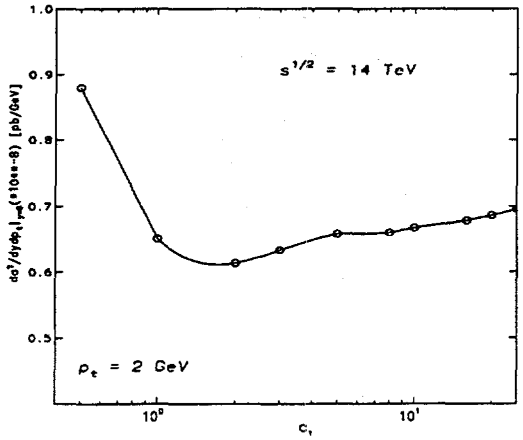

Figure 9a

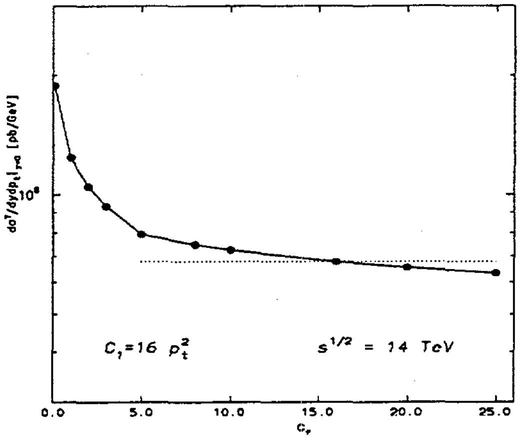

Figure 9b

Figure 9: Dependence of the cross section on the scale (a) C_f and (b) C_1 at $p_t = 2$ GeV for $\sqrt{s} = 14$ TeV for the structure function $D-'$.

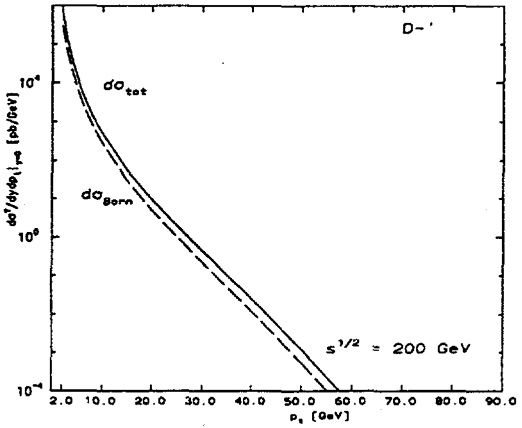

Figure 10a

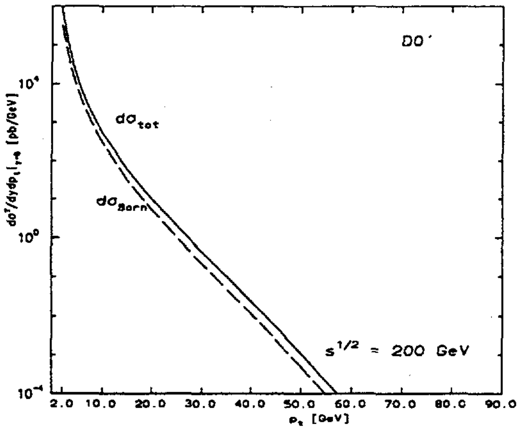

Figure 10b

Figure 10: Predictions for the photon cross section at $\sqrt{s} = 200$ GeV for the structure function (a) $D-'$ and (b)$D0'$.

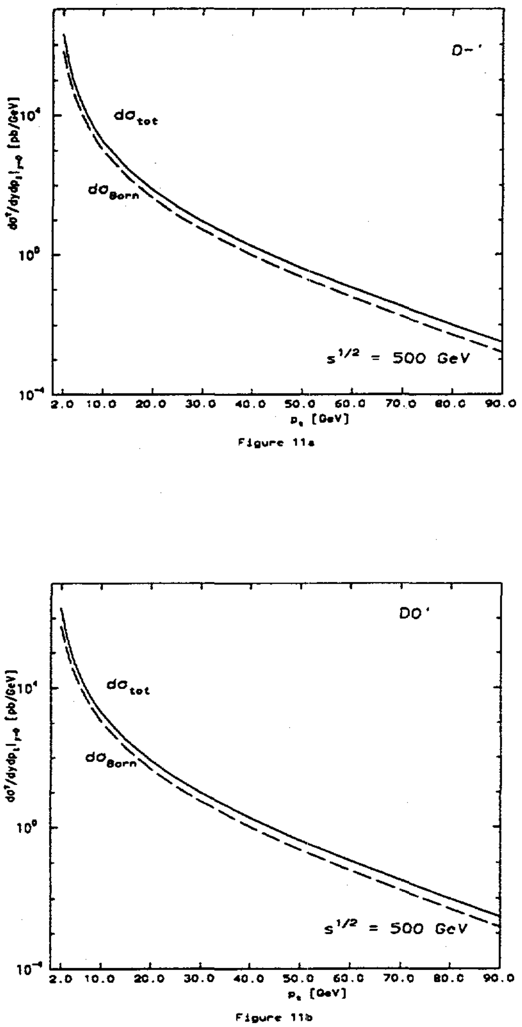

Figure 11: Predictions for the photon cross section at $\sqrt{s} = 500$ GeV for the structure function (a) $D-'$ and (b)$D0'$.

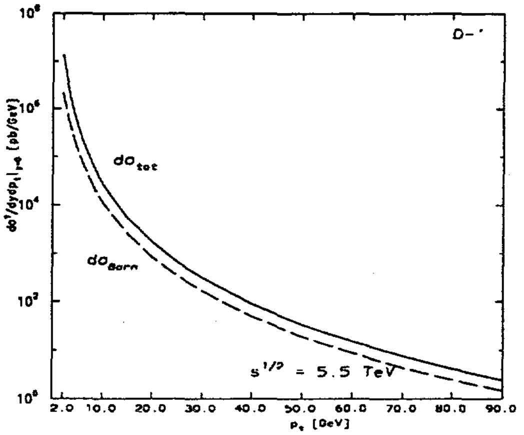

Figure 12a

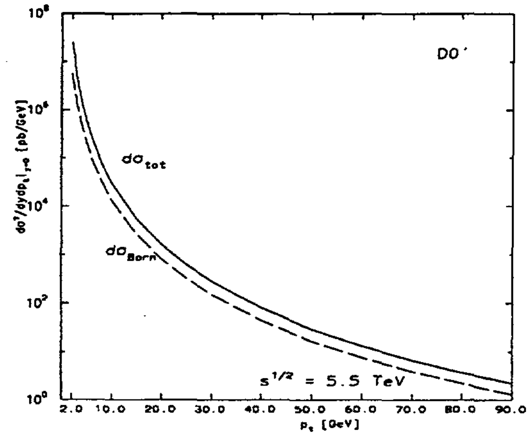

Figure 12b

Figure 12: Predictions for the photon cross section at $\sqrt{s} = 5.5$ TeV for the structure function (a)$D-'$ and (b) $D0'$.

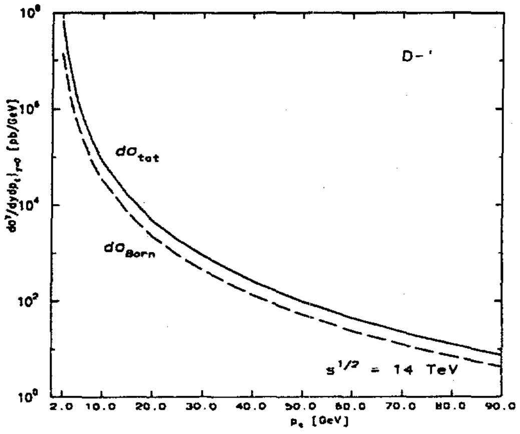

Figure 13a

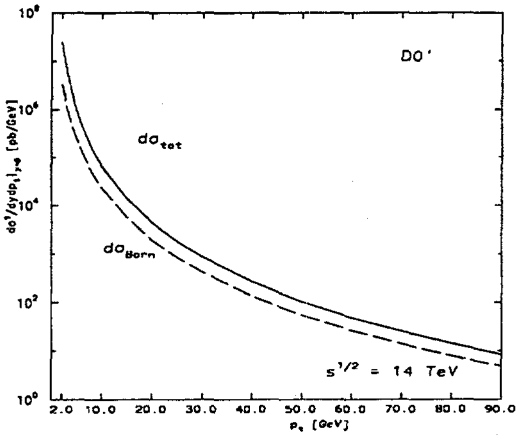

Figure 13b

Figure 13: Predictions for the photon cross section at $\sqrt{s} = 14$ TeV for the structure function (a) $D-'$ and (b) $D0'$.

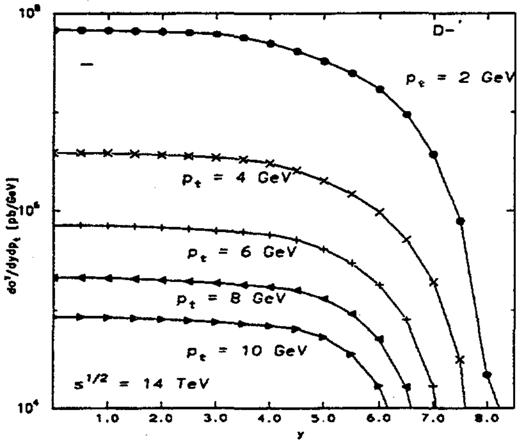

Figure 14

Figure 14: Photon cross section as a function of the rapidity y at $p_t = 2$ GeV for $\sqrt{s} = 14$ TeV for the structure function $D-'$.

[2] ZEUS Collaboration, M. Derrick *et al.*, DESY preprint 93-110, Phys. Lett. (to be published).

[3] H1 Collaboration, J. Abt *et al.*, Nucl. Phys. **B407**, 515 (1993) and Phys. Lett. **B321**, 161 (1994).

[4] P. Aurenche, A. Douiri, R. Baier, M. Fontannaz and D. Schiff, Phys. Lett. **140B**, 87 (1984).

[5] P. Aurenche, R. Baier, A. Douiri, M. Fontannaz, and D. Schiff, Z. f. Phys. C **29**, 495 (1985).

[6] P. Aurenche, R. Baier, M. Fontannaz and D. Schiff, Nucl. Phys. **B286**, 509 (1987).

[7] P. Aurenche, R. Baier, M. Fontannaz and D. Schiff, Nucl. Phys. **B297**, 661 (1988).

[8] P. Aurenche, R. Baier and M. Fontannaz, Phys. Rev. D **42**, 1440 (1990).

[9] C. De Marzo *et al.* (NA24 collaboration), Phys. Rev. D **36**, 8 (1987).

[10] M. Bonesini *et al.* (WA70 collaboration), Z. Phys. C **38**, 371 (1988).

[11] G. Sozzi *et al.* (UA6 collaboration), Phys. Lett. **B317**, 243 (1993).

[12] G. Alverson *et al.* (E706 collaboration), Phys. Rev. D **48**, 5 (1993)

[13] R. Ansari et al. (UA2 collaboration), Z. f. Phys. **C41**, 395 (1988)

[14] A. Smith (D0 collaboration), private communication.

Table 1 : Inclusive γ production in p-p collision
$d\sigma/dydp_t|_{y=0}$ [pb/GeV]
$s^{1/2} = 200$ GeV

p_t [GeV]	Inclusive $D-'$	Born $D-'$	Inclusive $D0'$	Born $D0'$
2.0	$0.729\ 10^{6}$	$0.292\ 10^{6}$	$0.811\ 10^{6}$	$0.316\ 10^{6}$
3.0	$0.124\ 10^{6}$	$0.584\ 10^{5}$	$0.141\ 10^{6}$	$0.659\ 10^{6}$
4.0	$0.348\ 10^{5}$	$0.178\ 10^{5}$	$0.399\ 10^{5}$	$0.203\ 10^{5}$
5.0	$0.128\ 10^{5}$	$0.685\ 10^{4}$	$0.147\ 10^{5}$	$0.783\ 10^{5}$
6.0	$0.558\ 10^{4}$	$0.305\ 10^{4}$	$0.639\ 10^{4}$	$0.347\ 10^{4}$
7.0	$0.280\ 10^{4}$	$0.155\ 10^{4}$	$0.318\ 10^{4}$	$0.175\ 10^{4}$
8.0	$0.145\ 10^{4}$	$0.802\ 10^{3}$	$0.164\ 10^{4}$	$0.903\ 10^{4}$
9.0	$0.818\ 10^{3}$	$0.453\ 10^{3}$	$0.922\ 10^{3}$	$0.507\ 10^{3}$
10.0	$0.485\ 10^{3}$	$0.268\ 10^{3}$	$0.544\ 10^{3}$	$0.298\ 10^{3}$
15.0	$0.554\ 10^{2}$	$0.298\ 10^{2}$	$0.602\ 10^{2}$	$0.321\ 10^{2}$
20.0	$0.943\ 10^{1}$	$0.494\ 10^{1}$	$0.996\ 10^{1}$	$0.517\ 10^{1}$
25.0	$0.195\ 10^{1}$	$0.993\ 10^{0}$	$0.200\ 10^{1}$	$0.101\ 10^{1}$
30.0	$0.444\ 10^{0}$	$0.221\ 10^{0}$	$0.443\ 10^{0}$	$0.218\ 10^{0}$
40.0	$0.251\ 10^{-1}$	$0.119\ 10^{-1}$	$0.237\ 10^{-1}$	$0.112\ 10^{-1}$
50.0	$0.124\ 10^{-2}$	$0.560\ 10^{-3}$	$0.112\ 10^{-2}$	$0.507\ 10^{-2}$
60.0	$0.447\ 10^{-4}$	$0.195\ 10^{-4}$	$0.392\ 10^{-4}$	$0.174\ 10^{-4}$
70.0	$0.843\ 10^{-6}$	$0.360\ 10^{-6}$	$0.733\ 10^{-6}$	$0.323\ 10^{-6}$
80.0	$0.444\ 10^{-8}$	$0.194\ 10^{-8}$	$0.400\ 10^{-8}$	$0.187\ 10^{-8}$

[15] S. E. Kuhlmann *et al.* (CDF collaboration), preprint Fermilab, FNAL-CONF-94-148-E (to be published).

[16] M. Bonesini *et al.* (WA70 collaboration), Z. Phys. C **38**, 535 (1988)

[17] P. J. Sutton, A. D. Martin, R. G. Roberts and W. J. Stirling, Phys. Rev. D **45**, 2349 (1992).

[18] P. Aurenche, R. Baier, M. Fontannaz, J.F. Owens and M. Werlen, Phys. Rev. D **39**, 3275 (1989).

[19] P. M. Stevenson, Phys. Rev. D **23**, 70 (1981); P. M. Stevenson and H. D. Politzer, Nucl. Phys. **B277**, 758 (1986).

[20] P. Aurenche and M. R. Whalley, Rutherford Appleton Laboratory preprint RAL-89-106, (unpublished).

Table 2 : Inclusive γ production in p-p collision
$d\sigma/dydp_t|_{y=0}$ [pb/GeV]
$s^{1/2} = 500$ GeV

p_t [GeV]	Inclusive $D-'$	Born $D-'$	Inclusive $D0'$	Born $D0'$
2.0	$0.199\ 10^{7}$	$0.637\ 10^{6}$	$0.196\ 10^{7}$	$0.587\ 10^{6}$
3.0	$0.344\ 10^{6}$	$0.136\ 10^{6}$	$0.365\ 10^{6}$	$0.140\ 10^{6}$
4.0	$0.986\ 10^{5}$	$0.442\ 10^{5}$	$0.108\ 10^{6}$	$0.477\ 10^{5}$
5.0	$0.373\ 10^{5}$	$0.181\ 10^{5}$	$0.418\ 10^{5}$	$0.201\ 10^{5}$
6.0	$0.168\ 10^{5}$	$0.858\ 10^{4}$	$0.190\ 10^{5}$	$0.966\ 10^{4}$
7.0	$0.874\ 10^{4}$	$0.465\ 10^{4}$	$0.994\ 10^{4}$	$0.527\ 10^{4}$
8.0	$0.473\ 10^{4}$	$0.258\ 10^{4}$	$0.539\ 10^{4}$	$0.294\ 10^{4}$
9.0	$0.282\ 10^{4}$	$0.156\ 10^{4}$	$0.323\ 10^{4}$	$0.178\ 10^{4}$
10.0	$0.177\ 10^{4}$	$0.989\ 10^{3}$	$0.203\ 10^{4}$	$0.113\ 10^{4}$
15.0	$0.283\ 10^{3}$	$0.161\ 10^{3}$	$0.321\ 10^{3}$	$0.182\ 10^{3}$
20.0	$0.721\ 10^{2}$	$0.411\ 10^{2}$	$0.808\ 10^{2}$	$0.459\ 10^{2}$
25.0	$0.236\ 10^{2}$	$0.134\ 10^{2}$	$0.262\ 10^{2}$	$0.148\ 10^{2}$
30.0	$0.903\ 10^{1}$	$0.510\ 10^{1}$	$0.988\ 10^{1}$	$0.554\ 10^{1}$
40.0	$0.175\ 10^{1}$	$0.973\ 10^{0}$	$0.187\ 10^{1}$	$0.103\ 10^{1}$
50.0	$0.411\ 10^{0}$	$0.224\ 10^{0}$	$0.429\ 10^{0}$	$0.232\ 10^{0}$
60.0	$0.112\ 10^{0}$	$0.601\ 10^{-1}$	$0.115\ 10^{0}$	$0.610\ 10^{-1}$
70.0	$0.329\ 10^{-1}$	$0.173\ 10^{-1}$	$0.329\ 10^{-1}$	$0.172\ 10^{-1}$
80.0	$0.100\ 10^{-1}$	$0.520\ 10^{-2}$	$0.983\ 10^{-2}$	$0.506\ 10^{-2}$
90.0	$0.312\ 10^{-2}$	$0.159\ 10^{-2}$	$0.299\ 10^{-2}$	$0.152\ 10^{-2}$
100.0	$0.968\ 10^{-3}$	$0.483\ 10^{-3}$	$0.911\ 10^{-3}$	$0.454\ 10^{-3}$

Table 3 : Inclusive γ production in p-p collision
$d\sigma/dydp_t|_{y=0}$ [pb/GeV]
$s^{1/2} = 5.5$ TeV

p_t [GeV]	Inclusive $D-'$	Born $D-'$	Inclusive $D0'$	Born $D0'$
2.0	0.133 10^8	0.213 10^7	0.258 10^8	0.565 10^7
3.0	0.301 10^7	0.652 10^6	0.475 10^7	0.129 10^7
4.0	0.101 10^7	0.265 10^6	0.142 10^7	0.444 10^6
5.0	0.427 10^6	0.128 10^6	0.557 10^6	0.192 10^6
6.0	0.207 10^6	0.689 10^5	0.256 10^6	0.953 10^5
7.0	0.116 10^6	0.415 10^5	0.137 10^6	0.540 10^5
8.0	0.654 10^5	0.252 10^5	0.753 10^5	0.313 10^5
9.0	0.413 10^5	0.166 10^5	0.461 10^5	0.198 10^5
10.0	0.272 10^5	0.113 10^5	0.298 10^5	0.131 10^5
15.0	0.539 10^4	0.250 10^4	0.544 10^4	0.260 10^4
20.0	0.167 10^4	0.827 10^3	0.161 10^4	0.809 10^3
25.0	0.663 10^3	0.343 10^3	0.621 10^3	0.324 10^3
30.0	0.310 10^3	0.165 10^3	0.284 10^3	0.152 10^3
40.0	0.914 10^2	0.506 10^2	0.821 10^2	0.455 10^2
50.0	0.340 10^2	0.192 10^2	0.302 10^2	0.171 10^2
60.0	0.153 10^2	0.882 10^1	0.135 10^2	0.777 10^1
70.0	0.772 10^1	0.450 10^1	0.680 10^1	0.395 10^1
80.0	0.424 10^1	0.249 10^1	0.373 10^1	0.219 10^1
90.0	0.249 10^1	0.147 10^1	0.219 10^1	0.129 10^1
100.0	0.154 10^1	0.912 10^0	0.135 10^1	0.803 10^0

Table 4 : Inclusive γ production in p-p collision
$d\sigma/dydp_t|_{y=0}$ [pb/GeV]
$s^{1/2}$ = 14TeV

p_t [GeV]	Inclusive $D-'$	Born $D-'$	Inclusive $D0'$	Born $D0'$
2.0	$0.678\ 10^{8}$	$0.138\ 10^{8}$	$0.249\ 10^{8}$	$0.328\ 10^{7}$
3.0	$0.128\ 10^{8}$	$0.320\ 10^{7}$	$0.608\ 10^{7}$	$0.109\ 10^{7}$
4.0	$0.390\ 10^{7}$	$0.111\ 10^{7}$	$0.214\ 10^{7}$	$0.464\ 10^{6}$
5.0	$0.155\ 10^{7}$	$0.486\ 10^{6}$	$0.933\ 10^{6}$	$0.233\ 10^{6}$
6.0	$0.718\ 10^{6}$	$0.244\ 10^{6}$	$0.464\ 10^{6}$	$0.130\ 10^{6}$
7.0	$0.389\ 10^{6}$	$0.140\ 10^{6}$	$0.266\ 10^{6}$	$0.803\ 10^{5}$
8.0	$0.214\ 10^{6}$	$0.816\ 10^{5}$	$0.152\ 10^{6}$	$0.500\ 10^{5}$
9.0	$0.132\ 10^{6}$	$0.518\ 10^{5}$	$0.975\ 10^{5}$	$0.335\ 10^{5}$
10.0	$0.860\ 10^{5}$	$0.345\ 10^{5}$	$0.653\ 10^{5}$	$0.233\ 10^{5}$
15.0	$0.161\ 10^{5}$	$0.706\ 10^{4}$	$0.136\ 10^{5}$	$0.554\ 10^{4}$
20.0	$0.487\ 10^{4}$	$0.225\ 10^{4}$	$0.439\ 10^{4}$	$0.193\ 10^{4}$
25.0	$0.191\ 10^{4}$	$0.920\ 10^{3}$	$0.180\ 10^{4}$	$0.836\ 10^{3}$
30.0	$0.890\ 10^{3}$	$0.440\ 10^{3}$	$0.866\ 10^{3}$	$0.417\ 10^{3}$
40.0	$0.263\ 10^{3}$	$0.136\ 10^{3}$	$0.269\ 10^{3}$	$0.136\ 10^{3}$
50.0	$0.986\ 10^{2}$	$0.523\ 10^{2}$	$0.104\ 10^{3}$	$0.545\ 10^{2}$
60.0	$0.451\ 10^{2}$	$0.244\ 10^{2}$	$0.484\ 10^{2}$	$0.261\ 10^{2}$
70.0	$0.231\ 10^{2}$	$0.127\ 10^{2}$	$0.252\ 10^{2}$	$0.138\ 10^{2}$
80.0	$0.129\ 10^{2}$	$0.722\ 10^{1}$	$0.142\ 10^{2}$	$0.795\ 10^{1}$
90.0	$0.773\ 10^{1}$	$0.436\ 10^{1}$	$0.858\ 10^{1}$	$0.485\ 10^{1}$
100.0	$0.486\ 10^{1}$	$0.277\ 10^{1}$	$0.544\ 10^{1}$	$0.310\ 10^{1}$

PRODUCTION OF DRELL–YAN PAIRS IN *pp* COLLISIONS

S. GAVIN[a], S. GUPTA[b], R. KAUFFMAN[a], P. V. RUUSKANEN[c],
D. K. SRIVASTAVA[d] and R. L. THEWS[e]

[a] *Department of Physics, Brookhaven National Laboratory,*
Upton, New York 11973, USA
[b] *Theory Group, Tata Institute of Fundamental Research,*
Homi Bhabha Road, Bombay 400 005, India
[c] *Institute for Theoretical Physics,*
P.O.Box 9, FIN-00014, University of Helsinki, Finland
[d] *Variable Energy Cyclotron Centre,*
1/AF Bidhan Nagar, Calcutta 700 064, India
[e] *Department of Physics, University of Arizona,*
Tucson, Arizona 85721, USA

We compute cross sections for the Drell-Yan process in N–N collisions at next-to-leading order in α_s. The mass, rapidity, transverse momentum, and angular dependence of these cross sections are presented. An estimate of higher order corrections is obtained from next-to-next-to-leading order calculation of the mass distribution. We compare the results with some of the existing data to show the quality of the agreement between calculations and data. We present predictions for energies which will become available at the RHIC and LHC colliders. Uncertainties in these predictions due to choices of scale, scheme and parton distribution are discussed.

INTRODUCTION

The aim of this study is to provide a systematic survey of theoretical predictions for the Drell–Yan process [1, 2] in nucleon–nucleon collisions at energies relevant to ion–ion experiments at RHIC and LHC, and to discuss confidence limits for these predictions. In an accompanying article, Van Neerven has reviewed the theory of the Drell–Yan process, emphasizing the dependence of the production rate on the dilepton's mass M and rapidity y. We present calculations of the M and y distributions using standard perturbative QCD. To supplement these calculations, we provide a skeletal theoretical discussion to fix the notation and identify the uncertainties. In addition, we study the experimentally-relevant transverse momentum and angular distributions of the dileptons. These topics are treated in separate subsections, since one must go beyond perturbation theory to compute these distributions.

Our predictions for $\mathrm{d}\sigma/\mathrm{d}M\mathrm{d}y$ are based on a perturbative analysis of the underlying partonic processes to order α_s [3, 4, 5, 6]. Results for $\mathrm{d}\sigma/\mathrm{d}M$ are reported to order α_s^2. We find that the perturbative corrections grow as M decreases. From the point of view of the heavy ion physics, the mass region from 3 to 10 GeV is of most interest. The relative magnitude of the $O(\alpha_s^2)$ correction in this range sets one limit on our confidence in the applicability of perturbation theory.

At fixed order the calculated cross sections depend on the renormalization scale μ_R, the factorization scale μ_F, and the regularization scheme. The form of the renormalized hard-scattering matrix elements and the definition of the parton distributions are specified by the regularization scheme; DIS and $\overline{\rm MS}$ schemes are widely used. The physical quantities such as α_s that enter the matrix elements are defined at the scale μ_R, while the parton distributions are set at μ_F. Although these scales are related to the momentum transfer Q, the precise relation is process dependent and not unique. The standard parton distribution sets have been obtained assuming $\mu_F = \mu_R \equiv \mu$ [7, 8, 9].

The scale and scheme dependence of our calculations provides an additional measure of the accuracy of the perturbative description at the given order. From the standpoint of perturbation theory, the choices of scales and scheme are arbitrary — varying these choices introduces corrections at the next order in α_s. However, changing the scales and scheme in practice alters the numerical predictions for collisions in the kinematic range relevant to heavy ion experiments. In this work we discuss results for the DIS and $\overline{\rm MS}$ schemes and vary μ to test the scale dependence.

Confidence in our predictions at the LHC heavy ion energy $\sqrt{s} \sim 5.5$ A·TeV is further limited by current experimental uncertainties in the parton distributions. Specifically, the production of dileptons with $M < 10$ GeV in nucleon–nucleon collisions at this energy probes the parton distributions at Bjorken $x < 10^{-2}$. This region is accessible only to the ongoing experiments at HERA [10]. Consequently the differences between the various parton distribution sets is largest in this region [7, 8, 9]. We base our predictions on computations using state–of–the–art parton distribution sets that are consistent with the current (1994) HERA data. To illustrate the maximum uncertainty in these predictions, we compare these results to calculations using a recent set that does not exhibit the 'low-x rise' seen by HERA [10], MRS D0′. As the experiments accumulate data, these uncertainties will be reduced, thereby enabling more refined predictions before the start of the LHC program.

We outline the theory used to study the mass, rapidity, transverse momentum and angular distribution of the dileptons in the next section. In the following section we compare our results to data and obtain predictions for RHIC and LHC. Results for $d\sigma/dMdy$ are obtained using a code provided by W. van Neerven and P. Rijken. Transverse momentum spectra and angular distributions are obtained following Refs. [11] and [12] respectively. The computation of these distributions — and the p_T spectrum in particular — requires a partial resummation of the perturbation series together with nonperturbative input not contained in standard parton distributions. The methods and uncertainties specific to these processes are discussed in the appropriate subsections.

THEORETICAL BACKGROUND

We now discuss the calculation of the Drell–Yan cross section in perturbative QCD. Our goal here is to outline the theory so that the reader can make use of our numerical results without extensive recourse to the literature. We provide a list of essential references, but those who are interested in a more detailed discussion of should consult the accompanying article of van Neerven [2].

Mass Distributions

The lowest order contribution to the Drell Yan process is quark–antiquark annihilation into a lepton pair. The annihilation cross section can be obtained from the $e^+e^- \to \mu^+\mu^-$ cross section by including the color factor 1/3 and the charge factor e_q^2 for the quarks. Since the variation of the center–of–mass energy $\sqrt{\hat{s}}$ of the incoming quark and antiquark leads to pairs of different masses, it is useful to consider a cross section that is differential in the mass M of the pair:

$$\frac{\mathrm{d}\hat{\sigma}}{\mathrm{d}M^2} = e_q^2 \hat{\sigma}_0 \delta(\hat{s} - M^2), \qquad \hat{\sigma}_0 = \frac{4\pi\alpha^2}{9M^2} \tag{1}$$

The four–momenta of the incoming partons are expressed in terms of the momentum fractions of the colliding hadrons as

$$p_1 = \frac{\sqrt{s}}{2}(x_1, 0, 0, x_1) \qquad\qquad p_2 = \frac{\sqrt{s}}{2}(x_2, 0, 0, -x_2), \tag{2}$$

where $\sqrt{s}$ is the center–of–mass energy of the hadrons. It follows that $\hat{s} = x_1 x_2 s$.

The lowest order hadronic cross section is now obtained by folding in the initial state quark and antiquark luminosities determined by the parton distribution functions:

$$\frac{\mathrm{d}\sigma}{\mathrm{d}M^2} = \hat{\sigma}_0 \int_0^1 dx_1 dx_2 \delta(x_1 x_2 s - M^2) \sum_k e_k^2 [q_k(x_1, \mu)\bar{q}_k(x_2, \mu) + (1 \leftrightarrow 2)]. \tag{3}$$

More precisely, the distributions q and $\bar{q}$ give the number densities of quarks and antiquarks at momentum fraction x and factorization scale μ which is of the order of M, the only scale entering the calculation of the mass distribution.

The momentum fractions of the incoming partons which contribute to the LO cross section can be expressed in terms of the rapidity of the pair, y, and a scaling variable $\tau = M^2/s$ as

$$x_{01} = \sqrt{\tau} e^y, \qquad x_{02} = \sqrt{\tau} e^{-y}. \tag{4}$$

Using $y = (1/2)\ln(x_{01}/x_{02})$, we write the double-differential cross section

$$\left(M^2 \frac{\mathrm{d}\sigma}{\mathrm{d}y\mathrm{d}M^2} \right)_{\text{Born}} = \hat{\sigma}_0 \tau \sum_k e_k^2 [q_k(x_{01}, \mu)\bar{q}_k(x_{02}, \mu) + (1 \leftrightarrow 2)] = F(\tau, \mu), \tag{5}$$

exhibiting a scaling behavior in τ at leading order (apart from the logarithmic dependence on the factorization scale μ).

The inclusive lepton pair cross section also includes contributions from processes in which the final state contains partons in addition to the lepton pair. These processes are higher order in the QCD coupling α_s. Perturbative QCD provides a systematic way to calculate order by order in α_s, the contributions from such processes as well as from those with virtual quanta. Graphs for the next to leading order processes include Compton, annihilation, and vertex corrections. The complete next to leading order cross section is [3]

$$\begin{aligned}\left(\frac{\mathrm{d}\sigma}{\mathrm{d}y\mathrm{d}M^2}\right)_{\mathrm{NLO}} &= \frac{\hat{\sigma}_0}{s}\int_0^1 dx_1\, dx_2\, dz\, \delta(x_1x_2z-\tau)\delta(y-\frac{1}{2}\ln\frac{x_1}{x_2}) \\ &\times \left\{\left[\sum_k e_k^2(q_k(x_1)\bar{q}_k(x_2)+[1\leftrightarrow 2])\right]\left[\delta(1-z)+\frac{\alpha_s(\mu)}{2\pi}f_q(z)\right]\right. \\ &+ \left.\left[\sum_k e_k^2(g(x_1)(q_k(x_2)+\bar{q}_k(x_2))+[1\leftrightarrow 2])\right]\left[\frac{\alpha_s(\mu)}{2\pi}f_g(z)\right]\right\},\end{aligned} \tag{6}$$

where the g and q_k are evaluated at the scale μ. The correction terms in the DIS regularization scheme are

$$\begin{aligned}f_q(z) &= C_F\left[\delta(1-z)\left(1+\frac{4\pi^2}{3}\right)-6-4z+\left(\frac{3}{1-z}\right)_+ +2(1+z^2)\left(\frac{\ln(1-z)}{1-z}\right)_+\right], \\ f_g(z) &= \frac{1}{2}\left[(z^2+(1-z)^2\ln(1-z)+\frac{3}{2}-5z+\frac{9}{2}z^2\right].\end{aligned} \tag{7}$$

Similar terms can be written down for the $\overline{MS}$ scheme [6].

We will focus on the behavior of the cross section at next to leading order. Although a complete $\mathcal{O}(\alpha_s^2)$ analysis exists for the total cross section and the rapidity integrated mass spectrum, the more experimentally useful double-differential cross section is known only to $\mathcal{O}(\alpha_s)$. The contributions from soft and virtual gluons, dominant at fixed target energies and $\tau > 0.01$ [2, 6], account for only part of the $\mathcal{O}(\alpha_s^2)$ corrections to $\mathrm{d}\sigma/\mathrm{d}y\mathrm{d}M^2$ at the higher collider energies. On the other hand, we find below that the $\mathcal{O}(\alpha_s^2)$ corrections to the rapidity integrated cross section are typically quite small for the kinematic range of interest. This result supports the reliability of the $\mathcal{O}(\alpha_s)$ prediction from (6) throughout the rapidity range that contributes most of the cross section. Such support is particularly useful in the low mass region ($M \sim M_{J/\psi}$), where a fast convergence of the perturbative series is far from self evident.

Transverse Momentum Distributions

Experiments show that the net transverse momenta of lepton pairs produced by the Drell-Yan process are of the order of 1 GeV for a dimuon mass, M, of 10 GeV. Such values are substantially smaller than the transverse momenta $\sim M/2$ carried by each of the leptons individually. On the other hand, the p_T of a Drell-Yan pair is much larger than the few-hundred MeV typical of soft QCD. If we neglect the transverse momentum of the incoming partons, then the lowest order process $q\bar{q} \to \gamma^* \to l^+l^-$ produces a final state with net $p_T = 0$. While any spread in the initial momentum will increase the final p_T on average, the intrinsic width of the parton distribution is rather small, $\langle p_T^2 \rangle_{\rm soft} \sim (0.3 \text{ GeV})^2$. This scale is determined by the inverse hadron size, since the target and projectile partons must be localized inside their parent hadrons. Therefore, we can attribute part of the measured p_T to the parton's intrinsic p_T, but not all.

The lepton pair acquires additional transverse momentum from production mechanisms that occur beyond leading order in perturbation theory [13, 14]. For example, in the Compton and annihilation processes

$$qg \to q\gamma^* \quad \text{and} \quad \bar{q}q \to \gamma^* g \tag{8}$$

p_T of the lepton pair can be balanced by the recoil of the final state quark or gluon. One can compute the p_T distribution perturbatively from these processes and their radiative corrections. The perturbation expansion is well behaved for $p_T \sim M$. However, at low p_T the expansion breaks down and a resummation of the perturbation series is required.

To see why this resummation is necessary, observe that the cross section in the region $p_T^2 \ll M^2$ is dominated by the leading-logarithm contributions:

$$\frac{d\sigma}{dp_T^2} \sim \frac{\alpha_s}{p_T^2} \ln\left(\frac{M^2}{p_T^2}\right) \left[v_1 + v_2 \alpha_s \ln^2\left(\frac{M^2}{p_T^2}\right) + v_3 \alpha_s^2 \ln^4\left(\frac{M^2}{p_T^2}\right) + \cdots \right], \tag{9}$$

where α_s is evaluated at the scale M^2. This series is effectively an expansion in $\alpha_s \ln^2(M^2/p_T^2)$, rather than α_s alone. The effective expansion parameter can be large at low p_T even if $\alpha_s(M^2)$ is small. The leading-logarithm series (9) describes the effect of soft gluon radiation from the initial state q and $\bar{q}$ prior to their annihilation. Specifically, these logarithms are remnants of the mass and collinear singularities arising from the radiated gluons. The annihilation process in (8) contributes the term $\propto \alpha_s \ln(M^2/p_T^2)/p_T^2$ and, in general, $q\bar{q} \to \gamma^* + n$ gluons produces the term of order α_s^n. Fortunately, the coefficients v_i of Eq. (9) are not independent and it is possible to sum the series exactly so that it applies even when $\alpha_s \ln^2(M^2/p_T^2)$ is large [15, 16, 17, 18]. In addition, 'subleading' logarithm contributions, though smaller, can also be important.

The formalism needed to sum the leading and subleading logarithms was developed by Collins, Soper and Sterman [17]. For each species of colliding partons, one finds

$$M^2 \frac{d\sigma}{dp_T^2\, dy dM^2}(\text{resum}) = \pi \hat{\sigma}_0 \tau e_q^2 \int \frac{d^2 b}{(2\pi)^2} e^{i\mathbf{b}\cdot\mathbf{p}_T} W(b), \tag{10}$$

$$\begin{aligned} W(b) &= \exp\left\{ -\int_{\beta^2/b^2}^{M^2} \frac{dq^2}{q^2} \left[\ln\left(\frac{M^2}{q^2}\right) A(\alpha_s(q^2)) + B(\alpha_s(q^2)) \right] \right\} \\ &\quad \times (C \circ f_1)(x_1; \beta^2/b^2) \times (C \circ f_2)(x_2; \beta^2/b^2). \end{aligned} \tag{11}$$

where s is the total hadronic center-of-mass energy, f_1 and f_2 are the projectile and target parton distributions of the two colliding particles, and x_1 and x_2 defined by (4) are the dominant values of x as $p_T \to 0$. Note that the f_i can be q, $\overline{q}$ or g, depending on the process considered. The integration variable b is the impact parameter, the variable conjugate to p_T, and $\beta \equiv 2\ \mathrm{e}^{-\gamma_{\mathrm{E}}}$, where γ_{E} is Euler's constant. To obtain the total Drell–Yan rate at next-to-leading order, one must sum (10,11) over $q\bar{q}$, $g\bar{q}$ and gq initial states for all appropriate quark flavors; see Appendix A in ref. [11] for details. The function C is a coefficient function that converts the parton distributions f into distributions $C \circ f$ specific to the process at hand. The functions A, B, and $C(x)$ have perturbative expansions in α_{s}, with A and B starting at order α_{s}. The expansion for C begins at order 1 for quarks and order α_{s} for gluons. These functions can be extracted to a given order from the perturbative result, and have been determined for the Drell–Yan process at next-to-leading order by Davies *et al.* [19].

The resummed result (10,11) applies only when $p_T^2 \ll M^2$ because it includes only those terms that diverge as p_T^{-2} as $p_T \to 0$. Omitted in (10) are nonsingular contributions that are $\propto \{p_T^2 + M^2\}^{-1}$ at small p_T. At $p_T \sim M$ the singular and nonsingular contributions become comparable. On the other hand, conventional perturbation theory works well at large p_T, describing the complete p_T dependence to a given order in α_{s}.

Bridging the low-p_T and perturbative regimes is accomplished by adding in the terms that are not resummed, the so-called remainder or nonsingular terms. Arnold and Kauffman developed a prescription for calculating the remainder terms that explicitly matches the high and low p_T results. Their prescription proceeds as follows. One first expands the resummed result (10) in powers of α_{s}. This series, $\mathrm{d}\sigma/\mathrm{d}p_T^2\,\mathrm{d}y\mathrm{d}M^2(\mathrm{asym})$, contains the singular $1/p_T^2$ part of complete perturbation series $\mathrm{d}\sigma/\mathrm{d}p_T^2\,\mathrm{d}y\mathrm{d}M^2(\mathrm{pert})$. We refer to $\mathrm{d}\sigma/\mathrm{d}p_T^2\,\mathrm{d}y\mathrm{d}M^2(\mathrm{asym})$ as 'asymptotic' because it describes the perturbation series asymptotically as $p_T \to 0$. The asymptotic result in ref. [11] is expressed as convolutions of parton distributions with the coefficient functions of (11) and with Altarelli–Parisi splitting functions arising from the scale dependence of the parton distributions. With the singular terms isolated in the asymptotic result, the remainder is the difference between the perturbative result and the asymptotic result,

$$R = \frac{\mathrm{d}\sigma}{\mathrm{d}p_T^2\,\mathrm{d}y\mathrm{d}M^2}(\mathrm{pert}) - \frac{\mathrm{d}\sigma}{\mathrm{d}p_T^2\,\mathrm{d}y\mathrm{d}M^2}(\mathrm{asym}). \tag{12}$$

The perturbation series for the p_T distribution — and therefore R — has been computed to 2nd order in ref. [14]. The total cross section is then written

$$\frac{\mathrm{d}\sigma}{\mathrm{d}p_T^2\,\mathrm{d}y\mathrm{d}M^2}(\mathrm{total}) = \frac{\mathrm{d}\sigma}{\mathrm{d}p_T^2\,\mathrm{d}y\mathrm{d}M^2}(\mathrm{resum}) + \frac{\mathrm{d}\sigma}{\mathrm{d}p_T^2\,\mathrm{d}y\mathrm{d}M^2}(\mathrm{pert}) - \frac{\mathrm{d}\sigma}{\mathrm{d}p_T^2\,\mathrm{d}y\mathrm{d}M^2}(\mathrm{asym}). \tag{13}$$

The "matching" is now manifest: at low p_T the perturbative and asymptotic pieces cancel, leaving the resummed; at high p_T the resummed and asymptotic pieces cancel to 2nd order, leaving the perturbative contribution. The relative error is explicitly of order α_{s}^2, see ref. [11].

At very high p_T the matching prescription breaks down and one must switch back to the perturbative result. This breakdown occurs because $\mathrm{d}\sigma/\mathrm{d}p_T^2\,\mathrm{d}y\mathrm{d}M^2(\mathrm{asym})$

is only known to 2nd order, while $d\sigma/dp_T^2\, dy dM^2$(resum) in effect contains all orders in α_s. For example, $d\sigma/dp_T^2\, dy dM^2$(resum) introduces terms $\propto \alpha_s^3(\ln p_T)^5/p_T^2$ that will not be cancelled in the 2nd order expression for $d\sigma/dp_T^2\, dy dM^2$(asym). Although such terms are higher order in α_s they become important at large p_T for kinematic reasons. The resummed and asymptotic cross sections depend on parton distributions evaluated at a fixed x, independent of p_T, whereas the parton distributions probed by the perturbative result fall with increasing p_T. Thus, the higher order terms come to dominate at large p_T and one must switch back to the perturbative result. An appropriate value of p_T at which to do this is when when $d\sigma/dp_T^2\, dy dM^2$ has fallen off to the extent that R is comparable to the total. At that point, the terms being resummed no longer dominate the cross section and at higher p_T the perturbative prediction is more reliable than (13). The switch is done at sufficiently high p_T so that the error incurred is free of large logarithms.

The form factor $W(b)$ contains α_s and parton distributions evaluated at the scale $1/b$, and its evaluation is problematic for $b > 1$ GeV^{-1}. Moreover, one wishes to include the effect of the intrinsic p_T of the partons. Both of these ends are met by replacing

$$W(b) \to W(b_*) e^{-S_{\rm np}(b)} \tag{14}$$

where $b_* = b/\sqrt{1+(b/b_{\rm max})^2}$ and $b_{\rm max} = 0.5$ GeV^{-1}. The Collins-Soper-Sterman formalism specifies that $S_{\rm np}$ have a term which depends on $\ln M$ and a term which does not and that the $\ln M$ term does not depend on the colliding hadrons or on the parton x's. However, beyond these constraints $S_{\rm np}$ is arbitrary and must be extracted from experiment. Ladinsky and Yuan parametrize

$$S_{\rm np} = g_1 b\,[b + g_3 \ln(\tau/\tau_1)] + g_2 b^2 \ln(M/2M_1), \tag{15}$$

where $\tau = x_1 x_2$ [20]. To fit the ISR p_T distribution from R209, they take $g_1 = 0.11$ GeV^2, $g_2 = 0.58$ GeV^2, $g_3 = -1.5$ GeV^2, $\tau_1 = 0.01$ and $M_1 = 1.6$ GeV. Note that these parameter choices are somewhat different from those in ref. [11, 19].

Momentum distributions presented in the work are computed using a code adapted from ref. [11]. One source of uncertainty in these predictions is the neglect of higher orders in α_s. The difference between the perturbative and matched results at high p_T is one indication of this uncertainty. Further ambiguity arises in our estimate of the intrinsic p_T smearing, which is entirely phenomenological.

Angular Distributions

It is possible to probe the spin structure of the production amplitudes by measuring the angular distribution of the dileptons.

The general form of the angular distribution is

$$\frac{d\sigma}{dM^2 dy dp_T^2 d\Omega} = \frac{3}{16\pi}\frac{d\sigma}{dM^2 dy dp_T^2} \times [1 + \cos^2\theta + \frac{A_0}{2}(1 - 3\cos^2\theta)$$

$$+ A_1 \sin 2\theta \cos\phi + \frac{A_2}{2}\sin^2\theta\cos 2\phi] \tag{16}$$

where the angles θ and ϕ are measured in the dilepton rest frame with respect to an arbitrary axis. For calculations with underlying QCD processes, it is convenient to evaluate the A_i in the Collins–Soper frame [21], where the reference axis is the bisector of the beam and (anti) target directions. This choice in some respect minimizes the effect of intrinsic parton transverse momenta.

For the experimental analysis, it is standard to use an alternate parameterization

$$\frac{\mathrm{d}\sigma}{\mathrm{d}\Omega} \sim 1 + \lambda \cos^2\theta + \mu \sin 2\theta \cos\phi + \frac{\nu}{2} \sin^2\theta \cos 2\phi \,. \tag{17}$$

The relationship is simply obtained

$$\begin{aligned} \lambda &= \frac{2 - 3A_0}{2 + A_0} \\ \mu &= \frac{2A_1}{2 + A_0} \\ \nu &= \frac{2A_2}{2 + A_0} \,. \end{aligned} \tag{18}$$

For calculations in perturbative QCD, one embeds the partonic expressions for $A_i \times \mathrm{d}\sigma/\mathrm{d}M^2\mathrm{d}y\mathrm{d}p_T{}^2$ into integrals over parton density functions just as in the previous sections. The Born term involves only zero transverse momentum, and the virtual photon production amplitude vanishes for zero helicity. Thus all of the A_i's are zero and the angular distribution is purely $1 + \cos^2\theta$. For the parton level A_i the leading order (LO) perturbative corrections of order α_s have been calculated through the spin amplitudes in the annihilation and Compton amplitudes. One finds in all cases the relationship $A_0 = A_2$, or equivalently $\lambda = 1 - 2\nu$, such that the θ and ϕ distributions are correlated. Calculations in NLO of order α_s^2 are much more complicated [22], but in general only alter the angular coefficients at the 10% level [23]. However, the correlation above is then violated.

In this study we have calculated the perturbative cross section and amplitudes A_0 and A_1 using the LO expressions (remember at this level $A_0 = A_2$).

$$\begin{aligned} \frac{\mathrm{d}\sigma}{\mathrm{d}M^2\mathrm{d}y\mathrm{d}p_T^2} A_i = {} & \frac{8\alpha^2\tau^2\alpha_s(\mu)}{27\pi M^6} \int_0^1 \frac{dx_1}{x_1} \int_0^1 \frac{dx_2}{x_2} \delta(x_1x_2 - x_1z_2 - x_2z_1 + \tau) \\ & \times \Big\{ \Big[\sum_k e_k^2 \big(q_k(x_1,\mu)\ \bar{q}_k(x_2,\mu) + (-1)^i (x_1 \leftrightarrow x_2)\big) \Big] \hat{A}_i^{q\bar{q}} \\ & + \Big[\sum_k e_k^2 \big(g(x_1,\mu)(q_k(x_2,\mu) + \bar{q}_k(x_2,\mu)) + (-1)^i (x_1 \leftrightarrow x_2)\big) \Big] \hat{A}_i^{gq} \Big\} , \end{aligned} \tag{19}$$

where $z_{1,2} \equiv [\tau(1+(p_T/M)^2]^{\frac{1}{2}} e^{\pm y}$ are generalizations of (4) for $p_T \neq 0$. To calculate the cross section alone, one replaces the parton-level $\hat{A}_i$ with the parton-level cross section $\hat{\Sigma}$. Expressions for these quantities are:

$$\begin{aligned}
\hat{\Sigma}^{q\bar{q}} &= \frac{(M^2-u)^2+(M^2-t)^2}{ut} \\
\hat{A}_0^{q\bar{q}} &= \frac{M^2-u}{M^2-t}+\frac{M^2-t}{M^2-u} \\
\hat{A}_1^{q\bar{q}} &= \left[\frac{M^2 s}{ut}\right]^{\frac{1}{2}}\left(\frac{M^2-u}{M^2-t}-\frac{M^2-t}{M^2-u}\right) \\
\hat{\Sigma}^{gq} &= \frac{(M^2-s)^2+(M^2-t)^2}{-st} \\
\hat{A}_0^{gq} &= \frac{-u\left[(s+M^2)^2+(M^2-t)^2\right]}{s(M^2-u)(M^2-t)} \\
\hat{A}_1^{gq} &= \left[\frac{M^2 u}{st}\right]^{\frac{1}{2}}\frac{(M^2-u)^2-2(M^2-t)^2}{(M^2-u)\,(M^2-t)}
\end{aligned} \tag{20}$$

and one must make the replacement $t \leftrightarrow u$ for the gluon-quark terms when interchanging projectile and target.

Note that the invariants s, t, u, and M^2 are calculated with parton momenta in the annihilation and Compton diagrams, and the $\hat{A}_i$ are given in the Collins–Soper frame. We have used the LO α_s values for each parton distribution set used in these calculations, as is appropriate for our LO angular distribution expressions. The scale is taken to be $\mu = M$ in all cases.

One can see from the structure of parton-level amplitudes in Eq (20) how the angular distribution coefficients change as the perturbative contributions grow with p_T. For the $q\bar{q}$ subprocess, one finds the relation

$$\hat{A}_0^{q\bar{q}} = \frac{p_T^2}{p_T^2+M^2}\hat{\Sigma}^{q\bar{q}}. \tag{21}$$

Since this relation holds for all parton momenta, one predicts that A_0 and hence λ will be independent of the parton distribution functions. It will also be independent of energy and rapidity, and exhibit a characteristic function of $w \equiv (p_T/M)^2$. This property was found some time ago [24, 25], and the prediction in the Collins–Soper frame at any fixed y is

$$\lambda^{q\bar{q}} = \frac{2-w}{2+3w}. \tag{22}$$

One sees that as w increases with p_T, the virtual photon polarization state increases in the zero helicity mode. The limiting value as $p_T \to \infty$ is $\lambda = -1/3$, corresponding to a factor of two for the ratio of longitudinal to transverse photon production. There is no corresponding relation for the A_1 amplitude.

A similar analysis for the gq amplitudes does not yield a relation such as Eq. (21). However, one can get an approximate result which only depends on the steeply-rising behavior of the parton distribution functions at small x. If the integral over parton momenta is saturated by the values at the smallest possible x–values, for small rapidity values one samples only at the point $-u = -t = p_T^2 + p_T\sqrt{p_T^2 + M^2}$. The corresponding amplitude relationship is then

$$\hat{A}_0^{gq} \approx \frac{5p_T^2}{M^2 + 5p_T^2}\hat{\Sigma}^{gq}, \tag{23}$$

which leads to a new characteristic function

$$\lambda^{gq} = \frac{2 - 5w}{2 + 15w}. \tag{24}$$

These relations were first found in the Gottfried–Jackson frame [25] for y-integrated quantities, but apply in the form above in the Collins–Soper frame at fixed y [26] sufficiently small such that $\hat{A}_1 \approx 0$. One can see that the characteristic functions are related by a rescaling of w by a factor of five between the $q\bar{q}$ and the gq subprocesses.

Our normalized $A_i's$ and calculated λ, μ, and ν values are valid only in a region of transverse momentum p_T large enough that the perturbative terms may be expected to dominate the amplitudes. At lower values of p_T, the soft gluon resummation technique must be used to calculate the p_T-dependence of the cross section. As noted by Chiapetta and Le Bellac [27], the A_i terms do not enter into the resummation, since only the part proportional to $1 + \cos^2\theta$ is able to combine with the soft gluon resummation amplitude. Thus at low p_T one should simply replace the perturbative cross section with the resummed differential cross section, and use this factor to normalize the A_i's integrated over parton distributions. It is unclear, however, how to determine in general where the perturbative region begins. At the Fermilab and CERN fixed-target and ISR energies which provide the data presently available for p_T distributions, it appears that the perturbative terms will dominate only when $p_T > M$. On the other hand, calculations for W and Z production at SPS and Tevatron energies indicate that the perturbative contributions are dominant already when $p_T \leq M/2$. Due to this uncertainty, we present for this study only the perturbative cross section and the perturbative A_i values, plus the calculated λ and μ values. In regions of small p_T, one should use the resummed cross sections to renormalize the A_i and recalculate the λ and μ values, but the crossover point in p_T must be determined independently for each collider energy and dilepton mass.

Nuclear Effects

We now comment on possible nuclear modification in the Drell–Yan process. On naive geometrical grounds, one expects that the cross sections differential in M and y in central ion-ion collisions increase with nuclear mass by a factor $\propto A^{4/3}$ relative to the $N-N$ cross section. Any modification of the parton distributions in the target and projectile nuclei will modify this dependence. In particular, one expects parton shadowing to be very important in the small x range probed by midrapidity Drell–Yan production at the RHIC and, especially, at the LHC. Shadowing can reduce the A dependence of the cross section relative to the expected increase by as much as a factor of $\sim A^{1/3} \sim 6$ in Au–Au collisions. Such a dramatic suppression would be larger than the combined uncertainties in our $N-N$ cross section calculations. It will nevertheless be crucial to measure the $N-N$ rates at RHIC and LHC to study shadowing and other such nuclear effects.

Initial state parton scattering has been measured in Drell–Yan studies of hadron–nucleus collisions. This scattering does not appreciably affect rapidity and mass distributions, but can modify the p_T spectrum. Specifically, initial state scattering broadens the transverse momentum distribution in a nuclear target relative to a hadron target, corresponding to an increase $\propto A^{1/3}$ in $\langle p_T^2 \rangle$. This broadening is measured experimentally. Note that it is because of this effect that we have not compared p_T calculations to nuclear target data.

COMPARISON WITH DATA

In this section we compare calculations to recent experiments in order to illustrate the level of agreement of the QCD calculations with data. We have chosen not to optimize the calculations, *e.g.*, by choosing the scales via some prescription [28]. Instead we vary the regularization scheme and scales in order to determine the level of uncertainty in the prediction. We exclude data on nuclear targets from our analysis, because nuclear effects are not addressed in this work. Even so, our comparisons with data are not exhaustive and we apologize to our experimental colleagues for our incompleteness.

Mass Distributions

A comparison of the perturbative calculations to the data from fixed–target experiments is discussed in detail by Rijken and van Neerven [6]. The overall feature of most of the fixed–target data for $\mathrm{d}\sigma/\mathrm{d}M$ is described by the Born term multiplied by a K factor in the range $1 < K < 2$. The reason for this 'factorization' is understood [16, 17], and the goal of perturbative calculations of the mass spectrum is to calculate the K factor. One finds that the $\mathcal{O}(\alpha_s)$ calculation can account for $50-75\%$ of the experimental K factor. It is not clear whether K can be calculated entirely using perturbation theory. As we discuss below the situation improves for the data at highest energies now available.

In addition Rijken and van Neerven calculate the NNLO, $\mathcal{O}(\alpha_s^2)$, contributions from soft and virtual gluons ($S+V$) to the double-differential cross section $\mathrm{d}\sigma/\mathrm{d}M\mathrm{d}x_F$ and study the validity of this approximation at the $\mathcal{O}(\alpha_s)$ where the exact result is known. They find the approximation valid that at the fixed–target energies for $\sqrt{\tau} = M/\sqrt{s} > 0.3$. Assuming this to be the case also for the NNLO contribution, they conclude that part of the discrepancy between the data and the $\mathcal{O}(\alpha_s)$ result can be attributed to the $S+V$ contributions [6].

We have extended the comparison in ref. [2] to the mass dependence of the double differential cross section, $\mathrm{d}\sigma/\mathrm{d}M\mathrm{d}x_F$, measured in the FNAL E772 experiment at 800 GeV ($\sqrt{s} = 38.8$ GeV) [29] and in the CERN ISR experiment R209 [30] at $\sqrt{s} = 44$ and 62 GeV. In Fig. 1 we show the mass distributions from the E772

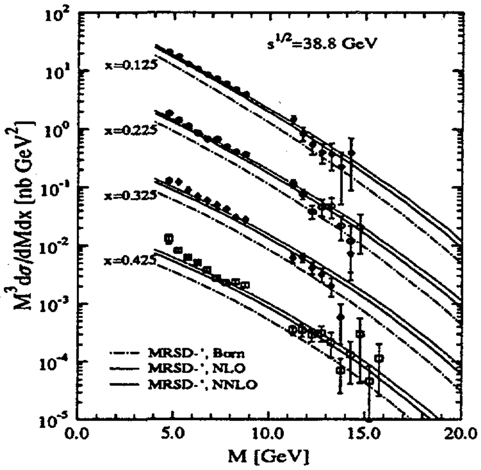

Figure 1: The calculated [6] scaling function $M^3 \mathrm{d}\sigma/\mathrm{d}M\mathrm{d}x$ for four values of Feynman $x_F \equiv x$ compared to $pp \to \mu^+\mu^-$ data at $\sqrt{s} = 38.8$ GeV from FNAL E772 [29]. Born, $\mathcal{O}\alpha_s$ and $\mathcal{O}\alpha_s^2$ cross sections are indicated by the dash-dotted, solid and dashed curves. Next-to-leading corrections are obtained in the $S+V$ approximation.

experiment [29] at four different x_F values for the pair, $x_F = 0.125$, 0.225, 0.325, and 0.425 together with results from a calculation in the $\overline{\mathrm{MS}}$ sceme using the MRS D$-'$ parton distributions [7, 8]. We take the scale μ equal to the mass of the pair, as discussed later. At low x_F the data and the perturbative calculation are in fairly good agreement. The calculated cross section is slightly below the data at the lower end of the measured mass range and slightly above at the higher end. With increasing x_F the difference between the data and the calculated results increases at the low-mass end of the spectrum.

At this energy the validity of the $S+V$ approximation for the $\mathcal{O}(\alpha_s)$ contribution is ~ 10 % at $M = 20$ GeV and decreases to ~ 50% for $M = 3$ GeV, the approximate result being larger than the exact calculation. If the pattern is the same for the second order corrections, the complete NNLO calculation would deviate from the NLO results even less than shown in Fig. 1.

In Figs. 2 and 3 the data on $\mathrm{d}\sigma/\mathrm{d}M\mathrm{d}x_F$ measured at CERN ISR [30] at $\sqrt{s} = 44$ and 62 GeV and at $x_F = 0$ are compared to calculations. At both energies the Born term alone reproduces the continuum data between the J/ψ and the Υ. For the large mass region the corrections improve the comparison. At $\sqrt{s} = 44$ GeV only results for the MRS D$-'$ structure functions and for the scales set to the mass of the pair, $\mu_F = \mu_R = M$, are shown. The NNLO correction calculated in the soft plus virtual gluon approximation is seen to be clearly smaller than the NLO correction. Its precise magnitude cannot, however, be trusted with decreasing values of $\tau = M^2/s$. At $\sqrt{s} = 62$ GeV the $S + V$ contribution in the NLO term is twice the complete result at small masses. This implies that the uncertainty in the NNLO correction in the mass (or τ) range of interest in our extrapolations to higher energies is of the order of the correction itself. Fortunately the correction is small, and in the following we choose to show results with NLO corrections only. We should like to emphasize that all the available information on the NNLO contributions, including the full calculation for the rapidity integrated and total cross sections, indicate that

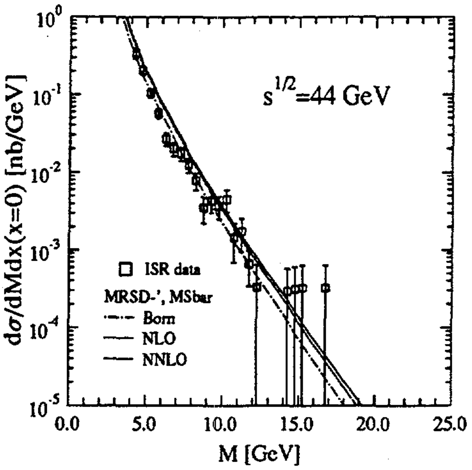

Figure 2: Same as Fig. 1 compared to ISR R209 data [31] at $\sqrt{s} = 44$ GeV.

the corrections add at most 20 % to the NLO corrected cross sections.

At $\sqrt{s} = 62$ GeV we show results for MRS D$-'$, D0$'$, and the GRV HO parton distribution sets [7, 8, 9] with $\mu_F = \mu_R = M$ and study the scale dependence in the case of MRS D$-'$ set using the NLO results. It is not surprising that the different sets give very similar results since they have been determined from data which covers or is close to the kinematic region we consider here. The differences are too small to discriminate between any of these sets. Varying the scale introduces a larger change in the results at this energy. Specifically, an increase of the scale reduces the calculated result. Nevertheless, for $M \leq 10$ GeV the change is inconsequential and we choose to present our extrapolations using $\mu_F = \mu_R = M$.

Transverse Momentum Distributions

Transverse momentum spectra computed at next-to-leading order following Arnold and Kauffman [11] are compared to data from ISR experiment R209 $\sqrt{s} = 62$ GeV [31] in Fig. 4. The nonperturbative parameters employed here (15) were obtained using a leading-order calculation in ref. [20] by fitting data from this experiment and FNAL experiment E288 at $\sqrt{s} = 27.4$ GeV [32]. Our NLO calculations are performed using the MRS D$-'$ parton distributions at the scale M.

We compare calculations to Fermilab experiment E772 at $\sqrt{s} = 38.8$ GeV in Fig. 5. The data in fig. 5 are averaged over the range $0.1 < x_F < 0.3$ for the three different mass bins shown. Our calculations at this lower energy are in excellent agreement with the shape of the momentum spectra. In particular, the variation of the p_T distributions with mass agrees with data. However, present calculations overpredict the integrated rate by $\sim 50\%$. In view of this disagreement, we present RHIC and LHC predictions for transverse momentum distributions normalized to the total cross section.

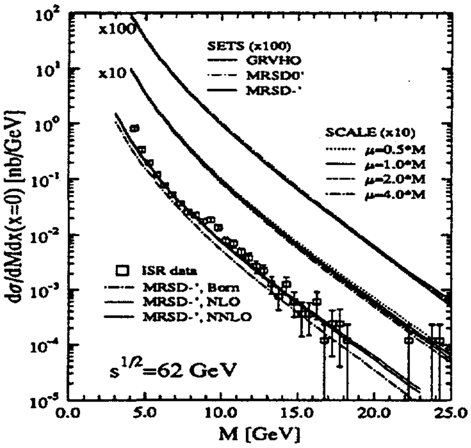

Figure 3: Same as Fig. 1 compared to ISR R209 data [31] at $\sqrt{s} = 62$ GeV. Additional curves multiplied by 10 and 100 indicate the dependence on scale and parton distributions.

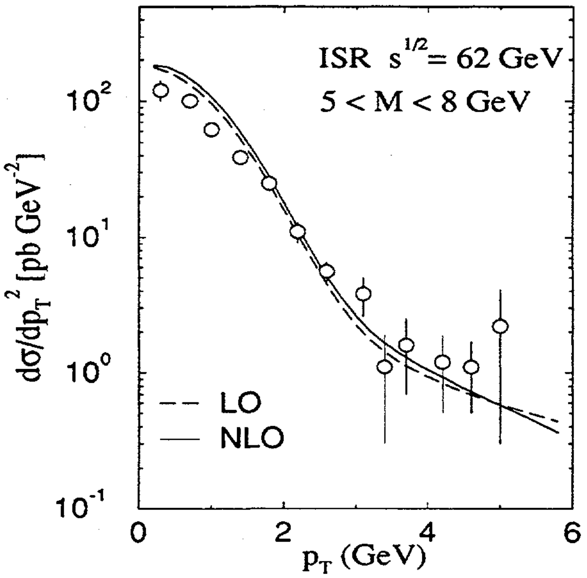

Figure 4: The rapidity-integrated cross section $d\sigma/dp_T^2$ in the mass range $5 < M < 8$ GeV at $\sqrt{s} = 62$ GeV compared to data from CERN R209. Note that the normalization of the calculation agrees with that of the data.

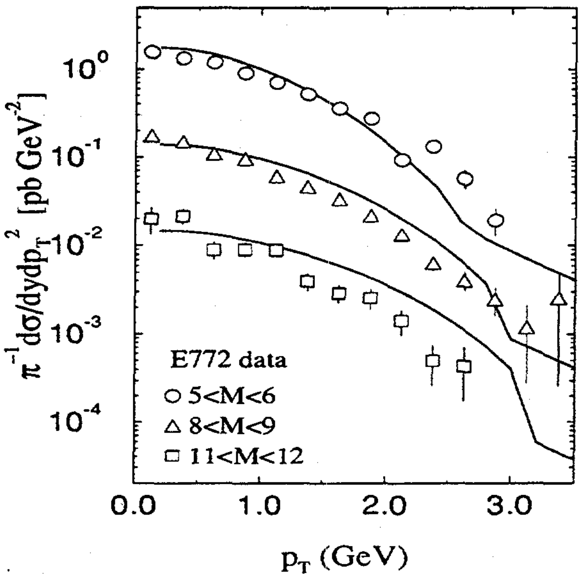

Figure 5: The invariant cross section for $pp \to \mu^+\mu^-$ at $\sqrt{s} = 40$ GeV are compared to measurements from FNAL E772. The circles, triangles, squares and the nearby curves represent data and calculations integrated over the three mass bins $5 < M < 6$ GeV, $8 < M < 9$ GeV and $11 < M < 12$ GeV, respectively. Data and calculations are averaged over the range $0.1 < x_F < 0.3$. Calculations are rescaled by an *ad hoc* overall factor of 0.63.

Angular Distributions

The only data presently available on the angular distribution coefficients are from fixed-target $\pi-N$ experiments at Fermilab E615 [33] and CERN NA10 [34, 26]. These experiments cover similar kinematic regions, roughly $\sqrt{s} \approx 20$ GeV, $4 \lesssim M \lesssim 8$ GeV, and $0 \lesssim p_T \lesssim 3$ GeV. The general trend of the data produces values of λ which are close to unity and almost independent of p_T, μ close to zero, and ν increasing with p_T. The perturbative predictions are in agreement with the μ and ν values, but fall below the λ values at the highest p_T. This behavior can be brought into agreement with data via the procedure of soft gluon resummation, which also appears necessary to reproduce the magnitude of the p_T dependent cross section [27]. However, this procedure then brings the predictions for ν down close to zero, in significant disagreement with data. The overall result is a violation of the relation $1 - \lambda - 2\nu = 0$ in either the perturbative or resummed predictions. This relation should hold exactly at LO QCD and has slightly positive contributions from the higher order corrections [23]. The data show definite negative values, which are difficult to understand in a QCD calculation. In fact, this has led to attempts to fit this data with models incorporating initial state correlations of color fields which lead to spin correlations [35]. A general conclusion must be drawn from the $\pi - N$ data that the angular distribution results are not well understood within perturbative QCD.

NUMERICAL RESULTS FOR RHIC AND LHC ENERGIES

We now turn to our predictions for RHIC and LHC energies and their uncertainties.

Mass and Rapidity Distributions

Mass distributions for p-p collisions are presented in Tables 1–4 and Figs. 6–11. In fig. 6 we show the scale dependence at $\sqrt{s} = 200$ (a) and 5500 GeV (b) for different fixed values of the pair mass as a function of μ/M. Not surprisingly, the dependence is stronger for smaller masses. The peak at small scale for $M = 4$ GeV is caused by the increase of $\alpha_s(M)$ as M approaches the $\Lambda_{\rm QCD}$. Perturbative calculations are not expected to be valid at such a small scale. For large values of the scale the dependence of the results is weak, although $\mathrm{d}\sigma/\mathrm{d}\mu$ does not vanish, as would be the case if σ were locally independent of μ. We take the scale to be M for our RHIC and LHC predictions. These results imply that the uncertainty in these prediction due to the scale ambiguity is $\sim 25\%$.

The scheme dependence of the double differential cross section is shown in Figs. 7 and 8 for $\sqrt{s} = 200$ GeV and 5.5 TeV. Observe that the scheme dependence of the parton distributions alone leads to a 10% difference in the Born terms. When the $\mathcal{O}(\alpha_s)$ corrections are added the difference between the schemes decreases. This difference is smaller than the calculated correction, as expected since the scheme dependence of the cross section is of higher order. The difference of the Born terms

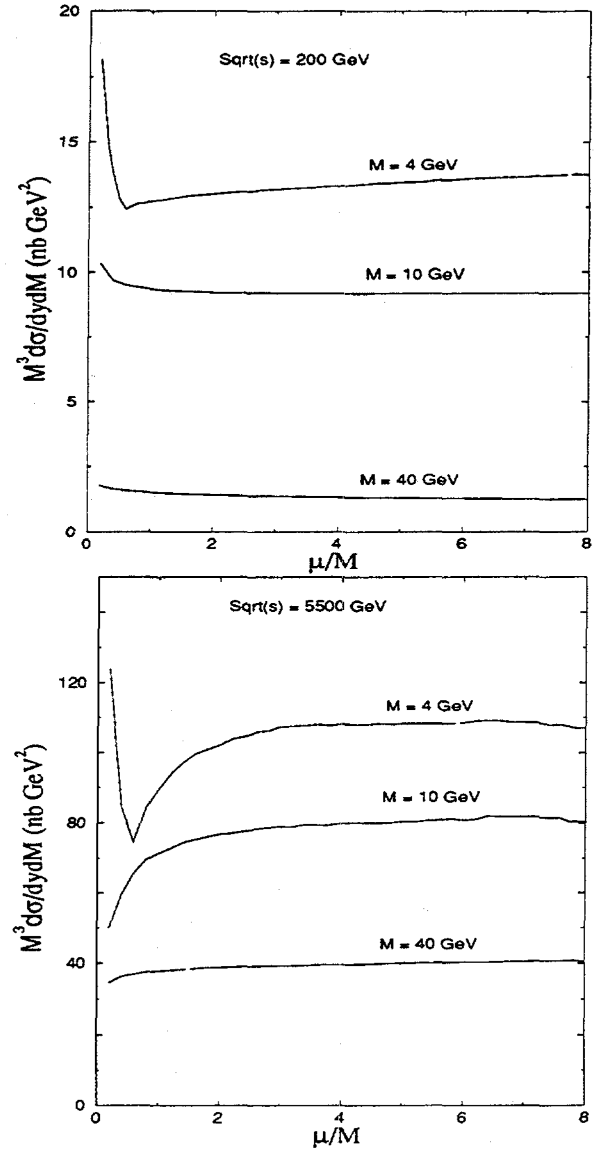

Figure 6: The scale dependence of the scaled cross section $M^3\mathrm{d}\sigma/\mathrm{d}M\mathrm{d}y$ at RHIC (a) and LHC (b) energies in the $\overline{\mathrm{MS}}$ scheme at $\mathcal{O}\alpha_s$. The scales are chosen to be equal, $\mu_R = \mu_F = \mu$.

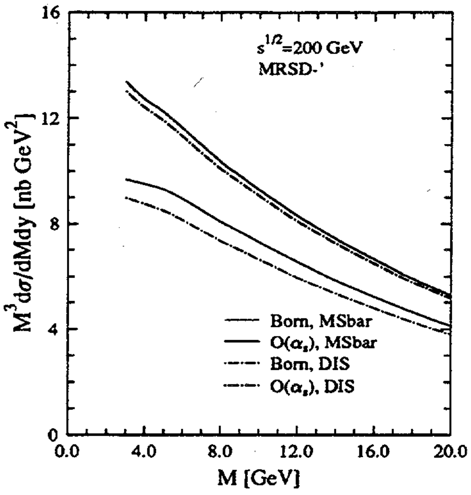

Figure 7: The scheme dependence of the $\mathcal{O}(\alpha_s)$ cross section at $\sqrt{s} = 200$ GeV for the MRS D−′ parton distribution set.

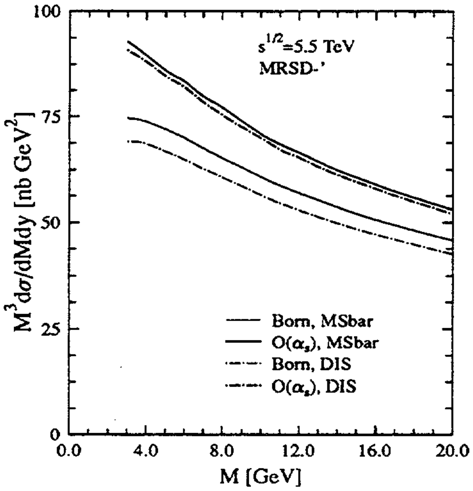

Figure 8: Same as in Fig. 2 but for the LHC energy, $\sqrt{s} = 5.5$ TeV.

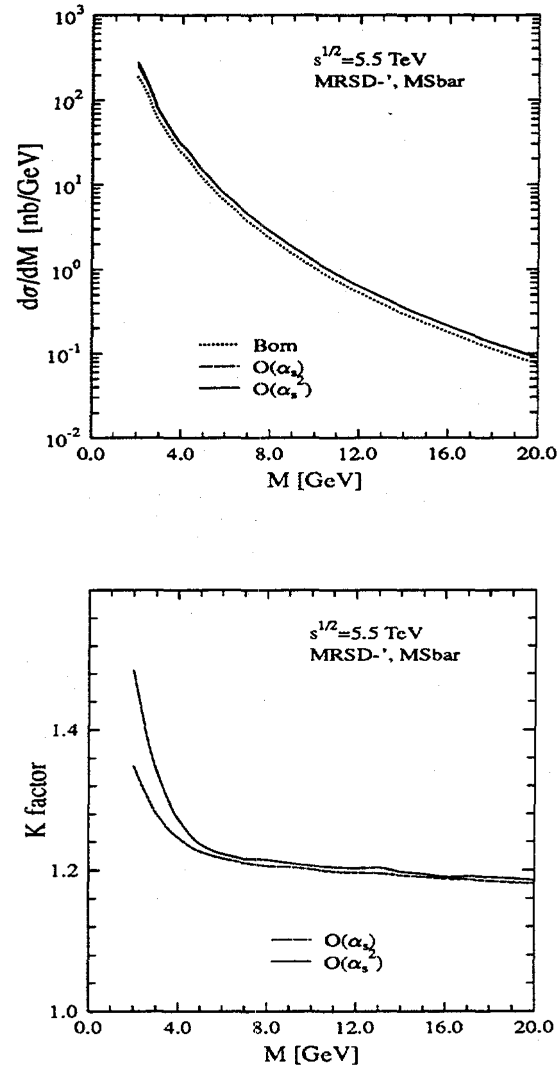

Figure 9: Rapidity integrated cross section $\mathrm{d}\sigma/\mathrm{d}M$ (a) and the theoretical K-factor (b) (see text for the definition) at $\sqrt{s} = 5.5$ TeV. In (a) the dotted curve shows the Born term, dashed curve the $O(\alpha_s)$, and the solid curve the $O(\alpha_s^2)$ result. In (b) the dashed curve shows the $O(\alpha_s)$ and the solid curve the $O(\alpha_s^2)$ K-factor.

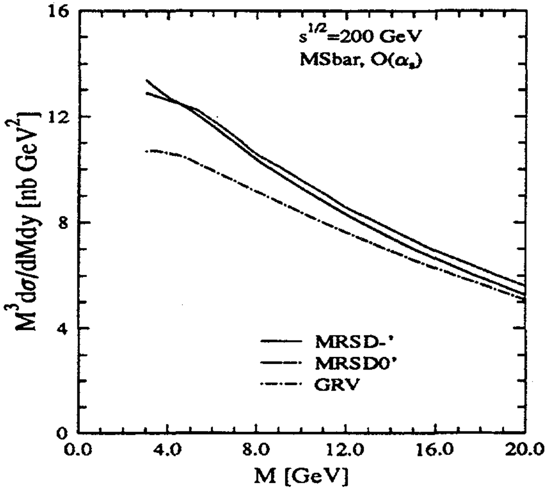

Figure 10: The cross section $d\sigma/dMdy$ at $y = 0$ as a function of M for different parton distribution functions for the LHC energy, $\sqrt{s} = 5.5$ TeV. Solid curve shows the result for MRS D−′ set, dash-dotted curve for the GRV HO set and dashed curve for the MRS D0′ set.

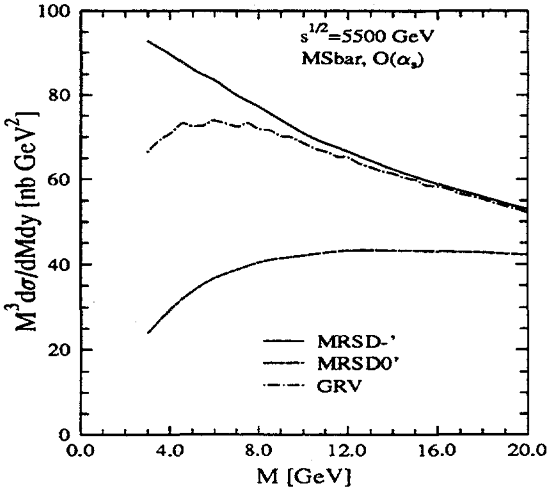

Figure 11: Same as Fig. 10, except for the RHIC energy, $\sqrt{s} = 200$ GeV.

is expected to be of the order α_s. This seems to be the case even though the difference is smaller than the $\mathcal{O}(\alpha_s)$ corrections.

As mentioned earlier, the $\mathcal{O}(\alpha_s^2)$ corrections to $d\sigma/dMdy$ have recently been studied [5, 6] but are not yet completely known. It has been shown [3] that at the present fixed-target energies the $\mathcal{O}\alpha_s$ corrections are dominated by the soft and virtual gluon corrections. Here we are interested in collisions at larger values of $\sqrt{s}$ and smaller masses, down to 2–3 GeV. It seems that the soft plus virtual gluon approximation breaks down in this domain. However, the full $\mathcal{O}(\alpha_s^2)$ result is known for the rapidity integrated cross section $d\sigma/dM$ [4]. We show the results at the LHC energy, $\sqrt{s} = 5.5$ TeV, both for the cross section, Fig. 9a, and the theoretical K factor Fig. 9b. Above $M = 4$ GeV the second order corrections are a small fraction of the first order corrections and the perturbation theory seems to converge rapidly. At smaller values of mass the perturbative results become less reliable but even at $M = 2$ GeV the second order correction is not more than $\sim$ 10% of the Born term. It seems that extending the perturbative calculations down to this mass region is still meaningful with an uncertainty of $\lesssim$ 25%.

The parton distribution functions are quite well known for $x \gtrsim 10^{-2}$ and recent parametrizations given by different groups [7] are essentially equivalent. We give the results at $\sqrt{s} = 200$ GeV and 5.5 TeV for three different sets: MRS D0′, D−′ [8], and GRV HO [9]. These sets differ from each other for $x < 10^{-2}$ and essentially span the interval compatible with the present HERA data. The D0′ set goes slightly below the data and the MRS D−′ set slightly above.

Fig. 10 shows the mass spectrum for dileptons at RHIC energy. The differences in the results for different parton distributions are $\lesssim$ 20%. For the LHC energy the situation is much worse, as shown in Fig. 11. The parton distributions are now probed down to $x = M/\sqrt{s} \sim 10^{-4}$ and the uncertainty in the cross section at $M = 3$ GeV is almost a factor of 4 decreasing to a factor less than 2 at 10 GeV.

Rapidity distributions at the RHIC energy are presented for fixed pair mass in Fig. 12 for the MRS D−′ parton distribution set. The interesting feature is the increase of the cross section at the smaller mass values as the rapidity increases from 0 to $\sim$ 3. As is seen from Eq. (4), x_1 increases and x_2 decreases with increasing y. The growth of the cross section reflects the faster increase of $x_2\bar{q}(x_2, \mu_F)$ with decreasing x_2 as compared to the decrease of $x_1 q(x_1, \mu_F)$ with increasing x_1. This depends on the detailed shape of the parton distributions at low x and, *e.g.*, for D0′ set the cross section is almost flat in the central rapidity region.

At $\sqrt{s} = 5.5$ TeV the increase of cross section with y occurs up to higher values of mass. For $M = 3$–10 GeV the cross section peaks at $y \sim 4$ where its value is typically twice that at $y = 0$ for the MRS D−′ set.

Transverse Momentum Distributions

Transverse momentum distributions for p-p collisions at the RHIC and LHC heavy-ion energies are shown in Figs. 13–19 normalized to the p_T-integrated cross section. To understand some of the features of these spectra, we focus on the RHIC results, Figs. 13–17. Fig. 13 shows $\rho(p_T)$, the normalized p_T distribution calculated at next-to-leading order for $M = 4$ GeV and $y = 0$. The normalization factor is

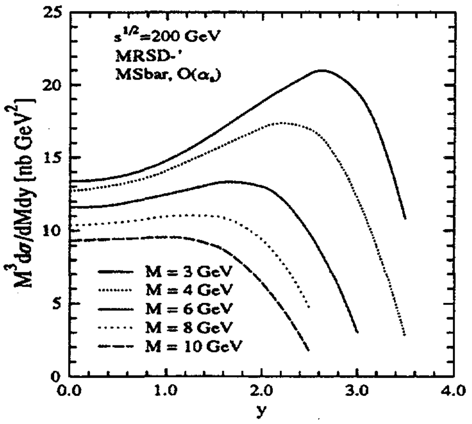

Figure 12: The cross section $\mathrm{d}\sigma/\mathrm{d}M\mathrm{d}y$ at fixed values of M as a function of y for the RHIC energy, $\sqrt{s} = 200$ GeV.

the p_T integrated cross section $\mathrm{d}\sigma/\mathrm{d}y\mathrm{d}M$. The dashed curve is the perturbative prediction valid at high p_T, while the solid thin curve is the matched total cross section (13). Fig. 14 shows the leading order result at the same energy. Observe that the difference between the matched and perturbative curves at high momentum is larger for the LO calculation compared to the NLO one.

Our prediction — the thick solid curve in Fig. 13 — switches between the matched and perturbative solutions, as discussed earlier. Although the matched result (13) formally applies at all momenta, it is not trustworthy at high p_T where the remainder R (dash-dotted curve) exceeds the total matched cross section. The difference between the matched and perturbative results is higher order in α_s; one can regard this difference as a measure of the uncertainty introduced by our truncation of the perturbation series. Observe that this uncertainty is quite small, as we emphasize in Fig. 15 by plotting the results with linear axes.

To illustrate how the matching works, we show the resummed, asymptotic and perturbative components of the matched solution (13) individually in Fig. 16. We see explicitly that the divergent asymptotic part (dash-dotted curve) dominates the perturbation series (thin solid curve) at low p_T. These contributions cancel at low p_T, so that the matched cross section is determined by the resummed result (10,11).

In Fig. 17 we show the p_T spectrum at RHIC for $M = 10$ GeV. The effect of switching is smaller at the higher mass scale. Figs. 18 and 19 show the p_T spectrum at LHC for $\sqrt{s} = 5.5$ TeV, $y = 0$ and $M = 4$ and 10 GeV at next-to-leading order. The matched expression is valid for the entire region $p_T \leq 2M$; switching is unnecessary in this range.

Angular Distributions

For the calculations of angular coefficients in Eqs. (16) and (17) the default parton distribution functions are the MRS D−′. We have used fixed-y values mainly at zero, but also up to maximum allowed by kinematics in some cases. We study

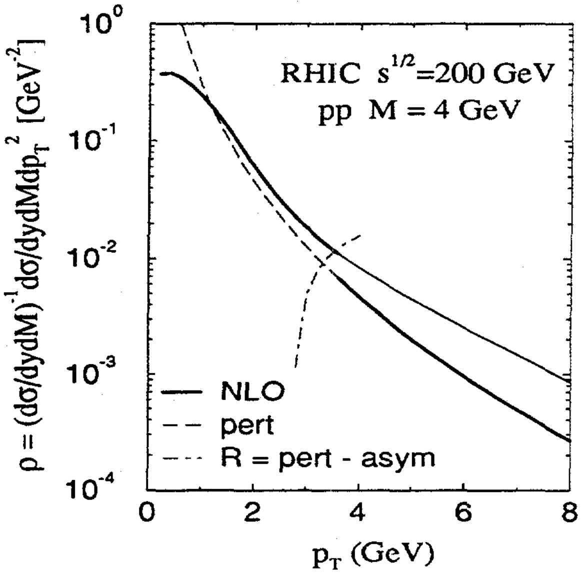

Figure 13: $\rho(p_T) = (\mathrm{d}\sigma/\mathrm{d}y\mathrm{d}M\mathrm{d}p_T^2)/(\mathrm{d}\sigma/\mathrm{d}y\mathrm{d}M)$, normalized transverse momentum spectrum (thick, solid curve) computed at next-to-leading order are shown for RHIC at $\sqrt{s} = 200$ GeV, $y = 0$, and $M = 4$ GeV. The dashed curve is the perturbative prediction valid at high p_T, while the solid thin curve is the matched asymptotic expansion that applies only at low p_T. The matched solution is not trustworthy at p_T's where the remainder R (dash-dotted curve) exceeds to the total matched cross section.

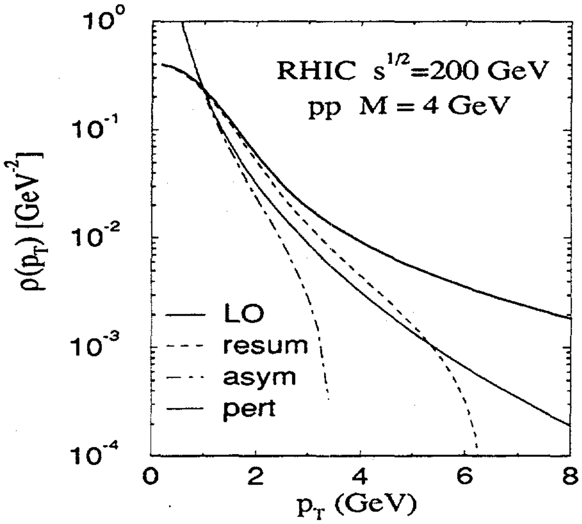

Figure 14: Same as Fig. 13, but for a leading order calculation. All contributions to Eq. (13) are shown explicitly for comparison to the NLO result in Fig. 16.

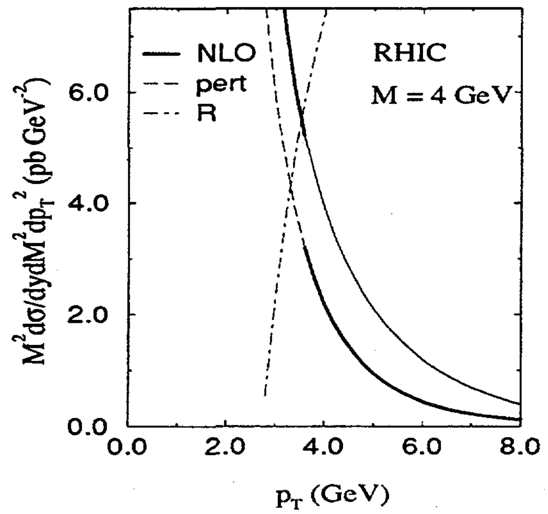

Figure 15: The cross section $d\sigma/dydM^2dp_T^2$ from Fig. 13 plotted without the normalization and with linear axes to exhibit the true magnitude of the discontinuity incurred by switching.

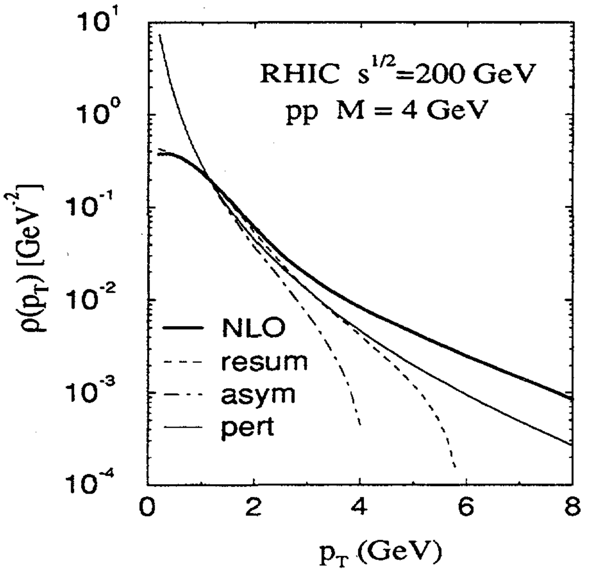

Figure 16: Same as Fig. 13, but showing all the components of the matched solution individually.

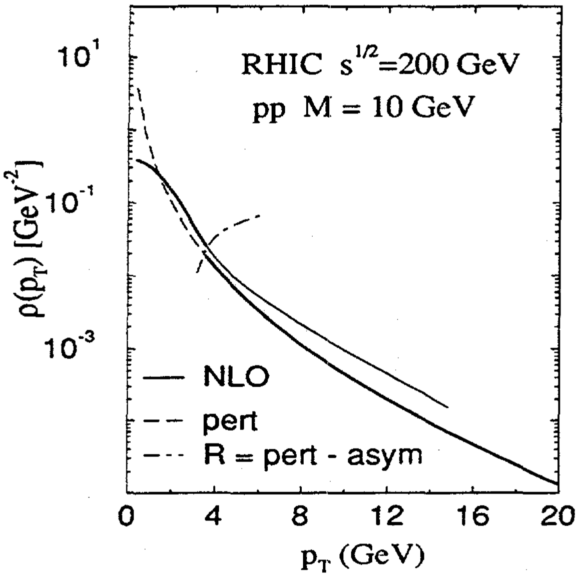

Figure 17: Normalized p_T spectrum at RHIC for $M = 10$ GeV. The effect of switching is smaller at the higher mass scale.

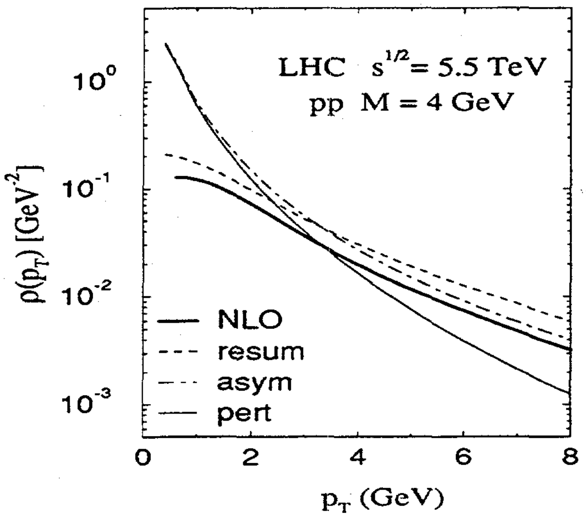

Figure 18: Normalized p_T spectrum at LHC for $\sqrt{s} = 5.5$ TeV, $y = 0$ and $M = 4$ GeV at next-to-leading order. Switching is not necessary for $p_T \leq 2M$.

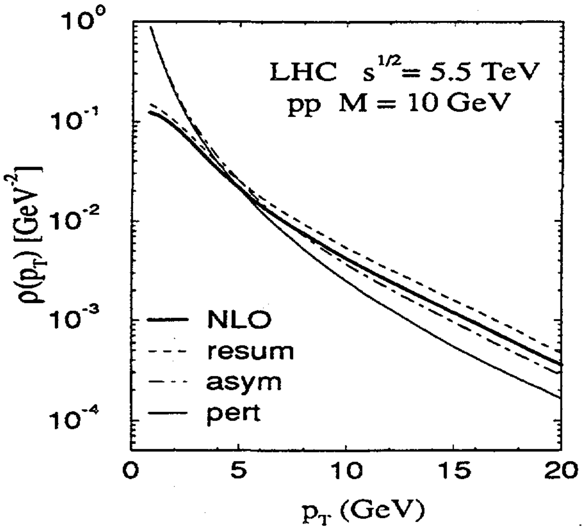

Figure 19: Same as Fig. 18 for $M = 10$ GeV.

the mass range $3 \leq M \leq 30$ GeV with $0 \leq p_T \leq 2M$ in each case.

Fig. 20 shows the λ coefficient at RHIC energy for the default values. As expected, it decreases with increasing p_T and approaches a minimum value of $-1/3$ for large p_T, and scales with p_T/M as predicted by either the $q\bar{q}$ (exact) or gq (approximate) subprocesses. The small scaling violations are an indication that the dominant subprocess must be gq, as one might expect in a p-p interaction. This is verified by separate calculation of the subprocess contributions. We have also verified that the predicted λ values are approximately independent of both $\sqrt{s}$ and the choice of structure function.

All of these calculations were done at $y = 0$, where μ is consistent with zero, as expected from the target-projectile interchange symmetry. At large y, however, we expect to see significant deviations from the simple scaling predictions. Fig. 21 shows the λ and μ values for several rapidities. We see that as the μ parameter becomes nonzero, a corresponding nonuniversal behavior sets in for the λ curves. The corresponding calculations at LHC energy are shown in Fig. 22, where much larger rapidities can be reached. In Fig. 23 we show the corresponding M-dependence at $y = 5$ for LHC. Clearly, no universal scaling appears, as exhibited by the same calculations as a function of p_T/M in Fig. 24.

At low p_T, all of these calculations will be modified by the soft gluon resummation procedure. In general, one would expect $\lambda \approx 1$ and $\mu \approx 0$ for p_T-values up to the point where the perturbative cross section becomes dominant. As an example, we calculate λ and μ at $\sqrt{s} = 38.8$ GeV, where the E772 experiment has measured the p_T distributions [29]. In Fig. 25 we compare their data with the LO perturbative

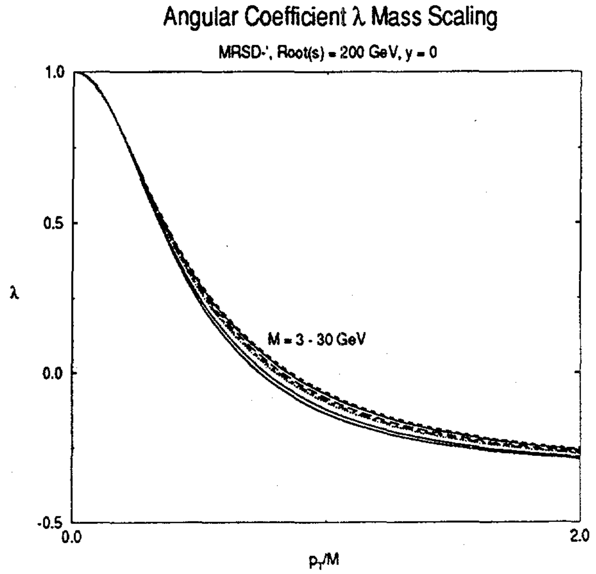

Figure 20: Angular coefficient λ scaling with p_T/M.

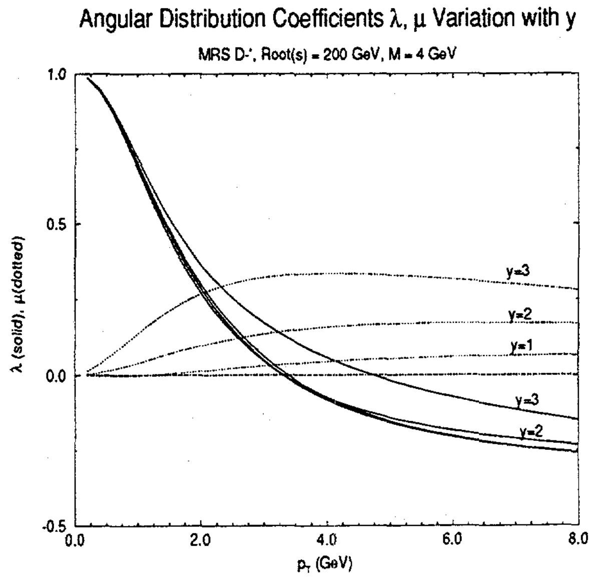

Figure 21: Angular coefficients λ and μ variation with rapidity at $\sqrt{s} = 200$ GeV.

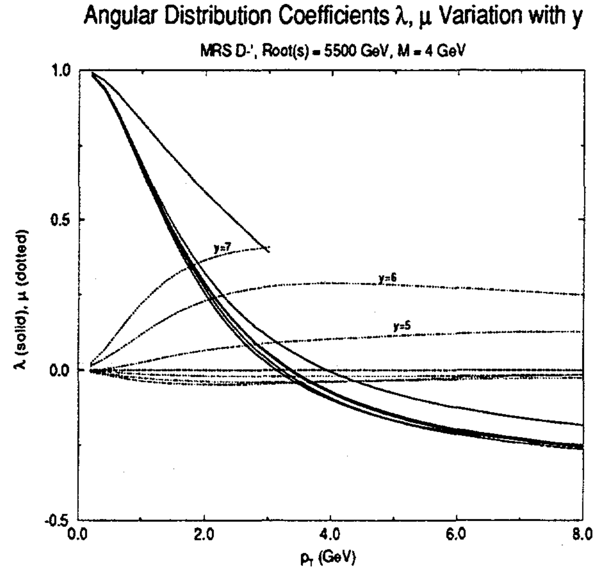
Angular Distribution Coefficients λ, μ Variation with y

MRS D-', Root(s) = 5500 GeV, M = 4 GeV

Figure 22: Same as Fig. 21 for $\sqrt{s} = 5500$ GeV.

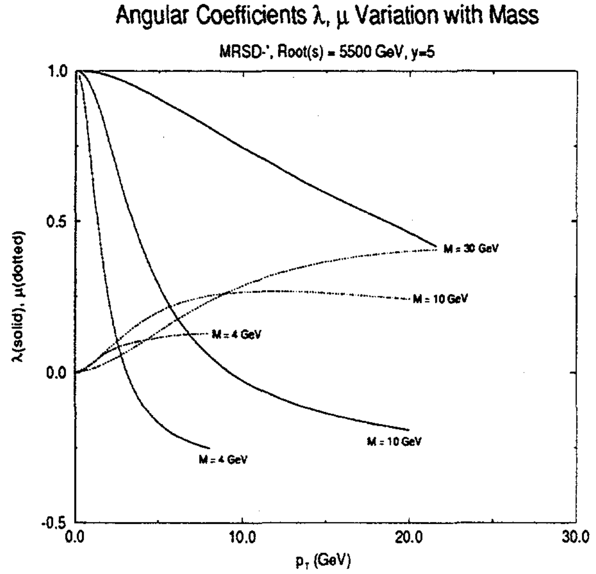
Angular Coefficients λ, μ Variation with Mass

MRSD-', Root(s) = 5500 GeV, y=5

Figure 23: Angular coefficients λ and μ variation with M at large rapidity.

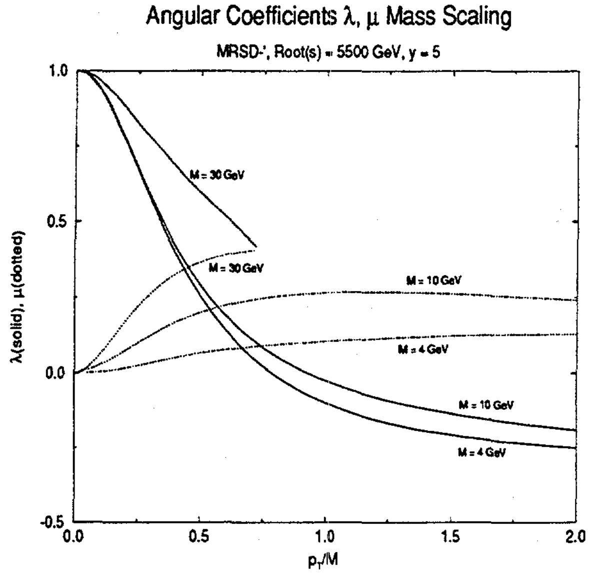

Figure 24: Angular coefficients λ and μ violation of M scaling at large rapidity.

calculations. As expected, the low-p_T region shows the perturbative divergences, the intermediate-p_T region is underestimated by the perturbative terms, and there is some evidence that the data is being matched by the perturbative calculation as p_T approaches values near M. We assume that a proper resummation procedure would match the data at low-p_T and simply rescale the perturbatively-calculated A_i with the ratio of measured to perturbative cross sections at each p_T. Shown in Fig. 26 are the λ and μ coefficients for each case. One sees that at low-p_T the resummation-corrected values remain closer to the uncorrected Born term predictions, *i.e.*, $\lambda = 1$, $\mu = 0$. Since the p_T values at which the perturbative calculations become dominant must be separately determined for each energy and mass value, we simply tabulate the perturbative cross section and the corresponding A_0 and A_1 values for this study at the appropriate RHIC and LHC energies. For each individual case at low p_T, one must then rescale the A_i with the ratio of perturbative cross section to resummed (or experimental) cross section values, and then recalculate the λ and μ parameters.

COMMENTS AND CONCLUSIONS

We have presented perturbative QCD calculations of the Drell-Yan process relevant to experiments with heavy ions at future high-energy colliders. The applicability of our perturbative calculations has also been addressed. In the energy range where experimental results are presently available, the calculations and the data agree to a level of $\sim$ 30% or better. In the high energy domain, $\sqrt{s} \gtrsim 200$ GeV, the perturbative series seems to converge well even down to pair mass of ~2–3

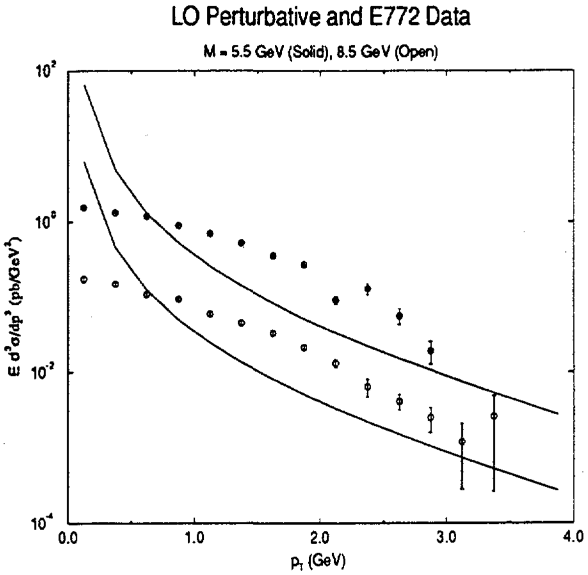

Figure 25: LO perturbative p_T dependence compared with E772 results.

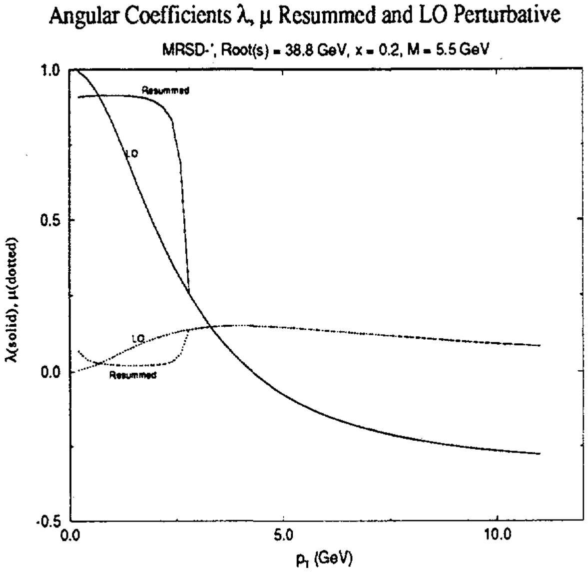

Figure 26: Angular coefficients λ and μ with resummation corrections at low p_T.

GeV with a NNLO contribution of the order of 10% in the rapidity integrated cross section, $d\sigma/dM$. The dependence on the factorization scheme and on the factorization and renormalization scales is not strong except for the smallest considered values of the pair mass, where we estimate the uncertainty to be ~20–30%.

At LHC energy the most serious uncertainty arises from the uncertainty in the parton distribution functions in the small$-x$ region. Different sets which are not ruled out by the present HERA data lead to estimates which differ by a factor of 3–4 for $M \sim 3$ GeV. Since a large pair rapidity indicates a small x for one of the incoming partons, the uncertainty in the parton distributions shows up also in the rapidity dependence of pairs. For the MRS D0′ set the rapidity distribution is flat in the central region but for the MRS D−′ it first increases with increasing y before the decrease at the phase space boundary.

From the cross sections for a hard process in a nucleon-nucleon interaction the number of such processes in a nucleus-nucleus collision can be obtained by multiplication with the overlap function for the colliding nuclei as defined in [36]. This approach presumes that factorization holds also for nuclear collisions. It also neglects the dependence of the shadowing of parton distributions on the local amount of overlap in the transverse plane. It should be kept in mind that further studies are needed on the shadowing and on the validity of the factorization assumption, especially for this relatively low-mass region of pairs in which we are interested.

Acknowledgements

We are grateful to W.L. van Neerven and P.J. Rijken for the programs of the $d\sigma/dM$ and $d\sigma/dMdy$ cross sections, to P.L. McGaughey for providing the E772 data and to R. Vogt for discussions and helpful comments.

References

[1] S. D. Drell and T. M. Yan, Phys. Rev. Lett. **25** (1970) 316.

[2] W. L. van Neerven, this volume.

[3] K. Kajantie, J. Lindfors and R. Raitio, Phys. Lett. **74B** (1978) 384;
J. Kubar-Andre and F. E. Paige, Phys. Rev. **D19** (1979) 221;
G. Altarelli, R. K. Ellis and G. Martinelli, Nucl. Phys. **B157** (1979) 461;
J. Kubar, M. le Bellac, J. L. Munier and G. Plaut, Nucl. Phys. **B175** (1980) 251; B. Humpert and W. L. van Neerven, Nucl. Phys. **B184** (1981) 225.

[4] R. Hamberg, W. L. van Neerven and T. Matsuura, Nucl. Phys. **B359** (1991) 343;
W. L. van Neerven and E.B. Zijlstra, Nucl. Phys. **B382** (1992) 11.

[5] T. Matsuura and W. L. van Neerven, Z. Phys. **C38** (1988) 623;
T. Matsuura, S. C. van der Marck and W. L. van Neerven, Nucl. Phys. **B319** (1989) 570; Phys. Lett. **211B** (1988) 171.

[6] P. J. Rijken and W. L. van Neerven, University of Leiden preprint, INLO-PUB-14/94.

[7] H. Plothow-Besch, Comp. Phys. Comm. **75** (1993) 396.

[8] A. D. Martin, W. J. Stirling and R. G. Roberts, Phys. Lett. **306B**, 145 (1993);

[9] M. Glück, E. Reya and A. Vogt, Z. Phys. **C53** (1992) 651.

[10] ZEUS Collaboration, M. Derrick et al., Phys. Lett. **316B** (1993) 412.

[11] P. Arnold and R. Kauffman, Nucl. Phys. **B349** (1991) 381.

[12] R. L. Thews, Phys. Lett. **100B** (1981) 339.

[13] K. Kajantie and R. Raitio, Nucl. Phys. **B139** (1978) 72; R. K. Ellis, G. Martinelli and R. Petronzio, Phys. Lett. **104B** (1981) 45; R. K. Ellis, G. Martinelli and R. Petronzio, Nucl. Phys. **B211** (1983) 106.

[14] P. Arnold and M. H. Reno, Nucl. Phys. **B319** (1989) 37; [Erratum **B330** (1990) 284]; P. Arnold, R. K. Ellis and M. H. Reno, Phys. Rev. **D40** (1989) 912; R. Gonsalves, J. Pawlovski, and C.-F. Wai, Phys. Rev. **D40** (1989) 2245.

[15] Yu. L. Dokshitzer, D. I. Dyakonov and S. I. Troyan, Phys. Reports **58** (1980) 269.

[16] J. C. Collins, D. E. Soper, Nucl. Phys. **B193** (1981) 381; **B197** (1982) 446; [Erratum **B213** (1983) 545].

[17] J. C. Collins, D. E. Soper and G. Sterman, Nucl. Phys. **B250** (1985) 199.

[18] G. Altarelli, R. K. Ellis, M. Greco and G. Martinelli, Nucl. Phys. **B246** (1984) 12.

[19] C. Davies and W. J. Stirling, Nucl. Phys. **B244** (1984) 337; C. Davies, B. Webber and W. J. Stirling, Nucl. Phys. **B256** (1985) 413.

[20] G. A. Ladinsky and C. P. Yuan, Phys. Rev. **D50** (1994) R4239.

[21] J. C. Collins and D. E. Soper, Phys. Rev. **D16** (1977) 2219.

[22] E. Mirkes, Nucl. Phys. **B387** (1992) 3.

[23] E. Mirkes, private communication.

[24] J. C. Collins, Phys. Rev. Lett. **42** (1979) 291.

[25] R. L. Thews, Phys. Rev. Lett. **43** (1979) 987, 1968(E).

[26] M. Guanziroli *et al.*: NA10 Collaboration, Z. Phys. **C37** (1988) 545.

[27] P. Chiapetta and M. LeBellac, Z. Phys. **C32** (1986) 521.

[28] S. J. Brodsky, G. P. Lepage and P. B. Mackenzie, Phys. Rev. **D28** (1983) 228; P. M. Stevenson, Phys. Rev. **D23**, 70 (1981); G. Grunberg, Phys. Lett. **95B** (1980) 70.

[29] P. L. McGaughey *et al.*, Phys. Rev. **D50** (1994) 3038.

[30] D. Antreasyan *et al.*, Phys. Rev. Lett. **48** (1982) 302.

Table 1. Inclusive cross section for Drell-Yan pairs in p-p collision

$$M^3 \frac{\mathrm{d}\sigma}{\mathrm{d}y\mathrm{d}M}\ [\mathrm{nb\,GeV}^2]$$

$$\sqrt{s} = 200\ \mathrm{GeV}$$

M [GeV]	Born MRS D−′	Born+LO MRS D−′	$K_{\rm th}$ MRS D−′	Born MRS D0′	Born+LO MRS D0′	$K_{\rm th}$ MRS D0′
3.0	0.9694E+01	0.1338E+02	1.380	0.9230E+01	0.1288E+02	1.395
4.0	0.9523E+01	0.1274E+02	1.338	0.9457E+01	0.1262E+02	1.334
5.0	0.9304E+01	0.1222E+02	1.313	0.9441E+01	0.1232E+02	1.305
6.0	0.8946E+01	0.1163E+02	1.299	0.9182E+01	0.1185E+02	1.290
7.0	0.8525E+01	0.1100E+02	1.289	0.8791E+01	0.1124E+02	1.278
8.0	0.8091E+01	0.1037E+02	1.281	0.8347E+01	0.1055E+02	1.264
9.0	0.7703E+01	0.9836E+01	1.276	0.8007E+01	0.1011E+02	1.262
10.0	0.7304E+01	0.9297E+01	1.272	0.7621E+01	0.9604E+01	1.260
11.0	0.6920E+01	0.8793E+01	1.270	0.7227E+01	0.9100E+01	1.259
12.0	0.6551E+01	0.8310E+01	1.268	0.6835E+01	0.8576E+01	1.254
13.0	0.6196E+01	0.7861E+01	1.268	0.6504E+01	0.8172E+01	1.256
14.0	0.5854E+01	0.7439E+01	1.270	0.6167E+01	0.7761E+01	1.258
15.0	0.5530E+01	0.7028E+01	1.271	0.5835E+01	0.7350E+01	1.259
16.0	0.5222E+01	0.6643E+01	1.272	0.5511E+01	0.6942E+01	1.259
17.0	0.4924E+01	0.6274E+01	1.274	0.5224E+01	0.6597E+01	1.262
18.0	0.4641E+01	0.5924E+01	1.276	0.4943E+01	0.6256E+01	1.265
19.0	0.4373E+01	0.5584E+01	1.276	0.4668E+01	0.5922E+01	1.268
20.0	0.4120E+01	0.5273E+01	1.279	0.4402E+01	0.5594E+01	1.270

[31] D. Antreasyan *et al.*, Phys. Rev. Lett. **48**, 302, (1982).

[32] A. S. Ito *et al.*, Phys. Rev. **D23**, 604, (1981).

[33] J. S. Conway *et al.*: E615 Collaboration, Phys. Rev. **D39** (1989) 92.

[34] S. Falciano *et al.*: NA10 Collaboration, Z. Phys. **C31** (1986) 513.

[35] A. Brandenburg, O. Nachtmann, and E. Mirkes, Z. Phys. **C60** (1993) 697.

[36] K.J. Eskola, R. Vogt and X.-N. Wang, "Nuclear Overlap Function", in this volume.

Table 2. Inclusive cross section for Drell-Yan pairs in p-p collision

$$M^3 \frac{\mathrm{d}\sigma}{\mathrm{d}y\mathrm{d}M} \; [\mathrm{nb\,GeV}^2]$$

$$\sqrt{s} = 500 \text{ GeV}$$

M [GeV]	Born MRS D−′	Born+LO MRS D−′	K_{th} MRS D−′	Born MRS D0′	Born+LO MRS D0′	K_{th} MRS D0′
3.0	0.1411E+02	0.1906E+02	1.350	0.1125E+02	0.1582E+02	1.405
4.0	0.1408E+02	0.1844E+02	1.309	0.1234E+02	0.1652E+02	1.338
5.0	0.1380E+02	0.1773E+02	1.284	0.1282E+02	0.1666E+02	1.299
6.0	0.1350E+02	0.1722E+02	1.276	0.1297E+02	0.1662E+02	1.281
7.0	0.1308E+02	0.1656E+02	1.265	0.1288E+02	0.1630E+02	1.265
8.0	0.1264E+02	0.1586E+02	1.254	0.1268E+02	0.1585E+02	1.250
9.0	0.1221E+02	0.1527E+02	1.250	0.1242E+02	0.1545E+02	1.244
10.0	0.1175E+02	0.1462E+02	1.243	0.1209E+02	0.1494E+02	1.235
11.0	0.1139E+02	0.1415E+02	1.242	0.1180E+02	0.1455E+02	1.233
12.0	0.1105E+02	0.1368E+02	1.238	0.1151E+02	0.1414E+02	1.228
13.0	0.1070E+02	0.1323E+02	1.236	0.1119E+02	0.1373E+02	1.226
14.0	0.1036E+02	0.1280E+02	1.235	0.1086E+02	0.1331E+02	1.225
15.0	0.1004E+02	0.1238E+02	1.233	0.1054E+02	0.1290E+02	1.223
16.0	0.9729E+01	0.1199E+02	1.232	0.1022E+02	0.1250E+02	1.222
17.0	0.9433E+01	0.1161E+02	1.231	0.9914E+01	0.1211E+02	1.221
18.0	0.9149E+01	0.1125E+02	1.229	0.9611E+01	0.1172E+02	1.218
19.0	0.8869E+01	0.1090E+02	1.228	0.9306E+01	0.1133E+02	1.218
20.0	0.8602E+01	0.1056E+02	1.227	0.9011E+01	0.1095E+02	1.215
25.0	0.7461E+01	0.9168E+01	1.228	0.7844E+01	0.9564E+01	1.219
30.0	0.6505E+01	0.8006E+01	1.230	0.6797E+01	0.8292E+01	1.220
35.0	0.5701E+01	0.7037E+01	1.234	0.5976E+01	0.7328E+01	1.226
40.0	0.5039E+01	0.6249E+01	1.240	0.5262E+01	0.6481E+01	1.231
45.0	0.4492E+01	0.5593E+01	1.245	0.4704E+01	0.5830E+01	1.239
50.0	0.4079E+01	0.5099E+01	1.250	0.4261E+01	0.5305E+01	1.245
55.0	0.3807E+01	0.4787E+01	1.257	0.3972E+01	0.4978E+01	1.253
60.0	0.3704E+01	0.4685E+01	1.264	0.3862E+01	0.4872E+01	1.261
65.0	0.3868E+01	0.4918E+01	1.271	0.4027E+01	0.5114E+01	1.269
70.0	0.4518E+01	0.5779E+01	1.279	0.4693E+01	0.5998E+01	1.278
75.0	0.6259E+01	0.8050E+01	1.286	0.6487E+01	0.8349E+01	1.286

Table 3. Inclusive cross section for Drell-Yan pairs in p-p collision

$$M^3 \frac{\mathrm{d}\sigma}{\mathrm{d}y\mathrm{d}M} \ [\mathrm{nb\,GeV^2}]$$

$$\sqrt{s} = 5500 \text{ GeV}$$

M [GeV]	Born MRS D−′	Born+LO MRS D−′	K_{th} MRS D−′	Born MRS D0′	Born+LO MRS D0′	K_{th} MRS D0′
3.0	0.7467E+02	0.9717E+02	1.301	0.1681E+02	0.2441E+02	1.452
4.0	0.7381E+02	0.9077E+02	1.229	0.2192E+02	0.2989E+02	1.363
5.0	0.7200E+02	0.8650E+02	1.201	0.2586E+02	0.3361E+02	1.299
6.0	0.6993E+02	0.8427E+02	1.205	0.2885E+02	0.3693E+02	1.279
7.0	0.6757E+02	0.7984E+02	1.181	0.3102E+02	0.3868E+02	1.247
8.0	0.6522E+02	0.7636E+02	1.170	0.3269E+02	0.4002E+02	1.224
9.0	0.6305E+02	0.7415E+02	1.176	0.3402E+02	0.4150E+02	1.219
10.0	0.6074E+02	0.7109E+02	1.170	0.3488E+02	0.4216E+02	1.208
11.0	0.5866E+02	0.6842E+02	1.166	0.3558E+02	0.4273E+02	1.201
12.0	0.5695E+02	0.6677E+02	1.172	0.3604E+02	0.4329E+02	1.201
13.0	0.5529E+02	0.6442E+02	1.165	0.3634E+02	0.4328E+02	1.190
14.0	0.5364E+02	0.6262E+02	1.167	0.3646E+02	0.4339E+02	1.190
15.0	0.5211E+02	0.6055E+02	1.161	0.3653E+02	0.4316E+02	1.181
16.0	0.5070E+02	0.5904E+02	1.164	0.3655E+02	0.4316E+02	1.180
17.0	0.4939E+02	0.5733E+02	1.160	0.3654E+02	0.4294E+02	1.175
18.0	0.4816E+02	0.5575E+02	1.157	0.3648E+02	0.4269E+02	1.170
19.0	0.4691E+02	0.5421E+02	1.155	0.3631E+02	0.4236E+02	1.166
20.0	0.4575E+02	0.5285E+02	1.155	0.3613E+02	0.4209E+02	1.165

Table 4. Inclusive cross section for Drell-Yan pairs in p-p collision

$$M^3 \frac{\mathrm{d}\sigma}{\mathrm{d}y\mathrm{d}M} \; [\mathrm{nb\,GeV}^2]$$

$\sqrt{s} = 14000$ GeV

M [GeV]	Born MRS D−′	Born+LO MRS D−′	K_{th} MRS D−′	Born MRS D0′	Born+LO MRS D0′	K_{th} MRS D0′
3.0	0.1671E+03	0.2167E+03	1.297	0.1878E+02	0.2814E+02	1.497
4.0	0.1659E+03	0.2073E+03	1.250	0.2623E+02	0.3637E+02	1.386
5.0	0.1616E+03	0.1918E+03	1.187	0.3253E+02	0.4260E+02	1.309
6.0	0.1564E+03	0.1797E+03	1.148	0.3774E+02	0.4773E+02	1.264
7.0	0.1508E+03	0.1642E+03	1.088	0.4184E+02	0.4911E+02	1.173
8.0	0.1454E+03	0.1632E+03	1.122	0.4522E+02	0.5374E+02	1.188
9.0	0.1405E+03	0.1612E+03	1.147	0.4806E+02	0.5802E+02	1.207
10.0	0.1355E+03	0.1534E+03	1.132	0.5013E+02	0.5998E+02	1.196
11.0	0.1309E+03	0.1459E+03	1.114	0.5191E+02	0.5996E+02	1.155
12.0	0.1269E+03	0.1468E+03	1.156	0.5341E+02	0.6409E+02	1.200
13.0	0.1231E+03	0.1406E+03	1.142	0.5459E+02	0.6431E+02	1.178
14.0	0.1193E+03	0.1374E+03	1.151	0.5543E+02	0.6556E+02	1.182
15.0	0.1160E+03	0.1333E+03	1.149	0.5609E+02	0.6611E+02	1.178
16.0	0.1129E+03	0.1295E+03	1.147	0.5665E+02	0.6650E+02	1.173
17.0	0.1100E+03	0.1249E+03	1.136	0.5713E+02	0.6639E+02	1.162
18.0	0.1072E+03	0.1209E+03	1.127	0.5750E+02	0.6622E+02	1.151
19.0	0.1045E+03	0.1186E+03	1.134	0.5765E+02	0.6661E+02	1.155
20.0	0.1019E+03	0.1146E+03	1.125	0.5776E+02	0.6618E+02	1.145
25.0	0.9120E+02	0.1037E+03	1.137	0.5786E+02	0.6657E+02	1.150
30.0	0.8283E+02	0.9371E+02	1.131	0.5698E+02	0.6505E+02	1.141
35.0	0.7664E+02	0.8638E+02	1.127	0.5601E+02	0.6346E+02	1.133
40.0	0.7179E+02	0.8131E+02	1.132	0.5510E+02	0.6264E+02	1.136
45.0	0.6848E+02	0.7750E+02	1.131	0.5479E+02	0.6214E+02	1.134
50.0	0.6693E+02	0.7538E+02	1.126	0.5550E+02	0.6257E+02	1.127
55.0	0.6752E+02	0.7622E+02	1.128	0.5774E+02	0.6518E+02	1.128
60.0	0.7175E+02	0.8103E+02	1.129	0.6286E+02	0.7095E+02	1.128
65.0	0.8248E+02	0.9345E+02	1.133	0.7378E+02	0.8349E+02	1.131
70.0	0.1068E+03	0.1207E+03	1.131	0.9728E+02	0.1098E+03	1.128
75.0	0.1648E+03	0.1864E+03	1.131	0.1526E+03	0.1722E+03	1.128
80.0	0.3334E+03	0.3776E+03	1.132	0.3136E+03	0.3541E+03	1.129

Table 5. Angular distribution factors for Drell-Yan pairs in p-p collision $\sqrt{s} = 200$ GeV, $M = 4$ GeV

p_T [GeV]	$d\sigma/dM^2dp_T{}^2dy$ [GeV^{-6}] y = 0	A_0	A_1	$d\sigma/dM^2dp_T{}^2dy$ [GeV^{-6}] y = 3	A_0	A_1
0.2	0.367D-06	0.0072	0.0000	0.170D-06	0.0062	0.0140
0.4	0.772D-07	0.0296	0.0000	0.297D-07	0.0268	0.0385
0.6	0.302D-07	0.0653	0.0000	0.995D-08	0.0607	0.0708
0.8	0.153D-07	0.1108	0.0000	0.435D-08	0.1038	0.1082
1.0	0.888D-08	0.1623	0.0000	0.219D-08	0.1521	0.1477
1.2	0.563D-08	0.2166	0.0000	0.121D-08	0.2017	0.1871
1.4	0.380D-08	0.2713	0.0000	0.710D-09	0.2502	0.2245
1.6	0.267D-08	0.3247	0.0000	0.434D-09	0.2960	0.2590
1.8	0.194D-08	0.3757	0.0000	0.273D-09	0.3384	0.2900
2.0	0.144D-08	0.4236	0.0000	0.175D-09	0.3770	0.3173
2.2	0.110D-08	0.4683	0.0000	0.114D-09	0.4121	0.3410
2.4	0.846D-09	0.5095	0.0000	0.751D-10	0.4438	0.3613
2.6	0.663D-09	0.5473	0.0000	0.498D-10	0.4726	0.3786
2.8	0.525D-09	0.5820	0.0000	0.333D-10	0.4987	0.3930
3.0	0.420D-09	0.6136	0.0000	0.223D-10	0.5225	0.4050
3.2	0.339D-09	0.6425	0.0000	0.149D-10	0.5444	0.4148
3.4	0.276D-09	0.6688	0.0000	0.100D-10	0.5644	0.4227
3.6	0.226D-09	0.6928	0.0000	0.671D-11	0.5830	0.4289
3.8	0.187D-09	0.7148	0.0000	0.448D-11	0.6002	0.4337
4.0	0.155D-09	0.7347	0.0000	0.299D-11	0.6162	0.4372
4.2	0.129D-09	0.7530	0.0000	0.198D-11	0.6311	0.4397
4.4	0.108D-09	0.7696	0.0000	0.131D-11	0.6452	0.4412
4.6	0.915D-10	0.7849	0.0000	0.860D-12	0.6584	0.4418
4.8	0.775D-10	0.7988	0.0000	0.560D-12	0.6708	0.4418
5.0	0.659D-10	0.8117	0.0000	0.362D-12	0.6826	0.4411
5.2	0.563D-10	0.8235	0.0000	0.231D-12	0.6938	0.4399
5.4	0.483D-10	0.8343	0.0000	0.146D-12	0.7044	0.4382
5.6	0.416D-10	0.8442	0.0000	0.910D-13	0.7145	0.4361
5.8	0.359D-10	0.8534	0.0000	0.558D-13	0.7241	0.4337
6.0	0.312D-10	0.8618	0.0000	0.336D-13	0.7333	0.4309
6.2	0.271D-10	0.8696	0.0000	0.198D-13	0.7421	0.4279
6.4	0.236D-10	0.8768	0.0000	0.114D-13	0.7505	0.4246
6.6	0.207D-10	0.8836	0.0000	0.641D-14	0.7585	0.4212
6.8	0.181D-10	0.8898	0.0000	0.348D-14	0.7662	0.4177
7.0	0.159D-10	0.8955	0.0000	0.181D-14	0.7736	0.4139
7.2	0.141D-10	0.9009	0.0000	0.896D-15	0.7808	0.4099
7.4	0.124D-10	0.9058	0.0000	0.416D-15	0.7879	0.4058
7.6	0.110D-10	0.9105	0.0000	0.180D-15	0.7948	0.4014
7.8	0.977D-11	0.9149	0.0000	0.722D-16	0.8013	0.3970
8.0	0.869D-11	0.9189	0.0000	0.268D-16	0.8073	0.3929

Table 6. Angular distribution factors for Drell-Yan pairs in p-p collision $\sqrt{s} = 5500$ GeV, $M = 4$ GeV

p_T [GeV]	$d\sigma/dM^2dp_T{}^2dy$ [GeV^{-6}] y = 0	A_0	A_1	$d\sigma/dM^2dp_T{}^2dy$ [GeV^{-6}] y = 3	A_0	A_1
0.2	0.389D-05	0.0085	0.0000	0.545D-05	0.0081	-0.0071
0.4	0.844D-06	0.0341	0.0000	0.118D-05	0.0329	-0.0154
0.6	0.337D-06	0.0736	0.0000	0.471D-06	0.0714	-0.0238
0.8	0.173D-06	0.1226	0.0000	0.241D-06	0.1194	-0.0317
1.0	0.101D-06	0.1768	0.0000	0.141D-06	0.1730	-0.0387
1.2	0.647D-07	0.2328	0.0000	0.905D-07	0.2287	-0.0448
1.4	0.438D-07	0.2882	0.0000	0.614D-07	0.2841	-0.0498
1.6	0.309D-07	0.3415	0.0000	0.434D-07	0.3377	-0.0538
1.8	0.225D-07	0.3916	0.0000	0.317D-07	0.3883	-0.0569
2.0	0.168D-07	0.4383	0.0000	0.237D-07	0.4357	-0.0592
2.2	0.128D-07	0.4813	0.0000	0.180D-07	0.4795	-0.0607
2.4	0.990D-08	0.5207	0.0000	0.140D-07	0.5198	-0.0615
2.6	0.776D-08	0.5566	0.0000	0.110D-07	0.5567	-0.0618
2.8	0.615D-08	0.5895	0.0000	0.872D-08	0.5903	-0.0616
3.0	0.493D-08	0.6193	0.0000	0.700D-08	0.6210	-0.0611
3.2	0.398D-08	0.6464	0.0000	0.567D-08	0.6489	-0.0602
3.4	0.325D-08	0.6712	0.0000	0.463D-08	0.6743	-0.0591
3.6	0.267D-08	0.6936	0.0000	0.381D-08	0.6975	-0.0577
3.8	0.220D-08	0.7142	0.0000	0.315D-08	0.7186	-0.0562
4.0	0.183D-08	0.7329	0.0000	0.262D-08	0.7378	-0.0546
4.2	0.153D-08	0.7500	0.0000	0.220D-08	0.7554	-0.0529
4.4	0.129D-08	0.7657	0.0000	0.185D-08	0.7714	-0.0512
4.6	0.109D-08	0.7801	0.0000	0.157D-08	0.7861	-0.0494
4.8	0.928D-09	0.7932	0.0000	0.133D-08	0.7996	-0.0476
5.0	0.793D-09	0.8054	0.0000	0.114D-08	0.8120	-0.0457
5.2	0.680D-09	0.8166	0.0000	0.977D-09	0.8234	-0.0439
5.4	0.586D-09	0.8268	0.0000	0.841D-09	0.8338	-0.0421
5.6	0.506D-09	0.8363	0.0000	0.727D-09	0.8434	-0.0403
5.8	0.439D-09	0.8450	0.0000	0.631D-09	0.8523	-0.0385
6.0	0.383D-09	0.8532	0.0000	0.550D-09	0.8605	-0.0368
6.2	0.335D-09	0.8608	0.0000	0.480D-09	0.8681	-0.0351
6.4	0.293D-09	0.8677	0.0000	0.421D-09	0.8752	-0.0334
6.6	0.258D-09	0.8743	0.0000	0.370D-09	0.8817	-0.0318
6.8	0.228D-09	0.8803	0.0000	0.326D-09	0.8878	-0.0302
7.0	0.202D-09	0.8860	0.0000	0.288D-09	0.8934	-0.0286
7.2	0.179D-09	0.8913	0.0000	0.256D-09	0.8987	-0.0271
7.4	0.159D-09	0.8962	0.0000	0.227D-09	0.9036	-0.0256
7.6	0.142D-09	0.9008	0.0000	0.203D-09	0.9082	-0.0242
7.8	0.127D-09	0.9052	0.0000	0.181D-09	0.9124	-0.0228
8.0	0.114D-09	0.9092	0.0000	0.162D-09	0.9165	-0.0214

HEAVY QUARK PRODUCTION IN pp COLLISIONS

P.L. McGAUGHEY[a], E. QUACK[b], P.V. RUUSKANEN[c*],
R. VOGT[d†] and X.-N. WANG[d†]

[a]*Los Alamos National Laboratory,*
Los Alamos, New Mexico 87545
[b]*Gesellschaft für Schwerionenforschung (GSI),*
D-64220 Darmstadt, Germany
[c]*Institute for Theoretical Physics,*
P. O. Box 9, FIN-00014, University of Helsinki, Helsinki, Finland
[d]*Nuclear Science Division, MS 70A-3307*
Lawrence Berkeley Laboratory,
University of California, Berkeley, California 94720

A systematic study of the inclusive single heavy quark and heavy-quark pair production cross sections in pp collisions is presented for RHIC and LHC energies. We compare with existing data when possible. The dependence of the rates on the renormalization and factorization scales is discussed. Predictions of the cross sections are given for two different sets of parton distribution functions.

INTRODUCTION

Charm and bottom quark production from the initial nucleon-nucleon collisions will be copious at the RHIC and LHC colliders. Heavy quark decay into leptons will represent a significant background to dilepton production [1] in heavy ion collisions. A quantitative knowledge of the production cross section in pp collisions is a prerequisite for the detection of collective effects, such as heavy quark production by rescattering and by the quark-gluon plasma, which would appear as a deviation from the simple superposition of hadronic collisions.

The lowest order (Born) calculations of the total cross section predict the correct energy dependence but differ from the experimental measurements by a "K factor" of 2-3. While the single-inclusive distributions as well as the mass and rapidity distributions of $Q\overline{Q}$ pairs are also well described to within a K factor by the Born cross section, the p_T and azimuthal double-differential distributions are not calculable at the Born level since the $Q\overline{Q}$ pair is always produced back-to-back in

---

[*] Department of Physics, University of Jyväskylä, Jyväskylä, Finland

[†] Supported by the U. S. Department of Energy under Contract No. DE-AC03-76SF00515.

lowest order. For this reason, a next-to-leading order (NLO) calculation is needed. The calculations we present here are done using a Monte Carlo program developed by Nason and collaborators [2, 3, 4]. Similar work on the total cross section and the single inclusive distributions was done by Smith, van Neerven, and collaborators [5].

In addition to the uncertainties in the parton distribution functions, uncertainties arise from the heavy quark mass and the renormalization and factorization scale parameters. At collider energies, the calculations become more uncertain due to the lightness of the heavy quark compared to the center of mass energy, $m_Q/\sqrt{s} \ll 1$. We first discuss the Born calculation and then outline the NLO calculation. We use the available data on $\sigma_{c\overline{c}}^{\rm tot}(s)$ to fix the charm quark mass and the scale parameters. The resulting parameter set provides a point from which to extrapolate to heavy-ion collider energies. We compare with single-inclusive and double-differential distributions from charm and bottom data when available. We present estimates of heavy quark production cross sections in proton-proton collisions at RHIC ($\sqrt{s}$ = 200 and 500 GeV) and LHC ($\sqrt{s}$ = 5.5 TeV and 14 TeV), according to our present theoretical knowledge. We provide both the Born and NLO results for the total $Q\overline{Q}$ production cross section, single inclusive y and p_T distributions, and double differential M, ϕ, y and p_T distributions.

HEAVY QUARK PRODUCTION IN PERTURBATIVE QCD

The most general expression for the double differential cross section for $Q\overline{Q}$ pair production from the collision of hadrons A and B is

$$\begin{aligned} E_Q E_{\overline{Q}} \frac{d\sigma_{AB}}{d^3p_Q d^3p_{\overline{Q}}} &= \sum_{i,j} \int dx_1\, dx_2 F_i^A(x_1,\mu_F) F_j^B(x_2,\mu_F) \\ & \qquad E_Q E_{\overline{Q}} \frac{d\widehat{\sigma}_{ij}(x_1P_1, x_2P_2, m_Q, \mu_R)}{d^3p_Q d^3p_{\overline{Q}}} \ . \end{aligned} \tag{1}$$

μ_F. Here i and j are the interacting partons and the functions F_i are the number densities of gluons, light quarks and antiquarks evaluated at momentum fraction x and factorization scale μ_F. The short-distance cross section, $\widehat{\sigma}_{ij}$, is calculable as a perturbation series in $\alpha_s(\mu_R)$ where the strong coupling constant is evaluated at the renormalization scale μ_R. Both scales are of the order of the heavy quark mass. At leading order, $\mu_F = \mu_R = \mu$ where $\mu = 2m_c$ has been commonly used. The scale dependence will be discussed in more detail below.

Leading Order

At leading order, $\mathcal{O}(\alpha_s^2)$, $Q\overline{Q}$ production proceeds by two basic processes,

$$q + \overline{q} \rightarrow Q + \overline{Q} \tag{2}$$

$$g + g \rightarrow Q + \overline{Q} \ . \tag{3}$$

The invariant cross section for the process $A + B \to H + \overline{H}$ where the $Q\overline{Q}$ pair has fragmented into hadrons $H(Q\overline{q})$ and $\overline{H}(\overline{Q}q)$ can be written as

$$\begin{aligned} E_H E_{\overline{H}} \frac{d\sigma_{AB}}{d^3p_H d^3p_{\overline{H}}} &= \int \frac{\hat{s}}{2\pi} dx_1 dx_2 dz_Q dz_{\overline{Q}} C(x_1, x_2) \frac{E_H E_{\overline{H}}}{E_Q E_{\overline{Q}}} \\ & \frac{D_{H/Q}(z_Q)}{z_Q^3} \frac{D_{\overline{H}/\overline{Q}}(z_{\overline{Q}})}{z_{\overline{Q}}^3} \delta^4(p_1 + p_2 - p_Q - p_{\overline{Q}}) \, , \end{aligned} \qquad (4)$$

where $\sqrt{\hat{s}}$, the parton-parton center of mass energy, is related to $\sqrt{s}$, the hadron-hadron center of mass energy, by $\hat{s} = x_1 x_2 s$. The intrinsic transverse momenta of the incoming partons have been neglected. The sum of the leading order subprocess cross sections convoluted with the parton number densities is contained in $C(x_1, x_2)$ where

$$C(x_1, x_2) = \sum_q [F_q^A(x_1) F_{\overline{q}}^B(x_2) + F_{\overline{q}}^A(x_1) F_q^B(x_2)] \frac{d\hat{\sigma}_{q\overline{q}}}{d\hat{t}} + F_g^A(x_1) F_g^B(x_2) \frac{d\hat{\sigma}_{gg}}{d\hat{t}} \, . \qquad (5)$$

Only light quark flavors, those with $m < m_Q$, are included in the sum over q. The dependence on the scale μ_F has been suppressed here.

Fragmentation affects the charmed hadron distributions, not the total $c\overline{c}$ production cross section. The fragmentation functions, $D_{H/Q}(z)$, describe the hadronization of the heavy quarks where $z = |\vec{p_H}|/|\vec{p_Q}|$ is the fraction of the heavy quark momentum carried by the final-state hadron. Some problems exist in the understanding of charmed hadron production at large x_F, see *e.g.*, [6, 7, 8]. However, this interesting regime may not be measurable at the RHIC and LHC colliders since the center of mass energy is high and the rapidity coverage is mostly confined to the central region. (The planned PHENIX muon spectrometer at RHIC will have a larger rapidity coverage, $1.5 \leq y \leq 2.5$ [9], but these effects will probably be out of reach at the maximum collider energy.)

Ignoring fragmentation effects for the moment, after taking four-momentum conservation into account, we are left with

$$\frac{d\sigma}{dp_T^2 dy_Q dy_{\overline{Q}}} = x_1 x_2 C(x_1, x_2) \, , \qquad (6)$$

where x_1 and x_2 are

$$\begin{aligned} x_1 &= \frac{\widehat{m}_Q}{\sqrt{s}} (e^{y_Q} + e^{y_{\overline{Q}}}) \, , \\ x_2 &= \frac{\widehat{m}_Q}{\sqrt{s}} (e^{-y_Q} + e^{-y_{\overline{Q}}}) \, , \end{aligned} \qquad (7)$$

and $\widehat{m}_Q = \sqrt{m_Q^2 + p_T^2}$. At $y_Q = y_{\overline{Q}} = 0$, $x_1 = x_2$. The target fractions, x_2, decrease with rapidity while the projectile fractions, x_1, increase. The subprocess cross sections for $Q\overline{Q}$ production by $q\overline{q}$ annihilation and gg fusion to order $\mathcal{O}(\alpha_s^2)$, expressed as a function of $\widehat{m}_Q$, y_Q, and $y_{\overline{Q}}$, are [10]

$$\frac{d\hat{\sigma}_{q\overline{q}}}{d\hat{t}} = \frac{\pi\alpha_s^2}{9\widehat{m}_Q^4} \frac{\cosh(y_Q - y_{\overline{Q}}) + m_Q^2/\widehat{m}_Q^2}{(1 + \cosh(y_Q - y_{\overline{Q}}))^3} \, , \qquad (8)$$

$$\frac{d\hat{\sigma}_{gg}}{d\hat{t}} = \frac{\pi\alpha_s^2}{96\hat{m}_Q^4}\frac{8\cosh(y_Q - y_{\overline{Q}}) - 1}{(1+\cosh(y_Q - y_{\overline{Q}}))^3}\left(\cosh(y_Q - y_{\overline{Q}}) + \frac{2m_Q^2}{\hat{m}_Q^2} - \frac{2m_Q^4}{\hat{m}_Q^4}\right) . \tag{9}$$

Next-to-Leading Order

We now discuss the NLO, $\mathcal{O}(\alpha_s^3)$, corrections to the $Q\overline{Q}$ production cross section. In addition to virtual corrections to the Born diagrams, production by

$$\begin{aligned} q+\overline{q} &\rightarrow Q+\overline{Q}+g & (10)\\ g+g &\rightarrow Q+\overline{Q}+g & (11)\\ q(\overline{q})+g &\rightarrow Q+\overline{Q}+(\overline{q})q\ , & (12)\end{aligned}$$

must also be included. The last process, quark-gluon scattering, is not present at leading order. The quark-gluon graphs have been interpreted at the Born level as the scattering of a heavy quark excited from the nucleon sea with a light quark or gluon and are referred to as flavor excitation [2]. The total short distance cross section $\hat{\sigma}_{ij}$ for a given production process can be expressed generally as

$$\hat{\sigma}_{ij}(\hat{s}, m_Q, \mu_R) = \frac{\alpha_s^2(\mu_R)}{m_Q^2} f_{ij}(\rho, \mu_R^2/m_Q^2)\ , \tag{13}$$

where $\rho = 4m_Q^2/\hat{s}$. The function f_{ij} can be expanded perturbatively as

$$f_{ij}(\rho, \mu_R^2/m_Q^2) = f_{ij}^0(\rho) + \frac{\alpha_s(\mu_R)}{4\pi}\left[f_{ij}^1(\rho) + \overline{f}_{ij}^1(\rho)\ln(\mu_R^2/m_Q^2)\right] + \mathcal{O}(\alpha_s^2)\ . \tag{14}$$

The Born contribution is given by f_{ij}^0 where $f_{qg}^0 = f_{\overline{q}g}^0 = f_{gq}^0 = f_{g\overline{q}}^0 = 0$. Only f_{gg}^0 and $f_{q\overline{q}}^0$ contribute and can be computed from the $\hat{t}$ integration of the differential cross sections given in (8) and (9). The physical cross section should be independent of the renormalization scale: the dependence in eq. (14) introduces an unphysical parameter in the calculation. If the perturbative expansion is sufficient, *i.e.* if further higher-order corrections are small, at some value of μ_R the physical $\mathcal{O}(\alpha_s^n)$ and $\mathcal{O}(\alpha_s^{n+1})$ cross sections should be equal[‡]. If the μ_R dependence is strong, the perturbative expansion is untrustworthy and the predictive power of the calculation is weak [10]. The rather large K-factor between the Born and NLO cross sections suggests that further higher-order corrections are needed, particularly for charm and bottom quarks which are rather "light" when $\sqrt{s}$ is large. Usually the renormalization scale in $\hat{\sigma}_{ij}$ and the factorization scale in the parton distribution functions are chosen to be equal. We follow this prescription in our calculations.

We have used two sets of recent parton distribution functions[§], GRV HO [12] and MRS D−′ [13]. The first begins with a low scale, $Q_{0,\mathrm{GRV}}^2 = 0.3$ GeV^2, and

---

[‡] The order of the expansion is represented by n. For $Q\overline{Q}$ production, $n \geq 2$. A calculation to order $\mathcal{O}(\alpha_s^n)$ introduces corrections at the order $\mathcal{O}(\alpha_s^{n+1})$. Thus the μ dependence is generally decreased when additional higher-order corrections are included if the quark mass is large enough.

[§] All available parton distribution functions are contained in the package PDFLIB [11], available in the CERN library routines.

valence-like parton distributions, therefore evolving very quickly with Q^2. The second, with $Q^2_{0,\mathrm{MRS}} = 5$ GeV^2, has sea quark and gluon distributions that grow as $\sim x^{-1/2}$ when $x \to 0$. Both are compatible with the recent deep-inelastic scattering data from HERA [14]. We also include estimates of the total cross section using the MRS D0$'$ [13] distributions. This set assumes a constant value for the sea and gluon distributions at $Q^2_{0,\mathrm{MRS}}$ as $x \to 0$ and lies below the HERA data. The GRV distributions assume a symmetric light quark sea, $\overline{u} = \overline{d}$, and no initial strange quark content, $x\overline{s}(x, Q^2_{0,\mathrm{GRV}}) = 0$, increasing to give $2\langle x\rangle_{\overline{s}}/(\langle x\rangle_{\overline{u}} + \langle x\rangle_{\overline{d}}) \simeq 0.53$ at $Q^2 = 10$ GeV^2 [12]. The MRS D sets allow $\overline{u} < \overline{d}$ to account for measurements of the Gottfried sum rule and assume $\overline{s} = (\overline{u} + \overline{d})/4$ at $Q^2_{0,\mathrm{MRS}}$ [13]. Thus the MRS distributions, arising from a global fit, provide a somewhat better overall description of the deep-inelastic scattering data for $x > 0.01$ than the GRV distributions [12, 13].

Since we compare two extreme cases for the nucleon parton distributions as $x \to 0$, MRS D$-'$ and GRV HO on one hand and MRS D0$'$ on the other, our results may be thought of as providing an upper and lower bound to the $Q\overline{Q}$ cross section at heavy-ion collider energies for fixed m_Q and scale. However, the gluon distribution function at low x is poorly known, particularly in the x region accessible at RHIC and LHC, $x \approx 10^{-2}$ and 10^{-4} around $y = 0$, respectively. The low x behavior has a significant effect on the shape of the gluon distribution at moderate values of x, as shown in Fig. 1. Steeply rising gluon distributions at low x are compensated for by a corresponding depletion at moderate x.

Heavy quark production by gluon fusion dominates the $pp \to Q\overline{Q}X$ production cross section in the central region. Thus we show the shape of the gluon distributions from the three sets of parton distribution functions Fig. 1(a) over the x range of the previous pp data, $0.01 < x < 1$. To facilitate comparison, all three are shown at $\mu = 2.4$ GeV. The solid curve is the GRV HO distribution, the dashed, MRS D0$'$, and the dot-dashed, MRS D$-'$. The GRV distribution at $\mu = 1.2$ GeV is also shown to demonstrate the effect of the Q^2 evolution. Since this set has a smaller initial scale, the evolution is quite fast. The D0$'$ distribution can be seen to turn over and begin to flatten as x decreases. However, for much of the range, it is above the D$-'$ distribution, reflected in a larger $\sigma^{\mathrm{tot}}_{c\overline{c}}$, as shown in Fig. 3. All three sets, evaluated in the $\overline{MS}$ scheme, have similar values of Λ_{QCD}. In Fig. 1(b), we show the running of the two loop value of α_s,

$$\alpha_s(\mu, f) = \frac{1}{b_f \ln(\mu^2/\Lambda_f^2)} \left[1 - \frac{b'_f \ln\ln(\mu^2/\Lambda_f^2)}{b_f \ln(\mu^2/\Lambda_f^2)}\right] , \tag{15}$$

where $b_f = (33 - 2f)/12\pi$, $b'_f = (153 - 19f)/(2\pi(33 - 2f))$, f is the number of active flavors, and Λ_f is the appropriate value of Λ_{QCD}. The number of active flavors depends on the quark mass. For charm and bottom production, $f = 3$ and 4 respectively. At $\mu = m_Q$, $\alpha_s(m_Q, f) = \alpha_s(m_Q, f + 1)$. The running of α_s is visible in the renormalization scale dependence, shown in Fig. 2(e). In the NLO $Q\overline{Q}$ production program [2, 3, 4], Λ_f is fixed by m_Q. Note that $\Lambda_3 > \Lambda_4 > \Lambda_5$. The threshold m_Q, fixed in each parton distribution set, can differ from our fitted m_Q.

While it is often possible to use a general prescription like the principle of minimal sensitivity (PMS) [15] to find values of μ_R and μ_F where the scale sensitivity is a minimum, the heavy quark production cross section has a strong μ dependence.

In Fig. 2 we show the variation of the $c\overline{c}$ and $b\overline{b}$ production cross sections at RHIC (a), (c) and LHC (b), (d) ion energies. The MRS distributions exhibit an artificial stability for low μ because for $\mu < 2m_c \approx Q_{0,\mathrm{MRS}}$. Thus the factorization scale is fixed at $Q_{0,\mathrm{MRS}}$ and only μ_R varies. We use the GRV HO parton distribution functions so that we can show the variation with $\mu = \mu_R = \mu_F$ at lower values of μ since μ_F is not fixed until $\mu_F \approx 0.4m_c \approx Q_{0,\mathrm{GRV}}$. When $\mu/m_c \approx 0.2$, the cross section diverges since $\mu/m_c \approx \Lambda_{\mathrm{QCD}}$. In any case, scales below 1 GeV are excluded because a perturbative calculation is no longer assumed to be valid. As μ/m_c increases, the cross section becomes more stable. The behavior we find is similar for RHIC and LHC energies. The $b\overline{b}$ cross section shows a smaller variation with μ, particularly at $\sqrt{s} = 200$ GeV. The dependence resembles the running of α_s shown in Fig. 1(b). Indeed, this running is a major source of instability in the NLO $Q\overline{Q}$ cross sections. For charm production at $\sqrt{s} = 5.5$ TeV the variation of the Born cross section with μ increases while $m_Q/\sqrt{s}$ decreases. The NLO results show less variation at this energy. There is no value of μ where the Born and the NLO calculations are equal, *i.e.* no obvious optimal scale, suggesting that higher-order corrections are needed for $m_Q/\sqrt{s} \ll 1$.

We show the change of the $c\overline{c}$ cross section at $\sqrt{s} = 200$ GeV induced by changing one scale with respect to the other: $\mu_R = m_Q$ in Fig. 2(e) and $\mu_F = m_Q$ in Fig. 2(f). The running of the coupling constant is clearly shown in 2(e). In 2(f), the increase with μ_F arises because at $\mu_F \approx Q_{0,\mathrm{GRV}}$ and low x, the GRV HO sea quark and gluon distributions show a valence-like behavior, decreasing as $x \rightarrow 0$ [12]. These results are different for the MRS distributions since the parton distribution functions are fixed when $\mu_F < Q_{0,\mathrm{MRS}}$. Note that taking $\mu_F \neq \mu_R$ introduces an additional parameter into the calculations. These results suggest that important uncertainties still remain in the absolute cross sections of $Q\overline{Q}$ production.

CALCULATIONS OF $\sigma_{Q\overline{Q}}^{\mathrm{tot}}$

Previous comparisons of the total charm production cross sections with leading order calculations [16] suggested that a constant K factor of ~ 2 was needed to reconcile the calculations with data when using $m_c = 1.5$ GeV, but not when $m_c = 1.2$ GeV was chosen. Initial NLO calculations seemed to suggest that the K factor was no longer needed with $m_c = 1.5$ GeV [17]. However, this result is very dependent upon the chosen scale parameters and the parton distribution functions, particularly the shape of the gluon distribution.

Comparison With Current Data

We compare our NLO calculations with the available data [18, 19, 20, 21, 22] on the total $c\overline{c}$ production cross section from pp and pA interactions in Fig. 3. When a nuclear target has been used, the cross section per nucleon is given, assuming an A^α dependence with $\alpha = 1$, supported by recent experimental studies of the A dependence [23]. We assume that we can compare the $c\overline{c}$ production cross section directly with charmed hadron measurements. Often single charmed mesons, denoted

$D/\overline{D}$ to include all charge states, in the region $x_F > 0$ are measured. The $c\overline{c}$ production cross section is symmetric around $x_F = 0$ in pp interactions so that $\sigma_{c\overline{c}}^{\rm tot} = 2\sigma_{c\overline{c}}(x_F > 0)$. While the question of how the $c\overline{c}$ pair hadronizes into $D\overline{D}$, $D\overline{\Lambda}_c$, $\Lambda_c\overline{D}$, $\Lambda_c\overline{\Lambda}_c$ *etc.* remains open, some assumptions must be made about how much of $\sigma_{c\overline{c}}^{\rm tot}$ is missing since not all channels are measured. If all single D mesons are assumed to originate from $D\overline{D}$ pairs, ignoring associated $\Lambda_c\overline{D}$ production, then by definition $\sigma(D\overline{D}) = \sigma(D/\overline{D})/2$. Thus the single D cross section for $x_F > 0$ is equal to the $D\overline{D}$ pair cross section over all x_F. However, the contribution to the $c\overline{c}$ total cross section from D_s and Λ_c production has been estimated to be $\sigma(D_s)/\sigma(D^0 + D^+) \simeq 0.2$ and $\sigma(\Lambda_c)/\sigma(D^0 + D^+) \simeq 0.3$. Thus to obtain the total $c\overline{c}$ cross section from $\sigma(D\overline{D})$, $\sigma(D\overline{D})$ should be multiplied by ≈ 1.5 [24]. This is also done in our data comparison. The data exist in the range $19 < \sqrt{s} \leq 63$ GeV, mostly from fixed target experiments. Below the ISR energies, $\sqrt{s} = 53$-63 GeV, the total cross section is primarily inferred from single D or $D\overline{D}$ measurements. At the ISR, the pair production cross section is often obtained from lepton measurements, either $e\mu$ and ee coincidence measurements or a lepton trigger in coincidence with a reconstructed D or Λ_c. Rather large $c\overline{c}$ cross sections were inferred from the latter analyses due to the assumed shape of the production cross sections: flat distributions in x_F for the Λ_c and $(1 - x_F)^3$ for the D, resulting in a large extrapolated total cross section. The ISR results must thus be taken with some care.

Modern parton distributions with $\Lambda_{\rm QCD}$ fixed by global fits cannot explain the absolute value of the total cross section in the measured energy range when using $m_c = 1.5$ GeV and $\mu_F = \mu_R = m_c$. Since $m_c^2 < Q_{0,{\rm MRS}}^2$ and the scale must be chosen so that $\mu^2 > Q_{0,{\rm MRS}}^2$ for sensible results, we take $\mu = 2m_c$ and vary m_c for the MRS distributions. We find reasonable agreement for $m_c = 1.2$ GeV for the D−′ and D0′ distributions. The results are shown in the solid and dashed curves respectively in Fig. 3. Note that the different low x behavior of these sets leads to a larger $c\overline{c}$ cross section with the D0′ distributions at these energies. Since the GRV HO distributions have a much lower initial scale, μ can be fixed to the quark mass. The dot-dashed curve is the GRV HO result with $m_c = 1.3$ GeV and $\mu = m_c$. All three curves give an equivalent description of the data with a tendency to underestimate the total cross section.

Our "fits" to the low energy data are to provide a reasonable point from which to extrapolate to higher energies. It is important to remember that significant uncertainties still exist which could change our estimates considerably when accounted for. These relatively low values of m_c effectively provide an upper bound on the charm production cross section at high energies with these scale choices. For comparison, we also show the cross section with the GRV HO distributions and $\mu = m_c = 1.5$ GeV in the dotted curve. It lies a factor of 2-3 below the other calculations. Note that such small values of m_c suggests that the bulk of the total cross section comes from invariant masses less than $2m_D$. In a recent work [24], the total cross section data was found to be in agreement with $m_c = 1.5$ GeV with some essential caveats: the factorization scale was fixed at $\mu_F \equiv 2m_c$ while μ_R was allowed to vary and an older set of parton distribution functions fits with a range of values of $\Lambda_{\rm QCD}$ was used. Decreasing μ_R with respect to μ_F and increasing $\Lambda_{\rm QCD}$ both result in a significantly larger cross section for a given m_c, as shown in Fig. 2(e). We choose to use the most up-to-date parton distribution functions and to keep $\mu_F = \mu_R$, facilitating a more direct extrapolation from the current data to the future collider results.

Since data on $c\overline{c}$ and $b\overline{b}$ production by pion beams are also available at fixed target energies, in Fig. 4 we compare this data with calculations using the same parton distributions with m_c and μ fixed from the pp comparison. The $c\overline{c}$ data [18, 25, 26, 27, 28] is based on the $x_F > 0$ single D cross section. However, the $\pi^- N$ x_F distribution is asymmetric, $\sigma(\text{all}x_F)/\sigma(x_F > 0) \sim 1.6$, so that $\sigma(D\overline{D})$ is obtained by dividing by 2 to get the pair cross section and then multiplying by 1.6 to account for the partial x_F coverage. The $b\overline{b}$ data, taken to be over all x_F, are generally obtained from multimuon studies [29, 30, 31, 32]. The data, especially for $b\overline{b}$ production, are not as extensive and have rather poor statistics. When a nuclear target was used, the cross section per nucleon is given, assuming a linear $\alpha = 1$ dependence.

The GRV HO pion distributions [33] are obtained from their proton set. In Fig. 4(a), the charm production cross section is calculated using the GRV HO proton and pion distributions. The solid curve shows the result with a nucleon target, where the nucleon distributions are the averaged proton and neutron distributions, while the dashed curve is the result for a proton target. The results are consistent for $\sqrt{s} \geq 30$ GeV; at lower energies, the cross section on a proton target is slightly larger than on a nucleon target. The calculations using the MRS D$-'$ distributions do not have the same consistency as those with GRV HO because their pion distribution functions, SMRS P1 and P2 [34], are obtained using an out-of-date set of MRS proton distributions. The SMRS distributions have $\Lambda_4 = 190$ MeV while MRS D$-'$ has $\Lambda_4 = 230$ MeV. In our calculations, we fix Λ_4 to the MRS D$-'$ value. The dot-dashed curve shows the MRS D$-'$ distributions with the SMRS P2 pion distributions while the dotted curve shows the P1 pion set. Both are calculated for a proton target. The P1 set has a steeper gluon distribution than P2. The results begin to differ as $\sqrt{s}$ increases since the gluon fusion contribution is becoming important while at low $\sqrt{s}$, valence quark annihilation dominates. Although the calculations and data again somewhat underpredict the data, we may assume that the same parameters are reasonable for both pion and proton projectiles. The comparison to the available $b\overline{b}$ production cross section data is given in Fig. 4(b). We use $m_b = 4.75$ GeV and $\mu = m_b$ for both sets of parton distributions. The solid curve shows the GRV HO results, the dashed is the MRS D$-'$ and SMRS P1 result. The agreement is not unreasonable given the quality of the data and the theoretical uncertainties.

Though our results tend to underpredict $\sigma_{c\overline{c}}^{\rm tot}$ and $\sigma_{b\overline{b}}^{\rm tot}$, we have tried to minimize the theoretical uncertainties and have found reasonable agreement. However, this underprediction should be kept in mind when extrapolating to higher energies.

Extrapolation To RHIC And LHC Energies

The total Born and NLO $Q\overline{Q}$ production cross sections at the ISR, $\sqrt{s} = 63$ GeV, and the proton and ion beam energies at RHIC and LHC are given in Table 1 for $c\overline{c}$ and 2 for $b\overline{b}$. The theoretical K factor, $\sigma_{Q\overline{Q}}^{\rm NLO}/\sigma_{Q\overline{Q}}^{\rm LO}$, tends to increase with energy and is rather large. There is no *a priori* reason why it should remain constant, rather the increase at collider energies would suggest that the perturbative expansion is becoming less reliable, as discussed below. Even though the MRS D−′ and GRV HO distributions give an equally valid description of the data at ISR energies and below, the results diverge at higher energies due to the different values of m_c and μ used. The MRS D−′ sea quark and gluon distributions grow faster at low x since $\mu_{\rm MRS} = 2\mu_{\rm GRV}$, resulting in a larger predicted cross section. Less difference is seen between the GRV HO and MRS D−′ distributions for the $b\overline{b}$ cross section since the same m_b and μ are used for both. Note that for $b\overline{b}$ production at 14 TeV, the results differ by 30% while the $c\overline{c}$ cross section is 3-5 times larger for MRS D−′ than the GRV HO at this energy. The D0′ distributions give smaller cross sections at LHC energies due to the different assumed behavior as $x \rightarrow 0$. We illustrate this effect using the Born contribution to the production cross section at fixed M and $y = 0$, approximated as

$$\frac{d\sigma}{dMdy}|_{y=0} \approx \frac{\alpha_s^2}{Ms}\left[F_g(M/\sqrt{s})\right]^2 \tag{16}$$

since gluon fusion is the dominant contribution to the Born cross section at high energy, with $x = M/\sqrt{s}$ at $y = 0$. At fixed M, σ_{gg} is proportional to $(\alpha_s^2/M^2)F_g^2$ where F_g^2 is the gluon luminosity. The gluon distribution at low x and $\mu = Q_0$ may be approximated as $F_g(x) = f(x)/x^{1+\delta}$. For a constant behavior at low x, such as in the MRS D0′ distribution, $\delta = 0$ and the cross section is independent of $\sqrt{s}$. At the other extreme, the MRS D−′ distribution assumes $\delta = 0.5$ at Q_0 so that the cross section grows as $s^\delta \sim \sqrt{s}$. Additionally, the $\mathcal{O}(\alpha_s^3)$ correction terms become large when $m/\sqrt{s} \ll 1$ for all heavy quarks. At the Born level, a quark is exchanged in the t-channel of the gg subprocess while at NLO a gluon is exchanged in the t-channel of the gg and $gq(\overline{q})$ subprocesses. The asymptotic behavior is dominated by the t-channel pole with the largest spin. This, together with the large gg and $gq(\overline{q})$ luminosities at small x, leads to large corrections. However, the perturbative expansion may still be valid if further higher-order corrections are small.

SINGLE AND DOUBLE DIFFERENTIAL DISTRIBUTIONS

In the presentation of the single inclusive and double differential distributions, we follow the prescription of Nason and collaborators [3, 4] and take $\mu_S = n\widehat{m}_Q$ for the single and $\mu_D = n\sqrt{m_Q + (p_{T_Q}^2 + p_{T_{\overline{Q}}}^2)/2}$ for the double differential distributions. When using MRS distributions for charm production, $n = 2$, in all other cases, $n = 1$. A word of caution is necessary when looking at our predictions for $Q\overline{Q}$ pair distributions. It is difficult to properly regularize the soft and collinear divergences to obtain a finite cross section over all phase space. Soft divergences cancel between real and virtual corrections when properly regularized. The collinear divergences need to be regularized and subtracted. For single inclusive heavy quark production, this is possible because the integration over the partonic recoil variables can be performed analytically and the singularities isolated.

In exclusive $Q\overline{Q}$ pair production, the cancellation of divergences is performed within the numerical integration. The price paid for this is often a negative cross section near the phase space boundaries, particularly when $p_T \longrightarrow 0$ and $\phi \longrightarrow \pi$ where ϕ is the difference in the azimuthal angle between the heavy quark and antiquark in the plane transverse to the beam axis. A positive differential cross section for $p_T \longrightarrow 0$ can only be obtained by resumming the full series of leading Sudakov logarithms corresponding to an arbitrary number of soft gluons. This has not been done for heavy quark production [4]. Thus when $m_Q/\sqrt{s} \ll 1$, fluctuations in the cross section due to incomplete numerical cancellations can become very large, resulting in negative components in the mass and rapidity distributions. The fluctuations are minimized by maximizing the event sampling at low p_T and increasing the number of iterations [35].

Comparison To Current Data

We now compare the NLO calculations with data on Q and $Q\overline{Q}$ distributions. First, we compare with the x_F and p_T^2 single D distributions at 800 GeV from the LEBC-MPS collaboration [19] in Fig. 5. The total cross section, $\sigma(D/\overline{D}) = 48 \pm 11\,\mu$b, corresponds to a $D\overline{D}$ production cross section of 24±8 μb. If the calculated total cross section agreed with the measured one, the normalization of the single distributions would be in better agreement. The solid curves are the MRS D−′ results, the dashed, the GRV HO calculations. Data on correlated $D\overline{D}$ production is also available at 800 GeV, from pEmulsion studies [36]. The event sample is rather small, only 35 correlated pairs. We compare the mass and p_T^2 of the pair and the azimuthal difference between the pair in Fig. 6 with the calculated NLO distributions. Again the solid curve shows MRS D−′, the dashed, GRV HO. The Born invariant mass distribution is parallel to the NLO results.

Single b quark p_T distributions are available from the $p\overline{p}$ colliders; UA 1, $\sqrt{s} =$ 630 GeV, and CDF, $\sqrt{s} = 1.8$ TeV. The measurements are in the central region, $|y| < 1.5$ for UA 1 and $|y| < 1$ for CDF, and are integrated over p_T above each $p_{T,\rm min}$. The comparisons with the NLO calculations are given in Fig. 7(a) for UA 1 [37] and Fig. 7(b) for CDF [38] and D0 [39]. Reasonable agreement is found for both GRV HO and MRS D−′ for UA 1 with $\mu_S = \sqrt{m_b^2 + p_T^2}$. However, the results from this same scale choice were somewhat below the early CDF data where J/ψ production was used to determine the B production cross section[¶]. As reported in Ref. [40], the scale $\mu = \mu_S/4$ was needed for good agreement with the absolute cross section when the MRS D0 distributions were used. More recent data using direct measurement of inclusive $b \rightarrow J/\psi$ and $b \rightarrow \psi'$ decays has shown that the previous results overestimated ψ production from b decays [38]. Better agreement with theory is now found for $\mu = \mu_S$, as shown in Fig. 7(b). Again the GRV HO and MRS D−′ distributions look similar, differing primarily for $p_{T,\rm min} < 10$ GeV. This difference is increased for the lower scale choice where $\mu_S/4 < Q_{0,\rm MRS}$ for $p_{T,\rm min} < 7.5$ GeV, cutting off the evolution of the MRS distributions below this $p_{T,\rm min}$. The GRV HO calculations evolve over all $p_{T,\rm min}$ since $\mu_S/4 > Q_{0,\rm GRV}$.

[¶] The inclusive decay, $B \rightarrow J/\psi X$, has a 1% branching ratio (BR) while the exclusive channel $B \rightarrow J/\psi K$ has an 0.1% branching ratio.

Extrapolation To RHIC And LHC Energies

We now show the predicted heavy quark distributions for RHIC ($\sqrt{s} = 200$ and 500 GeV) and LHC ($\sqrt{s} = 5.5$ and 14 TeV) using the MRS D−′ and GRV HO distributions in Figs. 8-15. In each figure we show the single quark p_T (a) and y (b) distributions[‖] and the p_T (c), rapidity (d), invariant mass (e), and azimuthal angle (f) distributions of the $Q\overline{Q}$ pair. The single and pair p_T distributions are also given with the rapidity cuts $y < |1|$ at the LHC and $y < |0.35|$ at RHIC, corresponding to the planned acceptances of ALICE [41] and the PHENIX central detector [9]. The bin widths have been divided out of these distributions. In general, the LO mass and rapidity distributions are nearly equivalent to the NLO results scaled by a theoretical K factor independent of M and y. When the scale runs with p_T, the single inclusive p_T distributions also exhibit a nearly constant theoretical K factor. In Tables 3-10 we give the y-integrated single p_T^2 NLO and Born distributions, the pair p_T^2 distributions with the rapidity cut, and the NLO and Born invariant mass distributions for c and b production at each energy for the MRS D−′ partons. Note that all distributions have a 2 GeV bin width and that neither it nor the rapidity bin width has been removed in the tables. The statistical uncertainties are less than 1% at low p_T^2 and M, increasing to 5-6% in the tails. The uncertainty also increases slightly with energy.

The development of a rapidity plateau can be seen in both the single and pair distributions as the energy increases. This plateau is generally broader for the single quarks than the pair since the pair mass enters into the estimate of the maximum pair rapidity while the smaller quark transverse mass fixes the maximum single quark rapidity. The plateau is broader for the MRS D−′ parton distributions. The plateau edge is artificial for charm production with the MRS partons at 14 TeV. The minimum x of the set, 10^{-5}, is reached at $y \sim 2.8$ for a single quark and a somewhat larger y for the pair. The GRV HO distributions have $x_{\rm min} = 10^{-6}$, corresponding to $y \sim 4.5$, off the scale of our graphs.

The average single quark and pair p_T increases with energy. For charmed quarks, $\langle p_T^2 \rangle$ is larger for the pair than for a single quark. The opposite result is seen for b quarks. The GRV distributions result in larger $\langle p_T^2 \rangle$ than the MRS distributions. Near $p_T \rightarrow 0$, the MRS parton distributions show a steeper slope than the GRV distributions. As p_T increases, the slopes become somewhat similar at RHIC energies.

Our predictions are less reliable at LHC energies because the expansion parameter becomes $\alpha_s \log(s/m_Q^2) \approx 1$ for $m_Q/\sqrt{s} \ll 1$, spoiling the convergence of the perturbative expansion [24]. Note that using μ_S for the single inclusive distributions and μ_D for the double differential distributions leads to a slight deviation of the integrated NLO cross sections from the results in Tables 1 and 2, calculated with $\mu = n m_Q$, since the correction terms grow with μ. The faster evolution of the parton distribution functions is partly compensated by the decrease of α_s with increasing μ.

[‖] Estimates of the single inclusive charm distributions at $\sqrt{s} = 200$ GeV and 5.5 TeV using the same code are given in Ref. [42].

$Q\overline{Q}$ Decays To Lepton Pairs

Since heavy quark decays are an important contribution to the dilepton continuum, we show $c\overline{c}$ and $b\overline{b}$ decays into dileptons at RHIC and LHC for the MRS D$-'$ sets. Because the decays are not incorporated into our double-differential calculation, the heavy quark pairs have been created from the final distributions. The decays to leptons are calculated using a Monte Carlo program based on D decays from Mark-III [43] and B decays from CLEO [44]. The inclusive branching ratio for D meson decay to leptons, averaged over charged and neutral D's, is $BR(D^0/D^+ \rightarrow l^+X) \sim 12\%$. The corresponding branching ratio for B mesons of unspecified charge is $BR(B \rightarrow l^+X) \sim 10.4\%$ [45]. B decays represent a special challenge since lepton pairs of opposite sign can be produced from the decay of a single B by $B \rightarrow DlX$ followed by $D \rightarrow lX$. Thus the $B\overline{B}$ decays can produce dileptons in several ways: two leptons from a single B, two leptons from primary B decays, two leptons from secondary decays, and a primary lepton from one B and a secondary lepton from the $\overline{B}$. The measurement of Ref. [44] is assumed to be for primary B decays to leptons. The heavy quark pair is specified according to the correlated distributions from the calculated cross section. The momentum vectors of the individual quarks are computed in the pair rest frame, using the rapidity gap between the quarks. The decays are calculated in the quark rest frame, according to the measured lepton momentum distributions, and then boosted back to the nucleon-nucleon center of mass, the lab frame for RHIC and LHC and M_{ll}, y_{ll}, and $p_{T,ll}$ are computed.

The average number of $Q\overline{Q}$ pairs at zero impact parameter, $N_{Q\overline{Q}}$, produced in a central nuclear collision is estimated by multiplying the cross section from Tables 1 and 2 by the nuclear thickness, $T_{AB}(0)$, given in the appendix. If $N_{Q\overline{Q}} < 1$, only correlated production is important. The number of correlated lepton pairs can be estimated by multiplying the number of $Q\overline{Q}$ pairs by the square of the meson, H, branching ratio to leptons: $N_{Q\overline{Q}} BR^2(H/\overline{H} \rightarrow l^{\pm}X)$. However, if $N_{Q\overline{Q}} > 1$, dilepton production from uncorrelated $Q\overline{Q}$ pairs should also be accounted for. Then two $Q\overline{Q}$ pairs are generated and the Q from one pair is decayed with the $\overline{Q}$ from the other. Thus for uncorrelated $Q\overline{Q}$ production, the average number of lepton pairs is approximately $N_{Q\overline{Q}}(N_{Q\overline{Q}} - 1)BR^2(H\overline{H} \rightarrow l^{\pm}X)$ when $N_{Q\overline{Q}} \gg 1$. If $N_{Q\overline{Q}} \approx 1$, a distribution in $N_{Q\overline{Q}}$ must be considered to calculate the uncorrelated pairs. In the following figures, we show the correlated dilepton cross section in pp collisions, $\sigma_{ll} = BR^2(H/\overline{H} \rightarrow l^{\pm}X)\sigma_{Q\overline{Q}}$.

In Fig. 16 we show the mass (a), rapidity (b), and p_T (c) distributions for the lepton pairs from $D\overline{D}$ and $B\overline{B}$ pair decays. The average mass of the lepton pairs from $D\overline{D}$ decays at RHIC ion energies is $\langle M_{ll} \rangle = 1.35$ GeV and the average lepton pair p_T, $\langle p_{T,ll} \rangle = 0.8$ GeV; from $B\overline{B}$ decays, $\langle M_{ll} \rangle = 3.17$ GeV and $\langle p_{T,ll} \rangle = 1.9$ GeV. A like-sign subtraction should eliminate most of the uncorrelated charm production at RHIC.

At LHC ion energies, the $c\overline{c}$ production cross sections are large enough for uncorrelated charm production to be substantial and difficult to subtract in nuclear collisions. The uncorrelated lepton pairs from $D\overline{D}$ decays at the LHC, shown in the dashed curves in Fig. 17 with the value of the correlated cross section since $N_{Q\overline{Q}} < 1$

in pp collisions. To find the correct scale in central AB collisions, calculate $N_{Q\overline{Q}}$ and then multiply the lepton pair cross section by $T_{AB}(0)(N_{Q\overline{Q}}-1)$. The average mass of the lepton pairs from correlated $D\overline{D}$ decays here is $\langle M_{ll}\rangle = 1.46$ GeV and the $\langle p_{T,ll}\rangle = 0.82$ GeV. When the pairs are uncorrelated, $\langle M_{ll}\rangle = 2.73$ GeV and $\langle p_{T,ll}\rangle = 1$ GeV. The average dilepton mass from uncorrelated $D\overline{D}$ pairs is larger since the rapidity gap between uncorrelated D and $\overline{D}$ mesons is larger on average than between correlated $D\overline{D}$ pairs. The $b\overline{b}$ cross section is still small enough at the LHC for uncorrelated lepton pair production from B meson decays to be small. However, the acceptance for the $B\overline{B}$ decay pairs will be larger than for charm decays since high mass lepton pairs from heavy quark decays have a large rapidity gap. When acceptance cuts are applied, at least one member of a lepton pair will have a large enough rapidity to escape undetected so that high mass pairs from heavy quark decays will have a strongly reduced acceptance. This reduction occurs at larger values of M_{ll} for $B\overline{B}$ than $D\overline{D}$ decays. ¿From $B\overline{B}$ decays, $\langle M_{ll}\rangle = 3.39$ GeV and $\langle p_{T,ll}\rangle = 2$ GeV. In Fig. 17, we show the mass (a), rapidity (b), and p_T (c) distributions for the dilepton pairs from correlated and uncorrelated $D\overline{D}$ and correlated $B\overline{B}$ pairs respectively.

SUMMARY

In this overview, we have attempted to use the theoretical state of the art to predict heavy quark production in pp collisions at RHIC and LHC energies. Although much progress has been made in the higher-order calculations of $Q\overline{Q}$ production, this is not meant to be the final word. Fragmentation and decay effects need to be incorporated into our next-to-leading order calculations. More structure function data from HERA, combined with collider data on jets and prompt photons, will produce further refined sets of parton distribution functions. Theoretical progress may allow resummation at low p_T or produce estimates of next-to-next-to-leading order corrections. New scale fixing techniques may result in a reduction of scale uncertainties. Thus, there is still room for improvement in these calculations.

Though the relative agreement with lower energy data allows us to extrapolate these results to RHIC and LHC energies, major uncertainties still exist, particularly at LHC energies. However, given our mass and scale parameters, the GRV HO and MRS D−′ parton distribution functions provide a rough upper and lower limit on the theoretical predictions. This might be useful in particular for the design of detectors and triggers at these facilities.

Acknowledgments

We gratefully acknowledge the help of M. L. Mangano and G. Ridolfi with their program package and G. Schuler and J. Smith for discussions.

References

[1] R. Vogt, B.V. Jacak, P.L. McGaughey and P.V. Ruuskanen, Phys. Rev. **D49** (1994) 3345.

[2] P. Nason, S. Dawson, and R.K. Ellis, Nucl. Phys. **B303** (1988) 607.

[3] P. Nason, S. Dawson, and R.K. Ellis, Nucl. Phys. **B327** (1989) 49.

[4] M.L. Mangano, P. Nason, and G. Ridolfi, Nucl. Phys. **B373** (1992) 295.

[5] W. Beenakker, H. Kuijf, W.L. van Neerven, and J. Smith, Phys. Rev. **D40** (1989) 54; W. Beenakker, W.L. van Neerven, R. Meng, G.A. Schuler, and J. Smith, Nucl. Phys. **B351** (1991) 507.

[6] R. Vogt and S.J. Brodsky, Nucl. Phys. **B**, in press.

[7] T. Sjöstrand, Comput. Phys. Commun. **39** (1986) 347. T. Sjöstrand and M. Bengtsson, Comput. Phys. Commun. **43** (1987) 367.

[8] M.L. Mangano, P. Nason, and G. Ridolfi, Nucl. Phys. **B405** (1993) 507.

[9] PHENIX Conceptual Design Report, 1993 (unpublished).

[10] R.K. Ellis, in *Physics at the 100 GeV Scale*, Proceedings of the 17th SLAC Summer Institute, Stanford, California, 1989, edited by E.C. Brennan (SLAC Report No. 361, Stanford, 1990).

[11] H. Plothow-Besch, Comp. Phys. Comm. **75**, (1993) 396; this volume.

[12] M. Glück, E. Reya and A. Vogt, Z. Phys. **C53** (1992) 127.

[13] A.D. Martin, W.J. Stirling and R.G. Roberts, Phys. Lett. **306B**, 145 (1993).

[14] M. Derrick *et al.*, ZEUS Collab., Phys. Lett. **B316** (1993) 515.

[15] P.M. Stevenson, Phys. Rev. **D23** (1981) 70; P.M. Stevenson and H.D. Politzer, Nucl. Phys. **B277** (1986) 758.

[16] S. Banerjee and S.N. Ganguli, Phys. Rev. **D33** (1986) 1278.

[17] G. Altarelli, M. Diemoz, G. Martinelli, and P. Nason, Nucl. Phys. **B308** (1988) 724.

[18] S.P.K. Tavernier, Rep. Prog. Phys. **50** (1987) 1439. This review contains references to all data prior to 1988, including the ISR measurements.

[19] R. Ammar *et al.*, LEBC-MPS Collab., Phys. Rev. Lett. **61** (1988) 2185.

[20] K. Kodama *et al.*, E653 Collab., Phys. Lett. **B263** (1991) 573.

[21] M. Aguilar-Benitez *et al.*, LEBC-EHS Collab., Z. Phys. **C40** (1988) 321.

[22] S. Barlag *et al.*, ACCMOR Collab., Z. Phys. **C39** (1988) 451.

[23] G.Alves et al., E769 Collab., Phys. Rev. Lett. 70 (1993) 722.

[24] S. Frixione, M.L. Mangano, P. Nason, and G. Ridolfi, Nucl. Phys. **B431** (1994) 453.

[25] M. Sarmiento *et al.*, E515 Collab., Phys. Rev. **D45** (1992) 2244.

[26] S. Barlag *et al.*, ACCMOR Collab., Z. Phys. **C49** (1991) 555.

[27] G. A. Alves *et al.*, E769 Collab., Phys. Rev. Lett. **69** (1992) 3147.

[28] K. Kodama *et al.*, E653 Collab., Phys. Lett. **B284** (1992) 461.

[29] P. Bordalo *et al.*, NA10 Collab., Z. Phys. **C39** (1988) 7.

[30] K. Kodama *et al.*, E653 Collab., Phys. Lett. **B303** (1993) 359.

[31] M.G. Catanesi *et al.*, WA78 Collab., Phys. Lett. **B231** (1989) 328.

[32] R. Jesik *et al.*, E672-E706 Collab., Fermilab-Pub-94/095-E.

[33] M. Glück, E. Reya and A. Vogt, Z. Phys. **C53** (1992) 651.

[34] P.J. Sutton, A.D. Martin, R.G. Roberts and W.J. Stirling, Phys. Rev. **D45** (1992) 2349.

[35] M.L. Mangano, private communication.

[36] K. Kodama *et al.*, E653 Collab., Phys. Lett. **B263** (1991) 579.

[37] C. Albajar *et al.*, UA1 Collab., Phys. Lett. **B256** (1991) 121.

[38] F. Abe *et al.*, CDF Collab., Fermilab-Conf-94/134-E; Fermilab-Conf-94/136-E; Fermilab-Conf-94/141-E.

[39] K. Bazizi, D0 Collab., to appear in the *Proceedings of the XXIX Rencontres de Moriond*, Méribel, France, March 1994.

[40] F. Abe *et al.*, CDF Collab., Phys. Rev. Lett. **68** (1992) 3403; **69** (1992) 3704; **71** (1993) 500, 2396, and 2537.

[41] ALICE Letter of Intent, CERN Report No. CERN/LHCC/93-16, 1993 (unpublished).

[42] I. Sarcevic and P. Valerio, Phys. Lett. **B338** (1994) 426; AZPH-TH/94-20.

[43] R.M. Baltrusaitis *et al.*, Mark-III Collab., Phys. Rev. Lett. **54** (1985) 1976.

[44] S. Behrends *et al.*, CLEO Collab., Phys. Rev. Lett. **59** (1987) 407.

[45] M. Aguilar-Benitez *et al.*, Particle Data Group, Phys. Rev. **D50** (1994) 1173.

	MRS D0′		GRV HO		MRS D−′	
$\sqrt{s}$(GeV)	$\sigma_{c\bar{c}}^{\rm LO}$ (μb)	$\sigma_{c\bar{c}}^{\rm NLO}$ (μb)	$\sigma_{c\bar{c}}^{\rm LO}$ (μb)	$\sigma_{c\bar{c}}^{\rm NLO}$ (μb)	$\sigma_{c\bar{c}}^{\rm LO}$ (μb)	$\sigma_{c\bar{c}}^{\rm NLO}$ (μb)
63	31.87	75.21	30.41	72.09	26.88	64.97
200	105	244.2	122.6	350.8	139.3	343.7
500	194.8	494	291.6	959	449.4	1138
5500	558.2	1694	1687	6742	7013	17680
14000	742.4	2323	2962	12440	16450	41770

Table 1: Total $c\bar{c}$ production cross sections at collider energies.

	MRS D0′		GRV HO		MRS D−′	
$\sqrt{s}$(GeV)	$\sigma_{b\bar{b}}^{\rm LO}$ (μb)	$\sigma_{b\bar{b}}^{\rm NLO}$ (μb)	$\sigma_{b\bar{b}}^{\rm LO}$ (μb)	$\sigma_{b\bar{b}}^{\rm NLO}$ (μb)	$\sigma_{b\bar{b}}^{\rm LO}$ (μb)	$\sigma_{b\bar{b}}^{\rm NLO}$ (μb)
63	0.0458	0.0884	0.0366	0.0684	0.0397	0.0746
200	0.981	1.82	0.818	1.51	0.796	1.47
500	4.075	8.048	4.276	8.251	3.847	7.597
5500	40.85	112	88.84	202.9	98.8	224
14000	78.46	233.9	222.9	538.4	296.8	687.5

Table 2: Total $b\bar{b}$ production cross sections at collider energies.

$c\bar{c}$ **Production** $\sqrt{s} = 200$ **GeV**

$d\sigma_c/dp_T^2$ (μb/2 GeV^2)			$d\sigma_{c\bar{c}}/dp_T^2dy$ (μb/2 GeV^2)		$d\sigma_{c\bar{c}}/dM$ (μb/2 GeV)		
p_T^2 (GeV^2)	NLO	LO	p_T^2 (GeV^2)	NLO	M (GeV)	NLO	LO
1	232.5	102.2	1	30.90			
3	37.93	15.14	3	3.916	3	172.8	76.41
5	12.37	4.589	5	1.548	5	77.05	34.18
7	5.362	1.924	7	0.8435	7	22.60	9.611
9	2.774	0.9704	9	0.4770	9	8.548	3.429
11	1.589	0.5435	11	0.3287	11	3.671	1.427
13	1.003	0.3389	13	0.2203	13	1.863	0.6871
15	0.6715	0.2206	15	0.1608	15	0.9122	0.3438
17	0.4612	0.1542	17	0.1277	17	0.5120	0.1917
19	0.3291	0.1079	19	0.0925	19	0.3154	0.1095
21	0.2399	0.0812	21	0.0786	21	0.1883	0.0651
23	0.1857	0.0602	23	0.0589	23	0.1210	0.0415
25	0.1369	0.0428	25	0.0478	25	0.0689	0.0245
27	0.1088	0.0355	27	0.0356	27	0.0520	0.0166
29	0.0864	0.0280	29	0.0350	29	0.0364	0.0105
31	0.0697	0.0225	31	0.0282	31	0.0257	0.00785
33	0.0574	0.0191	33	0.0206	33	0.0151	0.00538
35	0.0478	0.0160	35	0.0214	35	0.0111	0.00383
37	0.0400	0.0132	37	0.0160	37	0.0678	0.00222
39	0.0343	0.0111	39	0.0135	39	0.0480	0.00198

Table 3:
[The rapidity-integrated p_T^2 distribution is given for single charm (NLO and Born) and the p_T^2 distribution in the range $|y| < 0.35$ is given for $c\bar{c}$ pair production (NLO only). The tabulated results have not been corrected for the rapidity bin width. The rapidity-integrated pair mass distribution is also given. All distributions are at $\sqrt{s} = 200$ GeV and calculated with MRS D$-'$ parton distributions. Note the 2 GeV bin width for the distributions.]

$c\bar{c}$ **Production** $\sqrt{s} = 500$ **GeV**

$d\sigma_c/dp_T^2$ (μb/2 GeV^2)			$d\sigma_{c\bar{c}}/dp_T^2dy$ (μb/2 GeV^2)		$d\sigma_{c\bar{c}}/dM$ (μb/2 GeV)		
p_T^2 (GeV^2)	NLO	LO	p_T^2 (GeV^2)	NLO	M (GeV)	NLO	LO
1	739.7	332.0	1	68.64			
3	134.8	538.7	3	12.01	3	548.1	242.7
5	47.37	17.43	5	4.874	5	259.5	117.2
7	22.19	7.656	7	2.828	7	82.67	35.73
9	12.08	4.054	9	1.809	9	32.71	13.72
11	7.336	2.400	11	1.193	11	15.19	6.223
13	4.658	1.493	13	0.8440	13	7.878	3.108
15	3.281	1.041	15	0.6417	15	4.623	1.734
17	2.343	0.7234	17	0.5002	17	2.555	1.025
19	1.758	0.5370	19	0.3983	19	1.577	0.6242
21	1.328	0.3980	21	0.3345	21	1.143	0.4171
23	1.034	0.3052	23	0.2467	23	0.7373	0.2623
25	0.8118	0.2512	25	0.2098	25	0.4798	0.1905
27	0.6481	0.1950	27	0.1596	27	0.3227	0.1220
29	0.5411	0.1618	29	0.1371	29	0.2817	0.0886
31	0.4544	0.1284	31	0.1283	31	0.2028	0.0673
33	0.3600	0.0997	33	0.1137	33	0.1530	0.0472
35	0.3006	0.0897	35	0.0909	35	0.0997	0.0379
37	0.2701	0.0754	37	0.0758	37	0.0837	0.0293
39	0.2318	0.0643	39	0.0750	39	0.0627	0.0250

Table 4:

[The rapidity-integrated p_T^2 distribution is given for single charm (NLO and Born) and the p_T^2 distribution in the range $|y| < 0.35$ is given for $c\bar{c}$ pair production (NLO only). The tabulated results have not been corrected for the rapidity bin width. The rapidity-integrated pair mass distribution is also given. All distributions are at $\sqrt{s} = 500$ GeV and calculated with MRS D$-'$ parton distributions. Note the 2 GeV bin width for the distributions.]

$c\bar{c}$ **Production** $\sqrt{s} = 5.5$ **TeV**

$d\sigma_c/dp_T^2$ (μb/2 GeV^2)			$d\sigma_{c\bar{c}}/dp_T^2dy$ (μb/2 GeV^2)		$d\sigma_{c\bar{c}}/dM$ (μb/2 GeV)		
p_T^2 (GeV^2)	NLO	LO	p_T^2 (GeV^2)	NLO	M (GeV)	NLO	LO
1	10680.	5146.	1	1840.			
3	2453.	989.	3	441.5	3	7749.	3558.
5	974.8	350.1	5	196.9	5	4366.	2048.
7	502.2	166.9	7	111.3	7	1622.	709.2
9	289.8	93.10	9	75.68	9	693.7	297.5
11	186.6	57.12	11	51.60	11	351.	144.0
13	126.4	37.65	13	39.07	13	188.9	78.77
15	90.91	25.96	15	27.28	15	116.3	45.67
17	68.95	19.99	17	22.55	17	75.79	27.83
19	51.44	14.43	19	18.47	19	50.16	18.82
21	41.11	11.17	21	14.14	21	30.89	12.54
23	33.29	8.965	23	13.53	23	23.02	9.024
25	27.23	7.328	25	11.02	25	18.04	6.489
27	22.28	6.031	27	9.862	27	12.32	4.547
29	18.64	4.836	29	8.612	29	10.75	3.635
31	16.10	4.203	31	6.944	31	8.112	2.609
33	13.51	3.417	33	6.359	33	5.596	2.038
35	11.55	2.961	35	5.050	35	5.217	1.719
37	9.881	2.548	37	4.683	37	4.214	1.240
39	9.078	2.212	39	4.680	39	3.500	1.039

Table 5:

[The rapidity-integrated p_T^2 distribution is given for single charm (NLO and Born) and the p_T^2 distribution in the range $|y| < 1$ is given for $c\bar{c}$ pair production (NLO only). The tabulated results have not been corrected for the rapidity bin width. The rapidity-integrated pair mass distribution is also given. All distributions are at $\sqrt{s} = 5.5$ TeV and calculated with MRS D$-'$ parton distributions. Note the 2 GeV bin width for the distributions.]

$c\bar{c}$ Production $\sqrt{s} = 14$ TeV

$d\sigma_c/dp_T^2$ (μb/2 GeV^2)			$d\sigma_{c\bar{c}}/dp_T^2dy$ (μb/2 GeV^2)		$d\sigma_{c\bar{c}}/dM$ (μb/2 GeV)		
p_T^2 (GeV^2)	NLO	LO	p_T^2 (GeV^2)	NLO	M (GeV)	NLO	LO
1	23650.	11960.	1	4594.			
3	6067.	2473.	3	1129.	3	17250.	8046.
5	2576.	918.6	5	513.6	5	10240.	4960.
7	1368.	452.4	7	298.9	7	4119.	1840.
9	838.8	256.5	9	195.3	9	1875.	820.2
11	545.2	162.7	11	143.4	11	986.3	413.9
13	371.4	108.3	13	103.9	13	554.6	232.4
15	273.5	78.46	15	78.28	15	337.7	137.8
17	206.6	55.28	17	60.18	17	226.5	88.37
19	162.1	45.82	19	51.11	19	162.	57.77
21	130.4	33.90	21	40.63	21	107.4	41.12
23	102.5	26.90	23	34.76	23	71.90	28.14
25	84.26	22.64	25	28.13	25	59.46	21.23
27	70.85	18.27	27	24.60	27	38.62	15.25
29	60.26	15.58	29	21.12	29	30.19	12.05
31	51.43	13.08	31	17.05	31	25.45	8.619
33	45.92	11.02	33	17.66	33	22.84	6.839
35	40.26	9.718	35	16.21	35	15.55	5.642
37	33.92	7.860	37	12.86	37	13.24	4.484
39	29.80	7.281	39	10.61	39	11.64	3.454

Table 6:

[The rapidity-integrated p_T^2 distribution is given for single charm (NLO and Born) and the p_T^2 distribution in the range $|y| < 1$ is given for $c\bar{c}$ pair production (NLO only). The tabulated results have not been corrected for the rapidity bin width. The rapidity-integrated pair mass distribution is also given. All distributions are at $\sqrt{s} = 14$ TeV and calculated with MRS D$-'$ parton distributions. Note the 2 GeV bin width for the distributions.]

$b\bar{b}$ Production $\sqrt{s} = 200$ GeV

$d\sigma_b/dp_T^2$ (μb/2 GeV^2)			$d\sigma_{b\bar{b}}/dp_T^2dy$ (μb/2 GeV^2)		$d\sigma_{b\bar{b}}/dM$ (μb/2 GeV)		
p_T^2 (GeV^2)	NLO	LO	p_T^2 (GeV^2)	NLO	M (GeV)	NLO	LO
1	0.2201	0.1123	1	0.2073			
3	0.1704	0.0883	3	0.0524			
5	0.1558	0.0680	5	0.0263			
7	0.1064	0.0541	7	0.0170			
9	0.1035	0.0577	9	0.0118	9	0.0463	0.0320
11	0.0863	0.0406	11	0.00814	11	0.4363	0.2100
13	0.0605	0.0343	13	0.00660	13	0.3184	0.1640
15	0.0478	0.0255	15	0.00441	15	0.1987	0.1050
17	0.0458	0.0264	17	0.00341	17	0.1225	0.0637
19	0.0351	0.0190	19	0.00311	19	0.0753	0.0400
21	0.0359	0.0186	21	0.00274	21	0.0492	0.0249
23	0.0300	0.0139	23	0.00237	23	0.0318	0.0160
25	0.0244	0.0122	25	0.00201	25	0.0214	0.0104
27	0.0216	0.0116	27	0.00183	27	0.0145	0.00688
29	0.0202	0.0103	29	0.00156	29	0.0091	0.00466
31	0.0171	0.0080	31	0.00147	31	0.0069	0.00321
33	0.0159	0.0083	33	0.00121	33	0.0047	0.00215
35	0.0125	0.0054	35	0.00111	35	0.0032	0.00154
37	0.0101	0.0055	37	0.00111	37	0.0022	0.00108
39	0.0097	0.0049	39	0.00086	39	0.0016	0.00075

Table 7:
[The rapidity-integrated p_T^2 distribution is given for single b quarks(NLO and Born) and the p_T^2 distribution in the range $|y| < 0.35$ is given for $b\bar{b}$ pair production (NLO only). The tabulated results have not been corrected for the rapidity bin width. The rapidity-integrated pair mass distribution is also given. All distributions are at $\sqrt{s} = 200$ GeV and calculated with MRS D$-'$ parton distributions. Note the 2 GeV bin width for the distributions.]

$b\bar{b}$ Production $\sqrt{s} = 500$ GeV

$d\sigma_b/dp_T^2$ (μb/2 GeV^2)			$d\sigma_{b\bar{b}}/dp_T^2dy$ (μb/2 GeV^2)		$d\sigma_{b\bar{b}}/dM$ (μb/2 GeV)		
p_T^2 (GeV^2)	NLO	LO	p_T^2 (GeV^2)	NLO	M (GeV)	NLO	LO
1	0.9809	0.4798	1	0.3427			
3	0.7911	0.4024	3	0.2503			
5	0.6490	0.3362	5	0.1260			
7	0.5492	0.2801	7	0.0818			
9	0.4528	0.2358	9	0.0558	9	0.2652	0.1199
11	0.3807	0.1987	11	0.0426	11	1.737	0.8711
13	0.3256	0.1688	13	0.0341	13	1.436	0.7552
15	0.2781	0.1433	15	0.0285	15	0.9909	0.5222
17	0.2428	0.1248	17	0.0235	17	0.6646	0.3503
19	0.2068	0.1057	19	0.0197	19	0.4547	0.2356
21	0.1824	0.0932	21	0.0169	21	0.3132	0.1612
23	0.1595	0.0811	23	0.0147	23	0.2183	0.1121
25	0.1429	0.0719	25	0.0133	25	0.1566	0.0797
27	0.1240	0.0622	27	0.0122	27	0.1126	0.0578
29	0.1108	0.0557	29	0.0109	29	0.0850	0.0419
31	0.0984	0.0492	31	0.0098	31	0.0640	0.0315
33	0.0898	0.0435	33	0.0085	33	0.0469	0.0236
35	0.0789	0.0387	35	0.0076	35	0.0367	0.0179
37	0.0716	0.0350	37	0.0071	37	0.0291	0.0138
39	0.0646	0.0319	39	0.0074	39	0.0220	0.0108

Table 8:

[The rapidity-integrated p_T^2 distribution is given for single b quarks(NLO and Born) and the p_T^2 distribution in the range $|y| < 0.35$ is given for $b\bar{b}$ pair production (NLO only). The tabulated results have not been corrected for the rapidity bin width. The rapidity-integrated pair mass distribution is also given. All distributions are at $\sqrt{s} = 500$ GeV and calculated with MRS D−′ parton distributions. Note the 2 GeV bin width for the distributions.]

$b\bar{b}$ Production $\sqrt{s} = 5.5$ TeV

$d\sigma_b/dp_T^2$ (μb/2 GeV^2)			$d\sigma_{b\bar{b}}/dp_T^2dy$ (μb/2 GeV^2)		$d\sigma_{b\bar{b}}/dM$ (μb/2 GeV)		
p_T^2 (GeV^2)	NLO	LO	p_T^2 (GeV^2)	NLO	M (GeV)	NLO	LO
1	23.59	11.22	1	-2.366			
3	19.38	9.650	3	12.80			
5	16.25	8.253	5	6.634			
7	13.84	7.028	7	4.424			
9	11.83	6.065	9	3.303	9	6.102	2.498
11	10.14	5.148	11	2.496	11	42.57	19.58
13	8.916	4.469	13	1.946	13	37.41	18.51
15	7.776	3.890	15	1.726	15	27.66	13.89
17	6.883	3.424	17	1.439	17	20.00	9.930
19	6.132	3.004	19	1.199	19	14.41	7.187
21	5.436	2.650	21	1.073	21	10.53	5.190
23	4.825	2.296	23	0.9512	23	8.007	3.863
25	4.357	2.098	25	0.8151	25	6.028	2.911
27	3.959	1.875	27	0.7535	27	4.583	2.202
29	3.545	1.666	29	0.6718	29	3.577	1.721
31	3.208	1.526	31	0.5796	31	2.879	1.342
33	2.950	1.367	33	0.5276	33	2.248	1.078
35	2.683	1.207	35	0.5491	35	1.813	0.8730
37	2.468	1.131	37	0.4692	37	1.507	0.7100
39	2.255	1.034	39	0.4334	39	1.261	0.5682

Table 9:

[The rapidity-integrated p_T^2 distribution is given for single b quarks(NLO and Born) and the p_T^2 distribution in the range $|y| < 1$ is given for $b\bar{b}$ pair production (NLO only). The tabulated results have not been corrected for the rapidity bin width. The rapidity-integrated pair mass distribution is also given. All distributions are at $\sqrt{s} = 5.5$ TeV and calculated with MRS D$-'$ parton distributions. Note the 2 GeV bin width for the distributions.]

$b\bar{b}$ Production $\sqrt{s} = 14$ TeV

$d\sigma_b/dp_T^2$ (μb/2 GeV^2)			$d\sigma_{b\bar{b}}/dp_T^2 dy$ (μb/2 GeV^2)		$d\sigma_{b\bar{b}}/dM$ (μb/2 GeV)		
p_T^2 (GeV^2)	NLO	LO	p_T^2 (GeV^2)	NLO	M (GeV)	NLO	LO
1	68.43	32.54	1	-13.36			
3	56.73	28.24	3	34.99			
5	47.74	24.25	5	17.94			
7	41.32	20.92	7	11.83			
9	35.45	18.10	9	8.519	9	17.57	6.876
11	30.61	15.55	11	6.833	11	124.0	55.90
13	27.07	13.60	13	5.537	13	112.4	54.74
15	23.97	11.93	15	4.665	15	85.11	42.17
17	21.22	10.41	17	3.813	17	62.92	30.97
19	18.86	9.192	19	3.392	19	46.41	22.58
21	16.84	8.225	21	3.125	21	34.27	16.62
23	15.20	7.227	23	2.618	23	26.12	12.44
25	13.71	6.477	25	2.328	25	19.89	9.457
27	12.61	5.878	27	2.112	27	15.51	7.304
29	11.20	5.215	29	1.772	29	11.93	5.673
31	10.43	4.710	31	1.811	31	9.610	4.538
33	9.520	4.368	33	1.588	33	7.908	3.587
35	8.651	3.962	35	1.409	35	6.267	2.966
37	7.795	3.492	37	1.349	37	5.132	2.402
39	7.272	3.245	39	1.279	39	4.323	2.017

Table 10:

[The rapidity-integrated p_T^2 distribution is given for single b quarks(NLO and Born) and the p_T^2 distribution in the range $|y| < 1$ is given for $b\bar{b}$ pair production (NLO only). The tabulated results have not been corrected for the rapidity bin width. The rapidity-integrated pair mass distribution is also given. All distributions are at $\sqrt{s} = 14$ TeV and calculated with MRS D$-'$ parton distributions. Note the 2 GeV bin width for the distributions.]

Figure Captions

Fig. 1. (a) Gluon distributions from GRV HO (solid), MRS D0′ (dashed), MRS D−′ (dot-dashed) at $Q = 2.4$ GeV and GRV HO (dotted) at $Q = 1.2$ GeV. (b) The running of the coupling constant with scale.

Fig. 2. Investigation of uncertainties in the total cross section as a function of scale. Variation of the $c\bar{c}$ production cross sections with scale at (a) RHIC and (b) LHC. Variation of the $b\bar{b}$ production cross sections with scale at (c) RHIC and (d) LHC. Variation of the $c\bar{c}$ production cross sections at $\sqrt{s}$ at 200 GeV with μ_R at fixed μ_F (e) and with μ_F at fixed μ_R (b). In each case, the circles represent the NLO calculation, the crosses, the Born calculation.

Fig. 3. Total charm production cross sections from pp and pA measurements [18, 19, 20, 21, 22] compared to calculations. The curves are: MRS D−′ $m_c = 1.2$ GeV, $\mu = 2m_c$ (solid); MRS D0′ $m_c = 1.2$ GeV, $\mu = 2m_c$ (dashed); GRV HO $m_c = 1.3$ GeV, $\mu = m_c$ (dot-dashed); GRV HO $m_c = 1.5$ GeV, $\mu = m_c$ (dotted).

Fig. 4. (a) Total charm production cross sections from $\pi^- p$ measurements [18, 25, 26, 27, 28] compared to calculations. The curves are: GRV HO $m_c = 1.3$ GeV, $\mu = m_c$ on a nucleon (solid) and proton target (dashed); MRS D−′ $m_c = 1.2$ GeV, $\mu = 2m_c$ with SMRS P2 (dot-dashed) and SMRS P1 (dotted) on a proton target. (b) The $b\bar{b}$ production cross section from $\pi^- p$ interactions [29, 30, 31, 32]. The calculations use $m_b = 4.75$ GeV and $\mu = m_b$. The curves use GRV HO (solid) and MRS D-′ with SMRS P1 (dashed).

Fig. 5. Comparison with D meson (a) p_T^2 and (b) x_F distributions at 800 GeV [19]. The NLO calculations are with MRS D−′ (solid) and GRV HO (dashed) parton distributions.

Fig. 6. Comparison with $D\overline{D}$ production for (a) p_T^2 and (b) M and (c) ϕ at 800 GeV [36]. The NLO calculations are with MRS D−′ (solid) and GRV HO (dashed) parton distributions.

Fig. 7. Comparison with b quark production cross sections at (a) UA1 [37] and (b) CDF [38]. The NLO calculations are with MRS D−′ (solid) and GRV HO (dashed) parton distributions.

Fig. 8. The NLO predictions for c and $c\bar{c}$ production at $\sqrt{s} = 200$ GeV with MRS D−′ (solid) and GRV HO (dashed) parton distributions. The single inclusive c quark p_T and rapidity distributions are shown in (a) and (b) respectively. The $c\bar{c}$ pair distributions are shown in (c)-(f). The p_T and p_{T_p} distributions have a central rapidity cut with the rapidity bin widths divided out.

Fig. 9. The same as in Fig. 8 for c and $c\bar{c}$ production at $\sqrt{s} = 500$ GeV.

Fig. 10. The same as in Fig. 8 for c and $c\bar{c}$ production at $\sqrt{s} = 5.5$ TeV.

Fig. 11. The same as in Fig. 8 for c and $c\bar{c}$ production at $\sqrt{s} = 14$ TeV.

Fig. 12. The same as in Fig. 8 for b and $b\bar{b}$ production at $\sqrt{s} = 200$ GeV.

Fig. 13. The same as in Fig. 8 for b and $b\bar{b}$ production at $\sqrt{s} = 500$ GeV.

Fig. 14. The same as in Fig. 8 for b and $b\bar{b}$ production at $\sqrt{s} = 5.5$ TeV.

Fig. 15. The same as in Fig. 8 for b and $b\bar{b}$ production at $\sqrt{s} = 14$ TeV.

Fig. 16. Dilepton (a) mass, (b) rapidity, and (c) p_T distributions at $\sqrt{s} = 200$ GeV from $c\bar{c}$ decays (solid) and $b\bar{b}$ decays (dashed, scaled by a factor of 100) calculated using MRS D−′ distributions are shown.

Fig. 17. Dilepton distributions at $\sqrt{s} = 5.5$ TeV from correlated $c\bar{c}$ decays (solid), uncorrelated $c\bar{c}$ decays (dashed), and $b\bar{b}$ decays (dot-dashed, scaled by a factor of 10).

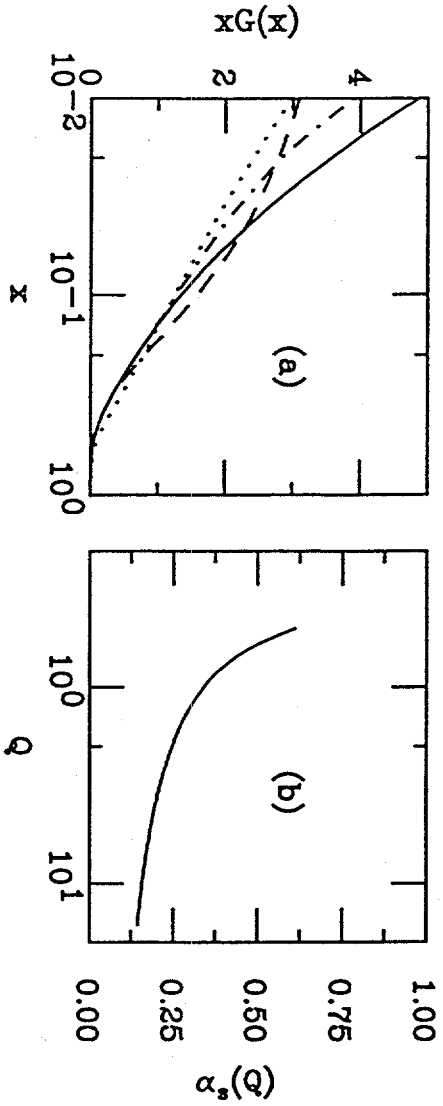

Figure 1

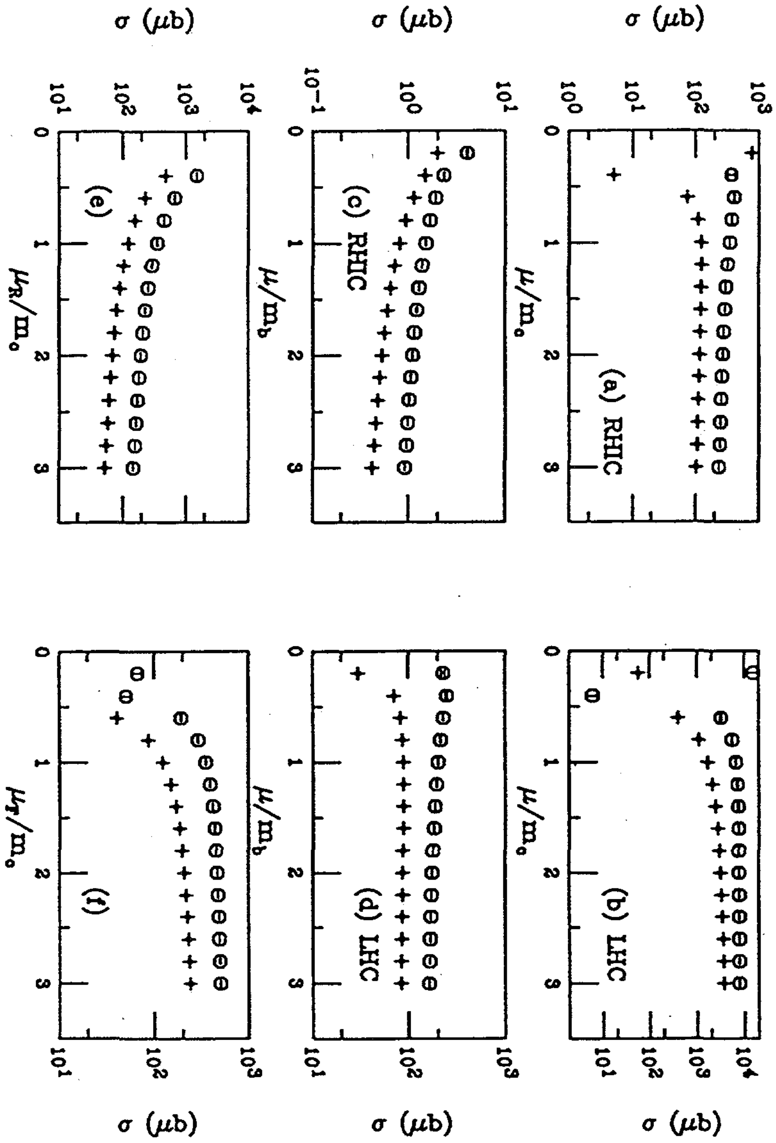
(a) RHIC
(b) LHC
(c) RHIC
(d) LHC
(e)
(f)
σ (μb)
μ/m_c
μ/m_b
μ_R/m_c
μ_F/m_c
0
1
2
3
10^{-1}
10^0
10^1
10^2
10^3
10^4

Figure 2

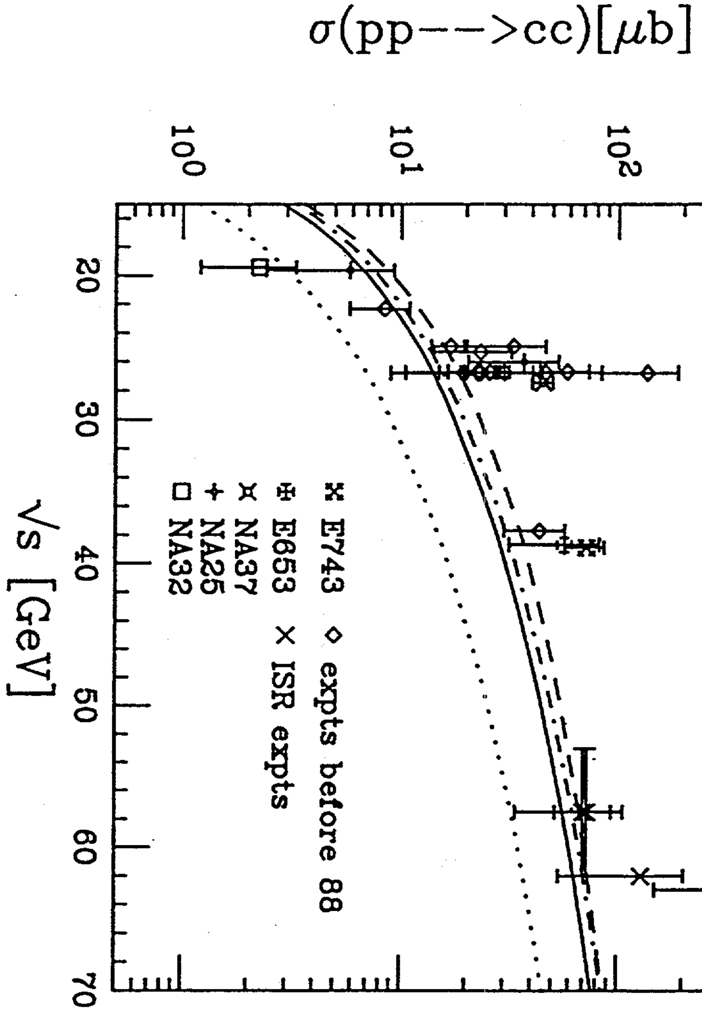
σ(pp-->cc)[μb]
10^0
10^1
10^2
10^3
20
30
40
50
60
70
√s [GeV]
E743
◇ expts before 88
E653
× ISR expts
NA37
NA25
NA32

Figure 3

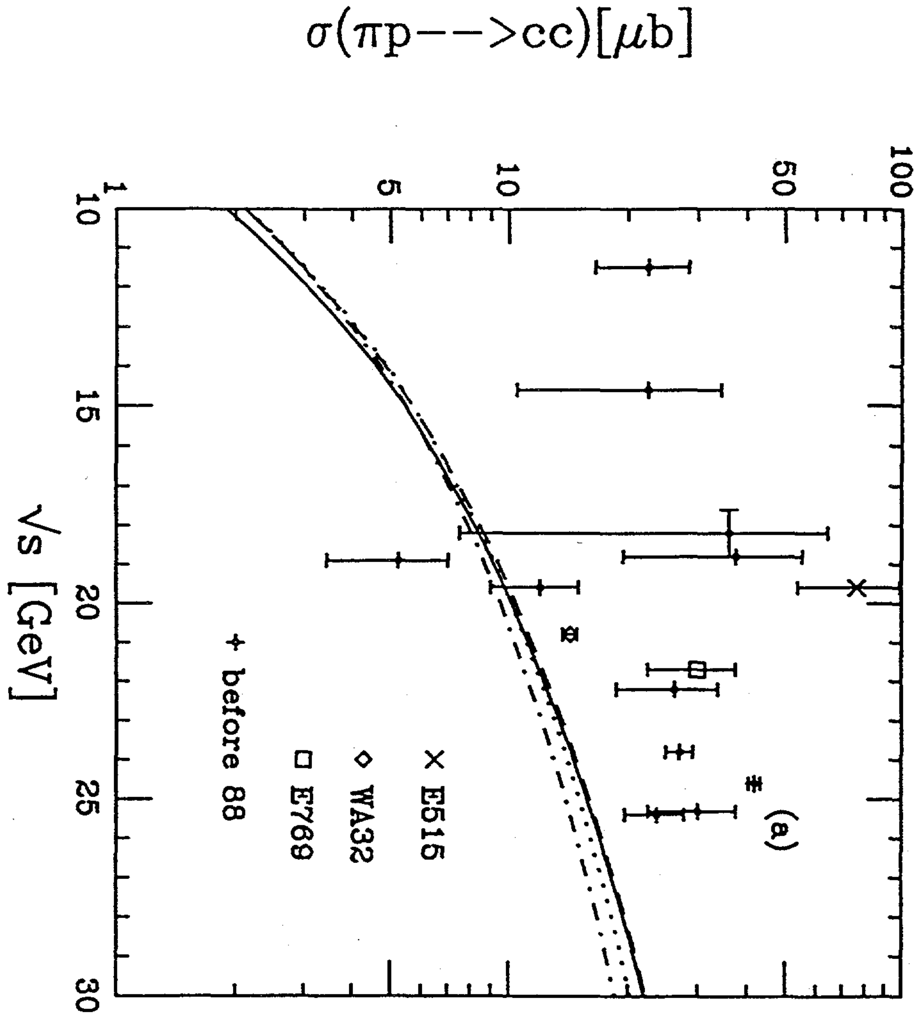
σ(πp-->cc)[μb]
100
50
10
5
1
10
15
20
25
30
√s [GeV]
(a)
× E515
◇ WA32
□ E769
+ before 88

Figure 4(a)

4b

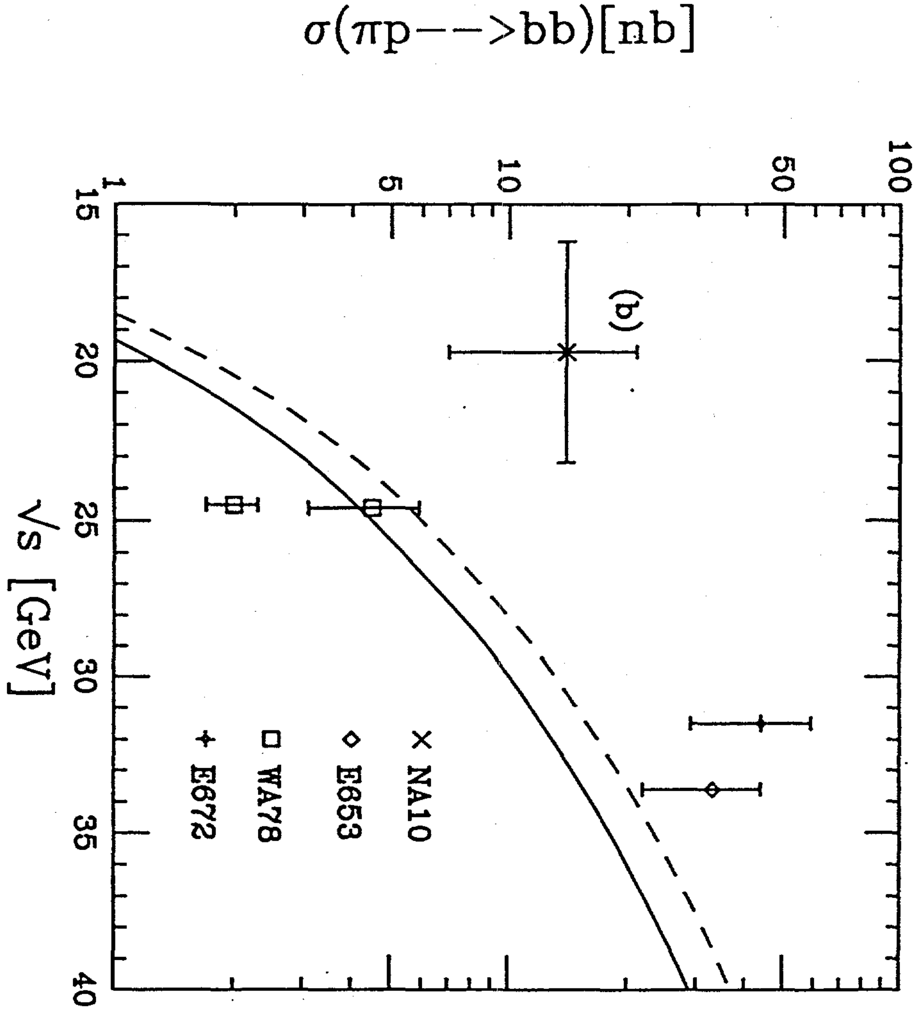

Figure 4(b)

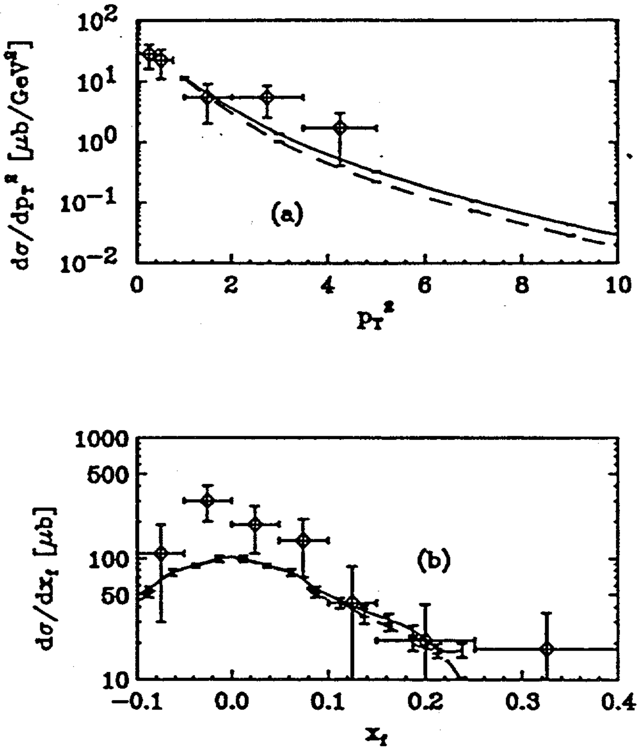
10^2
10^1
10^0
10^{-1}
10^{-2}
$d\sigma/dp_T{}^2$ [μb/GeV^2]
(a)
0
2
4
6
8
10
$p_T{}^2$
1000
500
100
50
10
$d\sigma/dx_f$ [μb]
(b)
−0.1
0.0
0.1
0.2
0.3
0.4
x_f

Figure 5

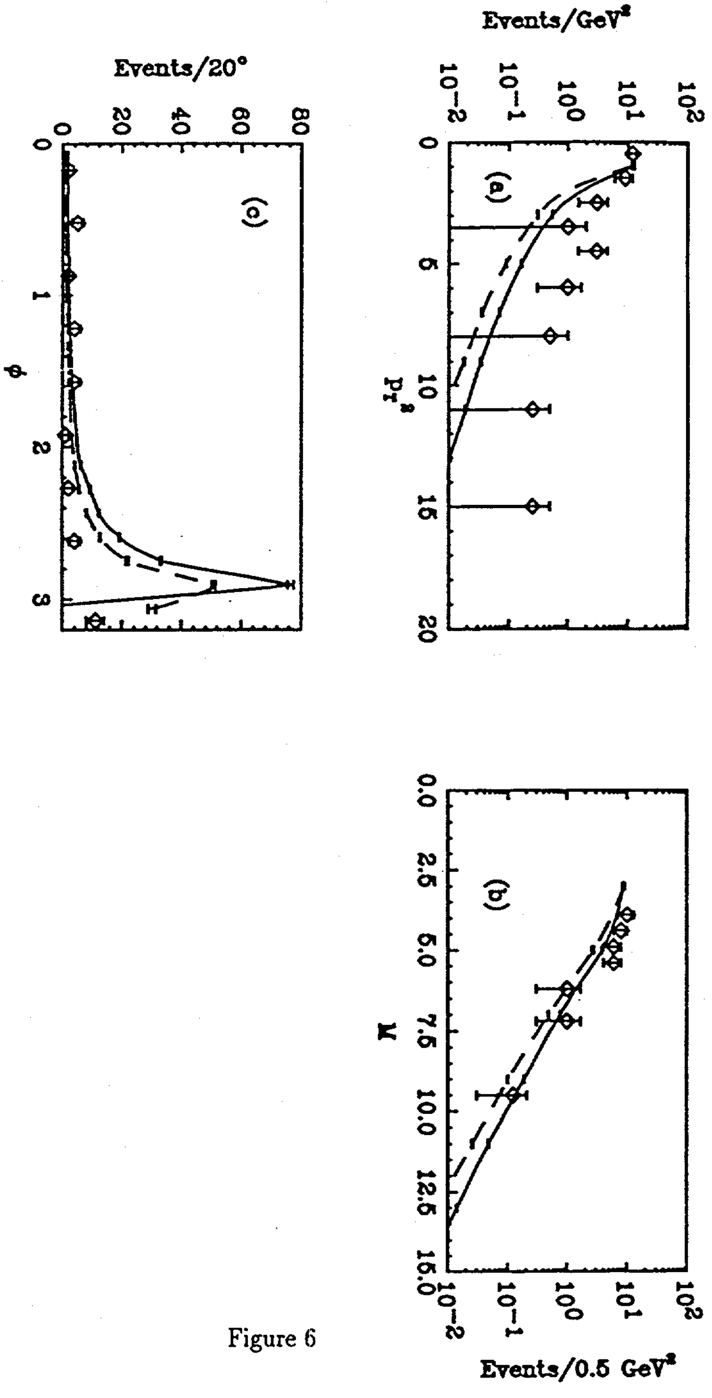
Events/GeV²
10²
10¹
10⁰
10⁻¹
10⁻²
(a)
0
5
10
15
20
P_T²
(b)
0.0
2.5
5.0
7.5
10.0
12.5
15.0
M
Events/0.5 GeV²
(c)
0
1
2
3
φ
Events/20°
0
20
40
60
80

Figure 6

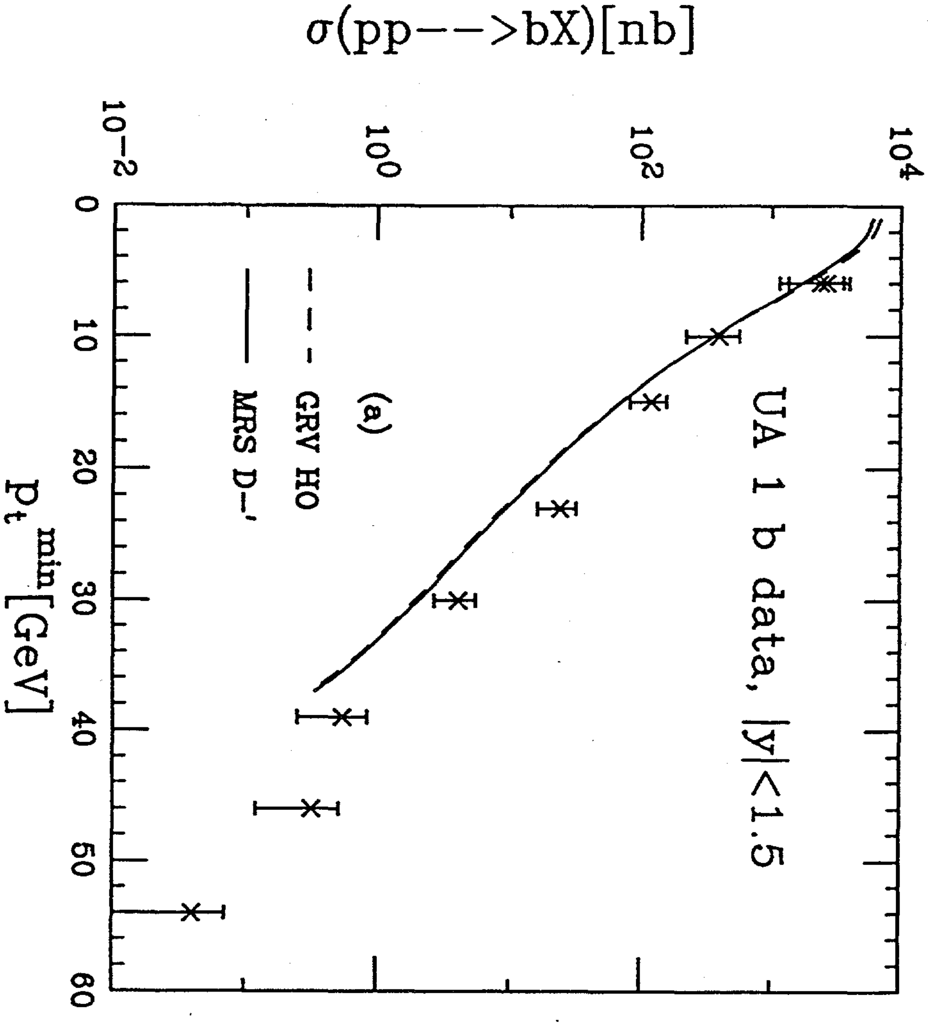
σ(pp-->bX)[nb]
10^4
10^2
10^0
10^{-2}
0
10
20
30
40
50
60
P_t^{min}[GeV]
UA 1 b data, |y|<1.5
(a)
GRV HO
MRS D-'

Figure 7(a)

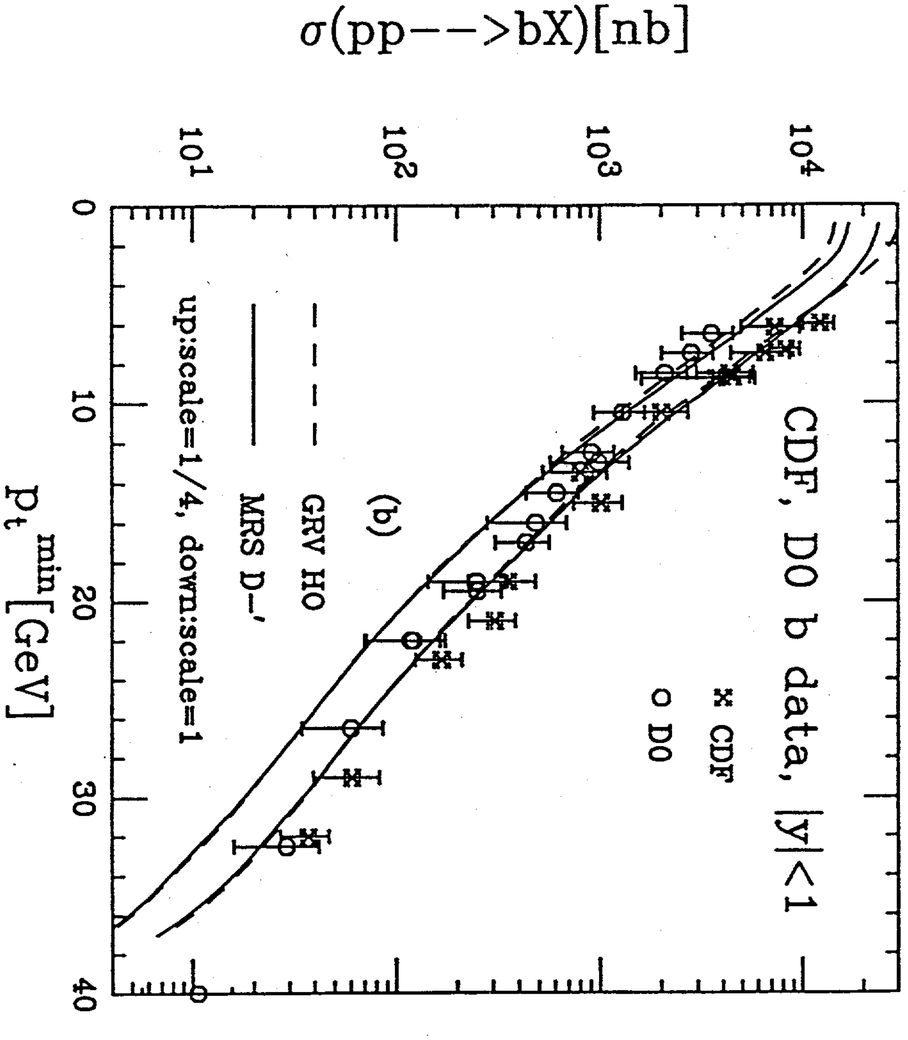
σ(pp-->bX)[nb]
10^1
10^2
10^3
10^4
0
10
20
30
40
P_t^{min}[GeV]
CDF, D0 b data, |y|<1
x CDF
o D0
(b)
GRV HO
MRS D-'
up:scale=1/4, down:scale=1

Figure 7(b)

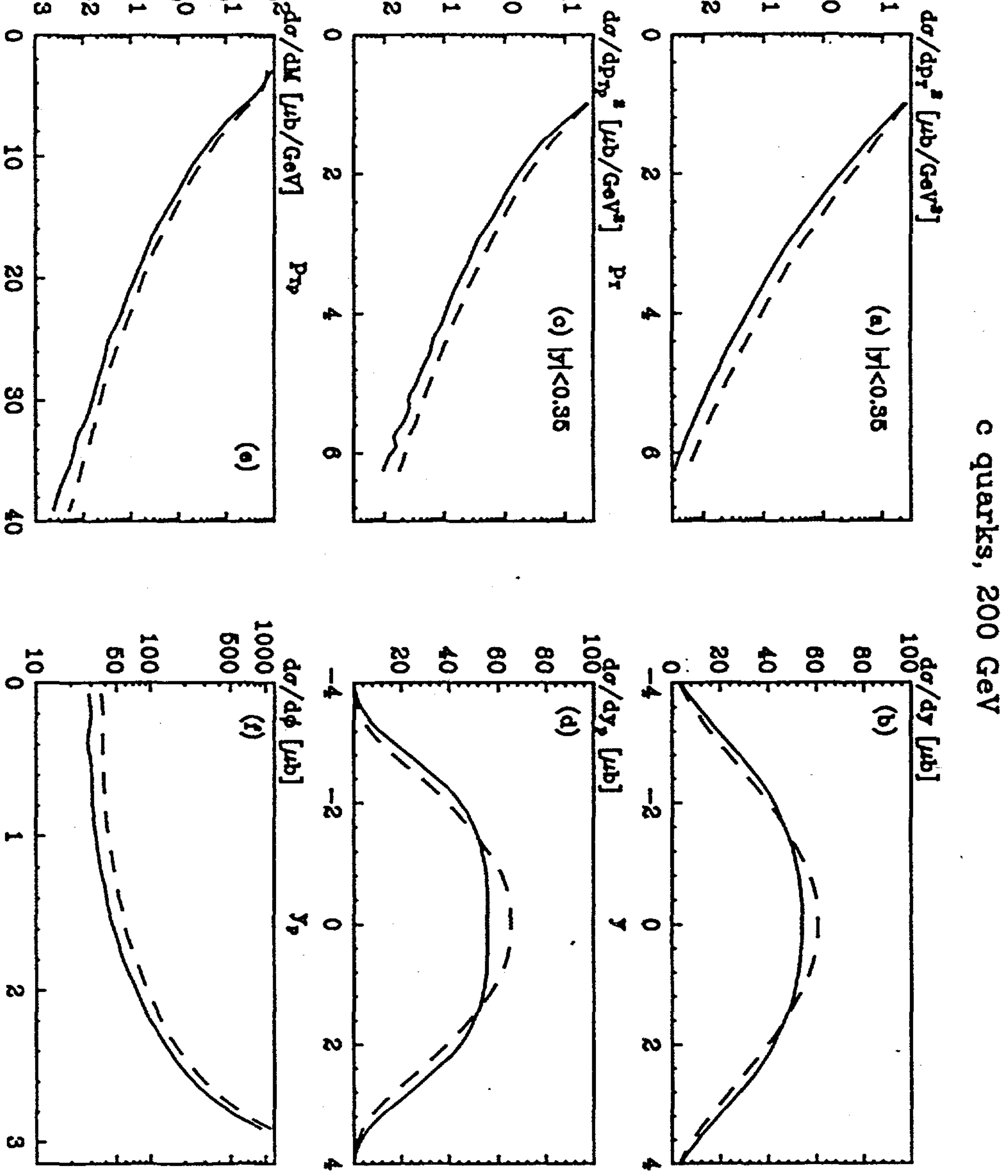
c quarks, 200 GeV
dσ/dp_T^2 [μb/GeV^2]
(a) |y|<0.35
p_T
dσ/dy [μb]
(b)
y
dσ/dp_Tp^2 [μb/GeV^2]
(c) |y|<0.35
p_Tp
dσ/dy_p [μb]
(d)
y_p
dσ/dM [μb/GeV]
(e)
M
dσ/dφ [μb]
(f)
φ

Figure 8

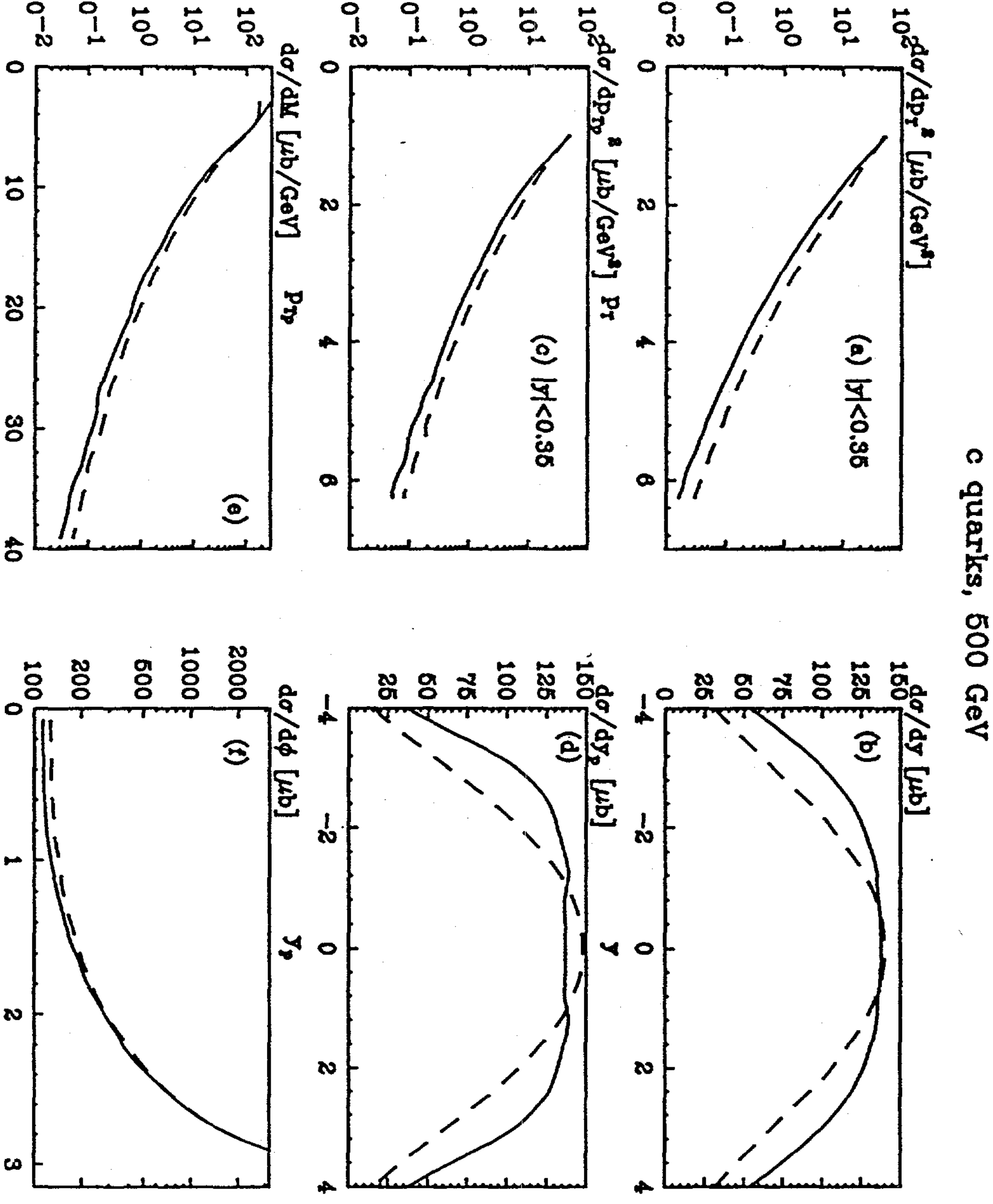
c quarks, 500 GeV
(a) |y|<0.35
dσ/dp_T² [μb/GeV²]
p_T
10²
10¹
10⁰
10⁻¹
10⁻²
0
2
4
6
(b)
dσ/dy [μb]
y
150
125
100
75
50
25
0
-4
-2
0
2
4
(c) |y|<0.35
dσ/dp_Tp² [μb/GeV²]
p_Tp
(d)
dσ/dy_p [μb]
y_p
(e)
dσ/dM [μb/GeV]
M
10
20
30
40
(f)
dσ/dφ [μb]
φ
100
200
500
1000
2000
1
3

Figure 9

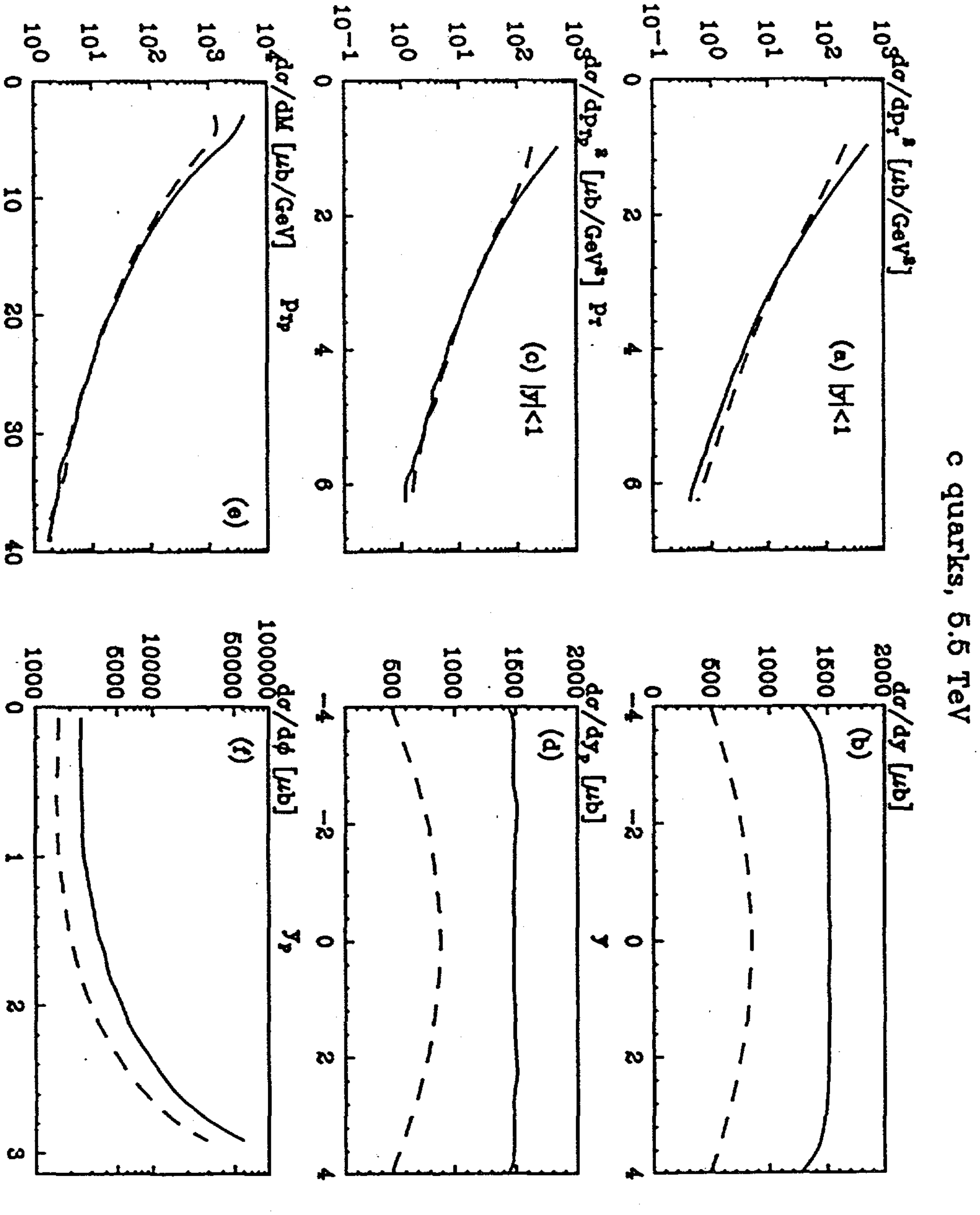
c quarks, 5.5 TeV
dσ/dp_T^2 [μb/GeV^2]
(a) |y|<1
p_T
10^3
10^2
10^1
10^0
10^-1
0
2
4
6
dσ/dy [μb]
(b)
y
2000
1500
1000
500
0
-4
-2
0
2
4
dσ/dp_Tp^2 [μb/GeV^2]
(c) |y|<1
p_Tp
dσ/dy_p [μb]
(d)
y_p
dσ/dM [μb/GeV]
(e)
M
10^4
10^3
10^2
10^1
10^0
0
10
20
30
40
dσ/dφ [μb]
(f)
φ
100000
50000
10000
5000
1000
0
1
2
3

Figure 10

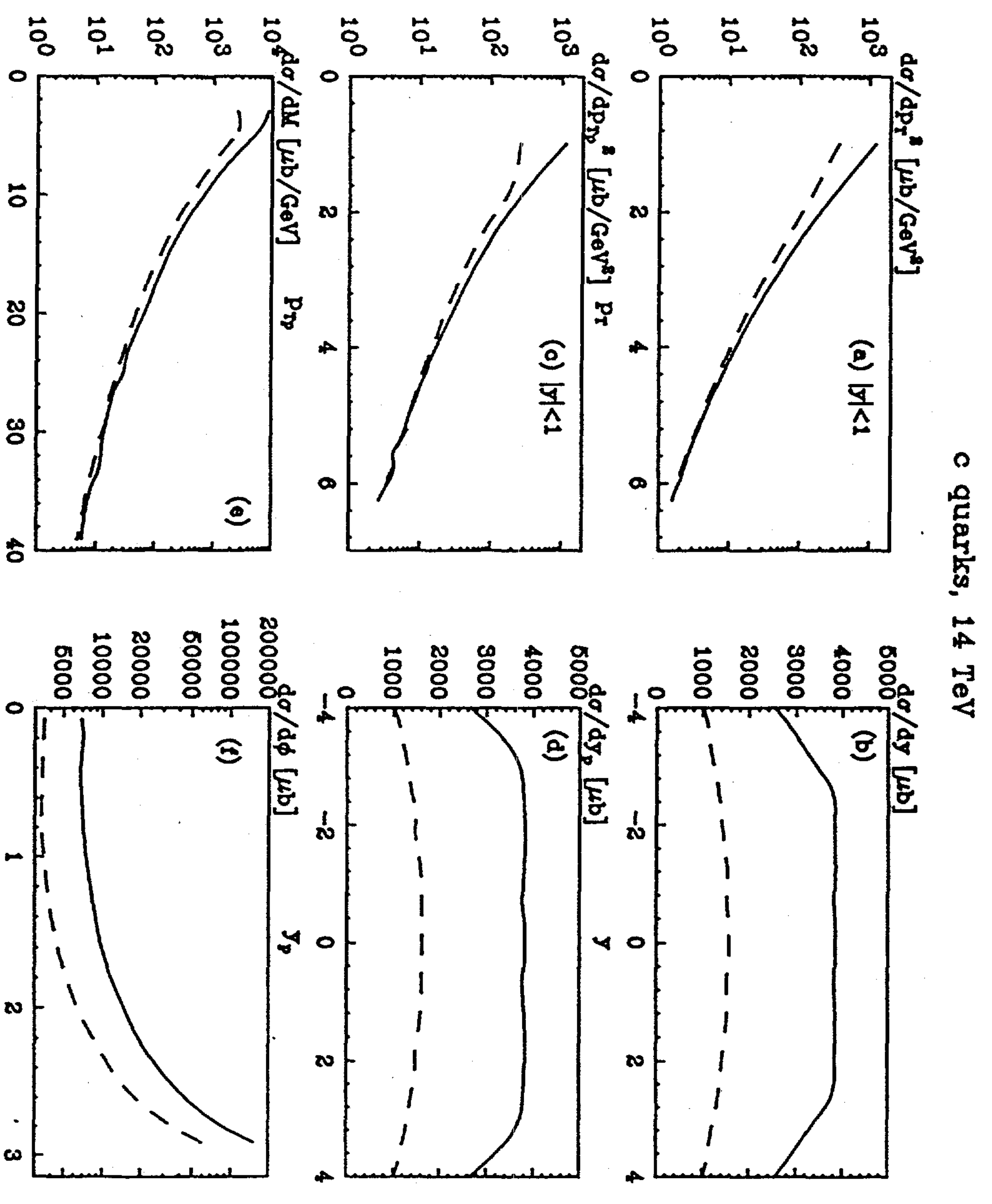
c quarks, 14 TeV
dσ/dp_T^2 [μb/GeV^2]
(a) |y|<1
p_T
dσ/dp_{Tp}^2 [μb/GeV^2]
(c) |y|<1
p_{Tp}
dσ/dM [μb/GeV]
(e)
M
dσ/dy [μb]
(b)
y
dσ/dy_p [μb]
(d)
y_p
dσ/dφ [μb]
(f)
φ
10^0
10^1
10^2
10^3
10^4
0
2
4
6
10
20
30
40
1000
2000
3000
4000
5000
-4
-2
0
2
4
5000
10000
20000
50000
100000
200000
1
3

Figure 11

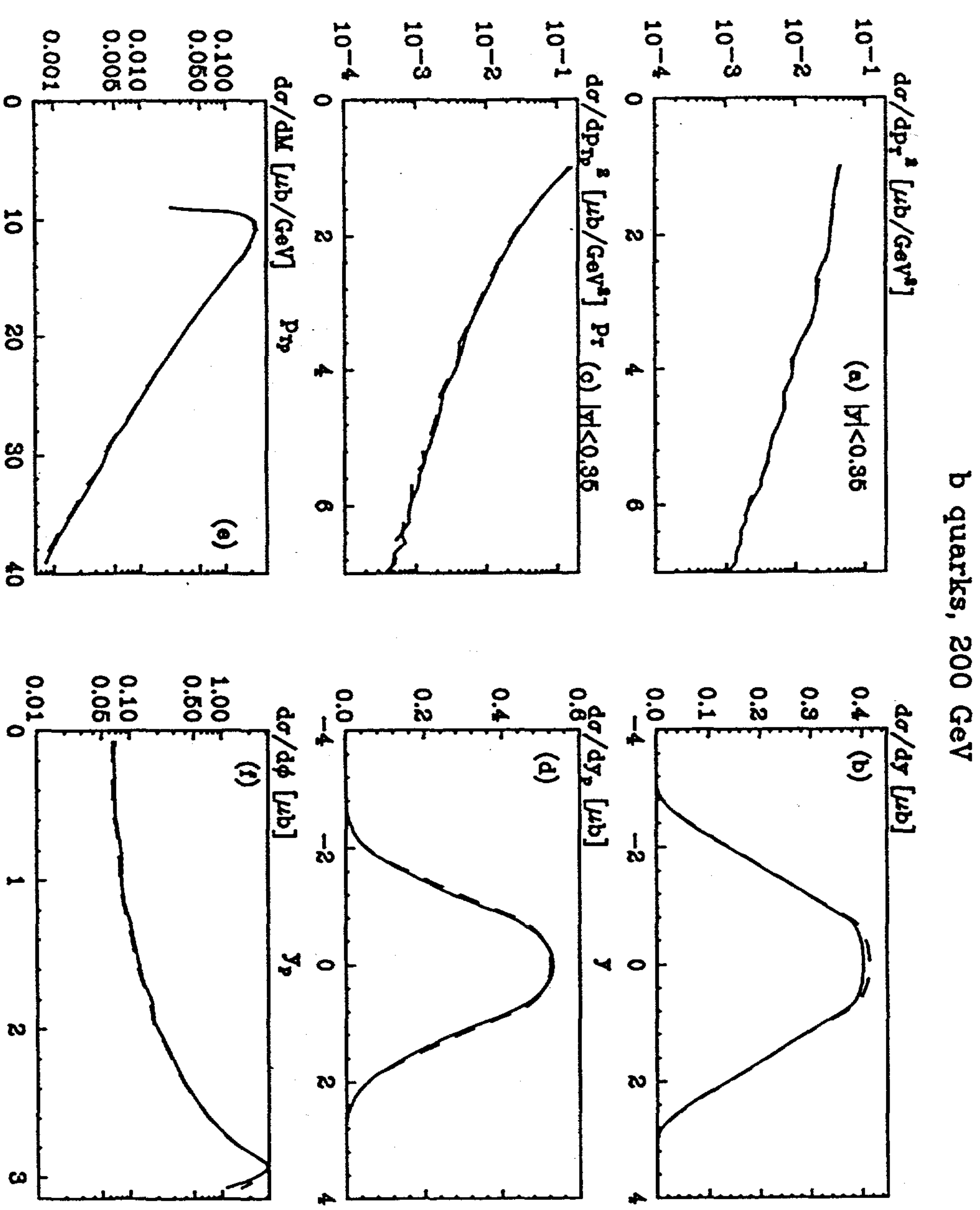
b quarks, 200 GeV
dσ/dp_T^2 [μb/GeV^2]
(a) |y|<0.35
10^-1
10^-2
10^-3
10^-4
0
2
4
6
p_T
dσ/dy [μb]
(b)
0.4
0.3
0.2
0.1
0.0
-4
-2
0
2
4
y
dσ/dp_Tp^2 [μb/GeV^2]
(c) |y|<0.35
10^-1
10^-2
10^-3
10^-4
0
2
4
6
p_Tp
dσ/dy_p [μb]
(d)
0.6
0.4
0.2
0.0
-4
-2
0
2
4
y_p
dσ/dM [μb/GeV]
(e)
0.100
0.050
0.010
0.005
0.001
0
10
20
30
40
M
dσ/dφ [μb]
(f)
1.00
0.50
0.10
0.05
0.01
0
1
2
3
φ

Figure 12

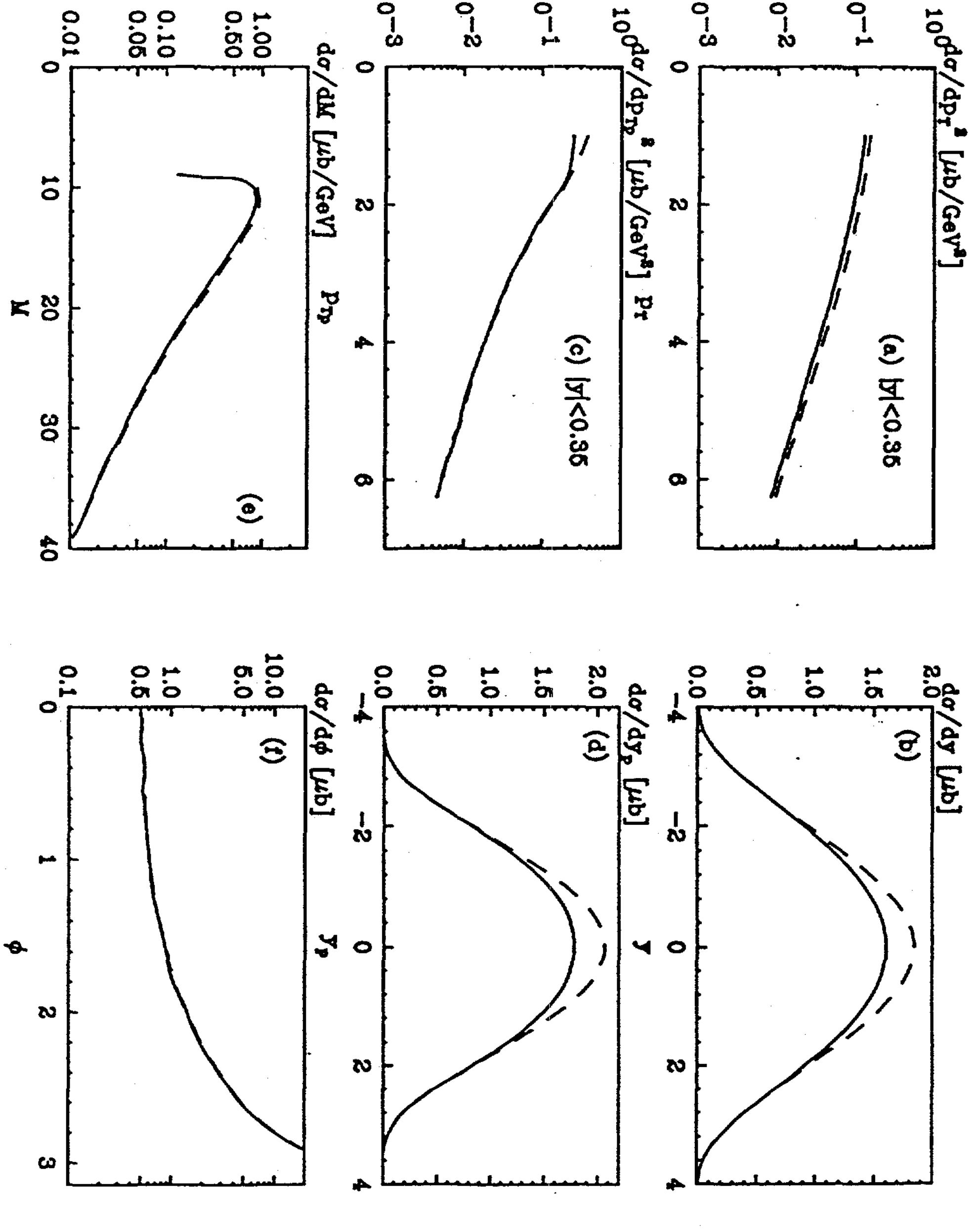
b quarks, 500 GeV
(a) |y|<0.35
$d\sigma/dp_T{}^2$ [μb/GeV²]
p_T
(b)
$d\sigma/dy$ [μb]
y
(c) |y|<0.35
$d\sigma/dp_{T_P}{}^2$ [μb/GeV²]
p_{T_P}
(d)
$d\sigma/dy_p$ [μb]
y_p
(e)
$d\sigma/dM$ [μb/GeV]
M
(f)
$d\sigma/d\phi$ [μb]
φ
10^0
10^{-1}
10^{-2}
10^{-3}
0
2
4
6
0.0
0.5
1.0
1.5
2.0
−4
−2
0
2
4
0.01
0.05
0.10
0.50
1.00
10
20
30
40
0.1
0.5
1.0
5.0
10.0
1
2
3

Figure 13

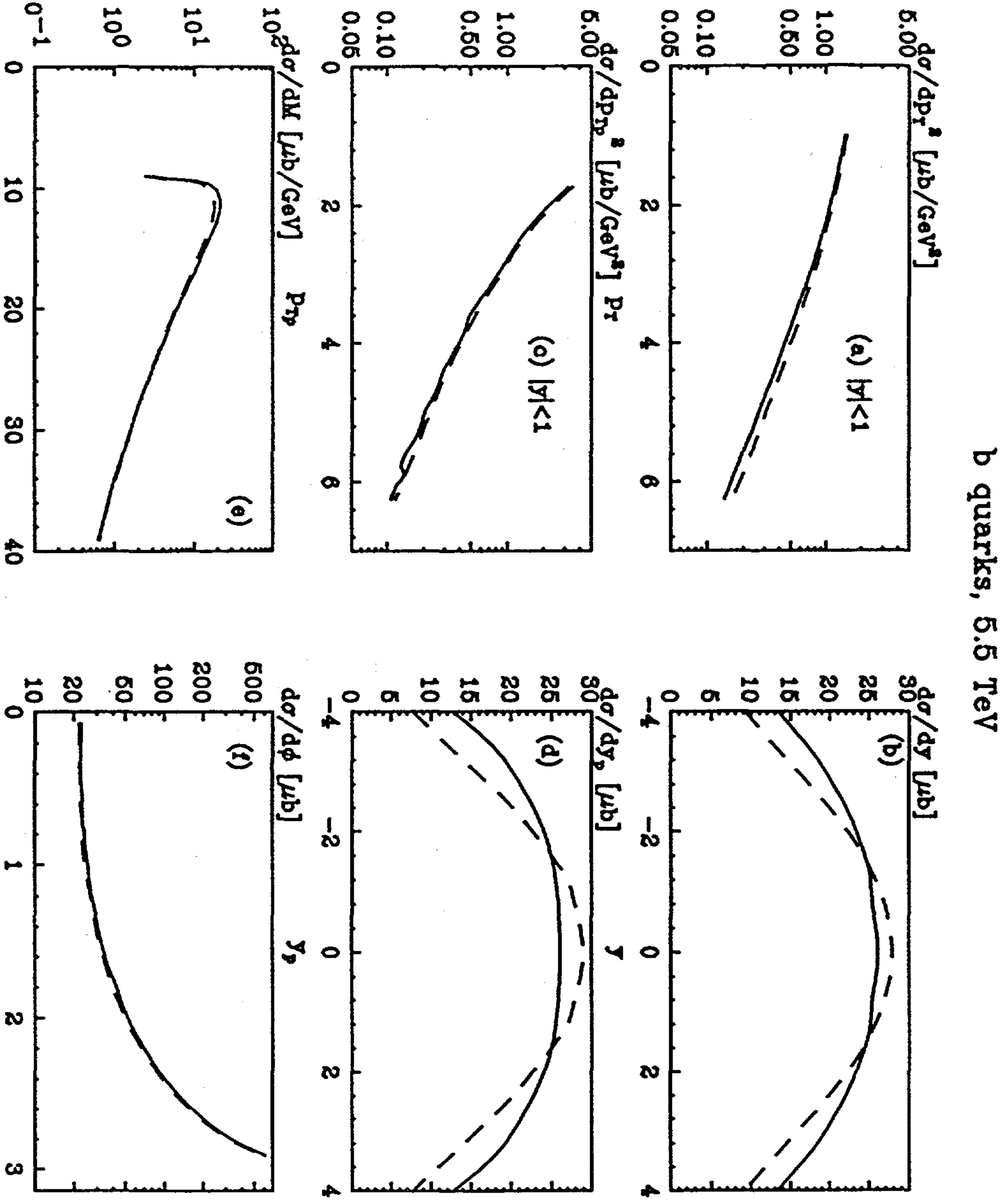
b quarks, 5.5 TeV
dσ/dp_T^2 [μb/GeV^2]
(a) |y|<1
p_T
dσ/dy [μb]
(b)
y
dσ/dp_{Tp}^2 [μb/GeV^2]
(c) |y|<1
p_{Tp}
dσ/dy_p [μb]
(d)
y_p
dσ/dM [μb/GeV]
(e)
M
dσ/dφ [μb]
(f)
φ
5.00
1.00
0.50
0.10
0.05
0
2
4
6
10^2
10^1
10^0
10^-1
10
20
30
40
5
15
25
-4
-2
500
200
100
50
1
3

Figure 14

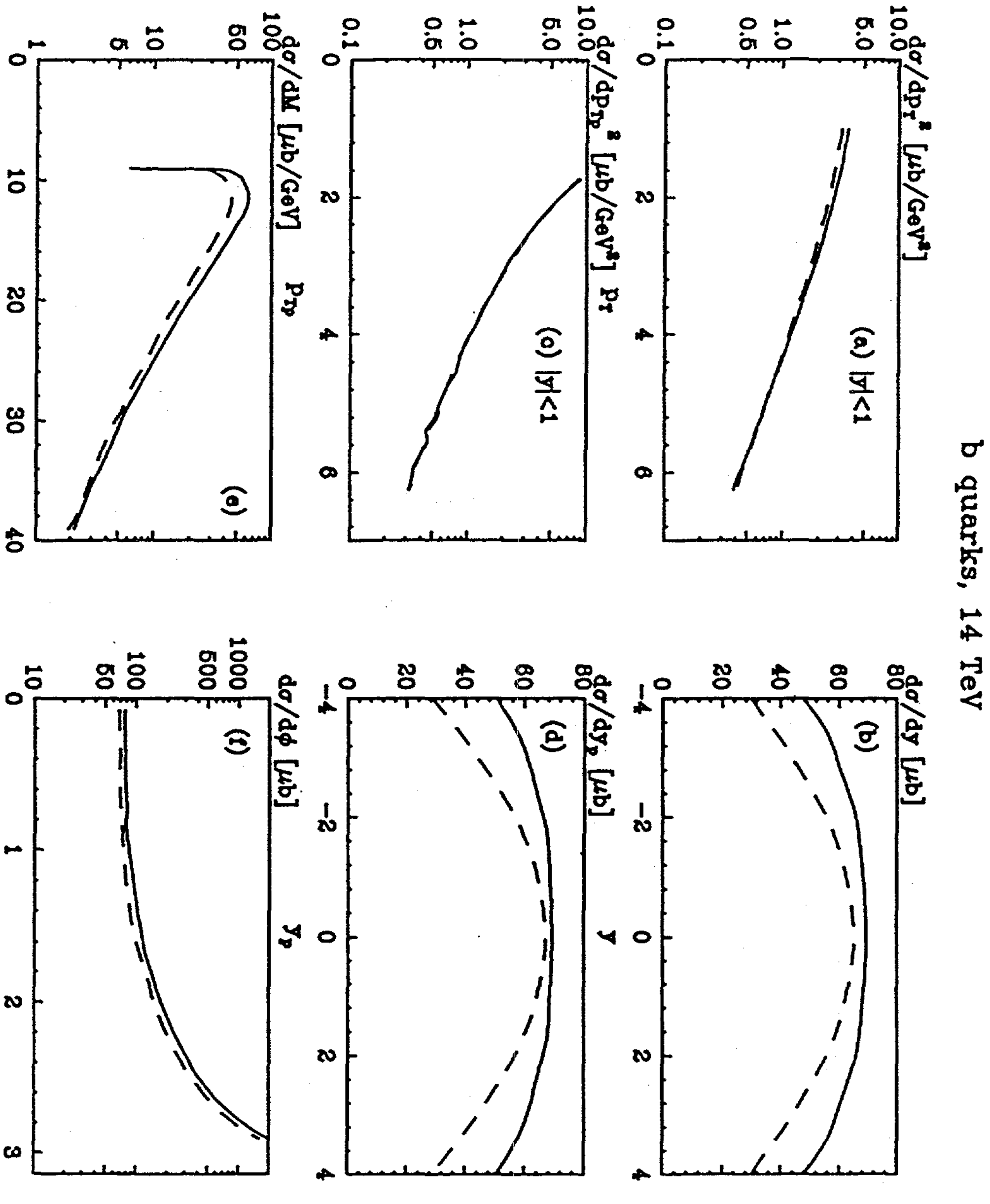
b quarks, 14 TeV
dσ/dp_T^2 [μb/GeV^2]
(a) |y|<1
p_T
dσ/dy [μb]
(b)
y
dσ/dp_{T_P}^2 [μb/GeV^2]
(c) |y|<1
p_{T_P}
dσ/dy_P [μb]
(d)
y_P
dσ/dM [μb/GeV]
(e)
M
dσ/dφ [μb]
(f)
φ
10.0
5.0
1.0
0.5
0.1
80
60
40
20
0
100
60
10
5
1
1000
500
100
50
10
0
2
4
6
10
20
30
40
-4
-2
0
2
4
1
3

Figure 15

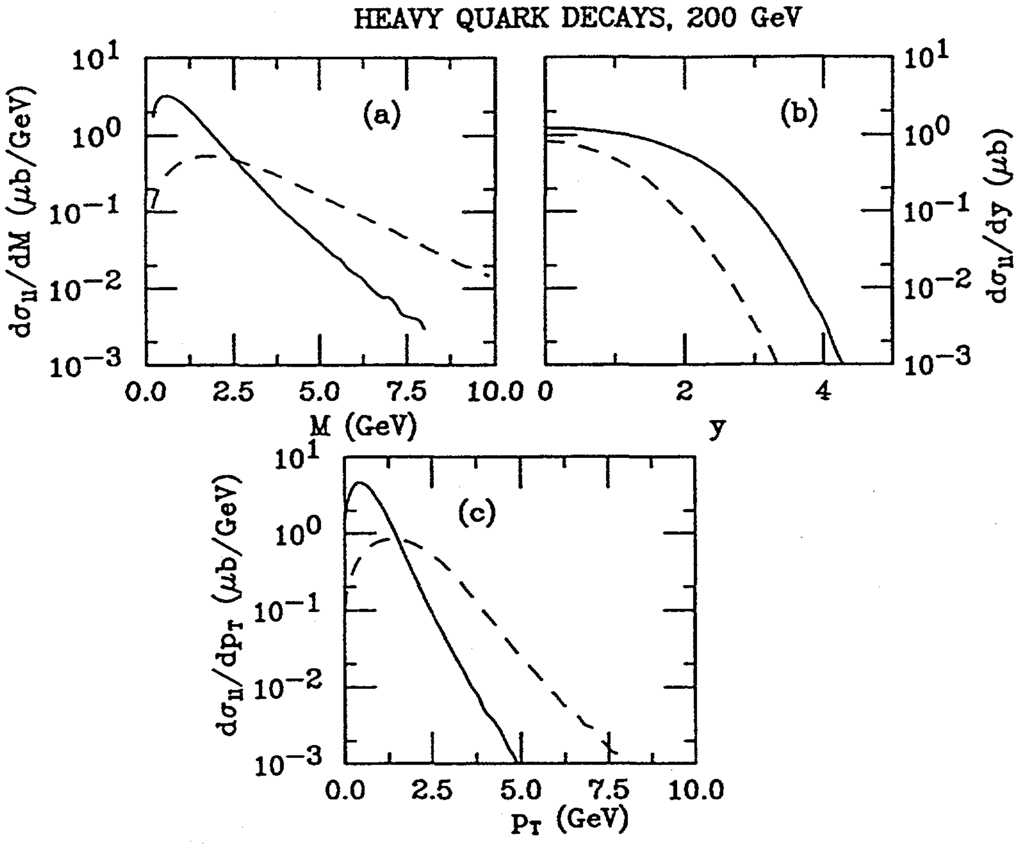
HEAVY QUARK DECAYS, 200 GeV
(a)
(b)
(c)
10^1
10^0
10^{-1}
10^{-2}
10^{-3}
$d\sigma_{ll}/dM$ (μb/GeV)
0.0
2.5
5.0
7.5
10.0
M (GeV)
0
2
4
y
$d\sigma_{ll}/dy$ (μb)
$d\sigma_{ll}/dp_T$ (μb/GeV)
p_T (GeV)

Figure 16

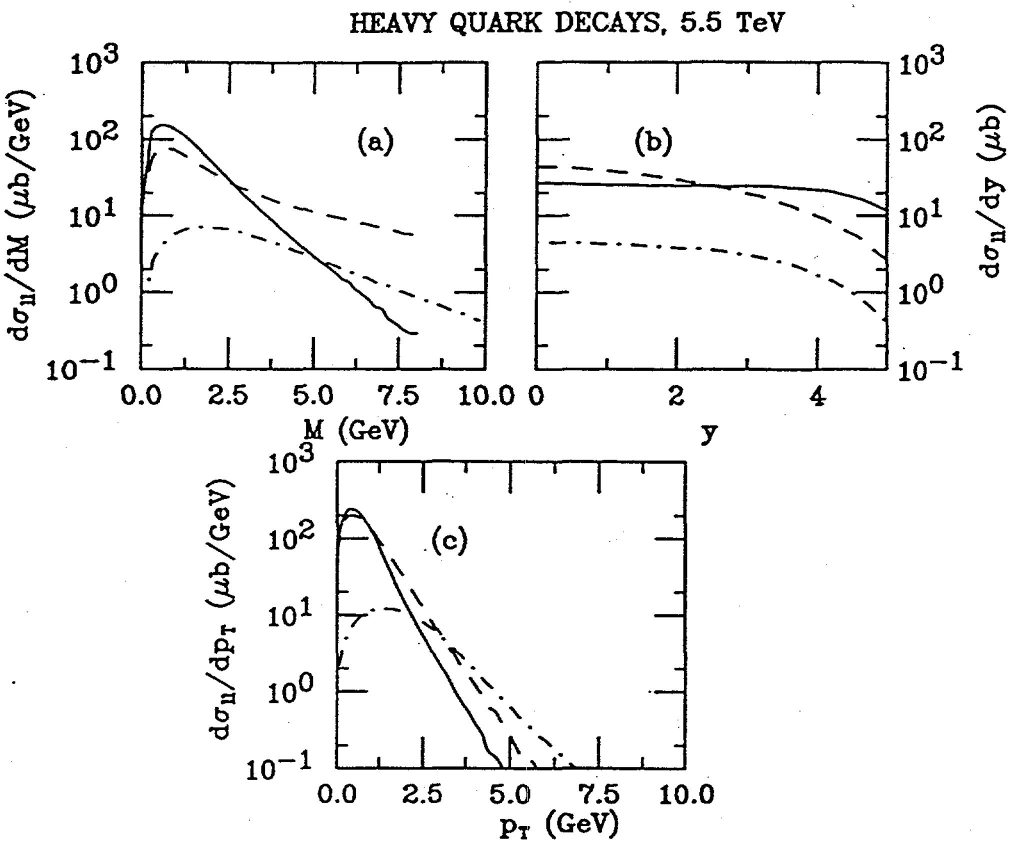
HEAVY QUARK DECAYS, 5.5 TeV
(a)
(b)
(c)
$d\sigma_{ll}/dM$ (μb/GeV)
$d\sigma_{ll}/dy$ (μb)
$d\sigma_{ll}/dp_T$ (μb/GeV)
10^3
10^2
10^1
10^0
10^{-1}
0.0
2.5
5.0
7.5
10.0
M (GeV)
0
2
4
y
p_T (GeV)

Figure 17

QUARKONIUM PRODUCTION IN HADRONIC COLLISIONS

R. GAVAI[a], D. KHARZEEV[b,c], H. SATZ[b,c]
G. A. SCHULER[b], K. SRIDHAR[b], R. VOGT[d]

[a] *Tata Institute of Fundamental Research*
Bombay 400 005, India
[b] *Theory Division, CERN*
CH-1211 Geneva 23, Switzerland
[c] *Fakultät für Physik, Universität Bielefeld*
D-33501 Bielefeld, Germany
[d] *Nuclear Science Division, LBL, University of California*
Berkeley CA 94720, USA

Abstract

We summarize the theoretical description of charmonium and bottonium production in hadronic collisions and compare it to the available data from hadron-nucleon interactions. With the parameters of the theory established by these data, we obtain predictions for quarkonium production at RHIC and LHC energies.

The production of quarkonium states below the open charm/bottom thresholds presents a particular challenge to QCD. Because of the relatively large quark masses, $c\bar{c}$ and $b\bar{b}$ production should be perturbatively calculable. However, the subsequent transition from the predominantly colour octet $Q\bar{Q}$ pairs to physical quarkonium states can introduce nonperturbative aspects. These may lead to some model-dependence, requiring cross checks with as much data as possible.

A generalisation of the colour evaporation model [1, 2, 3, 4, 5] provides a unified approach to the production of the different quarkonium states below the open charm (bottom) thresholds. As a specific example, we consider charmonium production, although all arguments apply to bottonium production as well. Parton-parton interactions lead to the production of $c\bar{c}$ pairs, as shown in Fig. 1. We calculate the total "hidden" charm cross section, $\tilde{\sigma}_{c\bar{c}}$, by integrating over the $c\bar{c}$ pair mass from $2m_c$ to $2m_D$. At high energy, the dominant production mechanism is gluon fusion (Fig. 1a), so that

$$\tilde{\sigma}_{c\bar{c}}(s) = \int_{4m_c^2}^{4m_D^2} d\hat{s} \int dx_1 dx_2 \; g(x_1) \; g(x_2) \; \sigma(\hat{s}) \; \delta(\hat{s} - x_1 x_2 s), \tag{1}$$

with $g(x)$ denoting the gluon density and σ the $gg \to c\bar{c}$ cross section. In pion-nucleon collisions, there are also significant quark-antiquark contributions (Fig. 1b), which become dominant at low energies. Subsequently, the $c\bar{c}$ pair neutralizes its colour by interaction with the collision-induced colour field ("colour evaporation"). During this process, the c and the $\bar{c}$ either combine with light quarks to produce charmed mesons, or they bind with each other to form a charmonium state. More than half of the subthreshold cross section $\tilde{\sigma}_{c\bar{c}}$ in fact goes into open charm production (assuming $m_c \lesssim 1.5$ GeV); the additional energy needed to produce charmed hadrons is obtained (in general nonperturbatively) from the colour field in the interaction region. The yield of all charmonium states below the $D\bar{D}$ threshold is thus only a part of the total sub-threshold cross section: in this aspect the model we consider is a generalisation of the original colour evaporation model [1, 5], which neglected the contribution of $\tilde{\sigma}_{c\bar{c}}$ to open charm production. Using duality arguments, it equated $\tilde{\sigma}_{c\bar{c}}$ to the sum over the charmonium states below the $D\bar{D}$ threshold.

Neither the division of $\tilde{\sigma}_{c\bar{c}}$ into open charm and charmonia nor the relative charmonium production rates are specified by the generalised colour evaporation model. Hence its essential prediction is that the energy dependence of *charmonium production is that of* $\tilde{\sigma}_{c\bar{c}}(s)$*. As a consequence, the ratios of different charmonium production cross sections are energy-independent.* In Fig. 2, we show the ratio of J/ψ production from the decay $\chi_c \to \gamma\ J/\psi$ to the total J/ψ production rate [5, 6]. It provides a measure of the $\chi_c/(J/\psi)$ rate and is seen to be independent of incident energy for both pion and proton beams. In Fig. 3, we show the measured $\psi'/(J/\psi)$ ratio [5, 7, 8]; it is also found to be independent of the incident energy, as well as of the projectile (pion or proton) and target (from protons to the heaviest nuclei [9]). Moreover, it is noteworthy that the ratio $\psi'/(J/\psi)$ measured at high transverse momenta at the Tevatron [10] is quite compatible with the p_T-integrated fixed target and ISR data (Fig. 4), as also observed in [11]. The available bottonium data [12, 13, 14, 15] also agree with constant production ratios, as seen in Fig. 5 for the ratios Υ'/Υ and Υ''/Υup to Tevatron energies.

The present data thus support one essential prediction of the colour evaporation model up to 1.8 TeV. We now check if it also correctly reproduces the variation of the production cross sections with incident energy in this region. In Figs. 6 and 7 we show the energy dependence of J/ψ production in pN collisions,

$$\sigma_{pN \to J/\psi}(s) = f^p_{J/\psi}\ \tilde{\sigma}_{c\bar{c}}(s), \qquad (2)$$

as obtained from the hidden charm cross section $\tilde{\sigma}_{c\bar{c}}$ calculated in next-to-leading order [16] and with the normalisation $f^p_{J/\psi}$ fixed empirically. We have used the MRS D-' [17] and GRV HO [18] parametrisations of the nucleon parton distributions functions [19]. For the GRV set, we have used $m_c = 1.3$ GeV, with both renormalisation and factorisation scales fixed to m_c. In the MRS calculation, m_c=1.2 GeV was used, with the scales set at $2m_c$. These parameters provide an adequate description of open charm production, although the results tend to lie somewhat below the measured total $c\bar{c}$ cross sections [20]. In Figs. 6 and 7 we show only the MRS D-' result; the GRV HO result differs by less than 5 % in this energy range. The agreement with the data [5] over the entire range is quite satisfactory, with the normalisation $f^p_{J/\psi} = 0.025$. In Fig. 8 we find equally good agreement for the energy dependence of J/ψ production with pion beams. However, the fraction of J/ψ in the hidden charm cross section must be slightly higher to reproduce the pion data well, with $f^\pi_{J/\psi} = 0.034$ for a good fit. This may well be due to greater uncertainties in the pionic parton distribution functions. We have also calculated the leading order cross section; the resulting theoretical K-factor, $K \equiv \tilde{\sigma}^{NLO}_{c\bar{c}}/\tilde{\sigma}^{LO}_{c\bar{c}}$, remains between 2.0 and 2.5 over the currently measured energy range for both sets of parton distribution functions and for pion and proton beams.

The fraction of $\tilde{\sigma}_{c\bar{c}}$ producing charmonium rather than open charm is thus about 10%. This is in accord with open charm calculations, which show [20] that much of the total cross section comes from subthreshold $c\bar{c}$ initial states which acquire the necessary energy for $D\bar{D}$ formation from the interaction colour field. To illustrate this, Fig. 9 shows the fraction of the total open charm cross section with $2\ m_c \leq M \leq 2\ M_D$, where $M \equiv \sqrt{\hat{s}}$. It remains quite large even at very high incident energies.

We further compare the longitudinal momentum dependence of charmonium production with recent experimental results. In fig. 10 we compare data with our calculations for the x_F dependence of J/ψ production at several energies and for $\pi - p$, $\bar{p} - p$ and $p - p$ collisions [21]. Since there is a spread of integrated cross section values around the average $\tilde{\sigma}_{c\bar{c}}$, as seen in Figs. 6 - 8, we have normalised the calculated x_F distribution to the integrated experimental one. We conclude that the x_F distributions are also consistent with the colour evaporation model.

Next we comment briefly on the transverse momentum distributions. We are interested in low p_T charmonium production, for which the model provides essentially no prediction. There is the intrinsic transverse momentum of the initial partons, the intrinsic momentum fluctuations of the colour field which neutralises the colour of the $c\bar{c}$ system in the evaporation process, and at larger p_T higher order perturbative terms. Since there is no way to separate these different contributions in the low p_T region, the model has no predictive power.

The colour evaporation model thus reproduces correctly both the energy dependence and the x_F distributions of charmonium production, up to an open normalisation constant for each charmonium state, which can be fixed empirically by data. Once this is done, integrated and differential cross sections can be predicted for RHIC and LHC energies. From the fits to the data shown in Figs. 6 and 7 we obtain

$$\left(\frac{d\sigma_{pN\rightarrow J/\psi}}{dy}\right)_{y=0} = 2.5\ \times 10^{-2}\ \left(\frac{d\tilde{\sigma}^{NLO}_{c\bar{c}}}{dy}\right)_{y=0} \tag{3}$$

for J/ψ production. In Fig. 11 we show the resulting $(d\sigma_{pN\to J/\psi}/dy)_{y=0}$ as function of the center of mass energy, $\sqrt{s}$, and in Fig. 12 we give the rapidity distributions at RHIC and LHC energies. The cross sections are listed in Table 1.

Before commenting on our predictions, we first repeat the analysis for Υ production. Because the data generally give the sum of Υ, Υ' and Υ" production, the branching ratios cannot simply be removed. Therefore we show in Fig. 13 the measured cross section for the sum of the three Υ states in the dilepton decay channel, denoted by $B(d\sigma/dy)_{y=0}$. We see that

$$B\left(\frac{d\sigma_{pN\to\Upsilon}}{dy}\right)_{y=0} = 1.6\ \times 10^{-3}\ \left(\frac{d\sigma_{b\bar{b}}^{NLO}}{dy}\right)_{y=0} \tag{4}$$

gives a good description of the data up to and including ISR results. The results are also calculated using the MRS D-' and GRV HO parton distribution functions, with $m_b = 4.75$ GeV and the scales equal to m_b. Assuming the bulk of the cross section to be from Υ(1S) production, and using the corresponding branching ratio, we estimate from eq. (4) that about 7% of the sub-threshold $b\bar{b}$ cross section leads to Υ production.

Using the normalisaton determined in Eq. (4), we obtain the cross section for high energy Υ production; the results are shown in Figs. 14 and 15 and in Table 2. The recent high energy data from UA1 [22] and CDF [15] agree very well with the predicted energy dependence, as seen in Fig. 13, giving strong support to the "new" parton distribution functions based on HERA data [23]. They also give us considerable confidence in the extrapolation to LHC energy.

We now comment on some features of our predictions. The two parton distribution functions, MRS D-' and GRV HO, provide fully compatible results in the measured energy range. The Υ predictions agree with data even up to energies close to the LHC range. The MRS D-' J/ψ cross section is about twice as large as the GRV HO prediction at LHC energies. This is because the MRS distributions require larger factorisation scales than the GRV distributions. Both parton distribution functions, with their chosen scales, also give acceptable fits to the measured open charm production cross sections (see [20] for more details). The difference thus gives some indication of the uncertainty of the J/ψ prediction. The Υresults agree over the entire energy range, since $m_b = 4.75$ GeV was used as the scale in both sets.

At LHC energies, both the J/ψ and Υ rapidity distributions remain rather constant out to $y \simeq 4$, using the MRS parton distributions. The GRV HO results show an even wider plateau. In either case, there is a large window for forward detection at high energies. At RHIC energies, the J/ψ distributions are not as broad, with a forward plateau of 2 - 3 units for the MRS set, while the GRV distributions are somewhat narrower. The Υ rapidity distributions at RHIC energies are quite similar for both sets.

Finally we note that the cross sections calculated with the recent parton distribution functions are considerably higher, typically by about a factor 20, than those given by an earlier empirical parametrisation, $\sim \exp(-15M/\sqrt{s})$, labelled CR in Figs. 11 and 14 [24, 25, 26]. This increase, confirmed by new high energy Υ data (Fig. 14), is mainly due to the increase in the gluon distribution functions at small x, as suggested by data from HERA [23].

The colour evaporation model addresses the common energy behaviour of the different quarkonium states. To determine their relative production rates, the colour evaporation process has to be specified in more detail. Let us consider one example of this. Assume that the initial colour octet state first neutralises its colour by interaction with the surrounding colour field, producing a colour singlet $c\bar{c}$ state. The relative weights of J/ψ and ψ' production can then be expressed [5] in terms of the corresponding masses and the squared charmonium wave functions at the origin,

$$\frac{\sigma(\psi')}{\sigma(\psi)} = \frac{R^2_{\psi'}(0)}{R^2_{\psi}(0)} \left(\frac{M_\psi}{M_{\psi'}}\right)^5 . \tag{5}$$

Here ψ denotes the directly produced 1S $c\bar{c}$ state, in contrast to the experimentally observed J/ψ, 40% of which originates from radiative χ_c decays (see Fig. 1). The wave functions at the origin can in turn be related to the dilepton decay widths $\Gamma_{ee} \sim (R^2(0)/M^2)$ [5], giving

$$\frac{\sigma(\psi')}{\sigma(\psi)} = \frac{\Gamma_{\psi'}}{\Gamma_{\psi}} \left(\frac{M_\psi}{M_{\psi'}}\right)^3 . \tag{6}$$

Inserting the measured masses and decay widths, we find

$$\frac{\sigma(\psi')}{\sigma(\psi)} \simeq 0.24 . \tag{7}$$

To compare this to the measured value of $\sigma(\psi')/\sigma(\psi)$, we have to remove the χ_c contributions from the experimental ratio,

$$\frac{\sigma(\psi')}{\sigma(\psi)} = \left[\frac{1}{1-(\sigma_{\chi_c}/\sigma_{J/\psi})}\right] \left[\frac{\sigma(\psi')}{\sigma(J/\psi)}\right]_{\text{exp}} . \tag{8}$$

With the experimental values $\sigma(\psi')/\sigma(J/\psi) \simeq 0.14$ (Figs. 2 and 3) and $(\sigma_{\chi_c}/\sigma_{J/\psi}) \simeq 0.4$ (Fig. 1), this yields $\sigma(\psi')/\sigma(\psi) \simeq 0.23$, in good agreement with the theoretical result (7). We thus find that the projection of the colour singlet $c\bar{c}$ state onto J/ψ and ψ' correctly describes their production ratios at all energies and transverse momenta.

The predictions for direct bottonium production ratios corresponding to eq. (7) are

$$\frac{\sigma(\Upsilon')}{\sigma(\Upsilon)} \simeq 0.36 \;\; ; \;\; \frac{\sigma(\Upsilon'')}{\sigma(\Upsilon)} \simeq 0.27 . \tag{9}$$

Since the contributions from indirect production through radiative χ_b decay are not yet known and there is also feeding from higher S-states, a quantitative comparison is not possible here. Nevertheless, the predicted values differ from the data (see Fig. 5) by less than 50 % and hence appear reasonable.

So far, the most complete description of the colour evaporation process is attempted in the colour singlet model [28], in which not only the $c\bar{c}$ formation but also the subsequent colour neutralisation is assumed to take place on a perturbative scale. The resonance formation is then determined by the appropriate wave functions with the right quantum numbers, as above. As a result, the production cross section for each charmonium state is completely determined to the order of perturbation theory used. Some characteristic production diagrams in lowest order are illustrated in Fig. 16. As generally formulated, the scale of the strong coupling constant in all perturbative diagrams is determined by the mass of the heavy quark.

Such a perturbative description of colour neutralisation can be justified only if *all* momentum scales are sufficiently large. However, as seen in Fig. 16, colour neutralisation for all but η_c, χ_0 and and χ_2 requires the emission or absorption of a "third" gluon. This restricts the possible applicability of the model to production at large transverse momentum. In the p_T-integration, the "third" gluon is soft ($k \sim \Lambda_{\rm QCD}$) in a significant part of phase space, and hence the model becomes unreliable here even though the integration is infrared finite. It is therefore not surprising that the colour singlet model leads to charmonium production ratios which disagree rather strongly with experiment. The quantum numbers of the χ_2 allow partonic production at order α_s^2, while J/ψ, χ_1 and ψ' production are all of order α_s^3. As a result, their production is much too strongly suppressed in comparison to the χ_2. Thus, while the model predicts $\chi_2/(J/\psi) \simeq 10$, the measured ratios are below 2 [6]; including certain relativistic corrections can somewhat reduce this discrepancy [5]. – The J/ψ polarisation also encounters difficulties [11]. Similar arguments hold for Υ production, although the soft part of the p_T-integration is relatively smaller, so that here the predictions may be closer to the data.

For the validity of a perturbative treatment, the "third" gluon has to be hard enough to resolve the $c\bar{c}$ into individual quarks. Hence its momentum must be higher than $1/r_{J/\psi} \simeq 1/(0.2 \text{ fm}) \simeq 1$ GeV. Below this limit, it is not clear how colour neutralisation is achieved; presumably nonperturbative interactions of the colour octet $c\bar{c}$ with the gluon condensate play a considerable role. Some additional contributions can perhaps also be obtained by summing classes of perturbative contributions [29]. However, as long as the additional interactions cannot be determined quantitatively, the prediction of the p_T-integrated production ratios of the different charmonium states is not possible. It is not known if this is also true for bottonium production, or if here the role of soft processes has become sufficiently reduced to allow a fully perturbative treatment.

References

[1] M. B. Einhorn and S. D. Ellis, Phys. Rev. D **12** (1975) 2007.

[2] H. Fritzsch, Phys. Lett. **67B** (1977) 217.

[3] M. Glück, J. F. Owens and E. Reya, Phys. Rev. D **17** (1978) 2324.

[4] J. Babcock, D. Sivers and S. Wolfram, Phys. Rev. D **18** (1978) 162.

[5] For a recent review, see G. A. Schuler, "Quarkonium Production and Decays", CERN Preprint CERN-TH.7170/94, February 1994.

[6] L. Antoniazzi *et al.*, Phys. Rev. Lett. **70** (1993) 383.

[7] L. Antoniazzi *et al.*, Phys. Rev. D **46** (1992) 4828.

[8] C. Lourenco, "$J/\psi,\psi'$ and Dimuon Production in $p-A$ and $S-U$ Collisions at 200 GeV/Nucleon", Dissertation, Technical University of Lisbon, Portugal.

[9] B. Ronceux, Nucl. Phys. **A566** (1994) 371c.

[10] The CDF Collaboration, "J/ψ, $\psi' \rightarrow \mu^+\mu^-$ and $B \rightarrow J/\psi$, ψ' Cross Sections", Fermilab Preprint Fermilab-Conf-94/136-E, May 1994 (Contribution to the International Conference on High Energy Physics, Glasgow, Scotland 1994);
E. Braaten *et al.*, Phys. Lett. **B333** (1994) 548.

[11] M. Vänttinen et al., "Hadroproduction and Polarization of Charmonium", SLAC Preprint SLAC-PUB-6637, August 1994.

[12] K. Ueno *et al.*, Phys. Rev. Lett. **42** (1979) 486.

[13] T. Yoshida *et al.*, Phys. Rev. D **39** (1989) 3516.

[14] G. Moreno *et al.*, Phys. Rev. D **43** (1991) 2815.

[15] V. Papadimitriou (CDF), "Υ Production at CDF", Fermilab Preprint Fermilab-Conf-94-221-E, August 1994.

[16] M. L. Mangano, P. Nason and G. Ridolfi, Nucl. Phys. **B405** (1993) 507.

[17] A. D. Martin, R. G. Roberts and W. J. Stirling, Phys. Lett. **B306** (1993) 145, and "Structure Functions and Parton Distributions, in this volume.

[18] M. Glück, E. Reya and A. Vogt, Z. Phys. C **53** (1993) 127.

[19] H. Plothow-Besch, Comp. Phys. Comm. **75** (1993) 396,
and "PDFLIB", in this volume.

[20] P. L. McGaughey *et al.*, "Heavy Quark Production in *pp* Collisons", in this volume.

[21] C. Akerlof *et al.*, Phys. Rev. D **48** (1993) 5067;
L. Antoniazzi *et al.*, Phys. Rev. D **46** (1992) 4828;
M. S. Kowitt *et al.*, Phys. Rev. Lett. **72** (1994) 1318;
C. Biino *et al.*, Phys. Rev. Lett. **58** (1987) 2523;
V. Abramov et al., "Properties of J/ψ production in $\pi^- - Be$ and $p - Be$ Collisions at 530 GeV/c", Fermilab Preprint FERMILAB-PUB-91/62-E.

[22] K. Eggert and A. Morsch (UA1), private communication.

[23] M. Derrick *et al.* (Zeus), Phys. Lett. **B316** (1993) 412;
I. Abt *et al.* (H1), Nucl. Phys. **B407** (1993) 515.

[24] N. Craigie, Phys. Rep. **47** (1978) 1.

[25] R.Vogt, Atomic Data and Nuclear Data Tables **50** (1992) 343.

[26] H. Satz, Nucl. Phys. **A544** (1992) 371c.

[27] R. Baier and R. Rückl, Z. Phys. C 19 (1983) 251; see also [1].

[28] C. H. Chang, Nucl. Phys. **B172** (1980) 425;
E. L. Berger and D. Jones, Phys. Rev. D **23** (1981) 1521;
R. Baier and R. Rückl, Phys. Lett. **B102** (1981) 364 and Z. Phys. C **19** (1983) 251.

[29] M. Beneke and V. M. Braun, "Naive Non-Abelianisation and Resummation of Fermion Bubble Chains", DESY Preprint DESY 94-200, November 1994;
M. Neubert, "Scale Setting in QCD and the Momentum Flow in Feynman Diagrams", CERN Preprint CERN-TH.7487/94, December 1994.

Table 1: J/ψ Production

$\sqrt{s}$ [GeV]	$(d\sigma/dy)^{\mathrm{MRS}}_{y=0}$ [μb]	$(d\sigma/dy)^{\mathrm{GRV}}_{y=0}$ [μb]
20	6.2×10^{-2}	5.8×10^{-2}
40	1.6×10^{-1}	1.5×10^{-1}
60	2.5×10^{-1}	2.4×10^{-1}
100	3.5×10^{-1}	3.4×10^{-1}
200	6.3×10^{-1}	5.9×10^{-1}
500	$1.5 \times 10^{+0}$	$1.2 \times 10^{+0}$
1000	$3.2 \times 10^{+0}$	$2.5 \times 10^{+0}$
5500	$1.6 \times 10^{+1}$	$5.9 \times 10^{+0}$
14000	$4.1 \times 10^{+1}$	$1.1 \times 10^{+1}$

Table 2: $(\Upsilon + \Upsilon' + \Upsilon'')$ Production

$\sqrt{s}$ [GeV]	$(Bd\sigma/dy)^{\mathrm{MRS}}_{y=0}$ [pb]	$(Bd\sigma/dy)^{\mathrm{GRV}}_{y=0}$ [pb]
15	3.1×10^{-4}	2.5×10^{-4}
30	9.7×10^{-1}	9.7×10^{-1}
60	$1.2 \times 10^{+1}$	$1.2 \times 10^{+1}$
100	$3.4 \times 10^{+1}$	$3.7 \times 10^{+1}$
200	$8.6 \times 10^{+1}$	$1.0 \times 10^{+2}$
500	$2.5 \times 10^{+2}$	$3.4 \times 10^{+2}$
1000	$5.5 \times 10^{+2}$	$8.8 \times 10^{+2}$
5500	$3.0 \times 10^{+3}$	$3.6 \times 10^{+3}$
14000	$7.8 \times 10^{+3}$	$7.7 \times 10^{+3}$

Figure Captions

Fig. 1. Lowest order $c\bar{c}$ production through gluon fusion (a) and quark-antiquark annihilation (b).

Fig. 2. The ratio of $(\chi_1 + \chi_2) \rightarrow J/\psi$ to total J/ψ production, as a function of the center of mass energy, $\sqrt{s}$, by proton (open symbols) and pion beams (solid symbols) [2].

Fig. 3a. The ratio of ψ' to J/ψ production as a function of the center of mass energy, $\sqrt{s}$, on proton (circles) and nuclear targets (squares) [3,4,5]. The average value is 0.14 ± 0.03.

Fig. 3b. The ratio of ψ' to J/ψ production by proton beams as a function of the atomic mass number A for data in the energy range $20 \leq \sqrt{s} \leq 40$ GeV [6]. The average value is 0.14 ± 0.01.

Fig. 4a. The ratio of ψ' to J/ψ production as a function of transverse momentum [7]; the shaded strip shows the average value of Fig. 3.

Fig. 4b. The ratio of ψ' to J/ψ production as a function of center of mass energy, $\sqrt{s}$. The fixed target and ISR data are integrated over the low p_T region, while the CDF point is the average over $5 \leq p_T \leq 15$ GeV.

Fig. 5. The ratios of Υ' and Υ" to Υ production as a function of the center of mass energy, $\sqrt{s}$ [8–9]. The average values are 0.53 ± 0.13 and 0.17 ± 0.06, respectively.

Fig. 6. The differential J/ψ production cross section $(d\sigma^{pN}_{J/\psi}/dy) = 2.5 \times 10^{-2}\,(d\tilde{\sigma}^{pN}_{c\bar{c}}/dy)$ at $y = 0$, calculated with MRS D-' parton distributions, compared to data [3].

Fig. 7. The J/ψ production cross section $\sigma^{pN}_{J/\psi} = 2.5 \times 10^{-2}\ \tilde{\sigma}^{pN}_{c\bar{c}}$ for $x_F > 0$, calculated with MRS D-' parton distributions, compared to data [3].

Fig. 8. The J/ψ production cross section $\sigma^{\pi N}_{J/\psi} = 3.4 \times 10^{-2}\ \tilde{\sigma}^{\pi N}_{c\bar{c}}$ for $x_F > 0$, calculated with MRS D-'/SMRS P2 parton distributions, compared to data [3].

Fig. 9. The fraction of the total open charm cross section due to the "hidden" charm mass interval $[2m_c, 2m_D]$.

Fig. 10a. The J/ψ longitudinal momentum distributions compared to $\bar{p}N$ and pN data [10], with $x_F = p_L(J/\psi)/p_{max}(J/\psi)$; the MRS results are denoted by a solid, the GRV by a dashed line.

Fig. 10b. The J/ψ longitudinal momentum distributions compared to πN data [10], with $x_F = p_L(J/\psi)/p_{max}(J/\psi)$. the MRS results are denoted by a solid, the GRV by a dashed line.

Fig. 11. Energy dependence of $(d\sigma^{pN}_{J/\psi}/dy)_{y=0}$ for J/ψ production, as obtained with MRS D-' and GRV HO parton distributions.

Fig. 12. Rapidity distributions for J/ψ production, calculated with MRS D-' parton distributions at RHIC and LHC energies.

Fig. 13. The differential Υ production cross section $(d\sigma^{pN}_{\Upsilon}/dy) = 1.8\times10^{-3}\,(d\sigma^{pN}_{b\bar{b}}/dy)$ at $y = 0$, calculated with MRS D-' parton distributions, compared to data [3]. The corresponding GRV HO predictions are very similar.

Fig. 14. Energy dependence of $(d\sigma^{pN}_{\Upsilon}/dy)_{y=0}$ for Υ production, with high energy data from [11,9]; the predictions of MRS D-' and GRV HO essentially coincide. Also shown (CR) is the phenomenological fit of [12].

Fig. 15. Rapidity distributions for Υ production calculated with MRS D-' parton distributions at RHIC and LHC energies.

Fig. 16. Lowest order contributions to charmonium production in the colour singlet model.

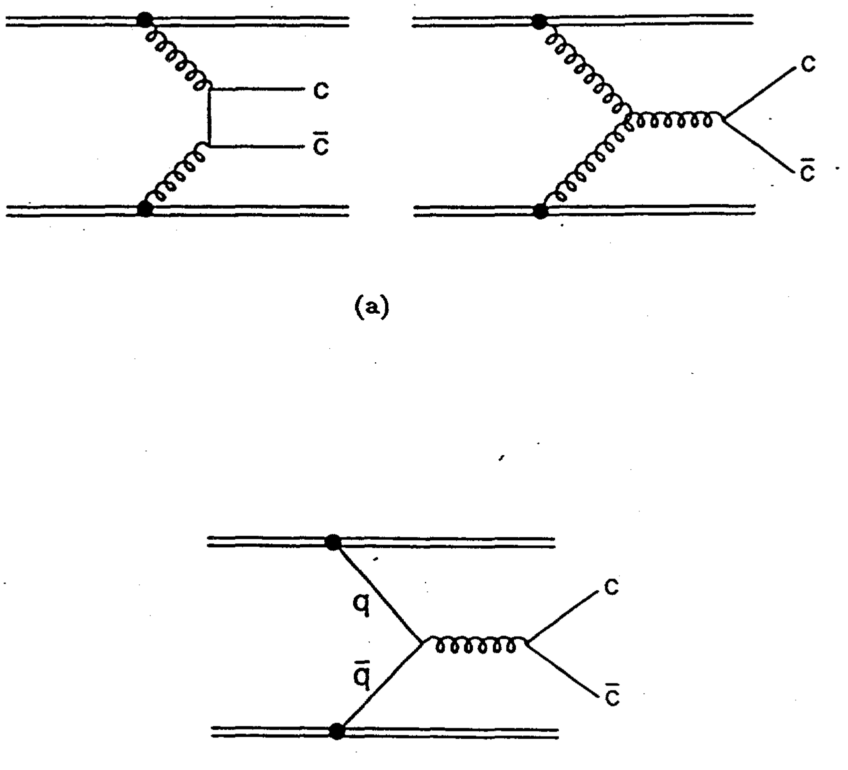

(a)

(b)

Fig. 1

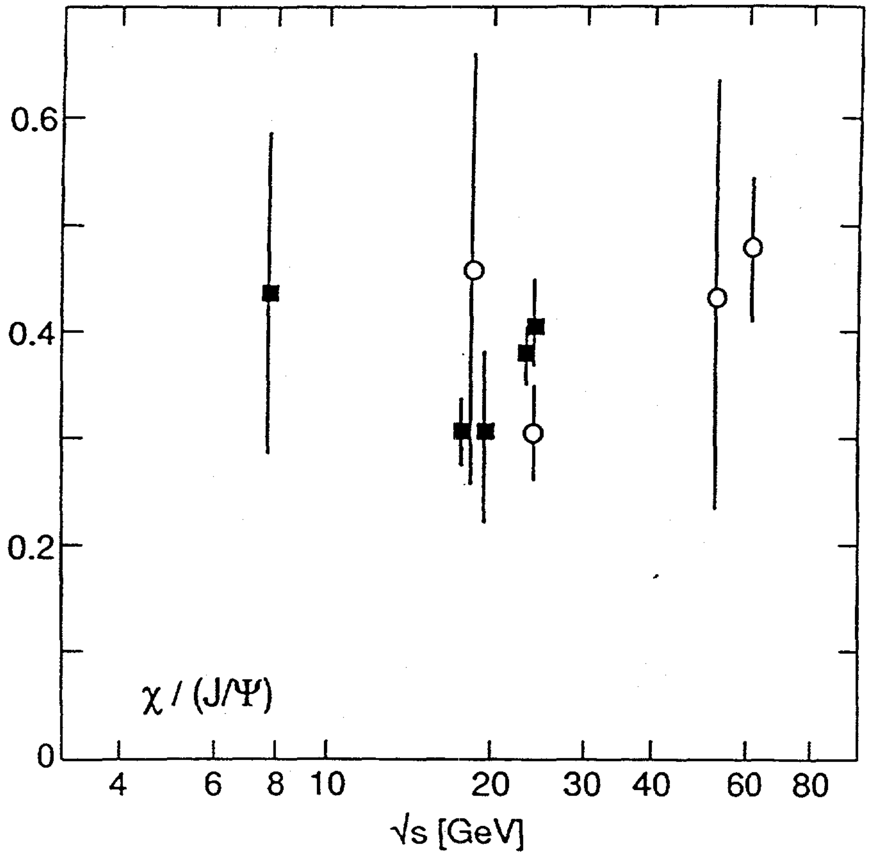

Fig. 2

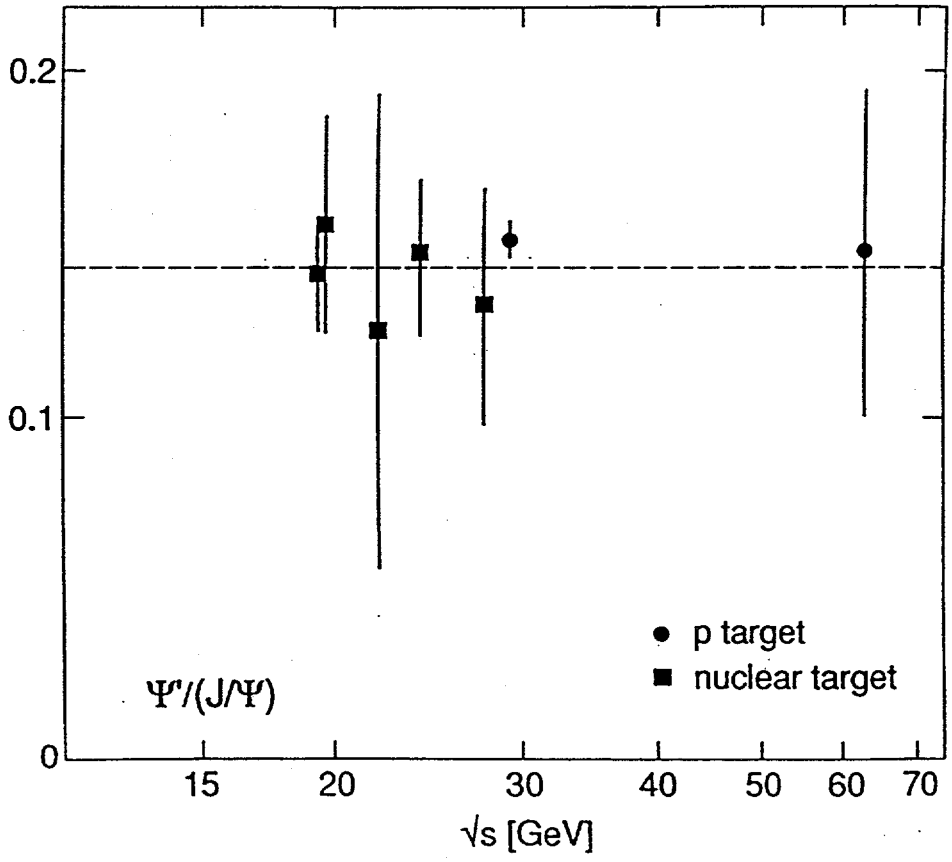

Fig. 3a

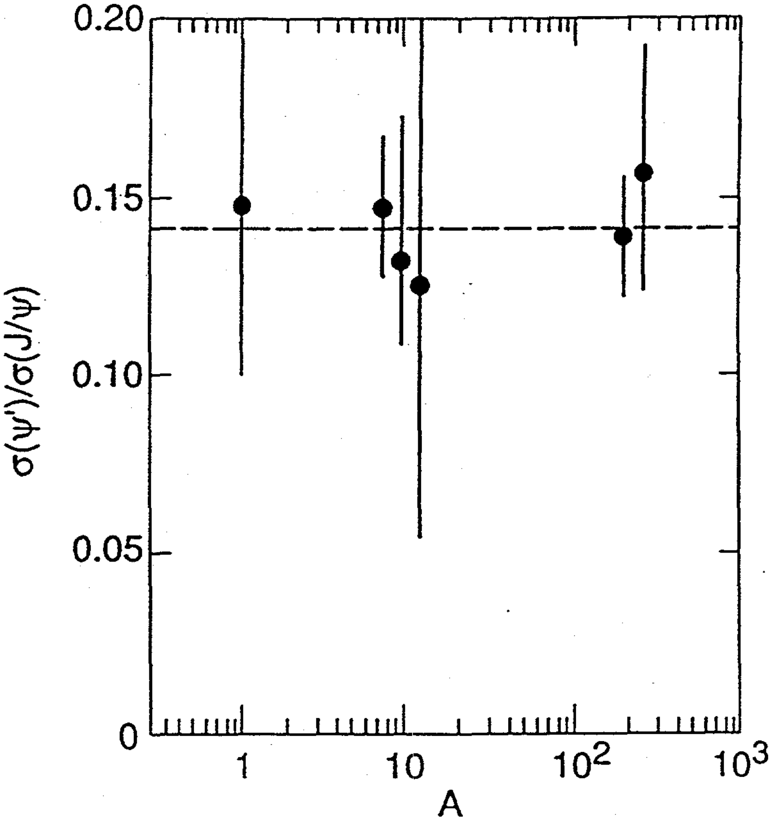

Fig. 3b

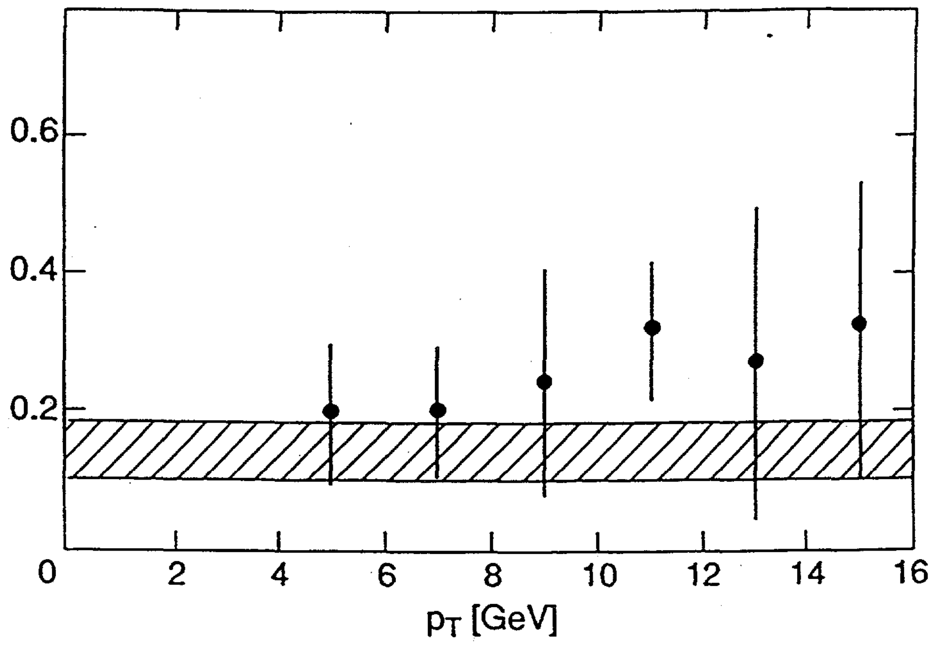

Fig. 4a

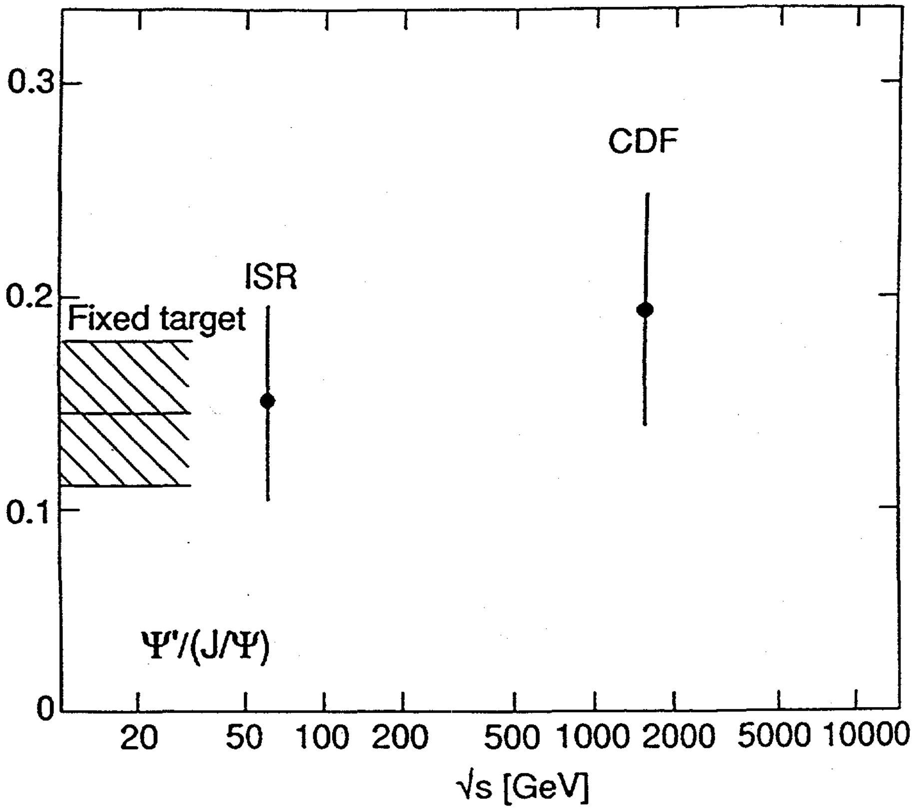
0.3
0.2
0.1
0
CDF
ISR
Fixed target
Ψ'/(J/Ψ)
20
50
100
200
500
1000
2000
5000
10000
√s [GeV]

Fig. 4b

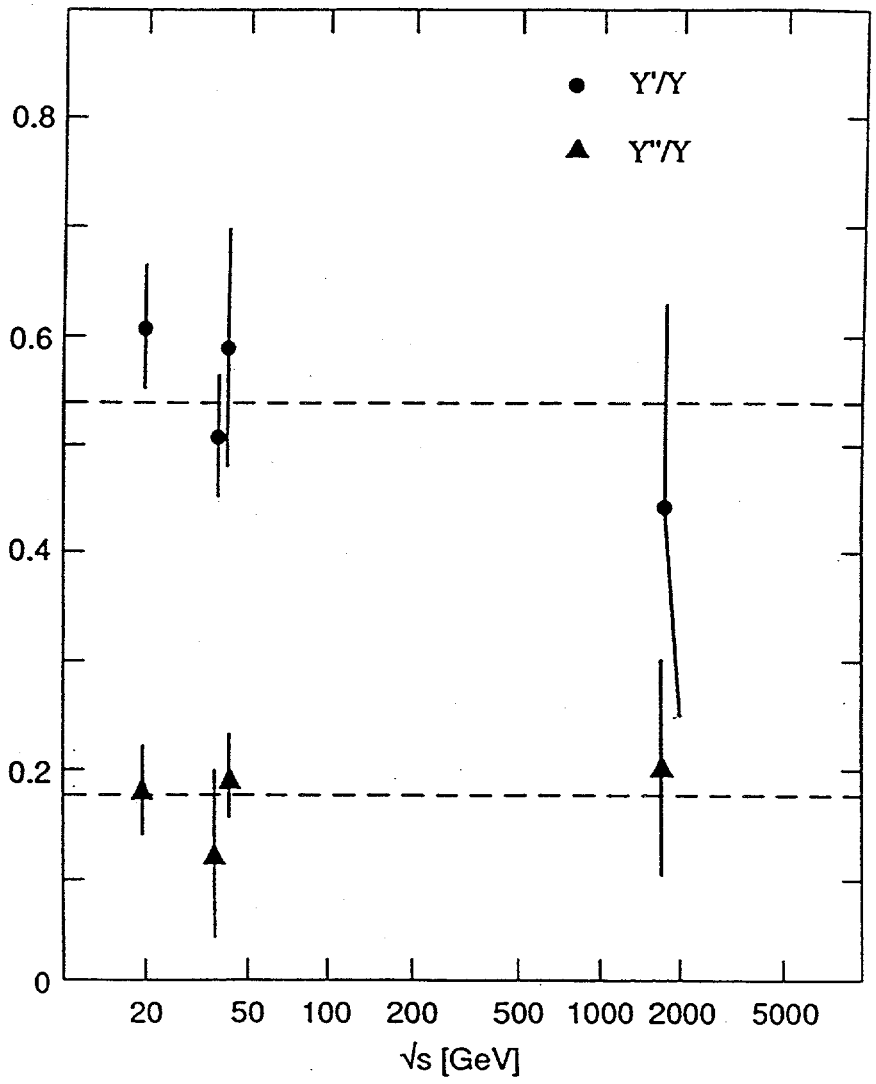

Fig. 5

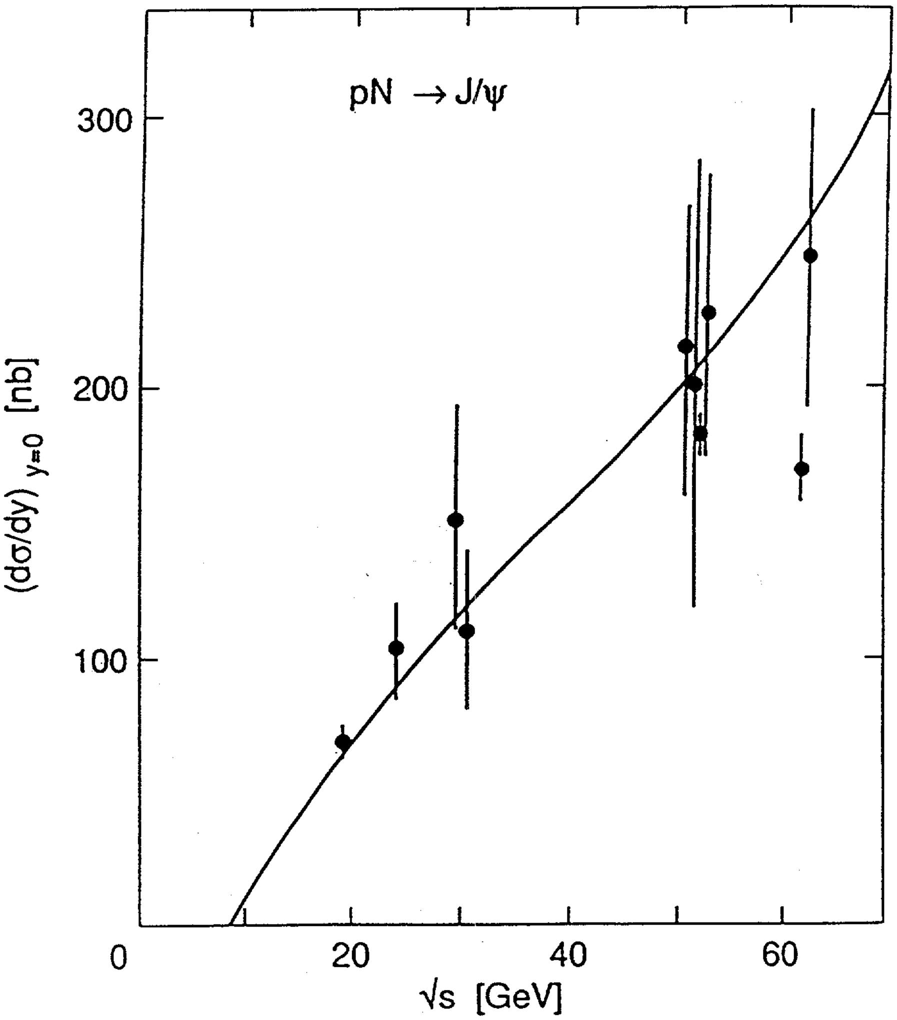

Fig. 6

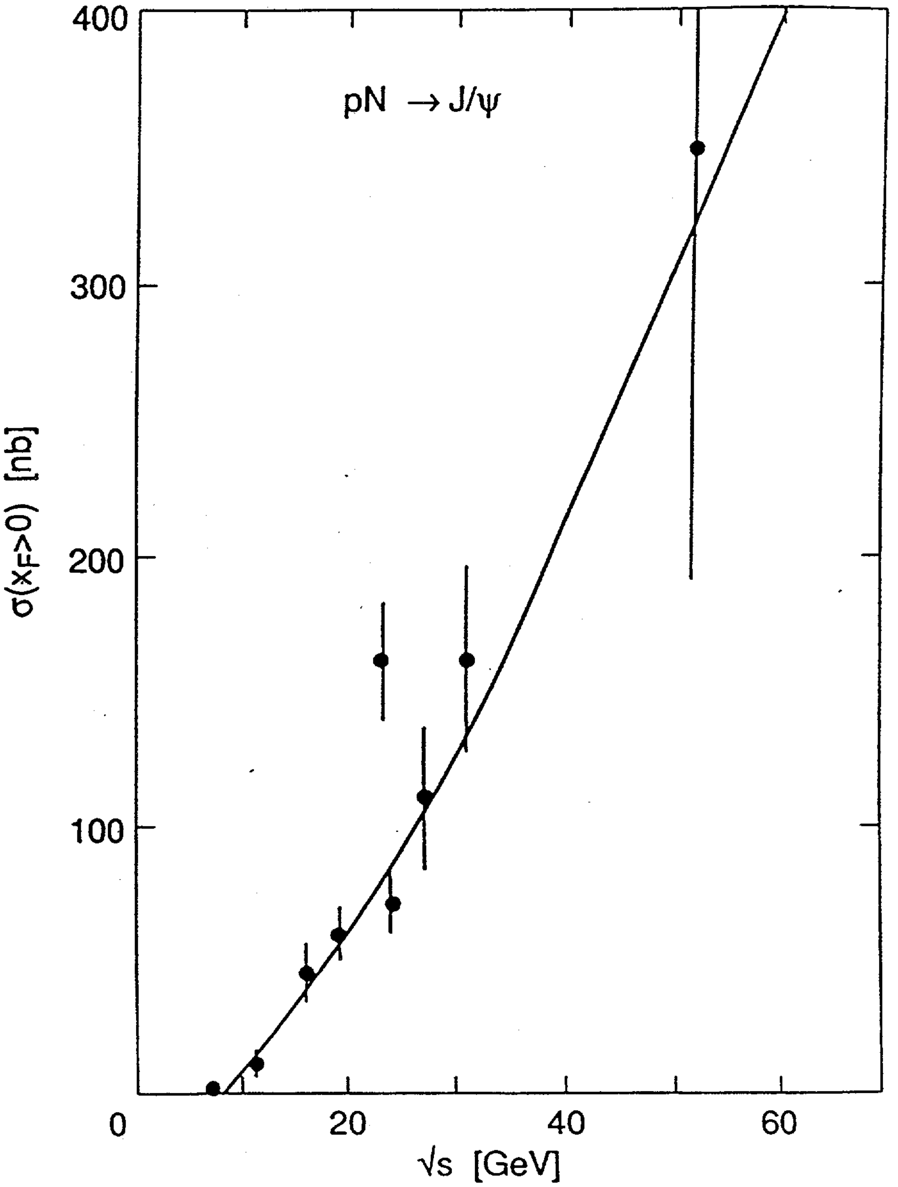

Fig. 7

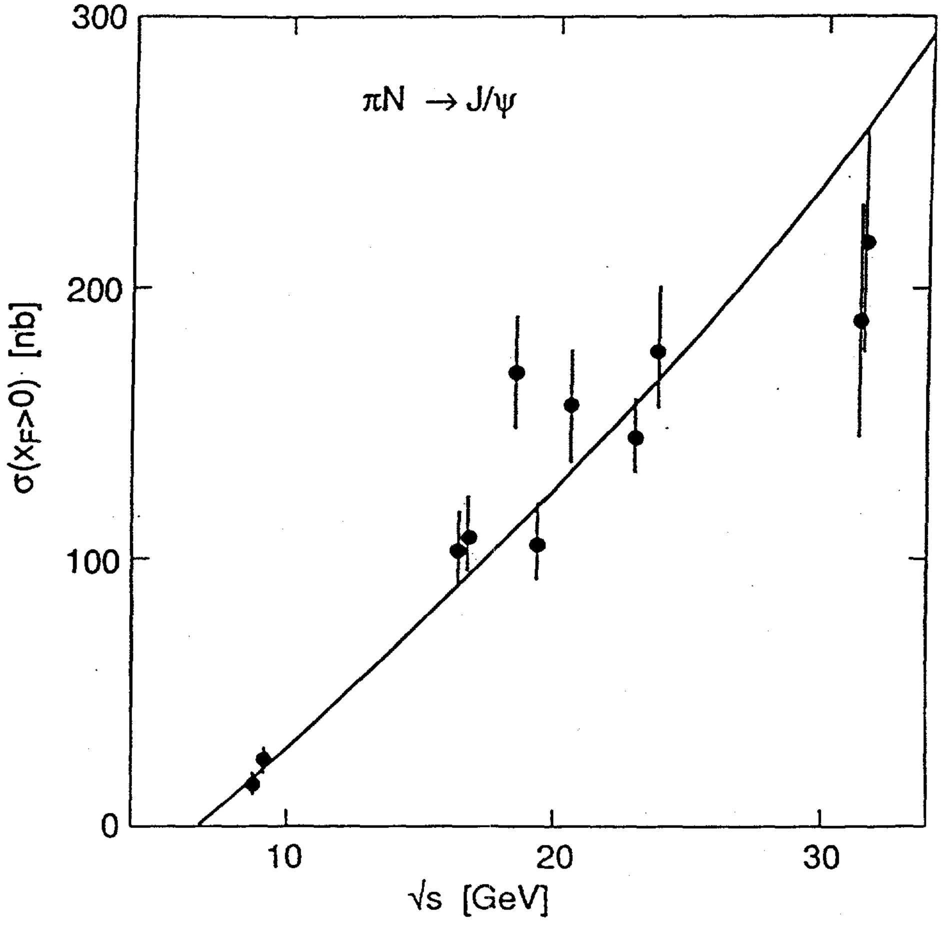

Fig. 8

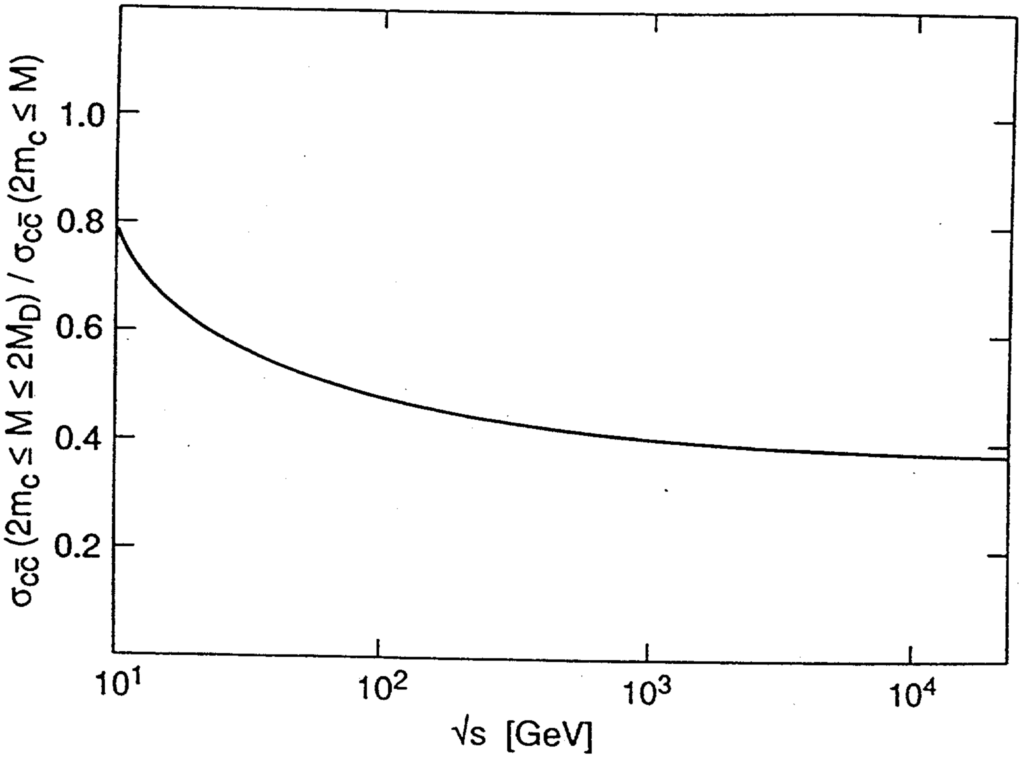

$\sigma_{c\bar{c}}(2m_c \le M \le 2M_D) / \sigma_{c\bar{c}}(2m_c \le M)$
1.0
0.8
0.6
0.4
0.2
10^1
10^2
10^3
10^4
$\sqrt{s}$ [GeV]

Fig. 9

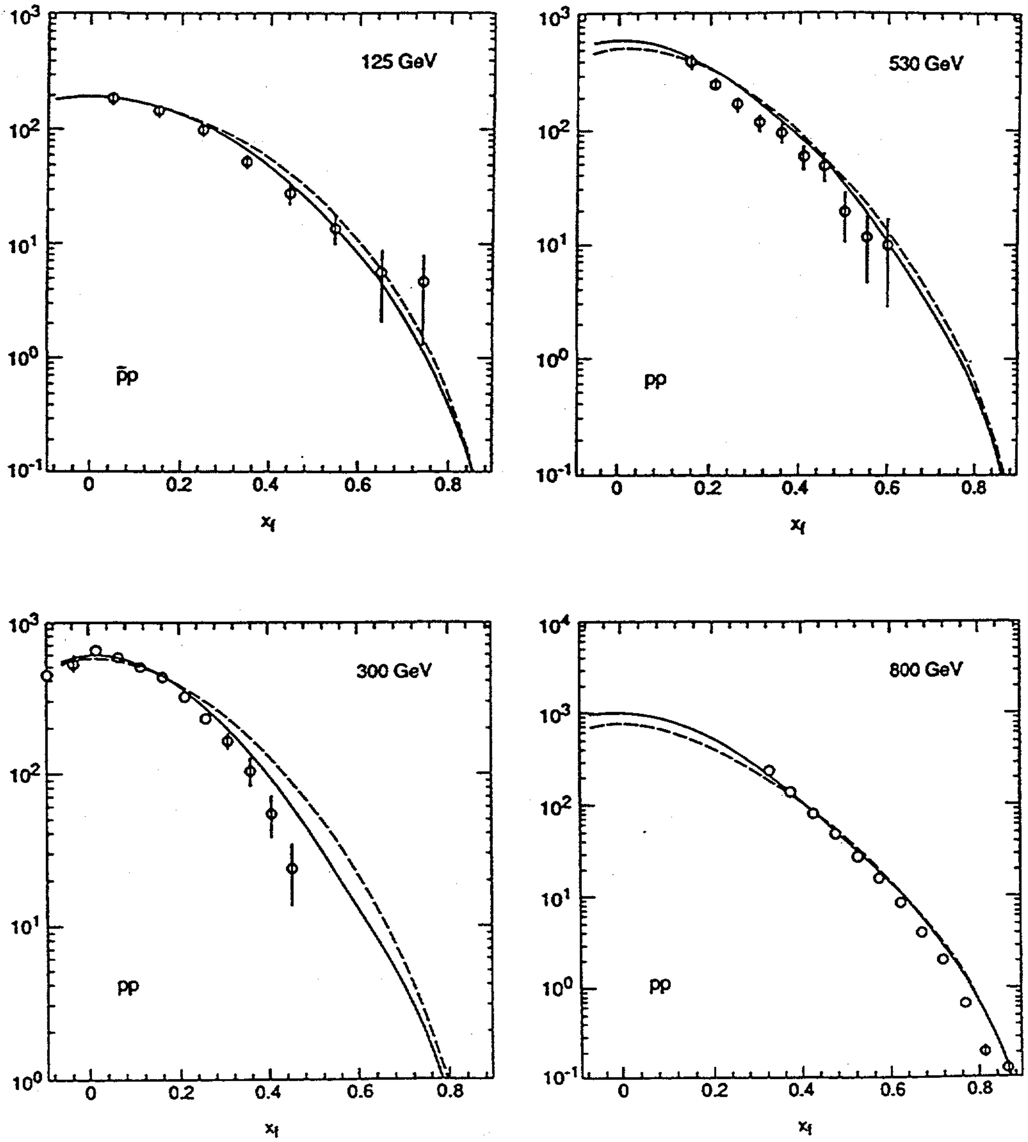
125 GeV
$\bar{p}p$
530 GeV
pp
300 GeV
pp
800 GeV
pp
10^{-1}
10^0
10^1
10^2
10^3
10^4
0
0.2
0.4
0.6
0.8
x_f

Fig. 10a

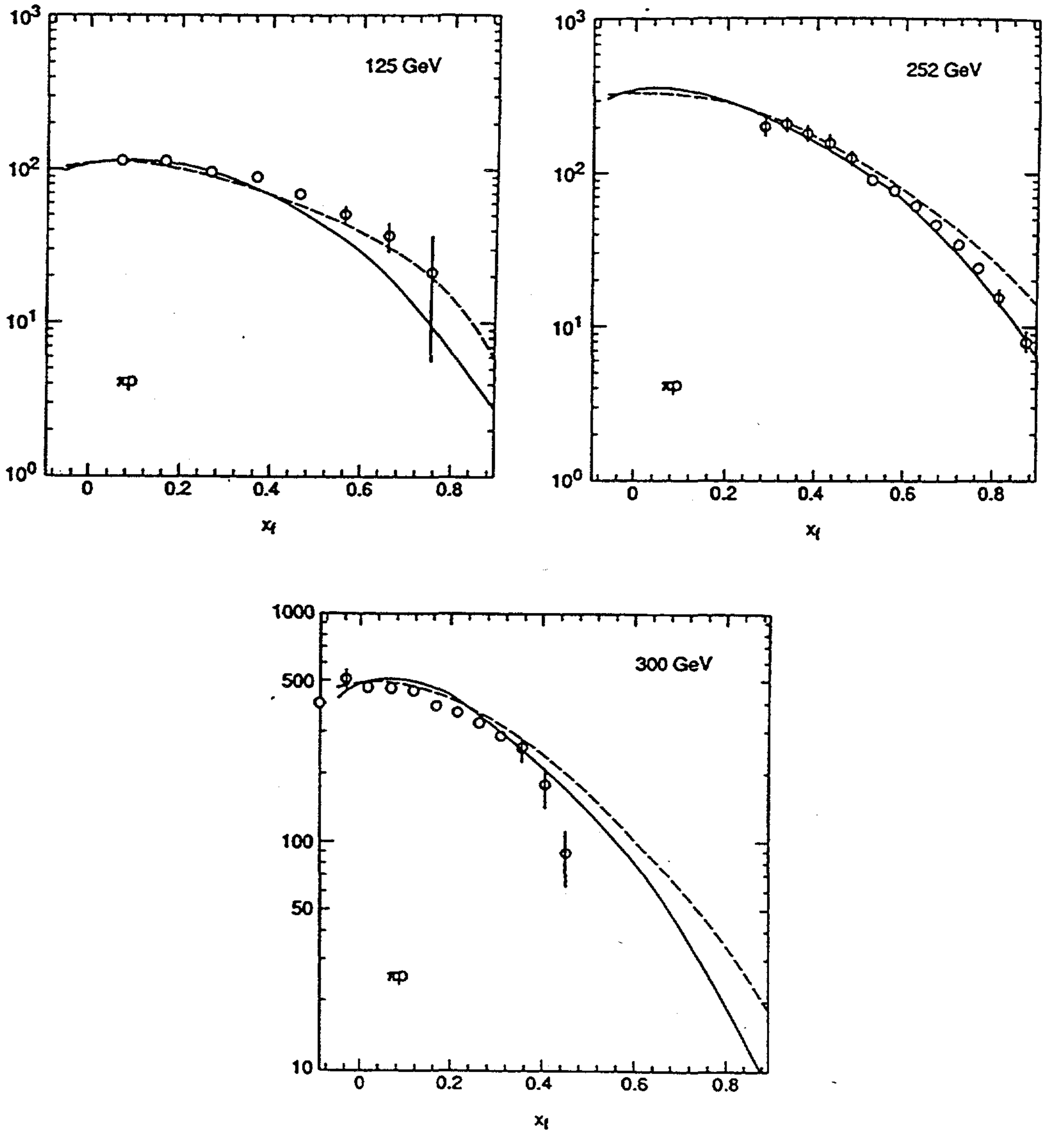

125 GeV
πp
10^3
10^2
10^1
10^0
0
0.2
0.4
0.6
0.8
x_f
252 GeV
πp
10^3
10^2
10^1
10^0
0
0.2
0.4
0.6
0.8
x_f
300 GeV
πp
1000
500
100
50
10
0
0.2
0.4
0.6
0.8
x_f

Fig. 10b

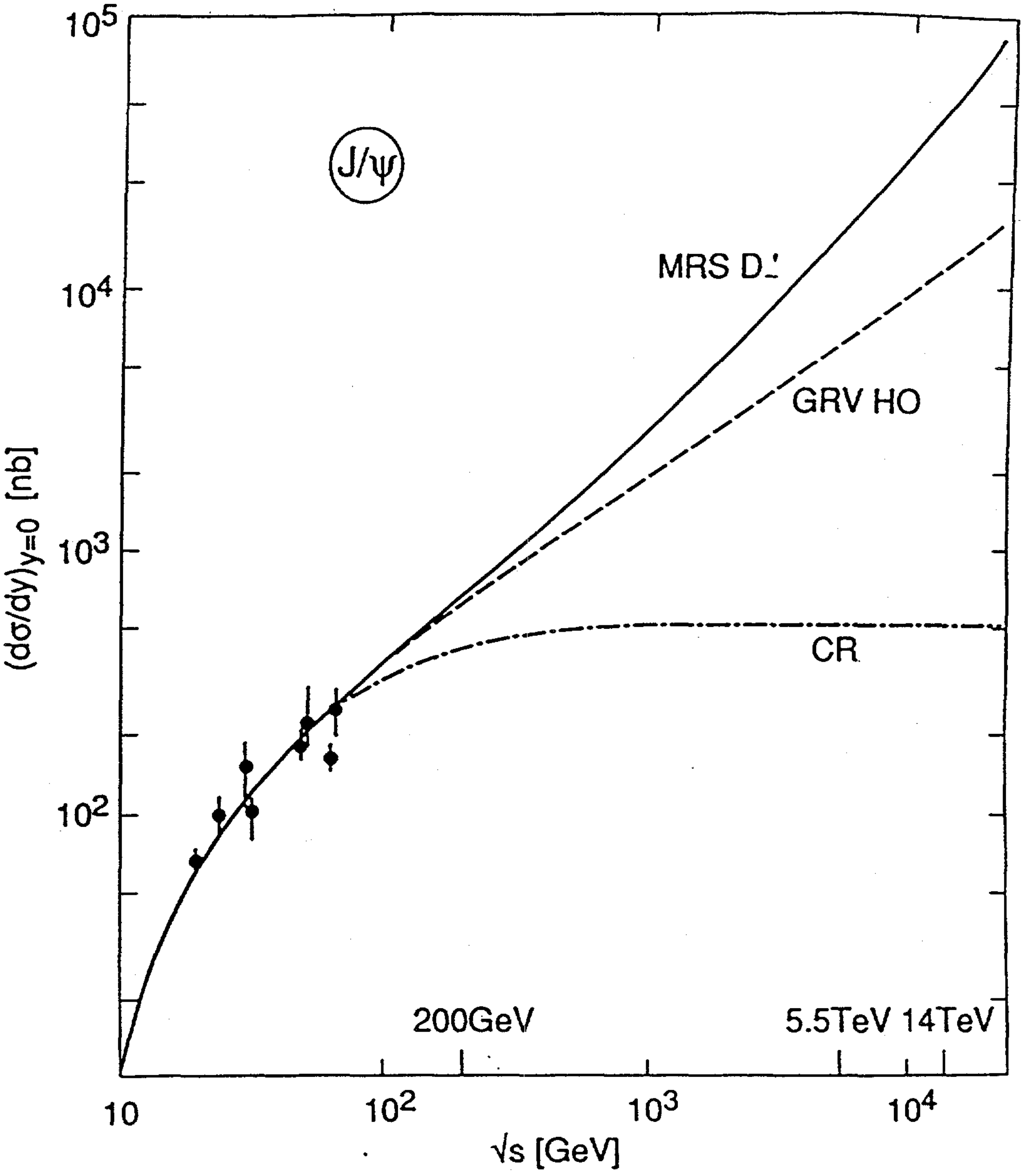

J/ψ
MRS D-'
GRV HO
CR
200GeV
5.5TeV 14TeV
10^5
10^4
10^3
10^2
$(d\sigma/dy)_{y=0}$ [nb]
10
10^2
10^3
10^4
√s [GeV]

Fig. 11

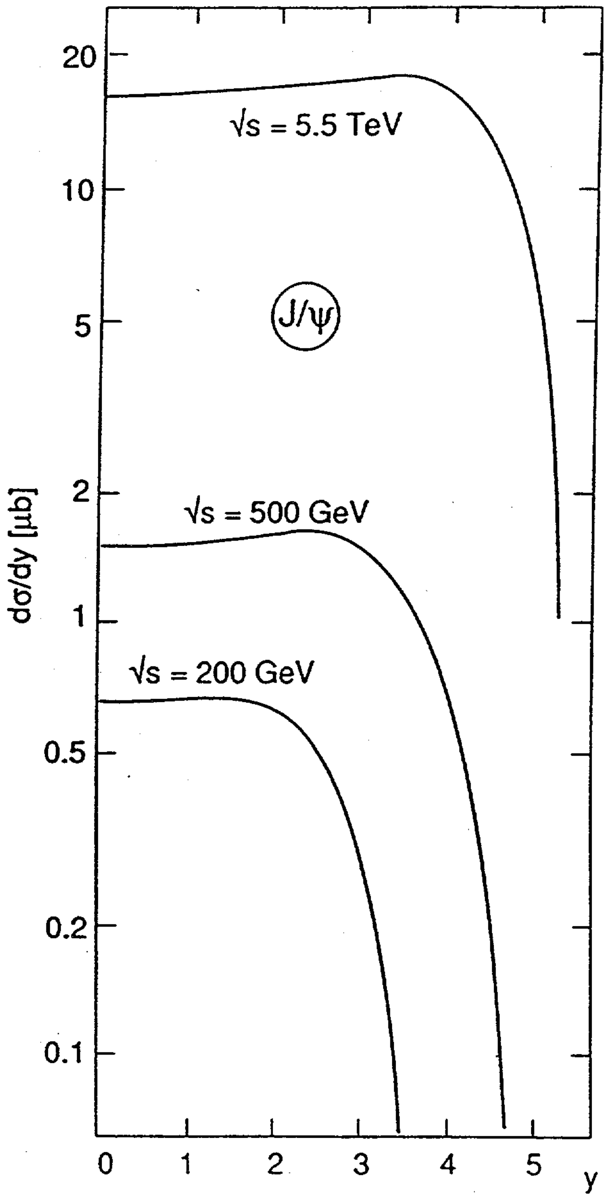

Fig. 12

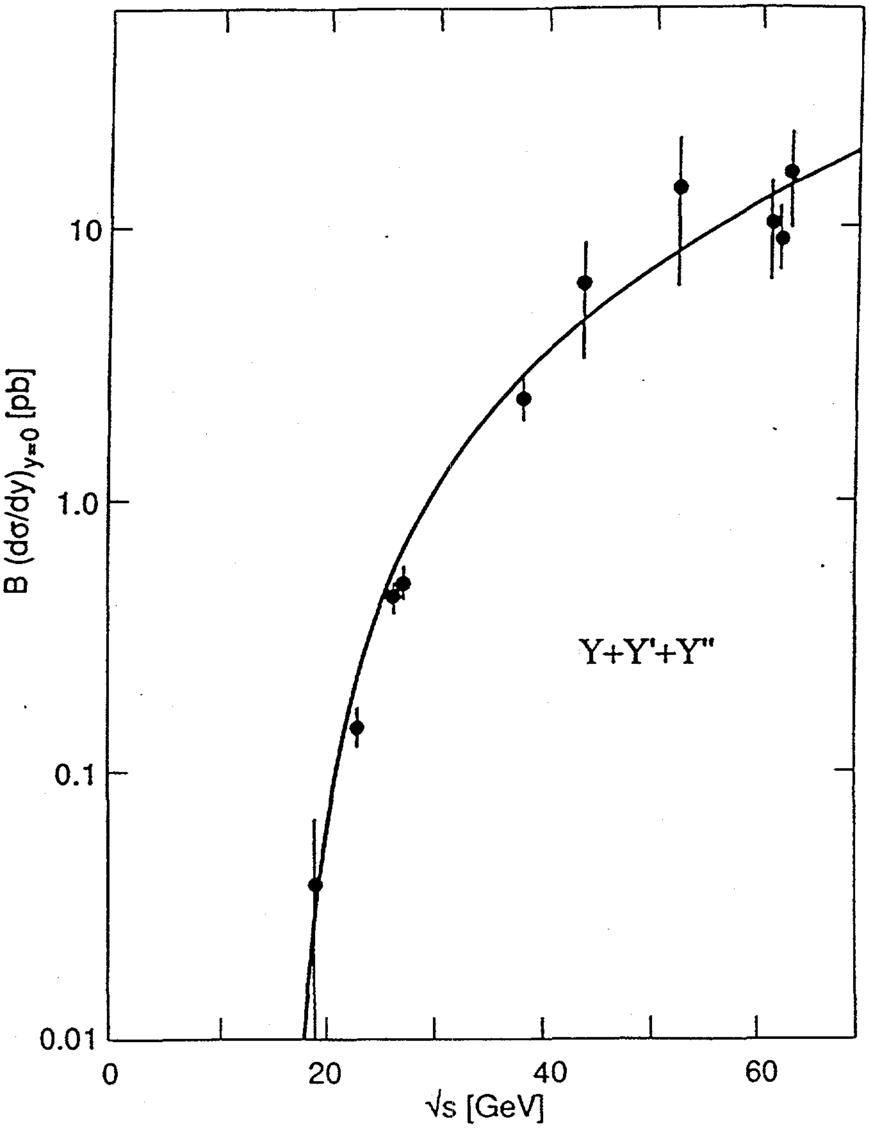

Fig. 13

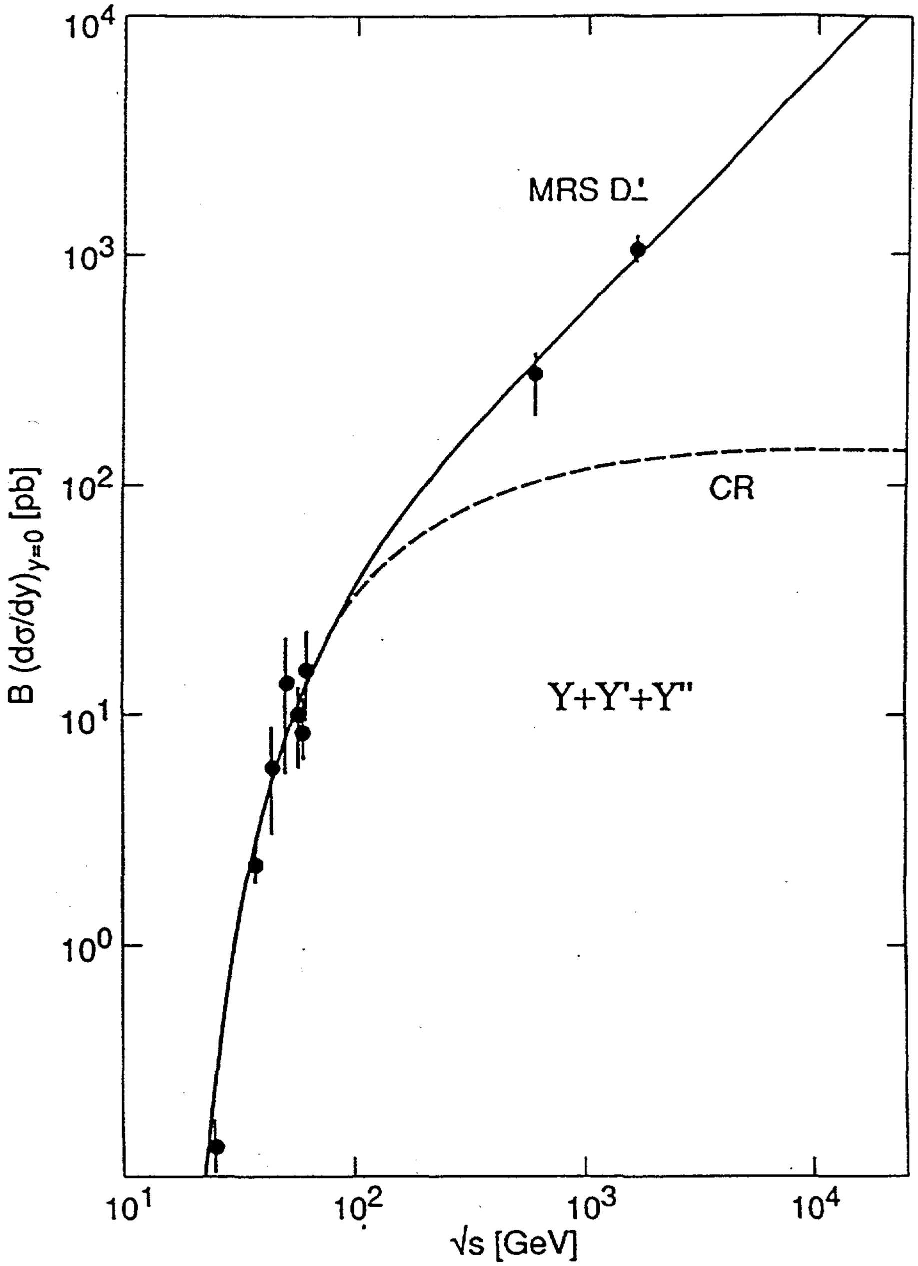

Fig. 14

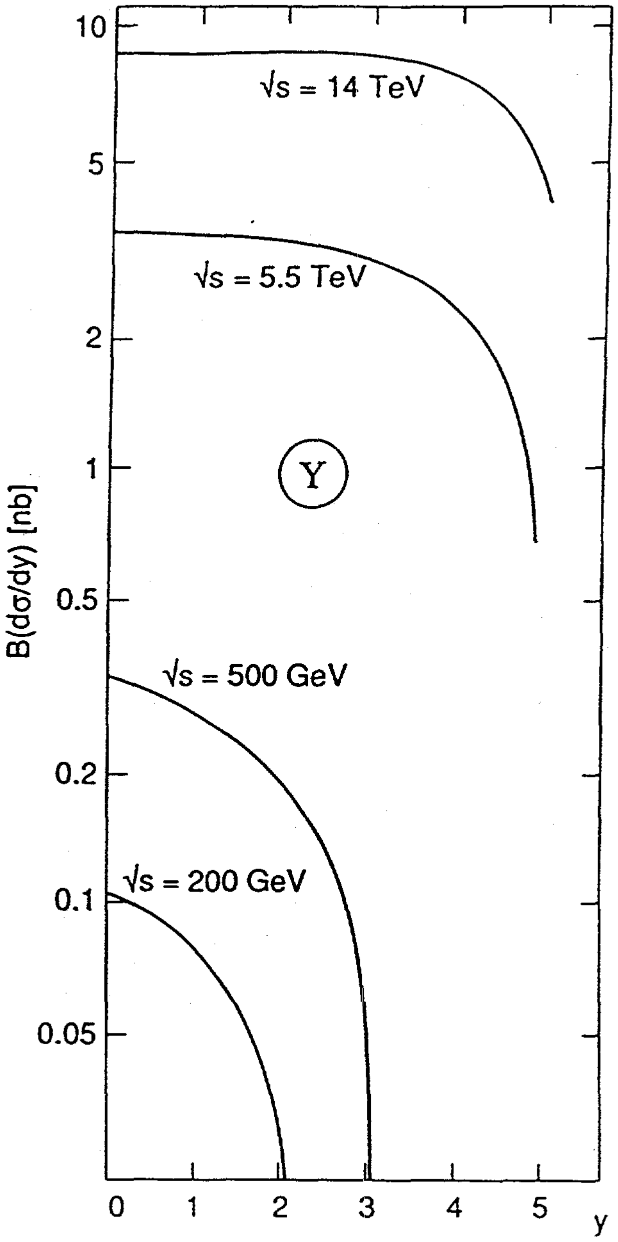
10
5
2
1
0.5
0.2
0.1
0.05
B(dσ/dy) [nb]
√s = 14 TeV
√s = 5.5 TeV
Υ
√s = 500 GeV
√s = 200 GeV
0
1
2
3
4
5
y

Fig. 15

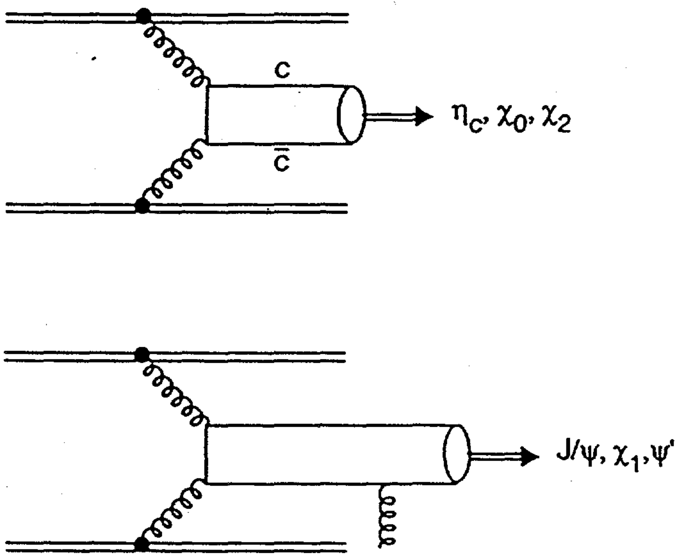

Fig. 16

HIGH p_T JET PRODUCTION IN pp COLLISIONS

K. J. ESKOLA[a] and X.-N. WANG[b]

[a] *Laboratory of High Energy Physics, P.O.Box 9*
FIN-00014, University of Helsinki, Finland

[b] *Nuclear Science Division, MS 70A-3307*
Lawrence Berkeley Laboratory, University of California
Berkeley, California 94720

Production rates of large p_T jets in pp collisions at RHIC and LHC energies are studied using the next-to-leading order calculation of S. D. Ellis, Z. Kunszt and D. Soper. The computed inclusive one-jet cross sections are compared against the CERN and Fermilab jet data from $p\bar{p}$ and pp collisions. The dependence of the results on the choice of parton distributions and renormalization/factorization scales is investigated.

INTRODUCTION

The emergence of hadronic jets in $p\bar{p}$ collisions at the CERN and Fermilab collider experiments provides a quantitative test of QCD [1, 2, 3, 4]. A jet with large transverse momentum in hadronic collisions is believed to be produced by large p_T partons scatterings. The inclusive parton production rates can be calculated within perturbative QCD. The lowest order calculation predicts the energy dependence of the inclusive one-jet distributions correctly, but generally differs from experimental measurements by a "K-factor" of $1.5 - 2$. To have a better understanding of the origin of the K-factor, and how the measured jet cross sections and partonic cross sections actually correspond to each other, a next-to-leading order (NLO) calculation has to be performed. This tedious task has recently been completed by two groups: S. D. Ellis, Z. Kunszt and D. Soper [5, 6, 7] and F. Aversa, P. Chiappetta, M. Greco and J. Ph. Guillet [8]. Both groups have used the matrix elements calculated by R. K. Ellis and Sexton [9]. In this study we use the results of S. D. Ellis *et al.*, including their program to compute the inclusive one-jet distributions. Our main goal here is to study production rates of large p_T jets in pp collisions at RHIC and LHC energies. We will study the underlying uncertainties of the predictions and how these uncertainties are reduced when the NLO contributions are included. We will also compare the rates with existing data on inclusive one-jet production from pp and $p\bar{p}$ collisions.

To introduce the characteristic features of jet production let us first consider the lowest order, $\mathcal{O}(\alpha_s^2)$, formula. The inclusive jet cross section is given by summing over all possible $2 \rightarrow 2$ parton scatterings,

$$\frac{d\sigma_{\text{jet}}}{dp_T dy} = p_{\mathrm{T}} \int dy_1 dy_2 \quad \sum_{\substack{ijkl= \\ q,\bar{q},g}} x_1 f_{i/N}(x_1,\mu^2) x_2 f_{j/N}(x_2,\mu^2) \frac{d\hat{\sigma}}{d\hat{t}}^{ij\rightarrow kl} \cdot [\delta(y-y_1)+\delta(y-y_2)] \tag{1}$$

where y_1 and y_2 are the rapidities of the final state partons, and the hatted symbols refer to the parton-parton subprocesses. Intrinsic transverse momentum of the incoming partons is neglected and all partons are massless. Then x_i can be considered as fractions of the light-cone or the longitudinal momenta so that $x_{1,2} = p_T[\mathrm{e}^{\pm y_1} + \mathrm{e}^{\pm y_2}]/\sqrt{s}$. Due to the conservation of transverse momentum, both outgoing partons have the same p_T and are always back-to-back in the azimuthal angle ϕ. The Born cross section does *not* depend on the jet size R in the (y,ϕ)-plane, whereas the experimental definition of a jet *is* R-dependent. Thus the Born cross section can at best be an order of magnitude estimate of the measured jet cross section. However, when the $\mathcal{O}(\alpha_s^3)$ terms are included, the cross section becomes R-dependent and therefore can be more precisely compared to the measurements. The NLO terms have both collinear and soft singularities but they are regulated by the introduction of a finite jet size R.

The factorization scale μ entering the parton distribution functions $f_{i/N}$ and the renormalization scale in α_s are usually chosen to be the same, $\mu \sim p_T$. In the lowest order, the scale cannot be reliably optimized and a large (50-100%) uncertainty arises from the variation of μ from $\mu \sim p_T/2$ to $\mu \sim 2p_T$. Again, when the $\mathcal{O}(\alpha_s^3)$ terms are included, the results depend less on the choice of the scale.

FEATURES OF THE NLO CALCULATION

Let us now proceed to the inclusion of the $\mathcal{O}(\alpha_s^3)$ terms, as described in detail by S.D. Ellis *et al.* in [5, 6, 7]. To this order, both $2 \rightarrow 3$ processes and virtual corrections to the $2 \rightarrow 2$ processes have to be considered. The kinematics of the $2 \rightarrow 2$ processes remains basically unchanged, and the jet consists of only one parton. The kinematics of the $2 \rightarrow 3$ processes will be different and the jet size R has to be defined since two final state partons can be near each other in the (y,ϕ)-plane. Ellis *et al.* use the following definition: the jet cone of radius R, centered on a cone axis (y_c, ϕ_c) is

$$(y-y_c)^2 + (\phi-\phi_c)^2 < R^2 < (\frac{\pi}{3})^2 \tag{2}$$

The transverse energy (momentum) p_T of the jet is

$$p_T = \sum_{i \in \text{cone}} p_{Ti}. \tag{3}$$

The jet axis is then defined by the weighted averages

$$y_{\mathrm{j}} = \frac{1}{p_T} \sum_{i \in \text{cone}} p_{Ti} y_i, \quad \phi_{\mathrm{j}} = \frac{1}{p_T} \sum_{i \in \text{cone}} p_{Ti} \phi_i, \tag{4}$$

and the cone axis (y_c, ϕ_c) must agree with the jet axis (y_j, ϕ_j). Naturally, again due to transverse momentum conservation, at most two partons can be combined into one jet in the NLO calculation. For more details and discussion, we simply refer to the original work in [5, 6, 7].

We next briefly describe the other elements of the NLO calculation by S.D. Ellis *et al.* The $\mathcal{O}(\alpha_s^3)$ matrix elements [9] are defined in $4-2\epsilon$ space-time dimensions in order to regularize the divergencies. Also, all the integrations over the parton momenta including the definition of the jet have to be performed in $4-2\epsilon$ dimensions as well. The virtual corrections to $2 \rightarrow 2$ processes contain $1/\epsilon$ and $1/\epsilon^2$ contributions arising from collinear and soft singularities in the virtual loop integrations. The $2 \rightarrow 3$ terms also bring divergent contributions proportional to $1/\epsilon$ and $1/\epsilon^2$, which result from integrations over the regions of two collinear partons or one soft parton. After these integrations, the divergent parts of the $2 \rightarrow 3$ terms cancel with the ones from the $2 \rightarrow 2$ terms. The key point here is that the finite size of the jet amounts to an integration over these crucial final state kinematical regions enabling the cancellation to occur. Since the cancellation happens between a negative infinity from the virtual corrections to the $2 \rightarrow 2$ process and a positive collinear singularity in the $2 \rightarrow 3$ process, the cross section diverges as $\sim \ln R$ as $R \rightarrow 0$. The collinear singularity arising from the integration where one of the final state partons becomes collinear with one of the initial state partons is effectively absorbed into the definition of the parton distributions in the $\overline{\mathrm{MS}}$ scheme.

The procedure for inclusion of the NLO terms into the jet cross section, especially the separation of the singular terms and the soft and collinear subtractions are described in detail by Kunszt and Soper in [7]. In addition, one has to go through massive bookkeeping required to take into account all possible subprocesses. All this is included in the program by Ellis, Kunszt and Soper for $d\sigma_{\mathrm{jet}}/dp_T dy$, which we have used to obtain the results discussed in the following sections. We have linked the 'Jet'-program (version 3.1) with PDFLIB [10] in order to study the effects of different parton distribution functions.

RESULTS

We first compare the NLO QCD jet cross section to the CERN and Fermilab data at different energies. Unless otherwise mentioned, in the computations we will use the parton distribution set MRS D−' [11]. Also, we have always chosen the renormalization scale in the running coupling constant and the factorization scale in the parton distributions to be the same.

In Fig. 1 we have plotted the Fermilab CDF data for the one-jet cross section $d\sigma/dE_T d\eta$ in $p\bar{p}$ collisions at $\sqrt{s} = 1.8$ TeV [4] as a function of the jet transverse energy. Since we neglect all masses, we replace E_T by p_T and η by y. In the CDF experiment, a jet size $R = 0.6$ was used, which was also chosen for the NLO computation. The data represent jets with $0.1 < |\eta| < 0.7$, so we show curves with two different rapidities: the solid curve for $y = 0$ and the dashed one for $y = 0.7$. Note that we have not done y-averaging as in the data. Note also that we have *not* done any scale optimization, we merely plot the results with fixed scale choices. The solid and dashed curves are the calculations with $\mu = p_T$, but for comparison,

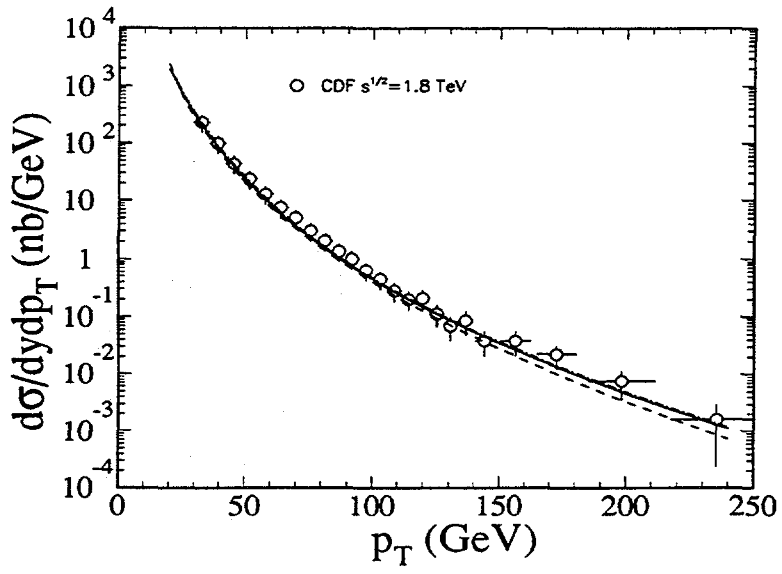

Figure 1: The NLO one-jet cross section $d\sigma/dp_Tdy$ vs. the jet transverse momentum p_T in $p\bar{p}$ collisions at $\sqrt{s} = 1.8$ TeV. The curves are for $y = 0$, $\mu = p_T$ (solid); for $y = 0$, $\mu = p_T/2$ (dot-dashed), and for $y = 0.7$, $\mu = p_T$ (dashed). The CDF data are from [4]. The jet size is $R = 0.6$ for the QCD curves and in the data. In the NLO calculation, we use MRS D–' parton distributions [11].

we also plot the result with $y = 0$, $\mu = p_T/2$ with the dot-dashed curve.

In Fig. 2 the CERN UA1 [2] and UA2 [1] inclusive jet data from $p\bar{p}$ collisions at $\sqrt{s} = 546$ GeV are shown together with the NLO QCD result. In the UA1 data and in the QCD prediction the jet size is $R = 1.0$. The UA1 data is averaged over $|\eta| < 0.7$, the UA2 data over $|\eta| < 0.85$, while the theoretical curves have $y = 0$. Again, we show the cross sections with two fixed scale choices: $\mu = p_T$ for the solid curve and $\mu = p_T/2$ for the dashed one. In the same figure we have also plotted the UA1 minijet data for $\sqrt{s} = 500$ GeV [3], as well as the corresponding NLO QCD predictions with the same scale choices and notations as above.

In Fig. 3 we plot the UA1 "minijet" data in $p\bar{p}$ collisions at $\sqrt{s} = 200$ GeV [3]. The NLO QCD result with $\mu = p_T$ is shown by the solid line. The jet size is $R = 1.0$. The minijet data is averaged over $|\eta| < 1.5$, the NLO curve has $y = 0$. The prediction with a scale choice $\mu = p_T/2$ is shown by the dashed line. Note that throughout the computation we have used $N_f = 5$ for quark flavors with the corresponding $\Lambda^{(5)}_{QCD}$ of the parton distribution set, even though with the scale $\mu = p_T/2$ one should actually have $N_f = 4$ for the lowest p_T bins. However, since our main interest here lies in the large p_T jets, we have not corrected for this.

In order to compare the results also to jet data from pp collisions, we plot the AFS data [12] at $\sqrt{s} = 63$ GeV and the NLO prediction in Fig 4. The curve shown here is with $R = 1.0$, $y = 0$ and $\mu = p_T$.

Next, we study the dependence of the NLO jet cross section on the choice

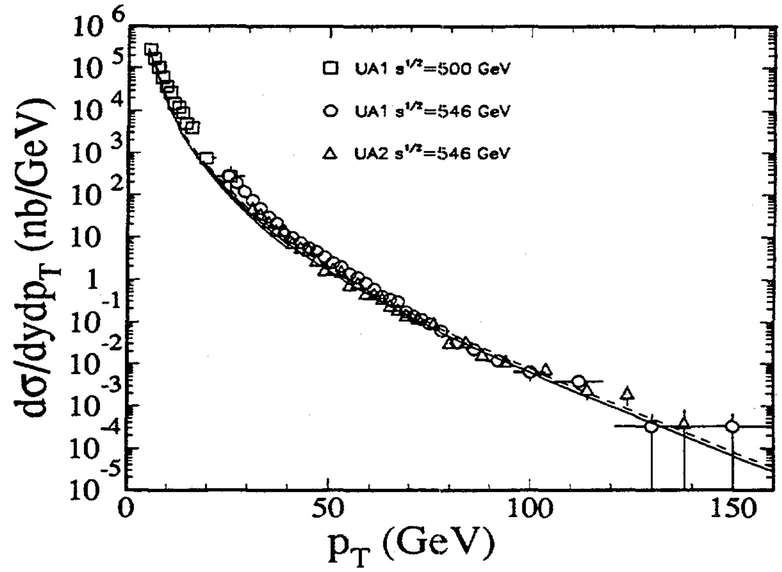

Figure 2: The NLO one-jet cross section $d\sigma/dp_Tdy$ at $y = 0$ in $p\bar{p}$ collisions at $\sqrt{s} = 500$ GeV (5 GeV< p_T <40 GeV) and at $\sqrt{s} = 546$ GeV (20 GeV< p_T < 160 GeV). The solid curves are with $\mu = p_T$, the dashed ones with $\mu = p_T/2$, and $R = 1.0$ for all curves. The UA1 and UA2 data shown here are from [1, 2, 3].

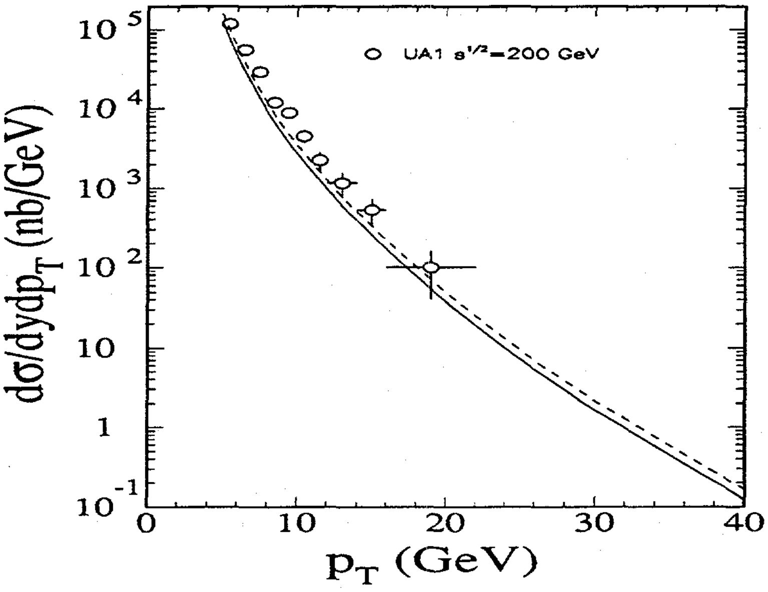

Figure 3: As Fig. 2 but for $\sqrt{s} = 200$ GeV. The data are from [3].

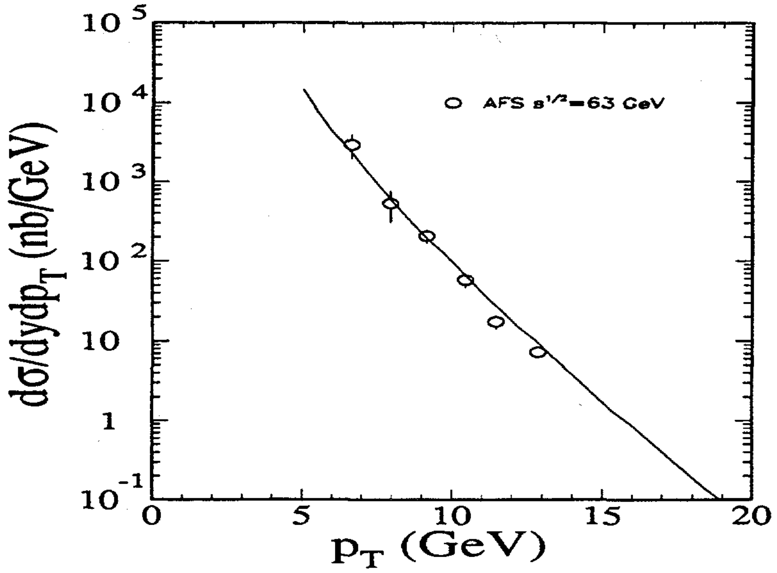

Figure 4: The NLO one-jet cross section $d\sigma/dp_T dy$ at $y = 0$ in pp collisions at $\sqrt{s} = 63$ GeV. In the QCD calculation $R = 1.0$ and $\mu = p_T$. The AFS data are from [12].

of parton distributions. The calculations above were done by using the set MRS D−' (in the $\overline{\text{MS}}$ scheme) since this set seems to be in agreement with the recent HERA data [13]. We have repeated the NLO calculation with other sets of parton distributions for $p\bar{p}$ at $\sqrt{s} = 1.8$ TeV with $y = 0$, $\mu = p_T$ and $R = 0.6$. We divide the experimental data and the calculated cross sections by the results with the MRS D−' set. The ratios are shown in Fig 5. as functions of p_T. The solid line is for GRV HO [14], the dashed line for CTEQ2pm [15] and the dot-dashed line for MRS D0' [11]. As can be seen from the figure, the difference in the kinematical region considered is at most 15-20%, and would be barely visible in the logarithmic plot.

Finally, we come to the main goal of our study, *i.e.* to calculate jet cross sections in pp collisions at RHIC and LHC energies. We will fix $y = 0$, $\mu = p_T$, $R = 1.0$, and use the MRS D−' parton distributions. In Fig. 6 we show the result for $\sqrt{s} = 200$ GeV, which is the maximum center-of-mass energy for RHIC $Au + Au$ collisions. In Fig. 7 the jet cross section is computed for the RHIC pp mode, $\sqrt{s} = 500$ GeV. In both figures, the solid curve is the NLO calculation. To study the theoretical K-factor ($\equiv$ NLO/LO), we also show the Born cross section in the dashed curves. In Fig. 8, we show the results for the maximum planned energy in LHC $Pb + Pb$ collisions, $\sqrt{s} = 5.5$ TeV, and for the LHC pp mode at $\sqrt{s} = 14$ TeV. We also give the LO result in dashed lines. The NLO and LO results for the four different energies are presented in Tables 1-3, where we also give the numerical (statistical) errors from the 'Jet'-program we are using.

To better illustrate the dependence of the results on the scale choice, we follow Ellis *et al.* and present in Figs. 9 and 10 the NLO and LO results as functions

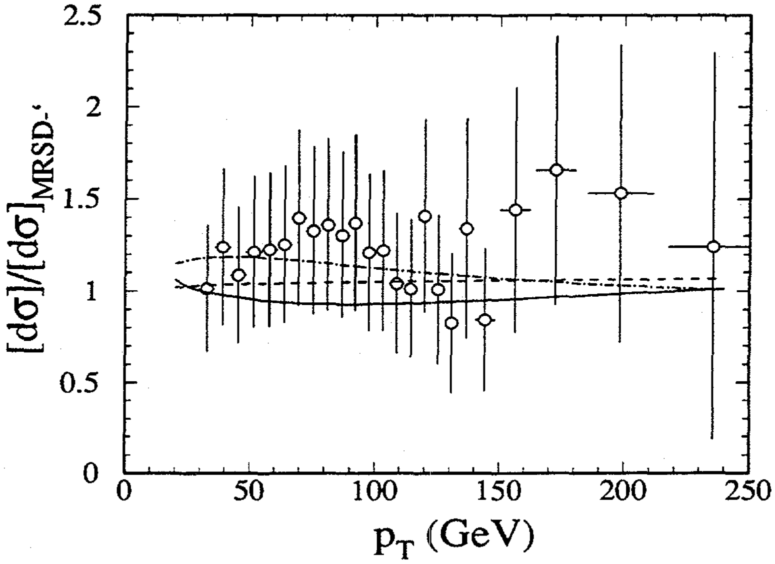

Figure 5: Dependence of the NLO one-jet cross section on the parton distributions for $p\bar{p}$ collisions at $\sqrt{s} = 1.8$ TeV at $y = 0$ and with $R = 0.6$, $\mu = p_T$. The cross sections calculated with GRV HO [14] (solid), CTEQ2pm [15] (dashed) and MRS D0' [11] (dot-dashed), and the CDF data [4] are normalized by the calculation with MRS D−' [11] set of parton distributions.

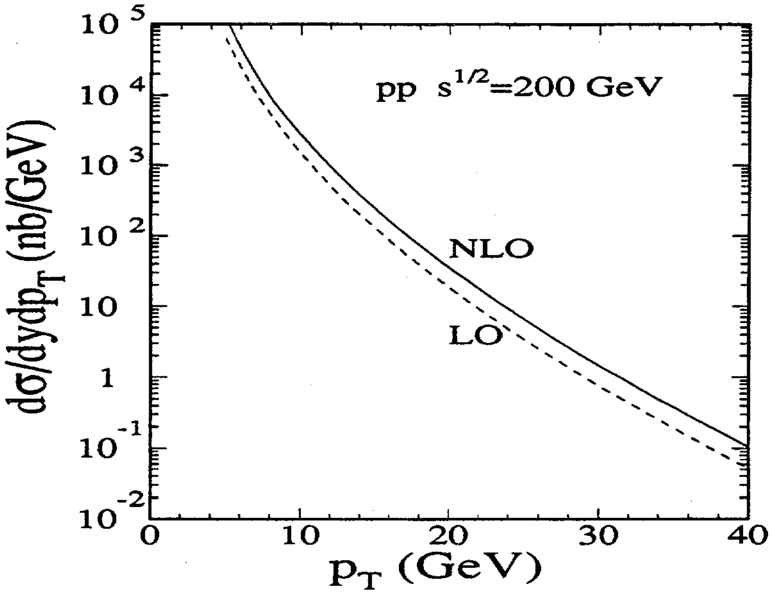

Figure 6: The one-jet cross section $d\sigma/dp_Tdy$ vs. p_T at $y = 0$ in pp collisions at $\sqrt{s} = 200$ GeV, as predicted by the NLO (solid) and LO (dashed) calculations with $\mu = p_T$. For the parton distributions, the set MRSD−' was used. For the NLO calculation $R = 1.0$.

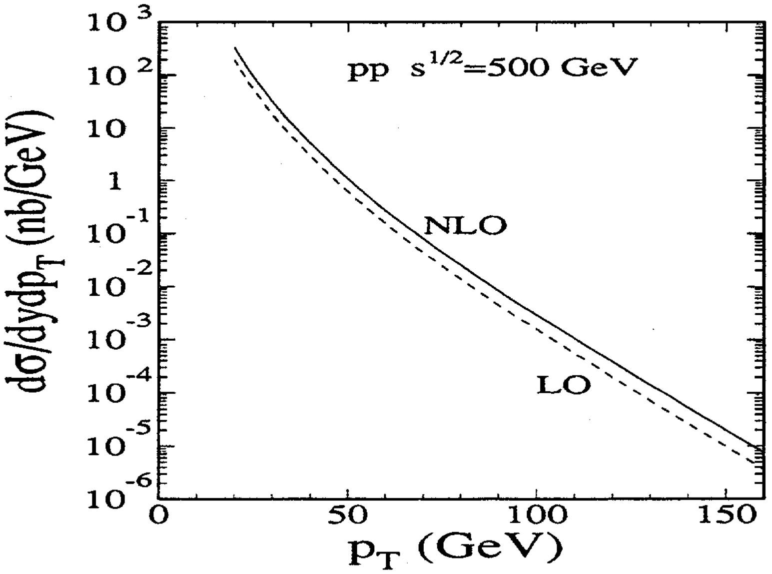

Figure 7: As Fig. 6 but for $\sqrt{s} = 500$ GeV.

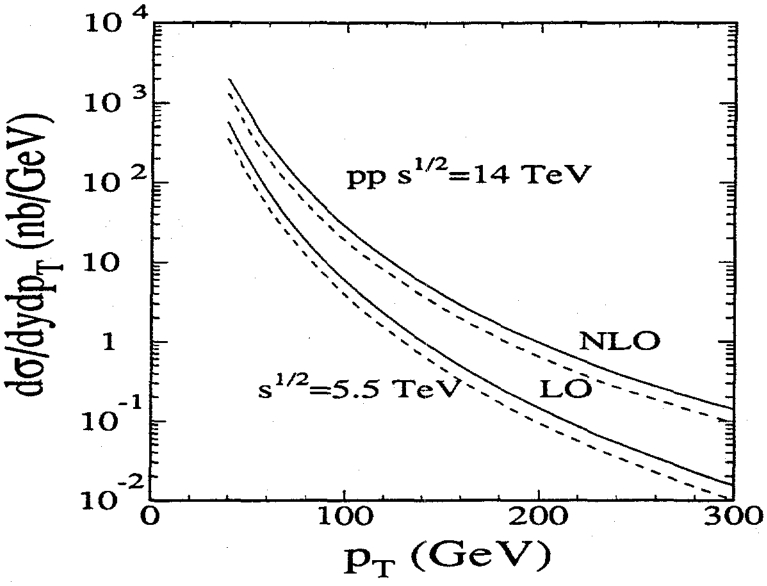

Figure 8: As Figs. 5-6 but for $\sqrt{s} = 5.5$ TeV (lower set of curves) and for $\sqrt{s} = 14$ TeV (upper set of curves). Again, the NLO (LO) results are shown by the solid (dashed) curves.

of the scale choice. We consider two fixed transverse momenta for both $\sqrt{s} = 200$ GeV and $\sqrt{s} = 5.5$ TeV, and vary μ between $0.2p_T$ and $2p_T$.

DISCUSSION AND CONCLUSIONS

An overall conclusion from the comparison to the data is that the NLO QCD prediction is successful in reproducing the observed energy dependence, shape, and absolute magnitude of the data. Certainly, within the (systematic) errors given by the experiments, the agreement between the data and the NLO results is good. What is remarkably different from the Born cross sections, is that no K-factors are used, and the results from experiments using different jet sizes are directly compared with the corresponding NLO predictions.

However, especially in comparison to the UA1 data at $\sqrt{s} = 500$ GeV and 546 GeV, there are slight deviations: the NLO prediction seems to fall below the measured points in Figs. 2 and 3. This could be due to the following uncertainties. The jet definition and jet finding algorithms in different experiments differ slightly from each other, and from what is used by Ellis *et al.* Moreover, since the experiments are observing final state hadrons, not partons, there exists also a nonperturbative uncertainty related to the hadronization of the partons. In their study [6], Ellis *et al* estimated an uncertainty $\sim 6\,\mathrm{GeV}/p_T$ resulting from a nonperturbative uncertainty of 1 GeV in the jet transverse energy. This becomes relatively larger at small p_T, and is therefore typically more in the ranges of p_T measured by UA1. Also, the size

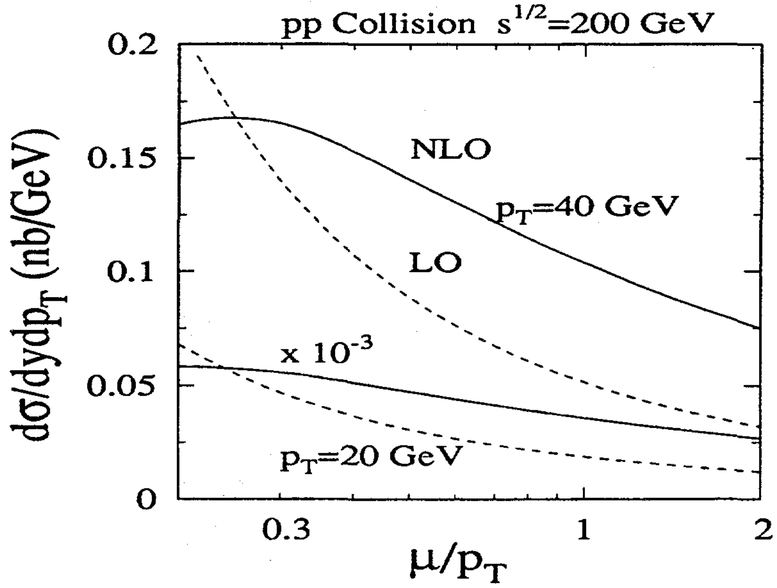

Figure 9: The dependence of the NLO (solid) and LO (dashed) one-jet cross sections on the scale choice μ. The curves shown are for pp collisions at $\sqrt{s}$ = 200 GeV, $y = 0$. The p_T is fixed to 40 GeV (upper set of curves) and to 20 GeV (lower set of curves, note the multiplication by 0.001). For the NLO calculation $R = 1.0$.

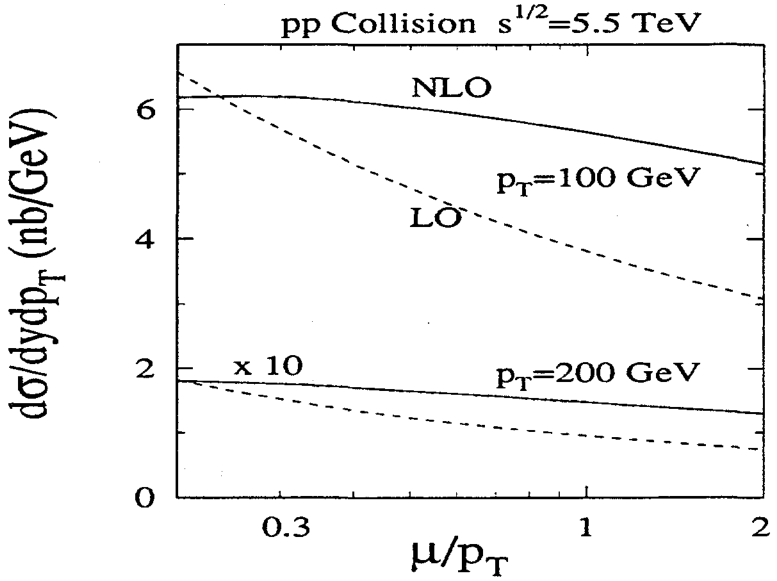

Figure 10: As Fig. 9 but for $\sqrt{s} = 5.5$ TeV, and for the p_T fixed to 100 GeV (upper set of curves) and to 200 GeV (lower set of curves, note the multiplication by 10).

of the jet is larger in the UA1 than in the CDF experiment. With a larger jet size, the nonperturbative uncertainty is also expected to be larger.

On the perturbative side, we expect a residual perturbative uncertainty to be related to the scale dependence of the results. As clearly seen in Figs. 9 and 10, and as discussed by Ellis *et al.*, inclusion of the NLO terms decreases this uncertainty from the LO case. For the NLO calculation at $\sqrt{s} = 200$ GeV with $\mu = p_T$ and with p_T fixed as in Fig. 9, the uncertainty is $\lesssim 60$ %. At $\sqrt{s} = 5.5$ GeV, as shown in Fig. 10, the uncertainty is $\lesssim 20$ %. The LO results clearly have a stronger scale dependence.

As shown in Fig. 5 for $\sqrt{s} = 1.8$ TeV, the theoretical uncertainty due to the parton distributions is at most 20 %. We expect this conclusion to hold for large p_T jets over a wide range of $\sqrt{s}$. However, with smaller p_T and larger $\sqrt{s}$, we expect this uncertainty to increase. Certainly, the results from HERA will help by excluding parton distributions which fail to explain the data from deep inelastic scattering.

An interesting result from Figs. 6-8 is that the Born cross section multiplied by a constant factor, $K \sim 2$ for $\sqrt{s} = 200$, 500 GeV and $K \sim 1.5$ for $\sqrt{s} = 5.5$ and 14 TeV, seems to account for the full result amazingly well over the whole range of p_T considered. Note that these numbers hold exactly only for the scale choice $\mu = p_T$. In general, however, the K-factor depends on the scale choice and especially on the jet size, so a general K-factor cannot be given. In Figs. 9 and 10 the scale dependence of the K-factor is explicitly demonstrated.

To conclude, we have calculated the inclusive one-jet cross sections by using the NLO calculation by S.D. Ellis, Z. Kunszt and D.E. Soper [5, 6, 7]. We have compared the NLO results to the CERN and the Fermilab jet data from $p\bar{p}$ and pp collisions at various energies. We have given the NLO predictions for pp collisions at RHIC and LHC energies and studied the dependence of the results on the scale choices and on the parton distributions. Also the K-factors have been studied. Our final conclusion is that due to the NLO QCD calculations [5, 6, 7, 8] the theoretical inclusive cross sections for large p_T jet production are well under control. The theoretical perturbative uncertainties have greatly been reduced by the inclusion of the NLO terms. We hope that together with the recent data from HERA, the jet measurements could be used to determine the gluon distributions in protons and, ultimately, in nuclei.

Acknowledgements

We thank S. D. Ellis and D. E. Soper for providing us with the program for calculating the NLO one-jet cross sections. We also thank them for discussions and helpful comments. We thank the theory group of CERN, and KJE thanks the Nuclear Theory Group of Lawrence Berkeley Laboratory for the hospitality during the time this study was completed. KJE also thanks the Academy of Finland for financial support. This work was supported by the Director, Office of Energy Research, Division of Nuclear Physics of the Office of High Energy and Nuclear Physics of the U.S. Department of Energy under Contract No. DE-AC03-76SF00098.

References

[1] UA2 Collaboration, J. A. Appel *et al.*, Phys. Lett. **B160**, 349 (1985).

[2] UA1 Collaboration, G. Arnison *et al.*, Phys. Lett. **B172**, 461 (1986).

[3] UA1 Collaboration, C. Albajar *et al.*, Nucl. Phys. **B309**, 405 (1988).

[4] CDF Collaboration, F. Abe *et al.*, Phys. Rev. Lett. **62**, 613 (1989).

[5] S. D. Ellis, Z. Kunszt and D. E. Soper, Phys. Rev. Lett. **62**, 726 (1989); Phys. Rev. D **40**, 2188 (1989).

[6] S. D. Ellis, Z. Kunszt and D. E. Soper, Phys. Rev. Lett. **69**, 1496 (1992).

[7] Z. Kunszt and D. E. Soper, Phys. Rev. D **46**, 192 (1992).

[8] F. Aversa, P. Chiappetta, M. Greco and J. Ph. Guillet, Phys. Rev. Lett. **65**, 401 (1990), Z. Phys. C **49**, 459 (1991).

[9] R. K. Ellis and J. C. Sexton, Nucl. Phys. **B269**, 445 (1986).

[10] H. Plothow-Besch, *PDFLIB: Nucleon, Pion and Photon Parton Density Functions and α_s Calculations*, User's Manual - Version 4.15, W5051 PDFLIB, 1993.11.30, CERN-PPE.

[11] A. D. Martin, W. J. Stirling and R. G. Roberts, Phys. Lett. **B306**, 145 (1993).

[12] AFS Collaboration, T. Åkesson *et al.*, Phys. Lett. **B123**, 133 (1983).

[13] H1 Collaboration, I. Abt *et al.*, Nucl. Phys. **B407** (1993) 515; Zeus Collaboration, M. Derrick *et al.*, Phys. Lett. **B 316** (1993) 412.

[14] M. Glück, E. Reya and A. Vogt, Z. Phys. C **53**, 127 (1992).

[15] CTEQ Collaboration, J. Botts *et al.*, to be published.

$d\sigma_{\text{jet}}/dp_T dy$ (nb/GeV) $y = 0$, pp, $\sqrt{s} = 200$ GeV		
p_T/GeV	NLO	LO
5.0	0.1227E+06	0.6277E+05
6.2	0.3891E+05	0.2079E+05
7.4	0.1441E+05	8042.
8.6	6281.	3525.
9.8	3082.	1685.
11.0	1611.	858.7
12.2	870.1	461.2
13.4	486.8	258.7
14.7	283.0	150.3
15.9	170.3	90.05
17.1	105.5	55.42
18.3	66.79	34.91
19.5	43.06	22.41
20.7	28.15	14.61
21.9	18.61	9.649
23.1	12.42	6.443
24.3	8.369	4.347
25.5	5.695	2.963
26.7	3.914	2.039
27.9	2.718	1.416
29.1	1.907	0.9918
30.3	1.349	0.6997
31.6	0.9626	0.4968
32.8	0.6912	0.3547
34.0	0.4990	0.2546
35.2	0.3619	0.1835
36.4	0.2636	0.1329
37.6	0.1926	0.9654E-01
38.8	0.1412	0.7039E-01
40.0	0.1038	0.5149E-01

Table 1.

The one-jet cross sections from Fig. 6. The numerical (statistical) error in the NLO calculation is expected to be less than 6%, and in the LO calculation less than 2 %.

$d\sigma_{\rm jet}/dp_Tdy$ (nb/GeV) $y = 0$, pp, $\sqrt{s} = 500$ GeV		
p_T/GeV	NLO	LO
20.0	339.2	201.1
24.8	100.3	58.05
29.7	34.63	19.81
34.5	13.58	7.725
39.3	5.843	3.297
44.1	2.670	1.505
49.0	1.278	0.7267
53.8	0.6428	0.3663
58.6	0.3377	0.1909
63.4	0.1833	0.1023
68.3	0.1017	0.5615E-01
73.1	0.5740E-01	0.3145E-01
77.9	0.3286E-01	0.1792E-01
82.8	0.1905E-01	0.1035E-01
87.6	0.1118E-01	0.6058E-02
92.4	0.6641E-02	0.3582E-02
97.2	0.3985E-02	0.2137E-02
102.1	0.2412E-02	0.1284E-02
106.9	0.1470E-02	0.7764E-03
111.7	0.9012E-03	0.4716E-03
116.6	0.5545E-03	0.2874E-03
121.4	0.3422E-03	0.1757E-03
126.2	0.2116E-03	0.1076E-03
131.0	0.1310E-03	0.6602E-04
135.9	0.8117E-04	0.4054E-04
140.7	0.5032E-04	0.2492E-04
145.5	0.3120E-04	0.1532E-04
150.3	0.1934E-04	0.9422E-05
155.2	0.1199E-04	0.5795E-05
160.0	0.7428E-05	0.3563E-05

Table 2.

The one-jet cross sections from Fig. 7. The numerical (statistical) error in the NLO calculation is expected to be less than 3%, and in the LO calculation at most 1%.

$d\sigma_{\rm jet}/dp_T dy$ (nb/GeV) at $y = 0$, pp				
$\frac{p_T}{\rm GeV}$	$\sqrt{s} = 5.5$ TeV		$\sqrt{s} = 14$ TeV	
	NLO	LO	NLO	LO
39.3	575.4	360.7	1999.	1295.
49.0	205.3	127.3	795.3	484.8
58.6	85.35	54.32	342.9	216.1
68.3	39.49	25.77	168.6	108.3
77.9	20.20	13.38	91.09	58.79
87.6	11.21	7.469	52.10	34.04
97.2	6.632	4.405	31.65	20.90
106.9	4.109	2.721	20.19	13.49
116.6	2.631	1.746	13.33	9.030
126.2	1.732	1.155	9.054	6.200
135.9	1.171	0.7830	6.318	4.344
145.5	0.8126	0.5428	4.523	3.102
155.2	0.5771	0.3838	3.310	2.256
164.8	0.4182	0.2763	2.470	1.671
174.5	0.3083	0.2023	1.875	1.260
184.1	0.2306	0.1503	1.444	0.9651
193.8	0.1746	0.1133	1.127	0.7508
203.4	0.1337	0.8659E-01	0.8903	0.5923
213.1	0.1035	0.6701E-01	0.7110	0.4733
222.8	0.8092E-01	0.5246E-01	0.5736	0.3827
232.4	0.6391E-01	0.4153E-01	0.4673	0.3129
242.1	0.5094E-01	0.3320E-01	0.3843	0.2584
251.7	0.4095E-01	0.2677E-01	0.3189	0.2154
261.4	0.3318E-01	0.2174E-01	0.2669	0.1811
271.0	0.2708E-01	0.1777E-01	0.2250	0.1533
280.7	0.2226E-01	0.1461E-01	0.1910	0.1305
290.3	0.1840E-01	0.1207E-01	0.1632	0.1117
300.0	0.1530E-01	0.1001E-01	0.1402	0.9604E-01

Table 3.

The one-jet cross sections from Fig. 8. The numerical (statistical) errors in the NLO calculations are expected to be less than 7.5 % (and less than 2 % at $p_T \gtrsim 110$ GeV). In the LO calculations, the statistical errors should be at most 3 %.

NUCLEAR OVERLAP FUNCTIONS

K. J. Eskola[a], R. Vogt[b] and X.-N. Wang[b]

[a]*Laboratory of High Energy Physics, P.O.Box 9*
FIN-00014, University of Helsinki, Finland

[b]*Nuclear Science Division, MS 70A-3307*
Lawrence Berkeley Laboratory,
University of California, Berkeley, California 94720

A three parameter Wood–Saxon shape is used to describe the nuclear density distribution,

$$\rho_A(r) = \rho_0 \frac{1+\omega(r/R_A)^2}{1+\exp((r-R_A)/z)} , \tag{1}$$

where R_A is the nuclear radius, z is the surface thickness, and ω allows for central irregularities. The electron scattering data of Ref. [1] is used where available for R_A, z, and ω. When data is unavailable, the parameters $\omega = 0$, $z = 0.54$ fm and $R_A = 1.19A^{1/3} - 1.61A^{-1/3}$ fm are used. The central density ρ_0 is found from the normalization $\int d^3r\rho_A(r) = A$. For results with other nuclear shape parameterizations, see the appendix of Ref. [2]. The nuclear shape parameters are given in Table 1.

In minimum bias (impact parameter averaged) AB collisions we expect the production cross section for these hard processes to grow approximately as

$$\sigma_{\mathrm{AB}} = \sigma_{pp}(AB)^\alpha , \tag{2}$$

where $\alpha \equiv 1$ when no nuclear effects are included. However, central collisions are of the greatest interest since it is there that high energy density effects are most likely to appear. Central collisions contribute larger than average values of E_T to the system, in the 'tail' of the E_T distribution, $d\sigma/dE_T$. We would like to determine which impact parameters are important in the high E_T tail, *i.e.* what range of b may be considered central. Considering only geometry, the inclusive production cross section increases as $d\sigma_{\mathrm{AB}} = d\sigma_{pp}T_{\mathrm{AB}}(b)d^2b$ and the average produced number

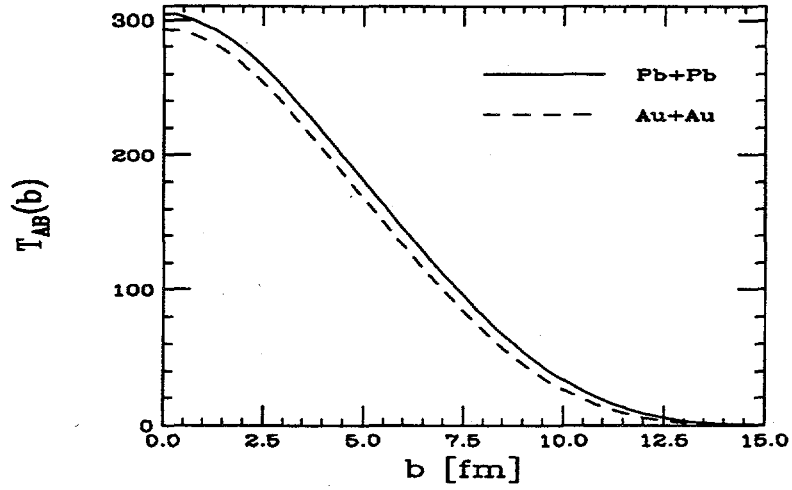

Figure 1: The nuclear overlap function $T_{\rm AB}(b)$ as a function of impact parameter b for Pb+Pb and Au+Au.

of hard probes grows as $d\overline{N}_{\rm AB}(b) = T_{\rm AB}(b) d\sigma_{pp}$ where $T_{\rm AB}(b)$ is the nuclear overlap integral,

$$T_{\rm AB}(\vec{b}) = \int d^2s\, T_{\rm A}(\vec{s})\, T_{\rm B}(\vec{b} - \vec{s}) \ , \tag{3}$$

and $T_{\rm A} = \int dz \rho_A(z, \vec{s})$ is the nuclear profile function. The nuclear overlap functions for Pb+Pb and Au+Au collisions are shown in Fig. 1 as a function of impact parameter. Integrating $T_{\rm AB}$ over all impact parameters we find

$$\int d^2b\, T_{\rm AB}(b) = AB \ . \tag{4}$$

The central fraction $f_{\rm AB}$, equivalent to the fraction of the total geometric cross section involved in a central collision, is defined as

$$f_{\rm AB} = \frac{2\pi}{AB} \int_0^{b_c} b\, db\, T_{\rm AB}(b) \ , \tag{5}$$

where b_c is the central impact parameter and $b < b_c$ are central. To make a similar 'centrality cut' in pA collisions, the fraction

$$f_{\rm A} = \frac{2\pi}{A} \int_0^{b_c} b\, db\, T_{\rm A}(b) \tag{6}$$

would be used. Fig. 2, taken from Ref. [3], shows the increase of $f_{\rm AB}$ with b_c for several symmetric systems. Note that $f_{\rm AA} \approx 1$ when $b_c \approx 2R_A$. For example, if we choose $\sigma_{\rm central} = 0.1\sigma_{\rm total}$, this corresponds to $b_c = 2.05$ fm in Au+Au collisions and $b_c = 1.05$ fm in O+O collisions. If we instead chose $\sigma_{\rm central} = 0.01\sigma_{\rm total}$ then

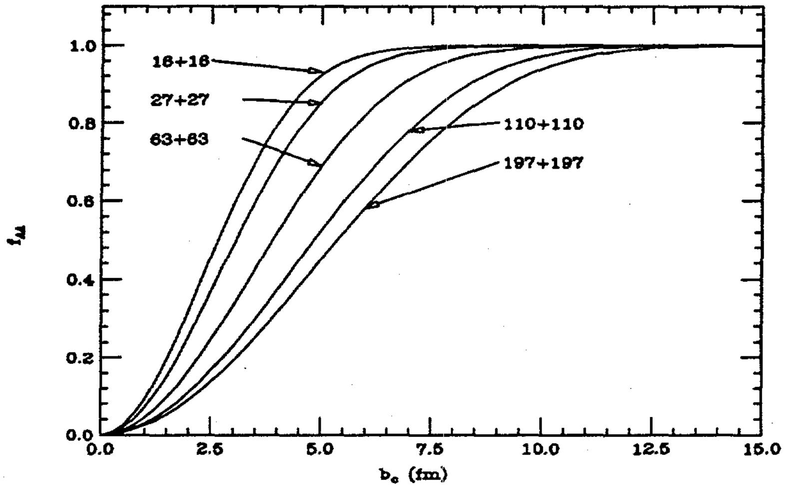

Figure 2: The central fraction of the total geometrical cross section as a function of the impact parameter cut b_c.

$b_c = 0.52$ fm in Au+Au and $b_c = 0.33$ fm in O+O collisions. In Table 2 we give the value of the overlap integral at $b = 0$ for a variety of colliding nuclei. We also give the integral of $T_{\rm AB}$ corresponding to a 5%, 10%, and 20% centrality cut on $\sigma_{\rm total}$, *i.e.* $f_{\rm AB} = 0.05$, 0.1, and 0.2, labeled f_{AB} in Table 2. Then the cross section for hard probe production in Au+Au collisions with a 10% centrality cut can be obtained by scaling the pp production cross section by $f_{\rm AA}A^2 = 3880$. As a specific example, the average number of $c\overline{c}$ pairs produced at $b = 0$ in Au+Au collisions is $\overline{N}(0) = T_{\rm AB}(0)\sigma^{c\overline{c}}_{\rm total}$. At $\sqrt{s} = 200$ GeV, with MRS D−′ parton distributions, $\sigma^{c\overline{c}}_{\rm total} = 0.344$ mb [4] and $T_{\rm AB} = 29.3$/mb, resulting in $\approx 10 c\overline{c}$ pairs per Au+Au collision.

References

[1] C.W. deJager, H. deVries, and C. deVries, Atomic Data and Nuclear Data Tables **14** (1974) 485.

[2] K.J. Eskola, K. Kajantie, and J. Lindfors, Nucl. Phys. **B323** (1989) 37.

[3] R. Vogt, Atomic Data and Nuclear Data Tables **50** (1992) 343.

[4] P.L. McGaughey *et. al.*, this volume.

A	R_A (fm)	z (fm)	ω	ρ_0 (fm^{-3})
16	2.608	0.513	-0.051	0.1654
27	3.07	0.519	0.	0.1739
40	3.766	0.586	-0.161	0.1699
63	4.214	0.586	0.	0.1701
110	5.33	0.535	0.	0.1577
197	6.38	0.535	0.	0.1693
208	6.624	0.549	0.	0.1600

Table 1: Nuclear shape parameters

$A+B$	$T_{AB}(0)$ (fm^{-2})	$f_{AB} = 0.05$	$f_{AB} = 0.1$	$f_{AB} = 0.2$
16+16	7.88	12.8	25.6	51.2
16+27	11.6	21.6	43.2	86.4
16+40	14.4	32.0	64.0	128.0
16+63	18.9	50.4	100.8	201.6
16+110	24.1	88.0	176.0	352.0
16+197	32.2	157.6	315.2	630.4
16+208	31.8	166.4	332.8	665.6
27+27	17.5	36.4	72.9	145.8
27+40	22.3	54.0	108.0	216.0
27+63	30.0	85.05	170.1	340.2
27+110	39.4	148.5	297.0	594.0
27+197	53.2	265.9	531.9	1063.8
27+208	52.7	280.8	561.6	1123.2
40+40	29.2	80.0	160.0	320.0
40+63	40.5	126.0	252.0	504.0
40+110	55.3	220.0	440.0	880.0
40+197	76.4	394.0	788.0	1576.0
40+208	75.7	416.0	832.0	1664.0
63+63	57.7	198.5	396.9	793.8
63+110	81.9	346.5	693.0	1386.0
63+197	116.1	620.6	1241.1	2482.2
63+208	115.7	655.2	1310.4	2620.8
110+110	124.3	605.0	1210.0	2420.0
110+197	185.4	1083.5	2167.0	4334.0
110+208	186.4	1144.0	2288.0	4576.0
197+197	293.2	1940.4	3880.9	7761.8
197+208	298.2	2048.8	4097.6	8195.2
208+208	304.2	2163.2	4326.4	8652.8

Table 2: Values of $T_{AB}(0)$ and the central multiplicative factor for several colliding systems.